Using high-resolution topography for spatial prioritisation of gully erosion management across catchments of the Great Barrier Reef, Australia

by

Simon John Walker

A thesis submitted for the degree of
Doctor of Philosophy
of the Australian National University
July 2021

Australian
National
University

Statement on the contribution of others

Research funding

Australian Government Research Training Program Domestic Scholarship (AGRTPSD) – Australian National University

PhD top-up scholarship – Commonwealth Scientific and Industrial Research Organisation

Thesis committee

Professor Albert Van Dijk

Dr Scott Wilkinson

Dr Peter Hairsine

Editorial support

Professor Albert Van Dijk

Dr Scott Wilkinson

Dr Peter Hairsine

Dr John Gallant

Dr Shaun Levick

Associate Professor Christian Conoscenti and an additional anonymous reviewer of published chapter 2 and two anonymous reviewers for published chapter 3.

Co-authorship in chapters for peer-reviewed publication

This thesis contains some collaborative work. Throughout the program I was responsible for project conceptualisation, development of methods, data analysis, and synthesis of the work into a publishable format. My supervisory panel, Professor Albert Van Dijk, Dr Peter Hairsine and Dr Scott Wilkinson all contributed to publications and offered a range of editorial support and advice toward improving the scientific quality of the work.

Acknowledgements

Throughout the writing of this dissertation, I have received a great deal of support and assistance. First, I would like to thank my supervisor Professor Albert Van Dijk. Your early encouragement really motivated me to give research my best shot and I'm so happy to have taken this path. Under your supervision I've been exposed to many amazing opportunities, and this has helped me to develop my skills greatly. I'm very grateful for that. I would also like to thank Dr Peter Hairsine and Dr Scott Wilkinson for support and helpful guidance right through the PhD, I feel very lucky to have had such good supervision through my PhD. I'd like to thank my friendly peers at the Fenner School at ANU, especially my friends and officemates Jiawei Hou, Li Zhao and Kan Sin-Ampol for a fantastic few years of friendship and occasional trips away. I would also like to thank Dr Bruce Doran, Dr Geoff Cary and Dr Jamie Pittock for involving me with their teaching over the years, I have always really enjoyed that aspect of the PhD. Most importantly I would like to thank my amazing wife Kathryn for always supporting me throughout the process, encouraging me every step of the way.

Abstract

The Great Barrier Reef (GBR) running along ~2 000km of the north-eastern coast of Australia is a UNESCO World Heritage site and is the largest living structure on Earth. The GBR is at the forefront of environmental issues currently faced by Australia, with significant economic, environmental, social, and cultural value. Terrigenous fine sediment affects water quality in the GBR and contributes to the degradation of significant marine environments. Gully erosion is believed to be an important contributor of this fine sediment, and this has garnered recent attention from the Australian Government.

A key challenge to managing gully erosion across catchments of the GBR is the large scale of the combined area (>400 000 km^2). Recent advances in Light Detection and Ranging (LiDAR) have enabled generation of high-resolution (~1 m) digital elevation models (DEMs) over large areas. Over recent years airborne LiDAR data captures have covered many areas of the GBR catchments, with ~50 000 km^2 of topography data with a spatial resolution of 1 m or finer. This newly available source of high-resolution data presents an opportunity to map and predict locations of gully erosion across large areas, reducing the need for time-consuming fieldwork. However, there is a need for further development of suitable methods to exploit this data.

The core aim of this PhD has been to develop a set of tools and algorithms for using high-resolution topography data to map gullies and areas susceptible to future gully erosion. Novel analysis methods were developed into open-source computer programs with a general focus on creating resources to assist researchers and practitioners managing and assessing gully erosion over large areas.

The overall approach is split into to two broad categories of analysis. The first focuses on gully management at small scales (tens of square kilometres), and the second focuses on large scales (hundreds to thousands of square kilometres). The algorithms developed from each of the two halves are designed to work in unison to prioritise gully erosion management first at large scales and subsequently at small scales.

This PhD has developed and assessed novel methods for using high-resolution topography data to map and predict gully erosion across catchments of the GBR. A

core focus has been on proposing ‘standard’ methods for computing the required inputs for topographic models of gully occurrence in the landscape. The broader goal of this was to help move the field closer to a set of tools that allow researchers to readily compare model results between landscapes and regions free of bias introduced by variations in sampling procedures. This work has highlighted the potential benefit of using high-resolution topography, particularly airborne LiDAR, but that consistency with methodologies is key to enabling comparisons across landscapes. The methods developed also have applications to other environments, particularly semi-arid regions, and have all been developed in open-source programming languages to help facilitate adoption. Results from applying two different topographic models of gullies showed that land clearing and a transition from natural forests to agricultural landscapes has likely led to increased gullying across catchments of the GBR. This finding is consistent with other studies globally and provides important context for gully management priorities in this region.

CONTENTS

List of tables

List of figures

Chapter 1: Introduction

1.1 Brief history and physiography of the Great Barrier Reef

The Great Barrier Reef (GBR) is the world's largest coral reef ecosystem and stretches ~2 300 km along Australia's north-eastern coast. The area was established as the Great Barrier Reef Marine Park in 1975 and received World Heritage status in 1981 (GBRMPA, 2017). Reef growth on the central GBR is estimated to have initiated ~600 000 years ago followed by stages of growth driven by large eccentricity-dominated sea level changes with a periodicity of ~100 ka (Alexander et al., 2001). The current reef morphology initiated ~8 500 years ago following post-glacial sea level changes, and growth proceeded through the mid to late-Holocene (Perry and Smithers, 2011) at a rate of roughly 6 m ka^{-1} (Hutchings et al., 2019). Throughout most of the Holocene evolution of the GBR, the land draining the reef was used by indigenous peoples with anthropogenic land alteration largely limited to burning(Gilbert and Brodie, 2001). However, with the arrival of Europeans ~200 years ago, this area has undergone significant land use modification and seen a large increase in population (Gilbert and Brodie, 2001, Saxton et al., 2012). Today, grazing lands approximate 75% of the broader GBR catchment area, 13% is used for conservation and 1% for cane sugar farming (Waters et al., 2014). Over the last ~150 years, land use changes implemented by European settlers have increased fine sediment loads entering the GBR lagoon, but this increase has varied across regions (Waterhouse et al., 2012).

The GBR lagoon is a relatively shallow water body with an average depth of 35 m for its inshore waters (GBRMPA, 2017). Water movement along the coastal margin is dominated by south to north wind-driven processes, and along the seaward margin water movement follows the prevailing north to south direction of the East Australian Current (Furnas and Mitchell, 1997). Large rivers along the GBR coastline deliver land-based sediments to the lagoon (Belperio, 1983, Devlin and Brodie, 2005, Fabricius et al., 2014). The general pattern of water movement disperses sediments in a north-westerly direction, leading to entrapment within northward-facing bays (Neil et al., 2002). The same pattern of water movement also largely restricts the extent of this sediment to coastal and inner shelf regions to a depth of ~20 m (Belperio, 1983). However, under conditions of light offshore winds, freshwater river plumes can carry sediment beyond this inner shelf region and out onto mid and outer-shelf reefs (Devlin et al., 2001).

1.2 Post-European land use change and erosion

Land use changes occurring post-European settlement have been considered a key driver of increased sediment and nutrient loads entering the GBR lagoon (Belperio, 1983, Haynes and Michalek-Wagner, 2000, McCulloch et al., 2003). Seminal research by McCulloch et al. (2003) used Barium (Ba) / Calcium (Ca) ratios in coral skeletons (a proxy measure for sediment runoff in flood plumes) to show

that since European settlement in ~1870, some coral communities of the inner GBR have experienced sediment fluxes of five to ten times pre-European levels. This finding was later reinforced by Lewis et al. (2007) who found, by examining temporal patterns of manganese (Mn) concentrations in *Porites* corals, that the introduction of grazing animals to northeast Australia led to widespread removal of topsoil as indicated by a sudden peak in Mn concentrations recorded in the skeletons of corals. Lewis et al. (2007) found that this transformation took just ~30 years, within the introduction grazing animals, to remove Mn-laden topsoil that had accumulated over thousands of years prior. Later, Kroon et al. (2012) also found that pre-European river concentrations of suspended solids, total nitrogen and total phosphorus have all increased.

Sediment accretion rates at nearshore locations of the GBR lagoon have also been shown to have increased significantly compared with geologic rates. Coates-Marnane et al. (2016) found that sediment accretion rates in Morton Bay over the last 100 years have been 3-9 times greater than geologic rates. Similarly, Lewis et al. (2014) found that sediment accumulation rates at a nearshore site northwest of the mouth of the Burdekin River have increased by a factor of 8 to 10 over the past ~210 years compared with the period ~540 to 210 years BP.

Well-developed coral reef ecosystems typically only exist in regions with low concentrations of suspended particulates and dissolved nutrients (Wolanski, 2000). Coral reefs are generally not found in locations where fine sediment has accumulated because coral larvae are unable to establish on muddy substrata (Hoegh-Guldberg, 2008). The mechanisms by which fine sediments negatively affect marine ecosystems include increased bio-available nutrient loads and associated increased likelihood of Crown-of-Thorns Starfish (CoTS) plagues (Brodie et al., 2005), decreases in thermal tolerance of inshore coral reefs (Wooldridge, 2009), and insufficient photosynthestically available radiation (PAR) resulting from diminished water quality (Rogers, 1990). The impacts can include decreases in coral species richness, growth rates, live coral cover, coral net productivity, calcification rates, and reef accretion rates (Rogers, 1990, Fabricius et al., 2005).

Given the evidence for the geologically recent increase in sediments entering the GBR lagoon from its catchments, and the detrimental impact this potentially has on significant marine ecosystems of the GBR, the Australia Government set a target to stop and reverse the decline of water quality entering the GBR lagoon by 2020 (Waterhouse et al., 2012). A key challenge in addressing erosion-related problems for the GBR is the requirement for scientifically-based catchment sediment reduction targets (Brodie and Waterhouse, 2012). Efforts to alleviate the damaging impacts of fine sediment on the GBR require specific knowledge of the types of erosion and spatial distribution of erosion across the GBR catchment(Hughes et al., 2009). Subsurface sources of fine sediment have been implicated as the most significant sources of sediment affecting water quality in the GBR lagoon (Hughes et al., 2009, Olley et al., 2013, Wilkinson et al., 2013, Hancock et al., 2014), and gully erosion plays an important role in that (Wilkinson et al., 2015a).

1.3 Gully erosion as a source of fine sediment

Hillslope erosion was long assumed to be the most important source of sediment entering the GBR lagoon via the river network (McKergow et al., 2005b). However, more recent evidence has found that for some catchments, riverbanks and gullies may be the most significant source of fine sediments(Hughes et al., 2009). Recent analyses of the Burdekin Basin, considered the biggest source of fine sediment entering the GBR lagoon in modern times (Bartley et al., 2015), found that subsurface sediment sources are the most important (Wilkinson et al., 2013, Bartley et al., 2014a). Specifically, gully erosion, initiated by widespread land clearing and a change to intensive land uses (Aksoy and Kavvas, 2005), was implicated as the likely prevailing subsurface erosion process.

Correct attribution of sources of fine sediment matters because studies from previous parts of Australia have found that incorrect attribution can lead to ineffective action on erosion remediation. For example, (Wasson et al., 2002) found that a large-scale revegetation program around the area of Lake Argyle in north-western Australia was largely unsuccessful due to the prior lack of knowledge about exact sources of fine sediment. They found that ~80% of accumulated sediment in Lake Argyle had in fact come from gullies and not hillslope erosion (as presumed), and this oversight ultimately led to the failure of management strategies to decrease the sedimentation rate of Lake Argyle. Similarly, Olley et al. (2013) found that previous assumptions about surface soil erosion being the major contributing source of sediment entering Princess Charlotte Bay in northern GBR were false, and that their results supported sub-surface sources as the dominant sources of fine sediment. Knowledge of the location of gullies across the GBR catchments, the conditions that permitted their formation and the factors that drive continuing erosion of active gullies is essential if suitable management strategies are to be implemented (Tindall et al., 2014b). Gullies in catchments of the GBR are often categorised as either hillsope gullies or alluvial gullies (Brooks et al., 2009) and this thesis will focus primarily on hillsope gullies due to their ubiquitous prescence across all catchments of the GBR.

1.4 Spatial prioritisation of gully erosion

Previous studies have cited the large spatial scale of erosion in the GBR catchments as being a significant hurdle in achieving measurable outcomes for the GBR (McKergow et al., 2005a). For this reason, it has been suggested that a prioritisation methodology is required to help ensure mitigation strategies focus on targeted areas chosen deliberately for their relatively high rates of erosion and potential for remediation (McKergow et al., 2005b, Wilkinson et al., 2015a). Furthermore, it has also been shown that the catchments contributing the largest total sediment loads (Burdekin and Fitzroy) are not the catchments with the highest area-specific yields (McKergow et al., 2005b), indicating finer-scale knowledge will likely allow for a better understanding of sediment ‘hotspots’. For a prioritisation scheme to work, and for the implementation of effective management strategies, there is a need for

better information on sources of anthropogenic sediment and related erosion processes (Bartley et al., 2014b).

Targeting specific areas for subsurface erosion reduction requires knowledge of the environments in which erosional features occur. For example, soil type has been shown to be correlated with gully presence (Whitford et al., 2010) and severe gullying has been associated specifically with sodic soils(Wong et al., 2010b). The current best estimates of total length of gullies present in the catchments of the GBR is >87 000 km, and gullies across the GBR catchments are responsible for about 40% of total fine sediment (with 30% coming from streambanks and 30% from hillslope erosion) exports to the lagoon (Wilkinson et al., 2015a). Although recent evidence points to subsurface erosion as the most important source of fine sediment exported to the GBR lagoon (Olley et al., 2013, Wilkinson et al., 2013, Wilkinson et al., 2015a), the large area of the GBR catchments, and large length of gully stream networks, creates a significant challenge in constraining the most important areas to target for erosion reduction (McKergow et al., 2005a, Wilkinson et al., 2015a).

Due to commonly limited spatiotemporal measurements and sparsely available data, often some form of modelling is required to analyse sediment contributions from a range of areas (McKergow et al., 2005a, Kinsey-Henderson et al., 2007). Models such as the spatially distributed sediment budget (SedNet) model (Prosser et al., 2001), have been used to model the contribution of hillslope, gully and streambank erosion transported to the GBR (McKergow et al., 2005b, Kroon et al., 2012). SedNet has also been used to estimate potential sediment savings due to various erosion management strategies (Kinsey-Henderson et al., 2007). While such models have been shown to perform reasonably well with end-of-catchment sediment load prediction (Kinsey-Henderson et al., 2007) there are limitations to their ability to resolve finer-scale erosion sources and processes. For example, in Australia many rivers are exposed to increasing sediment loads and this material is deposited on riverbeds over prolonged periods (Post et al., 2005, Wilkinson et al., 2006). With respect to modelling gully erosion, models can also fail to adequately capture the timescales at which gully erosion occurs. Results from recent attempts to map gully locations and assess rates of erosion found that large changes to gully size typically occur in single events of exceptionally intense localised rainfall (Tindall et al., 2014b). This episodic nature of gully erosions has been identified previously. Larcombe and Carter (2004) note that the delivery of new fine sediment to the GBR lagoon is driven primarily by cyclone events, not through gradual processes. (Whitford et al., 2010) suggested that this episodic nature of gully erosion is an important consideration in interpreting the results of models that are not designed to capture this sporadic behaviour. Likewise, Darnell et al. (2012) found that event-based monitoring is important for the GBR because the bulk of water quality pollutants are exported to the GBR during large runoff events.

One reason models such as SedNet struggle to resolve finer-scale erosion sources is their sensitivity to input data. For example, SedNet requires an input Digital Elevation Model (DEM) to derive a stream network (Wilkinson et al., 2009), but the resolution of the DEM can affect the accuracy

of stream delineation(Kinsey-Henderson et al., 2007). This shortcoming in quality of input data also extends to how gullies are treated in the model, and results in gullies often being treated as having a pre-defined cross-sectional area (McKergow et al., 2005b, Kinsey-Henderson et al., 2007). This has been identified as a particularly important issue as previous SedNet modelling studies (e.g. Kinsey-Henderson et al., 2007) have shown only a small response in sediment yield is expected due to gully remediation strategies; however, the same authors note that this observation may be due only to the inability of the model to correctly estimate gully erosion. McKergow et al. (2005a) suggest that the spatial patterns of sediment sources highlighted by models, not just the total river exports, need to be independently verified. This suggestion is echoed by Wilkinson et al. (2013) who point out that these modelled estimates have not been extensively validated against independent measurements. These various issues stand to benefit from more accurate large-scale assessments of gully presence in the landscape.

While there is evidence that sufficient reductions in river fine sediment load can potentially improve water quality and ecosystem health in the GBR lagoon (Fabricius et al., 2014); a recent assessment by Kroon et al. (2016) found the effectiveness of current strategies to reduce sediment and nutrient runoff into the GBR are inadequate, and unlikely to achieve required water quality outcomes. Improving current strategies requires that managers prioritise target areas effectively (Waterhouse et al., 2012), and to do this requires better knowledge of source areas of fine sediment and the processes that drive erosion in those locations (Wilkinson et al., 2013). It follows then that more accurate information across a range of environments will assist managers to make better decisions about erosion reduction strategies and ultimately help improve water quality in the GBR lagoon.

Independent sources of information are required to get a better understanding of the most important sources of fine sediment exported to the GBR lagoon (Wilkinson et al., 2013), and remote sensing offers such a potential independent source of information. Remote sensing of surficial processes is among the leading fields of Earth systems research and has the potential to transform the study of landscape change and evolution over short time periods (DeLong et al., 2012). Remote sensing has been used for a range of assessments related to understanding erosion and sediment runoff into the GBR. Aerial photography and satellite-based optical remote sensing have been used to map and monitor sediment plumes extending out into the GBR lagoon following rainfall events (Devlin and Brodie, 2005, Devlin and Schaffelke, 2009, Fabricius et al., 2014). Satellite-based optical remote sensing has also been used to map gully locations and extent (Knight et al., 2007, Gilad et al., 2012, Tindall et al., 2014b) and to estimate ground cover for input into erosion models (McKergow et al., 2005a, Guerschman et al., 2009). Although these studies have demonstrated that a range of remote sensing methods are suitable for analysing information about gully erosion, they have largely been either restricted to specific areas (e.g. Brooks et al., 2009, Goodwin et al., 2017) or have been problematic due to an array of issues relating to spatial accuracy and adequate resolution (Tindall et al., 2014b).

Linking fine sediment to water quality in the GBR requires a long chain of evidence (Hairsine, 2017). Various lines of evidence (including modelling, geochemical tracing, remote sensing, and field studies) have so far been used to construct a broad picture of gully erosion across the GBR catchments, but additional evidence and lines of inquiry will help to clarify some important points. One new source of data that has potential relevance specifically to gully mapping and modelling is high-resolution topography collected using either airborne light detection and ranging (LiDAR) or structure-from-motion (SfM) photogrammetry.

1.5 Trends in high-resolution topographic analysis

Satellite-based topographic surveys revolutionised our understanding of Earth surface processes. Widespread adoption of global digital elevation models (DEMs) for geomorphic investigation took off with the release of the Shuttle Radar and Topography Mission (SRTM) DEMs in 2004 (Mudd, 2020). With SRTM it became possible to conduct hillslope-scale analyses across large areas. However, the resolution of SRTM (~30 m) and similar, more recent, publicly available near-global DEMs is usually not sufficient to resolve small-scale features, such as gullies, and associated flow patterns (Schumann and Bates, 2018). A resolution of one or a few metres (referred to here as high-resolution) would be more likely to adequately represent such features. More recently, advances in LiDAR have enabled collection of high-resolution DEMs (Goodwin et al., 2017), but these have generally only been available over limited areas (Amatulli et al., 2020). Similarly, advances in structure from motion photogrammetry have contributed to global geomorphic investigations at small scales such as generating high-resolution DEMs river reaches and landslide scars (Tarolli, 2017). However, as with many LiDAR-based studies, these photogrammetry DEMs are typically very limited in spatial extent. New initiatives are starting to address this by collecting, collating, and merging high-resolution DEMs and making them publicly available. For example, the OpenTopography initiative (https://www.opentopography.org/) aims to facilitate community access to high-resolution topographic data and currently has 283 LiDAR and photogrammetric point clouds covering >230 000 km^2 of the United States (Crosby et al., 2020). In Australia, the ELVIS - Elevation and Depth – Foundation Spatial Data portal http://elevation.fsdf.org.au/ contains data from over 236 LiDAR surveys covering an area of >240 000 km^2. With large areas covered by high-resolution DEMs it has become possible to look more closely at some established geomorphic models for which the previous generation of DEM data was too coarse. Recent examples of high-resolution topographic benefitting geomorphic research Models of gully erosion are one such application, and this has potential to contribute valuable information to gully erosion management across catchments of the GBR.

1.6 Topographic studies of gullies using LiDAR

DEMs available for broad areas have not previously had the required spatial resolution to be useful for gully mapping exercises, but higher spatial resolution LiDAR DEMs have recently become more

widespread and accessible (Evans and Lindsay, 2010). Early studies found that using airborne laser altimetry provided benefits in being able to map gullies and channels in difficult to access areas(Ritchie et al., 1994). LiDAR provides a high-resolution data source for the monitoring and quantification of erosion processes (Höfle et al., 2013, Croke et al., 2015, Goodwin et al., 2017) and LiDAR DEMs have been used by various studies for delineating gullies (James et al., 2007, Eustace et al., 2009, Evans and Lindsay, 2010). For mapping gullies, the quality of LiDAR products is such that, at the gully network scale, it provides some of the highest accuracy maps available (James et al., 2007). LiDAR also allows for the monitoring of gully change across varying spatial scales (Goodwin et al., 2017), and gully change quantification over time (Perroy et al., 2010). Perroy et al. (2010) used LiDAR DEMs to also estimate total sediment yield of gullies by subtracting LiDAR DEMs from modelled pre-erosion surfaces. They found that, for this task, Aerial Laser Scanning (ALS) data was the preferred option due to its ability to cover larger areas more easily and better address gully bottom shadowing.

One area of gully modelling that stands to benefit from the proliferation of high-resolution DEMs is gully topographic threshold analysis. Over recent decades analysis of gully topographic thresholds has become ubiquitous among methods to understand the phenomena. Early work by Patton and Schumm (1975) took field observations of gully head positions and showed that simple relationship exists between the catchment area of a gully and the local slope of the land surface above the gully head. Various later studies (e.g. Montgomery and Dietrich, 1988, Montgomery and Dietrich, 1989, Montgomery and Dietrich, 1994, Willgoose, 1994) focused on further developing a theoretical explanation for the earlier field observations made by (Patton and Schumm, 1975). This analysis assumes that the position of a gully head represents a point in the landscape where, under current boundary conditions such as rainstorm intensity and ground cover, channel erosion cannot continue toward the drainage divide (Torri and Poesen, 2014). This transition zone demarcates the boundary where erosive processes move from fluvial erosive to diffusional (Montgomery and Dietrich, 1994, Hancock and Evans, 2006). Many studies, see Torri and Poesen (2014) for a full list, have since used this analysis in various environments to make inferences about the role vegetation, climate, and soils play in determining a threshold of gully incision given certain topographic conditions. Given the widespread use of gully topographic threshold analysis, and the potential benefits high-resolution topography offers, a core focus of the thesis will be on developing and testing a set of computer programs that enable researchers to conduct gully topographic threshold analysis in a fully automated way using the outputs from this thesis.

1.7 Thesis aims and objectives

Sediment eroded from hillslope gullies across catchments of the GBR primarily comes from upslope extension of gully heads (Wilkinson et al., 2013), and gully erosion contributes ~40% of fine suspended sediment exported to the GBR lagoon (Wilkinson et al., 2015a). Newly available high-resolution DEMs offer the opportunity to map and monitor gully head changes at metre-scale

resolutions, thereby enabling enhanced assessment of gully erosion. The core aim of this thesis is to investigate the potential for analysis of high-resolution topography data to contribute valuable information to the spatial prioritisation of gully erosion across catchments of the GBR. Results from these investigations are expected to also apply to other global locations with publicly-available high-resolution topography. The overall approach is split into to two broad categories of analysis. The first focuses on gully management at small scales (tens of square kilometres), and the second focuses on large scales (hundreds to thousands of square kilometres). The algorithms developed from each of the two halves are designed to work in unison to prioritise gully erosion management first at large scales and subsequently at small scales. A broader goal of the work is to bring a higher level of consistency to topographic analyses of gullies, enabling more direct comparisons between studies and regions, and in doing so help the field as a whole progress our understanding of gully erosion.

Specific research objectives are:

Objective 1: Investigate the potential to automatically identify gullies in high-resolution topographic data and use this information to assess relative erosion risk across landscapes.

Objective 2: Establish reliable and reproducible methods to estimate important properties of gullies, including contributing drainage area and gradient of the surrounding hillslope, using high-resolution topographic data.

Objective 3: Assess the potential to fully automate established gully topographic threshold models that have historically required fieldwork to collect the required inputs.

Objective 4: Develop a set of computer programs that work in unison to provide potential prioritisation of gully erosion remediation from regional scales down to the sub-catchment scale.

1.8 Overview of thesis structure

The thesis is composed of two broader components. The first component aims develop methods to compare zones of gully erosion susceptibility within catchments, and the second focuses on methods to compare gully susceptibility between catchments. These two halves are designed to work in unison, allowing assessment of gully erosion first at large scales and subsequently at small scales.

Chapter 2 outlines the development of a computer algorithm for mapping incised landform elements and estimating their potential for future expansion. It uses topographic information including elevation, slope, and profile curvature to identify topographic signatures of incised landform elements and map them across multiple scales. The algorithm concurrently computes landscape position, topographic wetness index and stream power index to isolate areas likely susceptible to future incision. The method was tested across several landscapes including a comparison between cleared and forested hillsides. The aim was to develop a computationally efficient method written in an open-source

programming language. Chapter 2 is presented in the same format as a corresponding published paper in the journal *Geomorphology* (Walker et al., 2020).

Chapter 3 investigates the impact of various DEM processing techniques on the estimation of contributing drainage areas above gully heads. The goal of this study was to determine the best methods for extracting reliable drainage area estimates from high-resolution DEMs as a first step toward a fully automated method for gully topographic threshold analysis (Chapter 5). We examined the impact that different flow routing algorithms, hydrologic enforcement methods and DEM spatial resolution have on drainage area estimation and the related sensitivity of parameter estimates in gully topographic threshold analysis. This involved the development of a computer program for tracing concentrated flow lines downslope of estimated gully head positions to provide reliable and reproducible estimates of drainage area. Chapter 3 is also presented in the same format as a corresponding published paper in the journal *Earth Surface Processes and Landforms* (Walker et al., 2021).

Chapter 4 presents a computer program designed to perform DEM-based geometric characterisation of gully headcuts. The primarily purpose of this algorithm is to automatically locate positions around gully heads from which to estimate the slope of the surrounding soil surface. It is designed to work together with the program presented in Chapter 3, and together offer suggested programmatic methods to estimate the two required inputs for gully topographic threshold analysis (slope of the soil surface around the gully head and its drainage area). Additionally, we use the program to extract gully headcut morphological variables for a large sample of gullies and compare relationships between these variables.

Chapter 5 takes the two algorithms described in Chapter 3 and 4 and combines them with a third computer program designed to determine where gully heads intersect concentrated flow lines across landscapes. These three stand-alone programs form the core requirements of fully automated gully topographic threshold analysis using high-resolution DEMs. The fully automated workflow is applied to 185 km^2 of gullied landscapes across four priority erosion management regions of the GBR (the Wet Tropics, the Burdekin Basin, the Fitzroy Basin, and the Burnett-Mary region). The method is tested for its ability to provide regional-scale assessments of gully erosion susceptibility and results are compared to global studies of topographic thresholds.

Chapter 6 summarises the key findings from the thesis and discusses the potential for the set of developed compute programs to help prioritise gully erosion management activities across catchments of the GBR (and other regions).

Chapter 2: A multi-resolution method to map and identify locations of future gully and channel incision

Walker, S. J., Wilkinson, S. N., Van Dijk, A. I. J. M. and Hairsine, P. B. 2020. A multi-resolution method to map and identify locations of future gully and channel incision. *Geomorphology*, 358, 107115.

Abstract

While channel erosion is recognised as a major, often-dominant, source of river sediment, channel geometry and its change remain impractical to measure for anything but small experimental watersheds. Designing remediation strategies in landscapes affected by channel erosion requires information on the extent and location of current incised channel features, as well as a method to determine locations where incision may occur in the future. We present a multi-resolution algorithm that uses topographic information to concurrently map both existing incised landform elements and areas at risk of future incision. The former uses elevation, slope and profile curvature to identify topographic signatures of incised landform elements, and the latter uses landscape position, topographic wetness index and stream power index to isolate areas likely susceptible to future incision.

We aimed to develop a computationally efficient method capable of operating across a broad range of landscapes. The algorithm was tested in three contrasting environments in eastern Australia with promising results. Sensitivity analysis indicates the method performs reasonably consistently across landscapes, but that outputs become more sensitive as the average slope of the landscape increases. A comparison between cleared and uncleared hillsides suggested that areas indicated at risk of future incision are plausible, and that cleared areas were more susceptible to channel incision.

The only required input is a digital elevation model, and outputs can provide a rapid visual assessment of landscapes affected by incisional erosion. This technique enables the identification of gully erosion and the planning of remediation works across landscapes of thousands of square kilometres. It may assist in prioritisation of works and further insights into the processes associated with channel incision.

2.1 Introduction

Channel incision causes environmental problems in many diverse landscapes across the world (Poesen et al., 2003). Some recent examples include impacts on ecosystem function in upland peatlands of the UK (Evans and Lindsay, 2010), loss of arable land in agricultural watersheds in central Navarre Spain (Casalí et al., 2008), siltation of reservoirs from gullying in the Ethiopian Highlands (Tebebu et al., 2010), and export of fine sediment to the Great Barrier Reef in Australia (Wilkinson et al., 2013). Remediation efforts in such cases would benefit from information on (1) the location and extent of erosive incised features and, (2) the potential for their future development in areas where they do not yet exist.

2.1.1 Automated methods to identify incised channels

Recent publications (e.g. Eustace et al., 2009, Evans and Lindsay, 2010, Höfle et al., 2013, Castillo et al., 2014, Korzeniowska et al., 2018) proposed automated computer-based methods for mapping erosive incised features, such as gullies, in high-resolution digital elevation models (DEMs). Such methods generally use topographic derivatives like slope and curvature along with elevation to assess topographic properties across a DEM grid. These can be combined into a set of “form-defining properties” (Minár and Evans, 2008) to describe elementary forms. Form-defining properties can be further assessed with respect to their local neighborhood and position in the landscape (Schmidt and Hewitt, 2004), creating ‘land elements’ (Minár and Evans, 2008) or ‘landform elements' (MacMillan and Shary, 2009). The landform elements of interest here are incised landform elements (ILEs), primarily gullies. In the Australian context, Speight (1990) define gullies as landform elements presenting as open depressions with short, precipitous walls and gently inclined floors eroded by channeled stream flow.

Automated methods to extract ILEs from DEMs have advantages over manual methods but, require a ruleset defining value thresholds, are susceptible to over-fitting, and are not necessarily transferrable across landscapes (Castillo et al., 2014). Nonetheless, they are necessary for any study assessing incisional erosion across large areas containing a wide range of environments. The first part of our algorithm was developed to address these requirements for automated mapping of ILEs.

2.1.2 Predicting areas at risk of future incision

Spatially predicting potential for future incision is important because early control can avoid further land degradation (Castillo and Gómez, 2016). Topographic indices such as stream power index (SPI) and topographic wetness index (TWI) have been used to map areas likely vulnerable to incision with some success (e.g. Moore et al., 1988a, Daba et al., 2003, Kheir et al., 2007, Conforti et al., 2011, Daggupati et al., 2013, Shit et al., 2015, Maerker et al., 2017). SPI is directly proportional to stream power, providing a measure of overland flow erosive power, and TWI spatially estimates zones of surface soil saturation (Moore et al., 1993).

TWI and SPI have been shown to relate strongly to gully presence (Moore et al., 1988a, Daba et al., 2003, Kheir et al., 2007, Kakembo et al., 2009, Le Roux and Sumner, 2012, Daggupati et al., 2013, Shit et al., 2015). Together they help define locations susceptible to channel incision by linking the ideas that drainage area and slope can (a) be combined to indicate regions susceptible to saturation overland flow (Daba et al., 2003), associated with channel incision (Montgomery and Dietrich, 1994), and (b) be used to assess locations likely to exceed a critical threshold of concentrated surface runoff required to initialise channel incision (Patton and Schumm, 1975).

2.1.3 Combining mapping of incised channels and predicted areas at risk

Given the spatial mapping needs described, we aimed to develop an algorithm that integrates a method for identifying incised landform elements with mapping of areas predicted to be at risk of future incision (Figure 2.1). Our goal was to develop a single workflow requiring only a DEM as input. To the best of our knowledge there is currently no method that combines these two requirements into a single workflow operating across multiple scales.

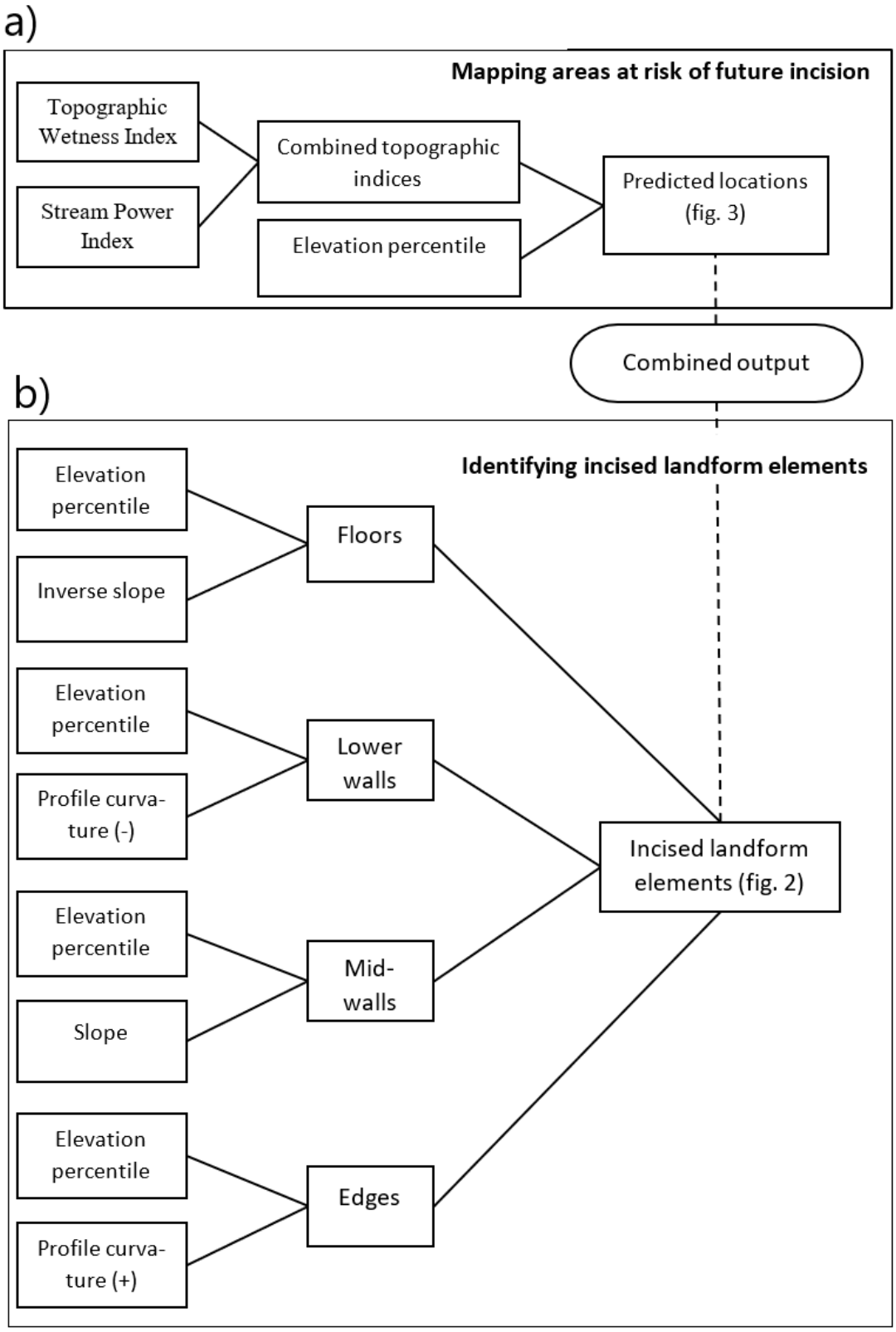

Figure 2.1: Process overview of each half of the algorithm conducted at each scale of analysis. Panel (a) shows inputs used to determine areas at risk of incision, and panel (b) shows inputs used to extract each component of existing incised landform elements.

2.1.4 Multi-resolution approach for a multi-scale problem

The inspiration for our method came from the Multi-Resolution Valley Bottom Flatness (MRVBF) algorithm of Gallant and Dowling (2003). The logical connection between MRVBF and the method developed here is that they both exploit topographic signatures of landscape features of interest to map them at multiple scales. The primary difference is that where MRVBF sought to map depositional features, the algorithm presented here seeks to map incisional ones.

A multi-scale approach was needed for two reasons. First, identifying specific landform elements requires a geometric definition of the target element - an 'ideal' model (Minár and Evans, 2008). However, the morphology of gullies and natural streams varies depending on the physical properties of a landscape, such as soil type (Poesen et al., 2003, Zucca et al., 2006). Hence finding a universal ideal model becomes increasingly difficult with a larger number of diverse landscapes. Typically, this has been handled by analysing relative values of topographic attributes at the 'local neighborhood' level (e.g. Castillo et al., 2014). Then, the geometric criteria of a target landform element can be assessed with respect to its immediate geomorphic setting only - its local neighborhood. The required size of the local neighborhood depends on the size of the target landform elements, which can vary between landscapes, thus requiring analysis at multiple scales. Second, the algorithm concurrently assesses areas at risk of future incision. These areas must be allowed to exist at scales greater than that of the incised elements forming within them, also requiring assessment at multiple scales.

Both requirements could be satisfied by using a window size sufficiently large to encompass all possible scales of interest. However, large window sizes significantly increase computational time. Instead, maintaining a relatively small window size and applying local neighborhood analyses while progressively adjusting the resolution of the DEM allows for an efficient method to identify target landform elements existing across a range of scales without significantly increasing computational time.

2.2 Methods

The methodology is structured around three sub-objectives; (1) identifying incised landform elements (ILEs) in high-resolution digital elevation data, (2) mapping these features as part of a continuous drainage network, and (3) predicting locations where

incision is likely to occur in the future. All three sub-objectives were handled within the multi-scale framework, acknowledging the fact that landforms exist at different scales (Schmidt and Andrew, 2005).

2.2.1 Identifying incised landform elements

We consider the morphological characteristics of ILEs to fit the general description of gullies given by Castillo et al. (2014) as land elements existing in locally low elevation positions composed of flat floors and steep walls. Taking this description, we used slope (S), profile curvature (C_p) and elevation percentile (P_i) to identify four key components defined to constitute the topographic signature of ILEs:

- Flat floors with a locally-low topographic position
- concave lower-walls
- relatively steep walls, and
- convex edges.

Curvature has been shown useful for mapping gullies (e.g. Korzeniowska et al., 2018), and is used here for the edges and lower-wall components. Flat floors and steep walls are both identified using slope. Constructing the target landform elements from these four components also aligns with the description of gullies given by Speight (1990) earlier. In keeping with this description, the floor component has an additional requirement that it must exist in a zone of concentrated flow. The implementation of this is discussed further in Section 1.1 of Appendix A.

In the model example (Figure 2.2) each component primarily occupies a unique space (with some overlap between components) but when all four are compiled they form a single contiguous object.

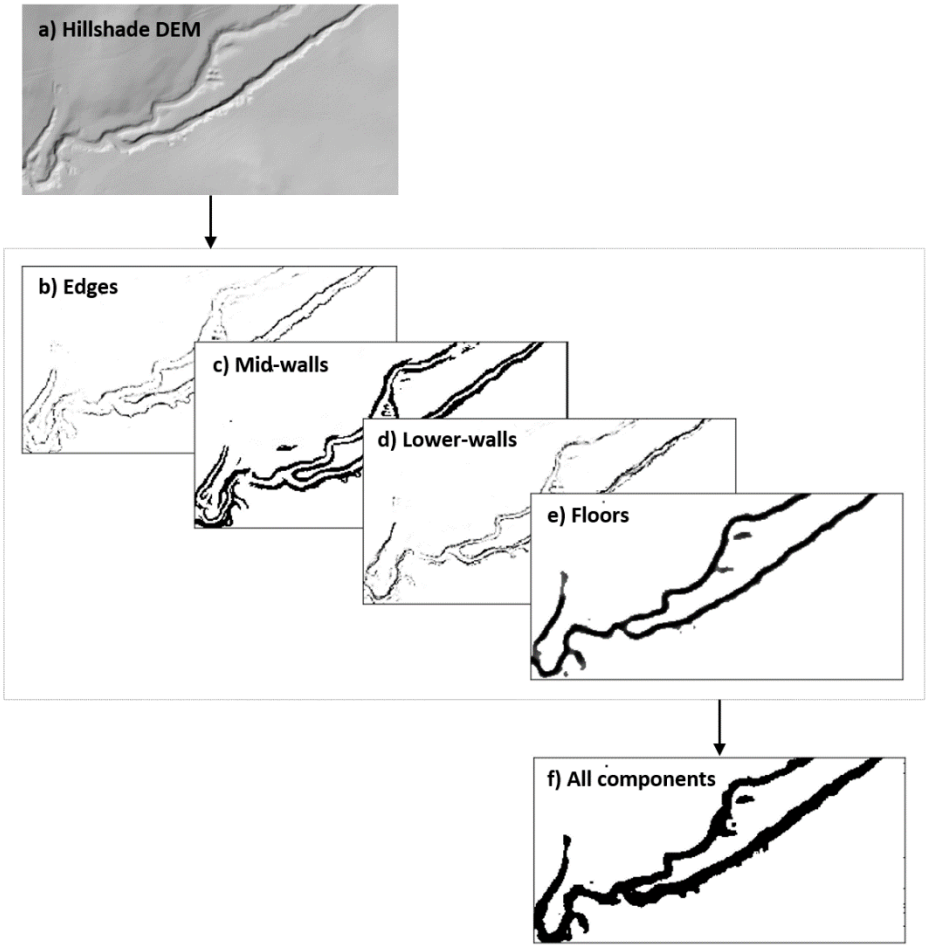

Figure 2.2: Identification and compilation of components of a gully off the Molonglo River in the Australian Capital Territory (35°16'S, 149°03'E). (a) Hillshade DEM of the gully. (b) Edges identified using positive profile curvature. (c) Steep walls. (d) Low negative profile curvature values at base of walls. (e) Feature floors with low slope and locally low position. (f) All four landform element components combined.

Section 1.2 of Appendix A details how grids of elevation percentile, slope and profile curvature are computed.

2.2.2 Creating fuzzy sets of incised landform element components

Identifying components of ILEs in a DEM requires grid cells to be grouped together according to their degree of membership to a pre-defined class. Here, fuzzy sets (Zadeh, 1965) are considered advantageous for their ability to accommodate the continuous nature of landscape variation (Burrough et al., 1992, Irvin et al., 1997, MacMillan et al., 2000, Gallant and Dowling, 2003, Evans, 2012).

A non-linear transformation function maps values onto the range [0, 1] creating fuzzy sets of each land surface parameter. This is the same function used by Gallant and Dowling (2003) in the MRVBF algorithm:

$$N(x,t,p) = \frac{1}{1+\left(\frac{x}{t}\right)^{p}} \quad (1)$$

Where *t* and *p* are threshold and shape parameters, respectively, and *x* is a grids cell's unadjusted value. When *x* is equal to *t* the function takes on a value of 0.5, with larger values of *p* increasing the steepness of the curve from 0.5 to 1 for $x > t$ and 0.5 to 0 for $x < t$. The threshold value for each component reflects the expected boundary value for membership to the component class at the given scale (Table 2.1).

Previous work found that isolating specific targets can be difficult (e.g. Tucker et al., 2001, Evans and Lindsay, 2010, Evans, 2012), but that multiple land surface parameters can be used together (e.g. curvature along with topographic position) to better delineate homogeneous landform elements. Accordingly, each ILE component is extracted using a combination of topographic position together with the relevant land surface parameter (Table 2.1).

Table 2.1: Land surface parameter threshold values used to extract each incised landform element component across five scales of analysis. As the algorithm moves to progressively finer scales the parameter threshold values increase sequentially.

ILE component (elevation percentile)	**Land surface parameter**	**Scale (grid resolution)**				
		DEM$_{5,5}$ (81m)	***DEM$_{4,4}$ (27m)***	***DEM$_{3,3}$ (9m)***	***DEM$_{2,2}$ (3m)***	***DEM$_{1,1}$ (1m)***
Edges (P_{40})	*Profile curvature (rad/100m)*	*≥ 0.004*	*≥ 0.006*	*≥ 0.009*	*≥ 0.0135*	*≥ 0.02*
Walls (P_{30})	*Slope (%)*	*≥ 4*	*≥ 6*	*≥ 9*	*≥ 13.5*	*≥ 20*
Lower-walls (P_{20})	*Profile curvature rad/100m)*	*≤ -0.004*	*≤ -0.006*	*≤ -0.009*	*≤ -0.0135*	*≤ -0.02*
Floors (P_{20})	*Slope (%)*	*≤ 4*	*≤ 6*	*≤ 9*	*≤ 13.5*	*≤ 20*

Values of properties used to define landform elements will vary with scale (Gallant and Dowling, 2003, Schmidt et al., 2003). Our algorithm facilitates this by allowing threshold values for *S*, S^{-1} and C_p to increase by ~50% at each finer scale of analysis while holding elevation position constant (Table 2.1). Allowing these parameters to vary with scale adjusts for the smoothing out of angles as DEMs are progressively

coarsened and allows the algorithm to identify larger features with less steep walls and rounder edges existing at broader scales.

2.2.3 Processing steps for mapping incised landform elements

Operating on a multi-resolution basis requires that the initial input DEM undergoes sequential smoothing and resampling. The notation to keep track of the scale analysis and working resolution of the DEM is borrowed from Gallant and Dowling (2003) and follows the convention $DEM_{L,L}$ with the first subscript indicating the level of generalisation and the second indicating the current working grid cell resolution. For example, a DEM with a grid resolution of 1m that has not undergone spatial smoothing would be denoted $DEM_{1,1}$, and after undergoing smoothing would then be denoted $DEM_{2,1}$. Resampling is always conducted by a factor of three, moving from a resolution of 1 m through 3 m, 9 m 27 m and 81 m. Typically the value of both subscripts will be equal, but two are used to allow the algorithm to vary scale and resolution independently where necessary.

At each scale of analysis, grids of incised landform element components (floors, walls, lower-walls and edges) are created one-by-one before being compiled into a single grid of ILEs. Steps one, two and three are carried out in sequence for each of the four ILE components.

2.2.3.1 Step one

First, equation (1) is used to transform the relevant land surface parameter (S, S^{-1} or C_p):

$$TLSP_{L,L} = 1 - N\left(LSP_{L,L}, t_L, 4\right) \quad (2)$$

Where $LSP_{L,L}$ represents the parameter being transformed, t_L is taken from Table 2.1 and $p = 4$. At the base grid cell resolution (1 m) these t and p values gave the best balance between separation of classes while maintaining roughly equal representation of each individual component in the final grid of delineated ILEs.

2.2.3.2 Step two

Elevation percentile values P_i are then transformed by centering them on the target elevation position P_t, corresponding to the component being processed (Table 2.1), and truncating to a maximum distance δ from P_t:

$$C(P_i, P_t, \delta) = \begin{cases} P_t - \delta, & P_i \leq P_t - \delta \\ P_t - |P_i - P_t|, & P_i > P_t - \delta \end{cases} \quad (3)$$

Grid cells with values $|P_i - P_t| > \delta$ will be outside the target elevation position. Outputs of (3) are then mapped onto the range [0, 1] using the non-linear function:

$$M[C(P_i, P_t, \delta), P_t] = 1 - sin\left[\pi + 10(C - P_t)\frac{\pi}{6}\right] \quad (4)$$

This function produces curves that are symmetric around P_t and can have their shape modified using equation (1) by adjusting *p* up or down while substituting $M[C(P_i, P_t, \delta), P_t]$ for *x* and holding *t* constant at 0.5. A grid of transformed elevation position is then computed for the target component:

$$TEP_{L,L} = M[C(P_{i\,L,L}, P_t, \delta), P_t] \quad (5)$$

Where P_t is the target elevation position for the component extracted by (2). Setting δ = 0.1 ensures that $TEP_{L,L}$ returns values ≥ 0.5 for P_i values ± 10 percentiles from P_t.

2.2.3.3 Step three

Transformed land surface parameters and elevation percentiles are then combined to produce grids of the four ILE components above (Figure 2.2).

$$ILE_{comp} = 1 - N\left(TLSP_{L,L} \cdot TEP_{L,L}, 0.25, 4\right) \quad (6)$$

Where the subscript *comp* represents one of floors (*fl*), lower-walls (*lw*), walls (*wa*) or edges (*ed*). Setting *t* = 0.25 allows the product of grid cells with a value of 0.5 in each of the inputs to maintain membership to the target class, and *p* = 4 is used again to give a relatively rapid transition to zero for values < 0.25.

2.2.3.4 Step four

Finally, the four components are combined to produce a grid of ILEs:

$$ILE_{L,L} = Max\left(ILE_{fl}, ILE_{lw}, ILE_{wa}, ILE_{ed}\right) \quad (7)$$

2.2.4 Combining incised landform element mapping outputs across scales

Conceptually, the algorithm begins by assessing the landscape at a broad scale and progressively moves to increasingly finer scales. Outputs from each scale are continually combined within a weighting scheme assigning higher class membership values to components mapped at finer scales. Again, we borrow the process and

equations for this from Gallant and Dowling (2003). Combining outputs of ILE identification at different scales (denoted $ILEC_L$ below) begins by combining outputs from the broadest scale of analysis ($ILE_{Lmax,\ Lmax}$) with the second broadest scale of analysis ($ILE_{Lmax\ -\ 1,\ Lmax\ -\ 1}$):

$$ILEC_1 = w_1\left(1 + ILE_{Lmax-1,Lmax-1}\right) + (1 - w_1)ILE_{Lmax,Lmax} \quad (8)$$

Where w_1 is a weighting derived using equation (1) as follows:

$$w_1 = 1 - N\left(ILE_{Lmax-1,Lmax-1}, 0.4, 6.68\right) \quad (9)$$

Setting t = 0.4 and p = 6.68 ensures that $ILEC_1$ values = 1.5 when $ILE_{Lmax\ -\ 1,\ Lmax\ -\ 1}$ = 0.6 and $ILE_{Lmax,\ Lmax}$ = 0. For each subsequent step (L) the combined grid is calculated as follows:

$$ILEC_L = w_L\left(1 + ILE_{Lmax-L,Lmax-L}\right) + (1 - w_L)ILEC_{L-1} \quad (10)$$

Where w_L is calculated such that $ILEC_L$ is always ≥ L – 0.5 when $ILE_{Lmax\ -\ L,\ Lmax\ -\ L}$ ≥ 0.6:

$$w_L = 1 - N\left(ILE_{L-1,L-1}, 0.4, p_L\right) \quad (11)$$

With the shape parameter (p_L) given by:

$$p_L = \frac{ln\left(\frac{L-0.5}{0.1}\right)}{ln(1.5)} \quad (12)$$

Combining results through five scales of analysis produces a single map of continuous values ranging from 0 to 5. Individual grid cell values correspond to the scale at which the grid cell was identified as an ILE component (Table 2.2).

Table 2.2: Interpretation of output values for the first phase of the algorithm aimed at identifying individual incised landform element (ILE) components.

Value range	Interpretation
0< x < 0.5	*ILE components not identifiable at any scale*
0.5 < x < 1.5	*ILE components identifiable at 81 m grid resolution*
1.5 < x < 2.5	*ILE components identifiable at 27 m grid resolution*
2.5 < x < 3.5	*ILE components identifiable at 9 m grid resolution*
3.5 < x ≤ 4.5	*ILE components identifiable at 3 m grid resolution*
4.5 < x ≤ 5	*ILE components identifiable at the finest scale of analysis (1m)*

2.2.5 Mapping potential for future channel incision

Low topographic position has been shown to be an important variable for predicting locations of ILEs such as gullies (Evans and Lindsay, 2010, Castillo et al., 2014, Tindall et al., 2014a). The development of incised channels is also strongly related to regolith depth (Menéndez-Duarte et al., 2007), and soil depth has an expected inverse relationship to elevation percentile (Gallant and Dowling, 2003). Given this, we use elevation percentile as a method to locate relatively low-lying areas as a first step to mapping areas at risk of incision.

At each scale a grid of P_i values is computed and transformed to a grid of provisional areas at risk of incision:

$$PAR_{L,L} = N\left(P_{i\,L,L}, t_L, 3\right) \quad (13)$$

At the finest scale, setting t = 0.4 and p = 3 allows for a relatively gentle decrease in function values for 0.4 < P_i < 0.5, with outputs quickly heading to 0 for P_i > 0.5. Setting the P_i threshold to the 40th percentile of elevation (t = 0.4) was found to provide a good separation of low-lying areas from higher parts of a landscape. When values of t were decreased below 0.4, upslope portions of ILEs visibly extended out of the mapped areas. Using t = 0.4 prevented this, but also created relatively large potential areas (Figure 2.3a).

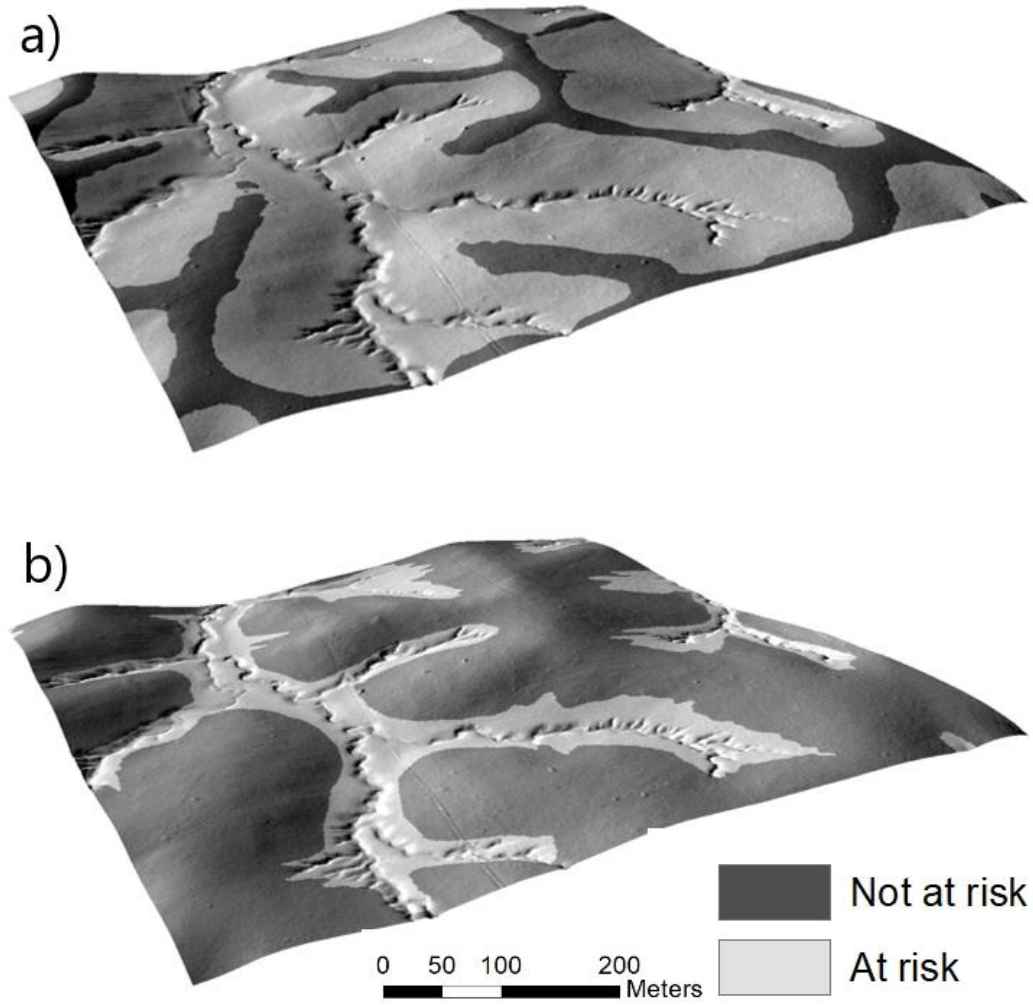

Figure 2.3: Two example results of methods to estimate areas at risk of incision. Panel a) shows the result of isolating low areas occupying the 40th percentile of elevation. Panel b) combines 40th percentile elevation with topographic wetness index and stream power index to find low areas susceptible to channel incision.

To address this, two secondary land surface parameters, TWI and SPI, were incorporated to further constrain areas likely to contain incised channels (Figure 2.3b). TWI was calculated following Beven and Kirkby (1979):

$$TWI = ln\left(\frac{A_S}{tan\beta}\right) \quad (14)$$

Where β represents slope angle in radians and A_S is specific catchment area (m^2 m^{-1}). SPI was calculate following Moore et al. (1988a):

$$SPI = A_S.tan\beta \quad (15)$$

Specific catchment area is calculated using conventional methods described by Gallant and Hutchinson (2011) as the upslope contributing area per unit contour length:

$$A_s = \frac{\mathrm{A}}{w} \quad (16)$$

Where upslope contributing area *A* (m^2) is derived using the M8 multiple flow direction router tool available in the Python-based Landlab landscape modelling package (Hobley et al., 2017a), and contour length *w* (m) is given by:

$$w = \begin{cases} R, \ cardinals \\ \sqrt{2}\,.R, \ diagonals \end{cases} \quad (17)$$

Where *R* is the working grid cell resolution. Prior to routing flow, the DEM is filled using the Priority-Flood depression filling algorithm (Barnes et al., 2014) implemented in the Landlab modelling package. The M8 method was preferred over a steepest downhill direction method (e.g. D8) to better represent the dispersive nature of flow on hillslopes and in flatter areas where a D8 algorithm can produce unrealistic concentrated flow lines (Desmet and Govers, 1996, Seibert and McGlynn, 2007). Such locations can include alluvial plains into which alluvial gullies have been cut, and this type of gully constitutes an important subclass of features in GBR catchment sediment generation (Wilkinson et al., 2013).

2.2.6 Processing steps for mapping areas at risk of incision

Previous work found that in eastern Australia incised features typically form in areas with TWI and SPI values of 6.8 and 18, respectively (Moore et al., 1988). These two values are used in the current study as the threshold values to determine areas at risk of incision.

2.2.6.1 Step one

At each scale of analysis, the function given by (1) is used to transform both TWI and SPI:

$$TTWI_{L,L} = 1 - N\left(TWI_{L,L}, 6.8, 4\right) \quad (18)$$

$$TSPI_{L,L} = 1 - N\left(SPI_{L,L}, 18, 4\right) \quad (19)$$

For (18) and (19) setting $p = 4$ allows function values to rapidly head to 0 as *x* values drop less than ~ 25% below *t* and to 1 as *x* values increase ~ 25% above *t*.

2.2.6.2 Step two

A grid of joint topographic indices is then created by combining (18) and (19):

$$JTI_{L,L} = 1 - N(TTWI_{LL} \cdot TSPI_{LL}, 0.25, 4) \quad (20)$$

Values for *t* and *p* are chosen by the same reasoning used when combining land surface parameters with elevation position in (6).

2.2.6.3 Step three

Finally, provisional areas at risk of incision ($PAR_{L,L}$) are combined with $JTI_{L,L}$ to produce a grid indicating areas at risk:

$$AR_{L,L} = 1 - N\left(\frac{JTI_{LL} + PAR_{LL}}{2}, 0.25, 4\right) \quad (21)$$

Here equal weighting is assumed for TWI/SPI and elevation percentile in determining areas at risk of incision.

Again, combining results through five scales of analysis produces a single map of continuous values ranging from 0 to 5. Individual grid cell values correspond to the scale at which the grid cell was identified as being at risk of incision (Table 2.3).

Table 2.3: Interpretation of output values for the second phase of the algorithm aimed at estimating areas at risk of incision.

Value range	Interpretation
0< x < 0.5	*Areas not at risk of channel incision*
0.5 < x < 1.5	*Areas at risk at 81m grid resolution*
1.5 < x < 2.5	*Areas at risk at 27m grid resolution*
2.5 < x < 3.5	*Areas at risk at 9m grid resolution*
3.5 < x ≤ 4.5	*Areas at risk at 3m grid resolution*
4.5 < x ≤ 5	*Areas at risk at the finest scale of analysis (1m)*

2.2.7 Combining mapping of areas at risk across scales

Grids of at-risk areas computed at each scale of analysis are then combined following the same process for combining grids of ILEs (Section 2.2.4). Details of the process are covered in Section 1.3 of Appendix A.

2.2.8 Background to the case study

An area within the catchments of the Great Barrier Reef (GBR), Australia, was chosen as a case study site. The GBR, stretching ~2 300 km along Australia's north-eastern coast, faces multiple environmental stressors, including poor water quality due to increased sediment carried in runoff (Brodie et al., 2005, Fabricius et al., 2005, Wooldridge, 2009, Pollock et al., 2014). Gullies and streambanks have been implicated as significant contributing sources of this pollutant sediment (Bartley et al., 2014a, Hancock et al., 2014, Bartley et al., 2015, Hairsine, 2017). Recent estimates for some parts of the GBR catchments found that erosion occurring in hillslope rills, streambanks and gullies accounts for between 77% and 89% of fine sediment loss (Wilkinson et al., 2013).

Targeted interventions require better information on the location, size and number of potential sources of fine sediment and associated erosion processes (McKergow et al., 2005b, Bartley et al., 2014a, Wilkinson et al., 2015b). Efforts to manage sediment runoff into the GBR need to address both remediation and prevention (Wilkinson et al., 2015b, Bartley et al., 2018). This issue was the primary reason for developing the method presented in this paper.

Testing required a site where multiple areas with a mix of protected natural forests and cleared farmland coexist relatively close to each other, and where incisional erosion was clearly visible. The difficulty encountered was that the extent of deforestation across Queensland, and Australia more broadly, over the past century has been so extensive (Bradshaw, 2012, Evans, 2016) that there are very few such locations that also have an available high-resolution DEM. One area was located (25° 15' S / 151° 54' E) along the Burnett river south-west of Bundaberg Queensland (Figure 2.4).

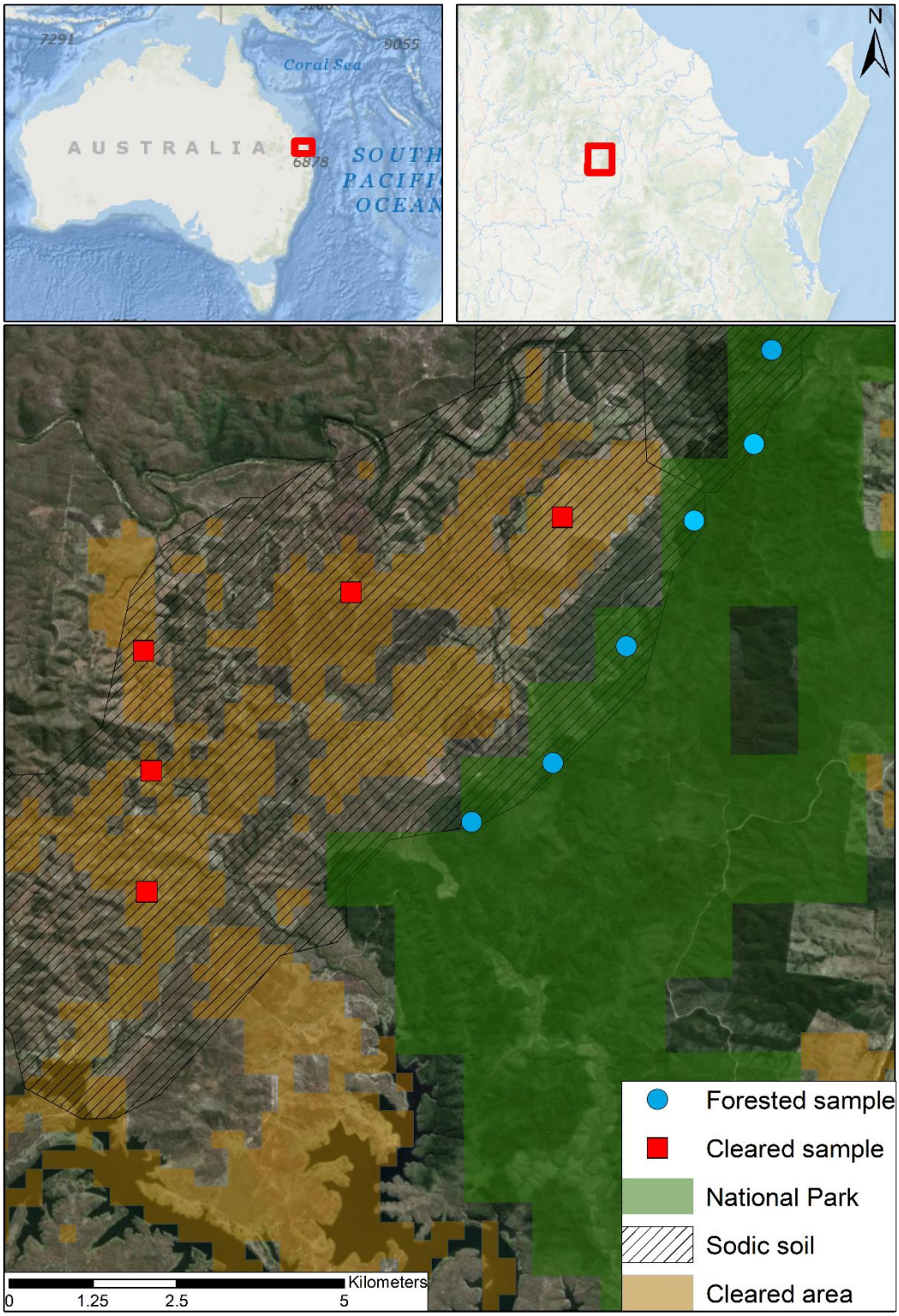

Figure 2.4: Locations chosen to take samples for testing the Potential Channel Development Index. This site was selected because it has cleared areas (red squares) existing alongside natural forest areas (blue dots) all existing on dispersive sodic soils (striped polygon). Index values were compared between cleared and forested areas.

2.2.9 Potential Channel Development Index (PCDI)

A core aim of the algorithm is to compare the current extent of incised channels with the area estimated to be at risk of incision. This is done by overlaying a map of existing ILEs (Sections 2.2.1 – 2.2.4) onto a map of areas estimated to be at risk of incision (Sections 2.2.5 – 2.2.7) and subtracting the former from the latter. The resulting value indicates the potential for future incision for a given area and is referred to as the potential channel development index (PCDI).

For testing, we focussed on at-risk areas mapped only at the finest scale of analysis (output values x in the range $4.5 \leq x \leq 5$, Table 2.2), considered as areas at most immediate risk of incision. In our case study site, these areas were typically elongated zones extending up drainage lines connected to second or third order streams and often with some amount of existing incision (Figure 2.5). Each such area, analogous to a Strahler first order stream (Strahler, 1957), was digitised (using the 'Draw' tools in ArcMap 10.5.) as a single sample area in which to calculate the PCDI.

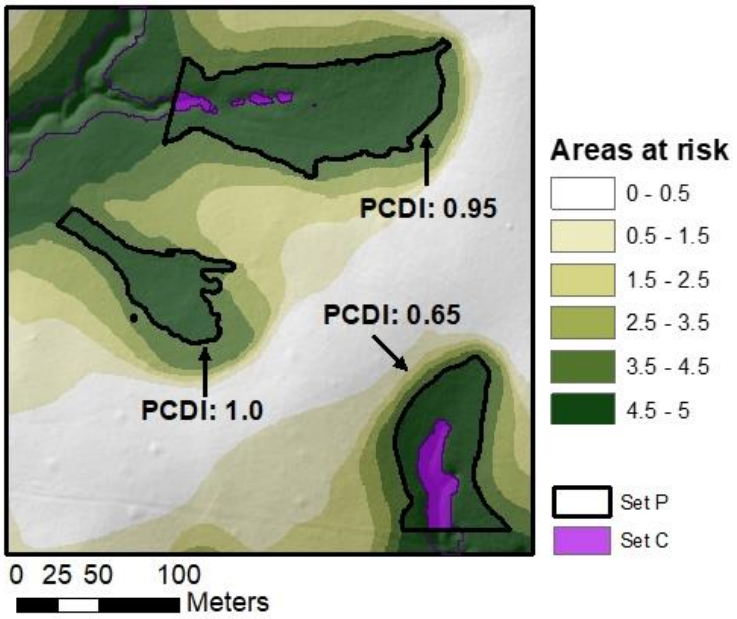

Figure 2.5: Three examples of digitised samples used to assess the Potential Channel Development Index. Each example shows the area with potential for incision outlined by thick black lines (Set P) and existing incision in purple shaded areas (Set C). Larger PCDI values correspond to areas where there is a larger area for potential future channel incision.

The example above shows three digitised samples with Set *C* denoting the area of existing ILEs and Set *P* the area at most immediate risk of future incision. The PCDI was calculated for each sample as the relative complement of *C* in *P* divided by *P*:

$$PCDI = \frac{(P \setminus C)}{P} \quad (22)$$

When *C* is half the area of *P*, the PCDI will equal 0.5. PCDI values range from 0 to 1 where 0 indicates the entire area at risk of incision has already been completely incised and 1 indicates the area has no existing incision. The index draws on the idea that topographic parameters, such as slope (*S*) and area (*A*), are helpful to assess potential for future channel erosion but also contain information about the erosive history of a catchment (McNamara et al., 2006).

2.2.10 Assessing the Potential Channel Development Index

Assessing the validity of the PCDI presented a challenge in that there was no straightforward way to determine whether channels will (or even can) form in the areas identified as being at risk of future incision. This was approached by drawing on the ideas that land clearing and a shift to intensive land uses facilitates channel initiation and development (e.g. Aksoy and Kavvas, 2005, Valentin et al., 2005, Vanwalleghem et al., 2005b, Menéndez-Duarte et al., 2007), and that soil resistance to erosion from concentrated flow increases along a natural gradient from croplands to grasslands and in to forest landscapes (Torri and Poesen, 2014). Accordingly, areas deforested and converted to intensive land uses are expected to have a greater extent of channel development and hence lower PCDI values than areas that have been left in a natural state.

The case study site contained relatively large and undisturbed natural vegetation (Goodnight National Park) alongside grazing lands with very low tree cover. The region also contains significant areas of sodic soil associated with channel erosion problems across Australian (Wong et al., 2010a).

A total of ~500 samples were taken across both forested and cleared areas of the site following the process outlined above (Section 2.2.9). The total sample size was split roughly equally between forested and cleared. All samples, forested and cleared, were taken on sodic soils to control for the potential influence of this soil type on channel development. Sodic soils were identified using national soil data provided by the Australian Collaborative Land Evaluation Program (ACLEP) from the Australian Soil Resource Information System (ASRIS) available at (http://www.asris.csiro.au).

The process of identifying areas at risk of incision assumes erosion is dominated by fluvial transport processes throughout the catchment. However, the balance

between fluvial transport dominated or diffusion dominated erosion processes varies depending on position within a catchment, with diffusive processes found to dominate closer to the catchment divide (Willgoose, 1994). For areas where slope increases substantially (e.g. near the catchment divide), calculated PCDI values may be affected by a shift in dominant erosion process. To help mitigate this, data was grouped by slope intervals before comparing PCDI values between forested and cleared areas (Figure 2.8). With samples grouped into slope classes, each was assigned its relevant land cover class (either 'Forested' or 'Cleared') and the PCDI value was calculated and plotted against slope class (Figure 2.9).

The 1 m LiDAR data for the site was collected in 2014 as part of project commissioned by the Queensland Department of Natural Resources, Mines and Energy and downloaded from http://elevation.fsdf.org.au/. The data accuracy was reported as +/- 0.15 m SE in the vertical direction and +/- 0.40 m in the horizontal direction at 68% confidence interval (CI_{68}). Cleared areas were identified as areas with < 20% tree cover in the same year (2014) that the LiDAR was collected. Cleared areas were identified using tree cover data derived from Landsat imagery (0.9 arcsecond resolution) downloaded from the Australia's Environment Explorer (http://ausenv.online). Forested areas were identified using Australian Collaborative Land Use and Management Program (ACLUMP) data produced by the Australian Bureau of Agricultural and Resource Economics and Sciences (ABARES). Only areas designated as 'National Park' status were used (green shaded area Figure 2.4). The data are available in Esri raster grid format and projected to GDA94 at a resolution of 0.01˚ (http://www.agriculture.gov.au/abares/aclump/land-use/data-download).

2.2.11 Parameter sensitivity to mapping incised channels

A second assessment approach was to test the sensitivity of outputs as a function of the primary attributes used to map existing incised landform elements. This analysis was done in three contrasting environments with different average slope, land use, geology and climate (Table 2.4; and Figure 2.6).

Table 2.4: Geographic setting of sites selected to test the sensitivity of incised landform identification to each primary land surface parameter. Climate data from the Australian Bureau of Meteorology (Australian Bureau of Meteorology, 2016). Geologic data from Geoscience Australia *(Geoscience Australia, 2012)*.

Site name and number	Mount Wickham (1)	Goodnight Scrub (2)	Coppins Creek (3)
Size	*2km x 2km*	*2km x 2km*	*2km x 2km*
Lat. / Lon.	*20°27'S/147°24'E*	*24°17'S/151°53'E*	*35°16'S/149°03'E*
Mean slope ± std.	*5° ± 7.7*	*11° ± 8.5*	*7.5° ± 6.9*
Elevation (range)	*85m (14)*	*170m (71)*	*575m (164)*
Mean ann. rain	*660mm*	*850mm*	*670mm*
Rain seasonality	*Summer dominant (650–1200mm)*	*Summer (650–1200mm)*	*Uniform (500–800mm)*
Geologic setting	*Carboniferous felsic intrusive igneous*	*Carboniferous low-grade metamorphosed siliciclastic*	*Silurian-Devonian felsic volcanic igneous*
Process	*Alluvial*	*Colluvial*	*Colluvial*

Site 1 (Mount Wickham) was selected because it is representative of grazing lands in the Burdekin river basin, the largest contributor of fine sediment to the GBR (Bartley et al., 2015). It is also located proximal to the river network making it a well-connected location in terms of potential sediment delivery. Site 2 (Goodnight Scrub) was chosen to assess how the algorithm handles environments with steep average slope and because it was part of the study area used in Section 2.2.8. Site 3 (Coppins Creek, ACT) was chosen to provide an example of a temperate environment at a relatively high elevation and different geologic history and setting.

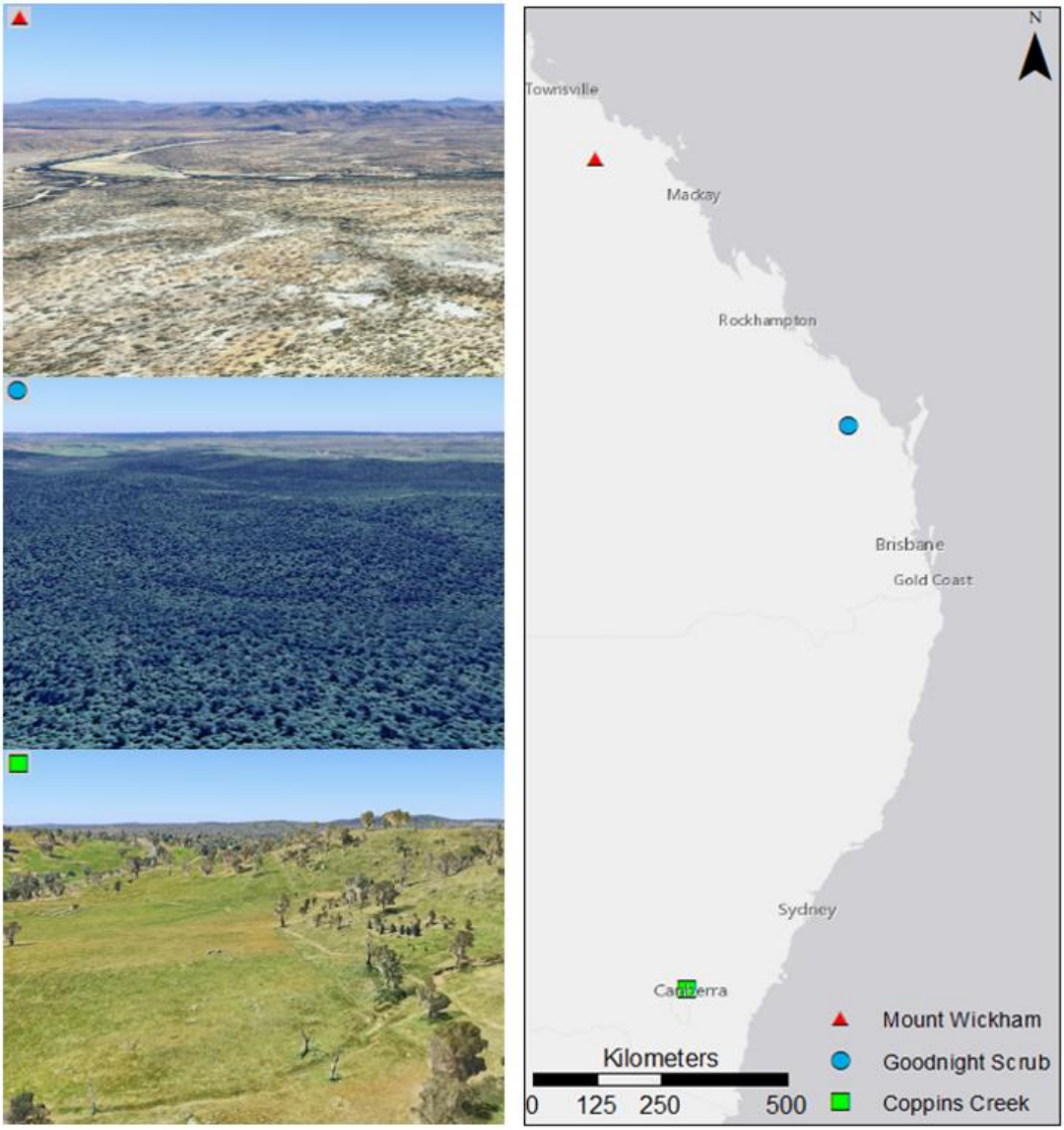

Figure 2.6: Location and setting of sites used for sensitivity analysis. From north to south the sites include (1) Mount Wickham, a relatively flat alluvial landscape on the Burdekin river, north Queensland. (2) Goodnight Scrub, a hilly national park located adjacent to the Burnett River, southeast Queensland. (3) Coppins Creek, a landscape of undulating hills located near the capital city of Canberra in the temperate southeast of Australia.

Sensitivity of each of the four ILE components (Section 2.3.3) to different threshold values was tested by repeatedly running the algorithm over a single grid while progressively adjusting the respective primary parameter threshold by 5% in each iteration of the algorithm, holding all other parameters constant. The representation of the component being tested was quantified as the number of grid cells classified, and then compared with the number classified using the original threshold.

For each site and ILE component, 20 subsets of 500m x 500m were randomly selected and for each subset the algorithm was run 20 times with the parameter threshold decreased by 5% each run, to a maximum of 100% decrease. Next, the algorithm was run 20 times with the parameter threshold increased by 5% each run to a maximum of 100% increase. Following this process, the algorithm was run a total of 800 times for each ILE component for each environment.

2.2.12 Algorithm inputs and availability

The inputs used in this study were all openly available bare-earth DEMs with a resolution of 1m and derived from Light Detection and Ranging (LiDAR). All data used is available on the Elevation and Depth – Foundation Spatial Data portal http://elevation.fsdf.org.au/, a joint initiative by the New South Wales, Queensland and Tasmania Governments together with ANZLIC Committee on Surveying and Mapping, and Geoscience Australia.

The algorithm is openly available for download on GitHub (https://github.com/Simon-JW/PCDI.git). It is written the Python programming language (version 3.7). The software repository contains a list of dependencies and instructions on use.

2.3 Results

2.3.1 Algorithm outputs

The algorithm produces one map of existing ILEs, one of areas at risk of incision and one overlaying existing ILEs onto at-risk areas (Figure 2.7). Here, algorithm outputs from a cleared area within the case study site show ILEs are only identifiable at the finest scale of analysis (Figure 2.7b), with no results to display at scales > 1m.

Areas at risk of incision will always be mapped up to the broadest scale specified (in this case 81m grid cell resolution), with at-risk areas expanding as the scale of analysis is broadened (Figure 2.7c).

Outputs from this location provide several useful examples of how the algorithm assesses a landscape (Figure 2.7d). The first two examples show (i) an area where incision has started but still has potential to continue growing, and (ii) an area where incision has continued up to the boundary of the potential area. Finally, there is also an example (iii) where incision is occurring on one side of a gully also shown to have

larger areas at risk of incision, and not occurring on the opposite side where the algorithm shows much lower potential for incision. This final example gives some preliminary support for the algorithm's ability to plausibly separate areas at risk of incision from areas that are not.

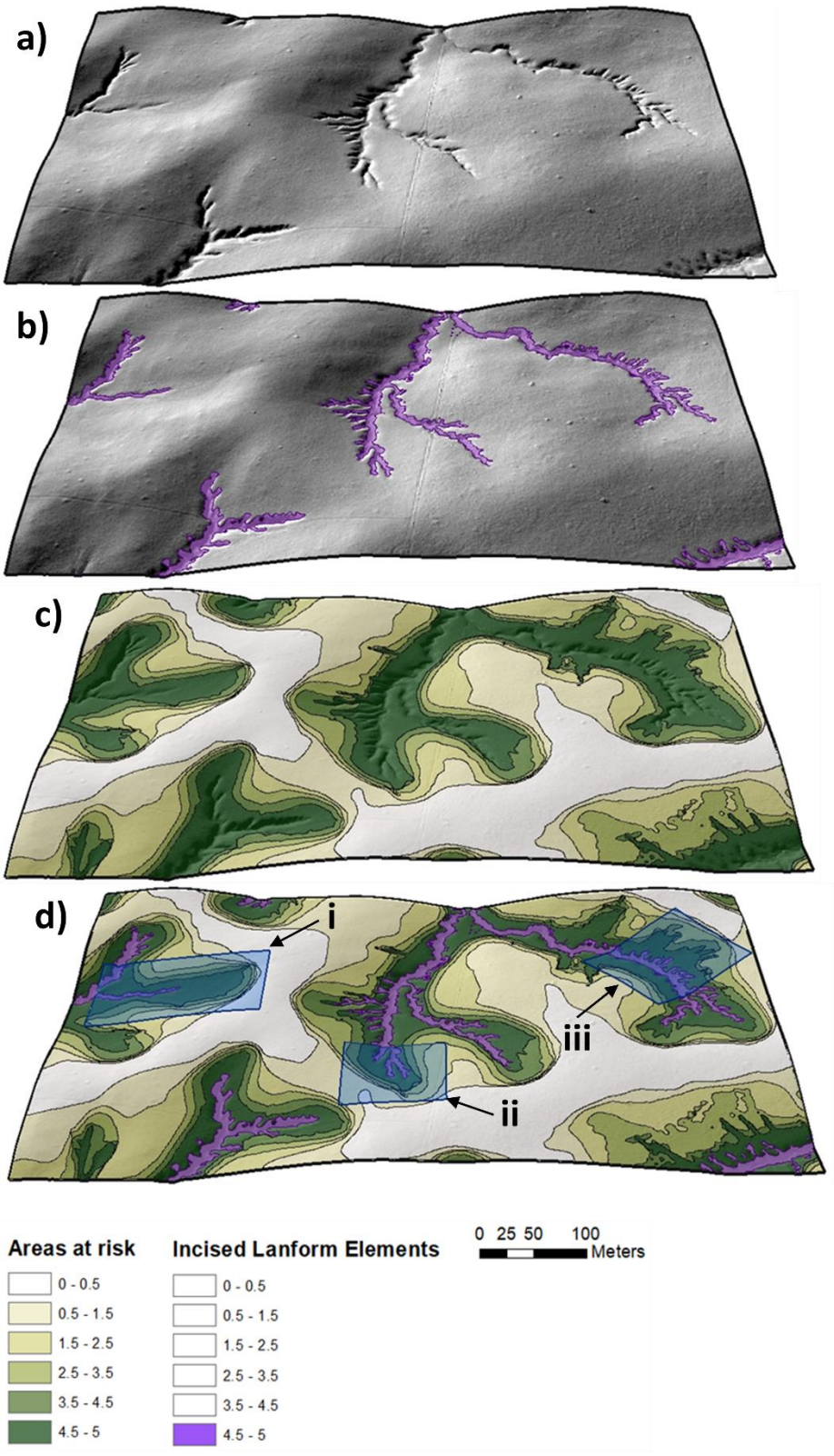

Figure 2.7: A cleared area on sodic soils within the Goodnight Scrub case study site (25°14'S, 151°53'E). Panel (a) shows a hillshaded DEM, (b) shows incised landform elements identified by the algorithm, (c) areas at risk of incision and (d) the result of combining (b) and (c). In this area ILEs are not identifiable at scales > 1 m and hence panel (b) shows no data for values < 4.5. Areas i, ii and iii are discussed in the text (Section 2.3.1).

2.3.2 PCDI outputs

PCDI values were first plotted against slope to test whether a relationship between the two exists. Results show a general inverse relationship between PCDI values and slope (Figure 2.8), with PCDI values steadily decreasing as slope approaches ~12°.

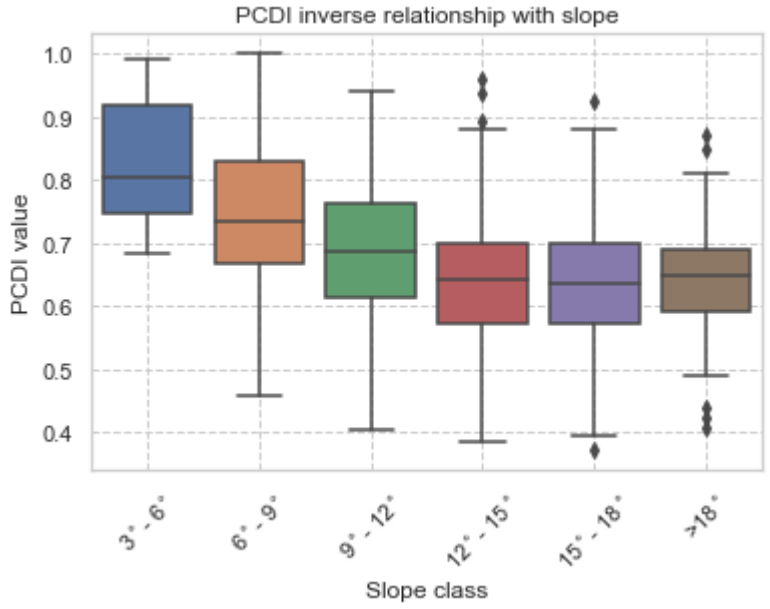

Figure 2.8: Samples were grouped by slope (without separating cleared and forested samples) and Potential Channel Development Index values were calculated for each slope class. The goal was to check for a relationship between PCDI values and slope. Results showed that a relationship existing at slopes ≤ 12°.

At slopes steeper than 12° there no longer appears to be any relationship. However, the trend observed at slopes < 12° confirms the need to group samples by slope class intervals before comparing PCDI values between forested and cleared areas.

When all forested and cleared areas across the study site are assessed, the average PCDI value is larger for the 'Forested' class than for the 'Cleared' class, as expected (Figure 2.9). However, at a CI_{90} there is substantial overlap at the 3 ° – 6 ° and > 18 ° slope classes. The wider PCDI distributions observed for forested samples on very low slopes and cleared samples on very high slopes are due to a smaller number of samples available for these land cover/slope class combinations.

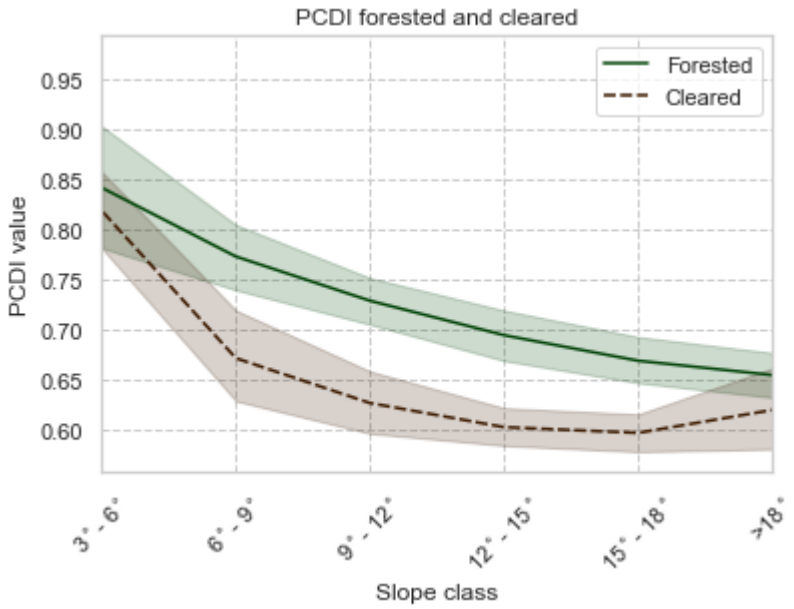

Figure 2.9: Plot showing Potential Channel Development Index for ~500 samples across cleared and natural forest areas. Samples are grouped into slope class and results show a consistent difference between PCDI for forested areas (green line) and cleared areas (brown line). The shaded band around each line represents the 90% confidence interval.

2.3.3 Sensitivity analysis results

Results from the sensitivity analysis are displayed with the graphs of the two ILE components using C_p (edges and lower walls) grouper together (Figure 2.10), and the two ILE components using S and S^{-1} (walls and floors) grouped together (Figure 2.11). In each case, values on the y-axis show the comparative representation of the corresponding feature component as threshold values are adjusted up and down. When thresholds are decreased, the area represented by the target component will increase; conversely, as the thresholds increase, the comparative area will decrease. For example, a 50% reduction in the S^{-1} parameter threshold results in the number of pixels classified as ILE walls increasing by a factor of two for the Mount Wickham image and by a factor of ten for the Goodnight Scrub image (Figure 2.11a).

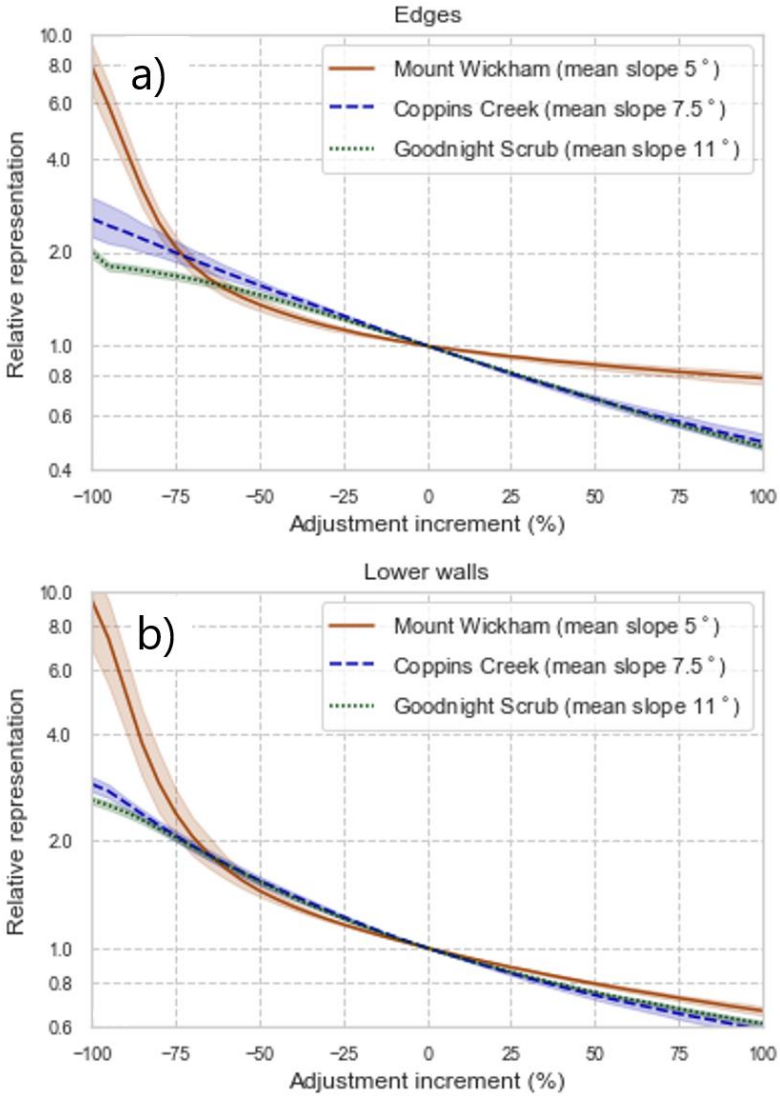

Figure 2.10: Sensitivity analysis showing the effect of adjusting profile curvature threshold values used to identify edges (a) and lower walls (b) of incised landform elements. Decreasing the threshold (x-axis) will always increase the total area classified and vice versa. The y-axis is on a logarithmic scale.

For the two components using C_p, sensitivity in the colluvial landscapes (Coppins Creek and Goodnight Scrub) is low and the graphs display an almost linear shape. However, the graph for the alluvial landscape (Mount Wickham), while showing a lower sensitivity of edges to positive adjustments, shows a rapid non-linear increase in area once adjustment values are pushed < -50%. (Figures 2.10a and 2.10b) for both edges and lower-walls.

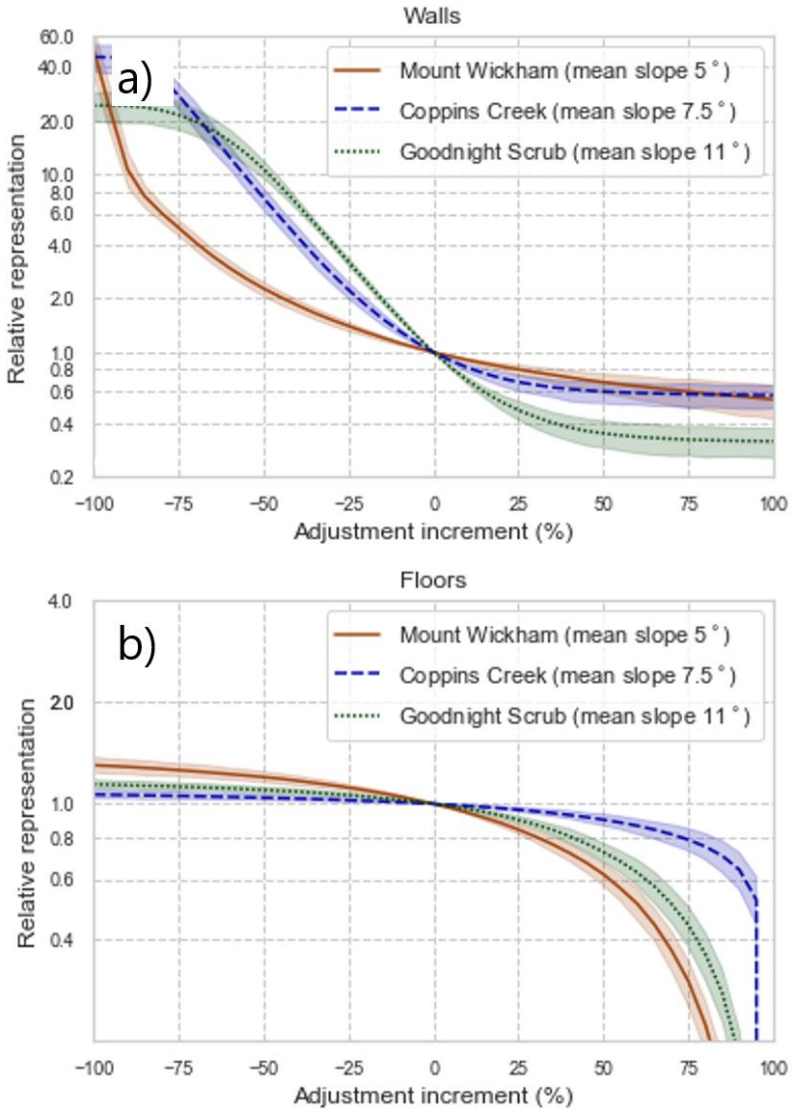

Figure 2.11: Sensitivity analysis showing the effect of adjusting slope threshold values used to identify walls (a) and floors (b) of incised landform elements. Decreasing the threshold (x-axis) will always increase the total area classified and vice versa. The y-axis is on a logarithmic scale.

The wall component, using S^{-1} as the primary parameter, shows similar sensitivity to the edge and lower-wall components when threshold values are increased; however, the graph shows a much faster rate of change when threshold values are decreased (Figure 2.11a). The shape of the curves is again the same for the two colluvial landscapes but different for alluvial landscape. As threshold values are decreased, the curves for the two colluvial landscapes show quickly increasing values until the adjustment reaches ~-75% when the rate of change rapidly flattens out. Meanwhile, the curve for the alluvial landscape displays a steadily increasing exponential rate as thresholds are decreased.

The floor component shows generally low sensitivity across all three landscapes, with the relative area rapidly approaching zero only as thresholds increase >50%. Interestingly, the landscape showing lowest sensitivity to the floor component was Coppins Creek, located in the temperate southeast of Australia.

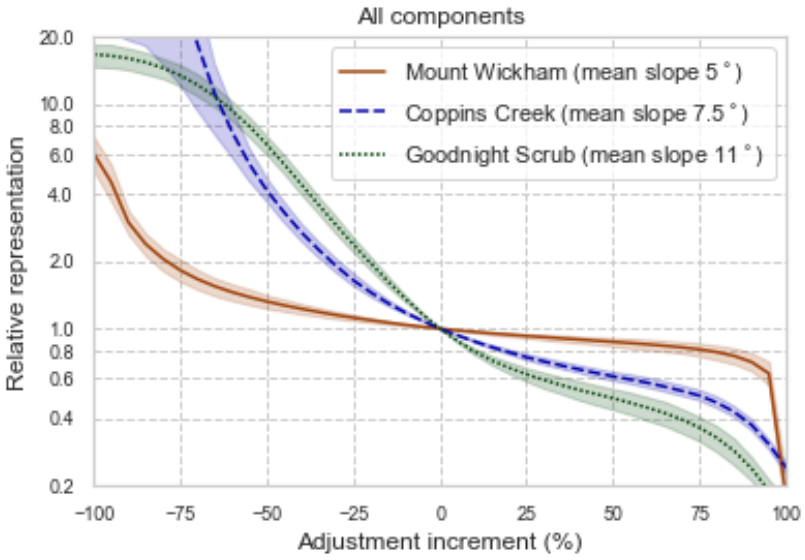

Figure 2.12: Sensitivity analysis showing the effect of simultaneously adjusting all land surface parameter threshold values used to identify incised landform elements. Decreasing the threshold (x-axis) will always increase the total area classified and vice versa. The y-axis is on a logarithmic scale.

When all components are adjusted simultaneously, the shape of the curves are dominated by the high sensitivity of the wall component (Figure 2.12). The other three parameters all show similar sensitivity to adjustment within ~±25% of their base threshold values.

2.4 discussion

2.4.1 Findings from Potential Channel Development Index (PCDI) outputs

Results from the case study indicate that in sections of land where clearing has occurred, there has been more incision happening than in neighboring locations left in a natural forested state (Figure 2.9). This finding supports the understanding that clearing encourages channel incision (e.g. Aksoy and Kavvas, 2005b, Menéndez-Duarte et al., 2007), and suggests that areas identified by the algorithm as being at risk of future incision are plausible.

Whether future incision will occur in areas identified as being at risk, however, also depends on non-topographic factors like soil, geology and rainfall (Valentin et al., 2005). Channel initiation may also require specific events to occur, such as a sufficiently intense rainstorm (Casalí et al., 1999), or a disturbance to groundcover in areas with a topographic setting enabling incision (Momm et al., 2012). There can be complex interactions between these factors too. For example, Prosser and Soufi (1998) found that the timing of extreme rainfall in the period immediately following clearing can determine whether incised channels will form. Similarly, Valentin et al. (2005) found that historic gully erosion aligns with periods of high-frequency extreme rainstorms as well as deforestation and land clearing.

For these reasons, analysis results are best suited to areas within close-proximity to one another. In our case study, geology, soils and climate were controlled for and land cover was used as the explanatory variable. A visual assessment of algorithm results (e.g. Figure 2.7d) was also conducted on a range of environments on Australia's eastern coastal margin from ~ 16 ° 30' S to ~ 35 ° 30' S, but quantitative comparison between cleared and forested areas was restricted to the case study site due to constraints discussed earlier (Section 2.2.8). This limits the confidence of extrapolating PCDI results to a wider range of environments. The case study, however, had a reasonably large sample size (n ≈ 500) of individual features within the study site and both the forested and cleared areas were well-represented.

A possible source of error for the index is the quality of the bare-earth DEM used for comparison. In this case, the DEM used was from the same source for all samples of both forested and cleared areas. However, in some cases forest cover may decrease LiDAR ground-return point density (James et al., 2007, Maguya et al., 2013) and this may affect the relative representation of potential and current channelled area.

2.4.2 Limitations of topographic analysis

Our method assumes that prediction of future channel erosion can be partly made by using land surface parameters to assess how water moves over the Earth's surface. Methods using elevation to assess the work done by gravity to direct the flow of water are well-suited to DEM analysis (Wilson, 2012), but flow will also be affected to a degree by the properties of the substrate (e.g. Gruber and Peckham, 2009). Hence, methods based on DEM analysis are expected to perform best in headwaters where elevation and topographic gradient have the largest relative influence (Gallant and

Hutchinson, 2011, Wilson, 2012). It is therefore expected that areas identified by the algorithm as being at risk of future incision will be more realistic in headwater catchments than in flatter landscapes. Outputs from running the algorithm in an alluvial landscape illustrate this limitation (Figure 2.13).

When an elevation position of 40th percentile (t = 0.4 in eq. 12) is used to estimate areas at risk of incision, existing ILEs are mapped outside of the area estimated to be at risk of incision (i and ii, Figure 2.13b). However, when elevation position is relaxed by ten percentiles to t = 0.5, areas estimated to be at risk of incision expand to encompass more of the mapped ILEs (i and ii, Figure 2.13c). The same response is not observed in the two colluvial landscapes when the elevation position threshold is relaxed. This provides some supporting evidence that stream indices are more relevant in steeper landscapes and suggests that in flatter landscapes elevation position alone becomes more important in estimating areas at risk of incision.

In Figure 13b there is only one clear example (iii) of an ILE existing entirely within the area mapped as being at risk of incision. This feature is being fed by a drainage line (dotted blue line) clearly visible in the hillshade DEM (Figure 2.13a). Logically, this would be a likely location for TWI and SPI to play a more important role.

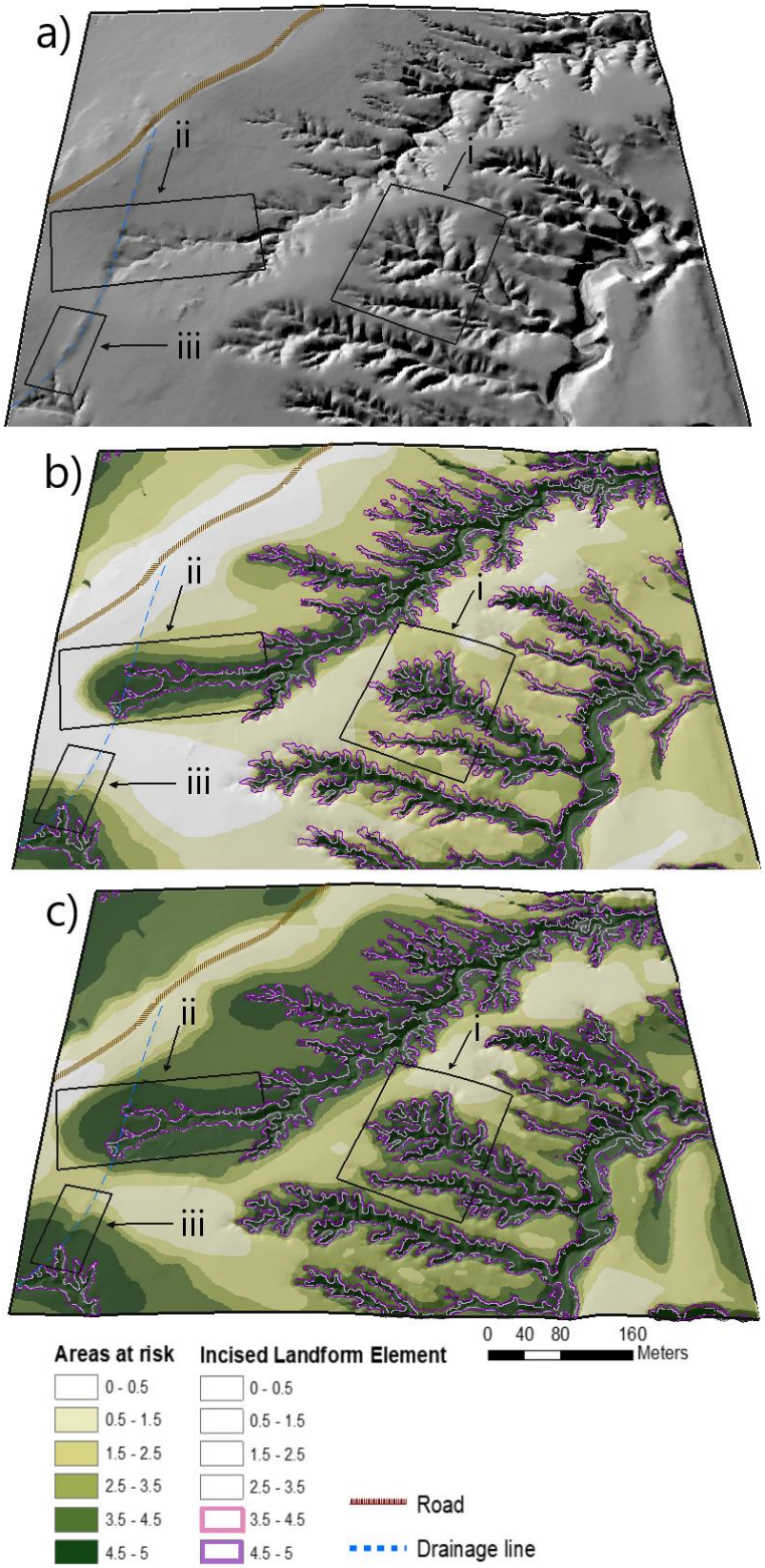

Figure 2.13: Algorithm results from an alluvial landscape (Mount Wickham, 20°27'S, 147°24'E). Panel (a) shows a hillshaded DEM. Panel (b) shows results where areas estimated to be at risk of incision have no adjustments to threshold parameter values, and (c) shows results when elevation position threshold is relaxed by ten percentiles. Areas i, ii and iii are discussed in the text (4.2).

Appropriate threshold values for TWI and SPI also depend on a range of factors (Momm et al., 2012). For example, calculating stream flow indices on a DEM implicitly assumes the entire catchment area contributes to runoff at the outlet, but runoff and infiltration are both influenced by physical landscape variables such as soil type and vegetation cover (e.g. Roa-García et al., 2011). Hence only some proportion of a catchment will typically contribute to runoff, and computed catchment areas will generally be over-estimated (Torri and Poesen, 2014). Similarly, a multi-flow director was used in the calculation of catchment areas to help mitigate some known issues with single steepest direction methods. However, multiple flow direction algorithms can produce artefacts as a product of routing flow to multiple downhill grid cells even in convergent scenarios (Quinn et al., 1991) and can be susceptible to over-dispersion (Tarboton, 1997). Locations identified as being at risk of future incision will, consequently, be more reliable in cases where landscape variables such as soil type and vegetation cover have a smaller influence on runoff.

2.4.3 Uses for the algorithm

Three possible uses for the algorithm are to (1) provide a visual assessment of landscapes requiring remediation of incisional erosion, (2) enable spatial prioritisation of erosion remediation and mitigation strategies across hundreds of square kilometres, and (3) help identify landscape attributes of potential relevance to process models.

Results illustrated in Figure 2.7 provide an example of the second suggested application by highlighting an area at risk of incision (i) where some incision has occurred but with a relatively large area remaining for it to continue expanding into. This would be considered a candidate for potential erosion mitigation efforts to prevent, or reduce rates of, further incision. A similar candidate area is identified by box (iii) in Figure 2.13, where a drainage line is flowing into an ILE, likely encouraging further channel incision.

Assessing outputs for both alluvial and colluvial landscapes also provides an example of how the algorithm may help to inform process models. For estimating areas at risk of incision, elevation position appears more important in the flatter landscape while stream flow indices appear more important in steeper landscape. This suggests the dominant erosion processes driving channel incision may differ between the two landscape types.

2.4.4 Topographic thresholds and gully types

In our study we used fixed threshold values for TWI and SPI found by Moore et al. (1988b) to correspond with ephemeral gully incision on agricultural landscapes in eastern Australia. The term ‘ephemeral gully’ has been used widely to distinguish small recurrent gullies from classical or permanent gullies, but with no consistent definition (Poesen et al., 2003).

Recently Bennett and Wells (2019) found that inconsistent vocabulary remains an issue in research referencing gully erosion. They suggest that the form of small features, with respect to geomorphic setting, and processes that drive their incision may differ from relatively large features, and that separation of the two may be useful. In our study we do not classify incised landform elements into groups, and instead assume conditions required to initiate ephemeral gullies are the same as those for permanent gullies. This reflects the understanding that incised landform elements including rills, ephemeral gullies and classical gullies all exist on a continuous spectrum, and their separation into discrete groups is necessarily subjective (Poesen et al., 2003).

2.4.5 Interpreting sensitivity results

Steps were taken to avoid misclassification errors in identification of ILEs, but it was still expected that results would be most adversely affected in environments with rough surfaces (high local variance in elevation), or with steep and highly variable slopes. This is because a rough surface can create noise in a DEM (e.g. Evans and Lindsay, 2010), and gully identification methods using slope as a parameter will have difficulty where the slope of walls in gullies differs within or between environments (Castillo et al., 2014). The ILE component expected to be most sensitive to this was the wall component, using S^{-1} as the primary parameter. Indeed, results showed that the wall component was the most sensitive across all landscapes (Figure 2.11a).

The higher sensitivity attributed to the S^{-1} parameter also dominated the overall sensitivity when all ILE components were assessed simultaneously (Figure 2.12). This suggests that prescribed threshold values for S^{-1} require the most attention to ensure accurate mapping results.

Conversely, identification of ILE floors showed comparatively low sensitivity (Figure 2.11b), suggesting that elevation position alone is sufficient to identify this

component and the flatness requirement can likely be omitted with minimal impact on results.

An unexpected insight from the sensitivity analysis was that the shape of the curves representing ILE identification as a function of parameter threshold adjustment (Figures 2.10 and 2.11a) are very similar for the two colluvial landscapes but different for the alluvial landscape. The two colluvial landscapes exist under different climates and are separated by a distance of > 1000 km. This suggests that the dominant landscape process may also be an important factor to consider in future improvements to this method or other similar methods aiming to identify ILEs in DEMs.

2.4.6 Usefulness of the multi-resolution approach

Operating on a multi-resolution basis allows the algorithm to identify ILEs across a broad range of scales, permitting a broader range of landscapes to be assessed. It also allows the algorithm to be used with DEMs of varying resolutions. For example, if a 10m gridded DEM were to be used as an initial input, then the algorithm can simply be initiated with thresholds corresponding to a 1m DEM that has undergone two steps of resampling ($DEM_{3,3}$, Table 2.1). In this example, ILE components would need to be identifiable at 10 m grid resolutions which would correspond to features with a width of ~20 – 30 m.

On a windows laptop computer with an i7 processor and 16 GB of RAM, the algorithm took ~11 minutes to produce the map shown in Figure 6, an area of ~1km^2 constituting ~1 x 10^6 grid cells at a resolution of 1m. Testing the sensitivity of the outputs across several landscapes required ~10 000 runs of the algorithm in total. This type of analysis was only possible on a regular laptop with a single quad-core processor due to the efficiency afforded by a multi-resolution approach.

2.5 Conclusion

We developed an algorithm that combines automated mapping of incised landform elements together with an assessment of areas at risk of future incision. Slope, curvature and elevation position were used to identify existing incised features while stream flow indices were used to determine areas at risk of future incision. A multi-resolution method was used as a computationally efficient approach to achieve both objectives simultaneously across multiple landscape scales.

The algorithm was used to develop an index of potential for future incision, called the Potential Channel Development Index. Testing at a case study site within the catchments of the Great Barrier Reef, Australia, found that forested areas have, on average, larger index values than cleared areas. This result met the expectation that cleared areas will typically be more incised than neighboring areas left in a natural state. Although the scope for testing was limited by availability of appropriate sites, this result suggests that index values are plausible, and that the algorithm has potential to identify candidate areas for erosion mitigation.

Sensitivity analysis conducted across three diverse landscapes indicated that the algorithm is reasonably robust and will likely be suitable for application across a range of landscapes. However, it also revealed that as average slope increases so too does the sensitivity of the outputs. This increased sensitivity was attributed to the part of the algorithm aimed at identifying the walls of incised landform elements, requiring slope as a parameter.

Results from an alluvial environment suggested that stream flow indices may not be as important in estimating areas at risk of incision as they are in steeper colluvial environments. This was not an unexpected result, and indicates that parameters used by the algorithm to determine areas at risk of incision should be adjusted according to dominant erosive processes driving channel erosion in a given landscape.

There is no incorporation of ancillary variables such as soil, rainfall or vegetation cover into the algorithm. Where the relative importance of these variables is greater than landscape morphology, outputs of the algorithm are expected to be less reliable. Future work should test whether combining the algorithm with simple process models can help to further refine candidate areas for erosion remediation. The addition of a method to separate gullies from natural streams would also extend the range of applications.

Chapter 3: A comparison of hillslope drainage area estimation methods using high-resolution DEMs with implications for topographic studies of gullies

Walker, S. J., Van Dijk, A. I. J. M., and Hairsine, P. B. 2021. A comparison of hillslope drainage area estimation methods using high-resolution DEMs with implications for topographic studies of gullies. *Earth Surface Processes and Landforms*, online version of record before inclusion in an issue.

Abstract

Topographic models provide a useful tool for understanding gully occurrence in the landscape but require reliable estimates of gully head drainage areas. Modern high-resolution topography data (collected using structure from motion photogrammetry or light detection and ranging) is increasingly used for topographic studies of gullies, but little work has been done to assess the variability of gully head drainage area estimates using different methods. This study evaluated alternative approaches to using high-resolution digital elevation models (DEMs) so that gully topographic models can be more readily applied to any area with suitably high-resolution data. Specifically, we investigated the impact of single- or multiple-direction flow routing algorithms, DEM hydrologic-enforcement procedures and spatial resolution on gully head drainage area estimation. We tested these methods on a 40 km^2 site centred on Weany Creek, a low-relief semi-arid landscape draining towards the Great Barrier Reef, Australia. Using a subroutine to separate gully heads into those with divergent or convergent flow patterns upslope we found that divergent flow conditions occurred at half of 484 studied gullies. Drainage areas estimated by different flow routing algorithms were more variable in these divergent cases than for convergent cases. This variation caused a significant difference between topographic threshold parameters (slope *b* and intercept *k*) derived from single- or multiple-direction flow routing algorithms, respectively. Different methods of hydrologic-enforcement (filling or breaching) also affected threshold analysis, resulting in estimates of the exponent *b* being ~188% higher if the DEM was filled than if breached. The testing of the methods to date indicates a finer resolution (≤2 m) DEM and a multiple-direction flow routing algorithm achieve most realistic drainage area estimates

in low-relief landscapes. For Weany Creek we estimated threshold parameters k = 0.033 and b = 0.189, indicating it is highly susceptible to gully erosion.

3.1 Introduction

3.1.1 Gully head topographic threshold analysis

Channel formation on hillslopes is controlled by factors including soil type, vegetation cover and rainfall (e.g. Montgomery and Dietrich, 1988, Sidle et al., 2019, Yibeltal et al., 2019b, Conoscenti and Rotigliano, 2020). The position of gully heads in a catchment holds information about the relative importance of these factors to channel development (Torri and Poesen, 2014). Early work by Patton and Schumm (1975) looked at this in terms of the relationship between soil surface slope just above the gully head and drainage area. Plotting one against the other, they observed a clear threshold between gullied and un-gullied hillslopes. Many studies have since investigated thresholds across different landscapes using the theoretical model proposed by Montgomery and Dietrich (1994):

$$s \geq ka^{-b} \quad (1)$$

where s (m m^{-1}) is the slope of the soil surface above the gully head and a (ha) is drainage area (A) per unit contour width, both measured in the field or derived from topographic data, while k and b are empirical parameters. Equation 1 was initially formulated in terms of specific catchment area (a), but most subsequent applications have used drainage area (A) as a substitute (Torri and Poesen, 2014). The parameter k is influenced by vegetation and rock fragment cover, soil type and climate (Gudino-Elizondo et al., 2018). The exponent b varies depending if gully erosion is driven by surface or sub-surface processes and is expected to depend on whether flow above the gully head is turbulent or laminar (Montgomery and Dietrich, 1994). Values for k and b typically range between 0.01-0.9 and 0.1-0.5, respectively (Torri and Poesen, 2014).

A recent review by Torri and Poesen (2014) sought to move towards more reliable and physically based predictive models by analysing the behavior k and b across different environments. While they were able to observe general trends in k, they encountered a wide range of variability in the methods applied in individual studies. Even with a standardised methodology to measure slope (e.g., Nyssen et al. (2002)) there remained differences in methods to estimate drainage area. Some studies measured drainage area from visual field surveys (e.g. Vandekerckhove et al., 2000, Nyssen et al., 2002), but most estimated it through digital elevation model (DEM)

analysis. For the latter, variations in estimated area arise due to differences in resolution of the DEM (e.g. Walker and Willgoose, 1999) and the methods used for computing drainage area (e.g. Desmet and Govers, 1996).

3.1.2 Drainage area, flow routing algorithms and DEM resolution

Variations in hillslope drainage area estimates have implications for a range of hydrologic and geomorphic applications. Some examples include predicting zones of saturation overland flow (e.g. Shelef and Hilley, 2013), computing topographic indices such as the topographic wetness index (e.g. Seibert and McGlynn, 2007, Buchanan et al., 2014), evaluating erosion models such as the Universal Soil Loss Equation (e.g. Liu et al., 2011) and interpreting landscape evolution over long timescales (e.g. Pelletier, 2004). Critically in the present context, the problem extends to models of gully erosion where drainage area plays an important role (e.g. Vanmaercke et al., 2016). Issues arise when microtopographic features complicate delineation of drainage areas (Gudino-Elizondo et al., 2018). Our current study was partly motivated by the cursory observation that across the study site, microtopographic features (here defined as small-scale geomorphic features spanning one to a few metres) were causing flow divergence upslope of some gully heads (Figure S1 in supplementary material). This was leading to distinct differences in estimated upslope drainage area (Figure 3.1).

3.1.3 Aims

The primary aim of this work was to evaluate the impact that different flow routing algorithms, DEM resolutions and hydrologic-enforcement (sink filling and breaching) have on gully topographic threshold analysis (‘threshold analysis’ from here on). Within this broader aim, we wished to investigate four questions: (1) How often does microtopography cause divergent flow upslope of gully heads? (2) How do different flow routing algorithms perform under different hillslope flow conditions? (3) What is the influence of resolution and DEM hydrologic-enforcement on drainage area estimates? (4) How sensitive is threshold analysis to uncertain drainage area estimates? Our overarching goal was to contribute towards a standardised methodology for threshold analysis across large areas using high-resolution DEMs (where “high-resolution” is defined as a spatial resolution of ~1-5 m).

3.2 Methods

Our experiment was designed to quantify the variability in drainage area estimates across five DEM resolutions (1, 2, 3, 4 and 5 m) and test single-direction and multiple-direction routing algorithms. We used 1 m as the finest resolution because it is a common resolution for publicly available datasets (e.g., most DEM datasets in ELVIS, http://elevation.fsdf.org.au/). We chose 5 m as the coarsest resolution because most contemporary DEMs do not exceed 5 m resolution. Additionally, we tested three methods for removing pits and sinks from the DEM: filling, breaching and hybrid breaching-filling.

Throughout our analyses, gully heads were separated into two groups with either (a) convergent or (b) divergent flow patterns upslope of the gully head (section 3.2.7). This was motivated by early visual indications that different routing algorithms showed more variation where hillslope divergence occurred (cf. Figure 3.1).

3.2.1 Study site

We studied an area of ~40 km^2 centered on Weany Creek (S19°53′06.79″, E146°32′06.65″), a small (~13.6 km^2) catchment within the Burdekin River Basin which covers ~130 000 km^2 of the wet-dry tropics of Queensland, Australia (Figure S2, supplementary material). Weany Creek has been a long-term erosion monitoring site with various studies investigating gully erosion, sediment loads and vegetation change (e.g. Bartley et al., 2010b, Bartley et al., 2014b, Wilkinson et al., 2018, Koci et al., 2020b). The area is underlain by the Ravenswood Batholith (granodiorite) which evolved in several stages over the Ordovician to early-Permian (Woods and Rienks, 1992). The soils are predominantly red chromosol (Figure 3.2a, b and d), a duplex textured sandy clay loam known locally as the ‘red goldfields’ (Bartley et al., 2010b, Wilkinson et al., 2018). Chromosol soils in this region have a relatively high prevalence of gullying compared to other soil orders (Gilad et al., 2012).

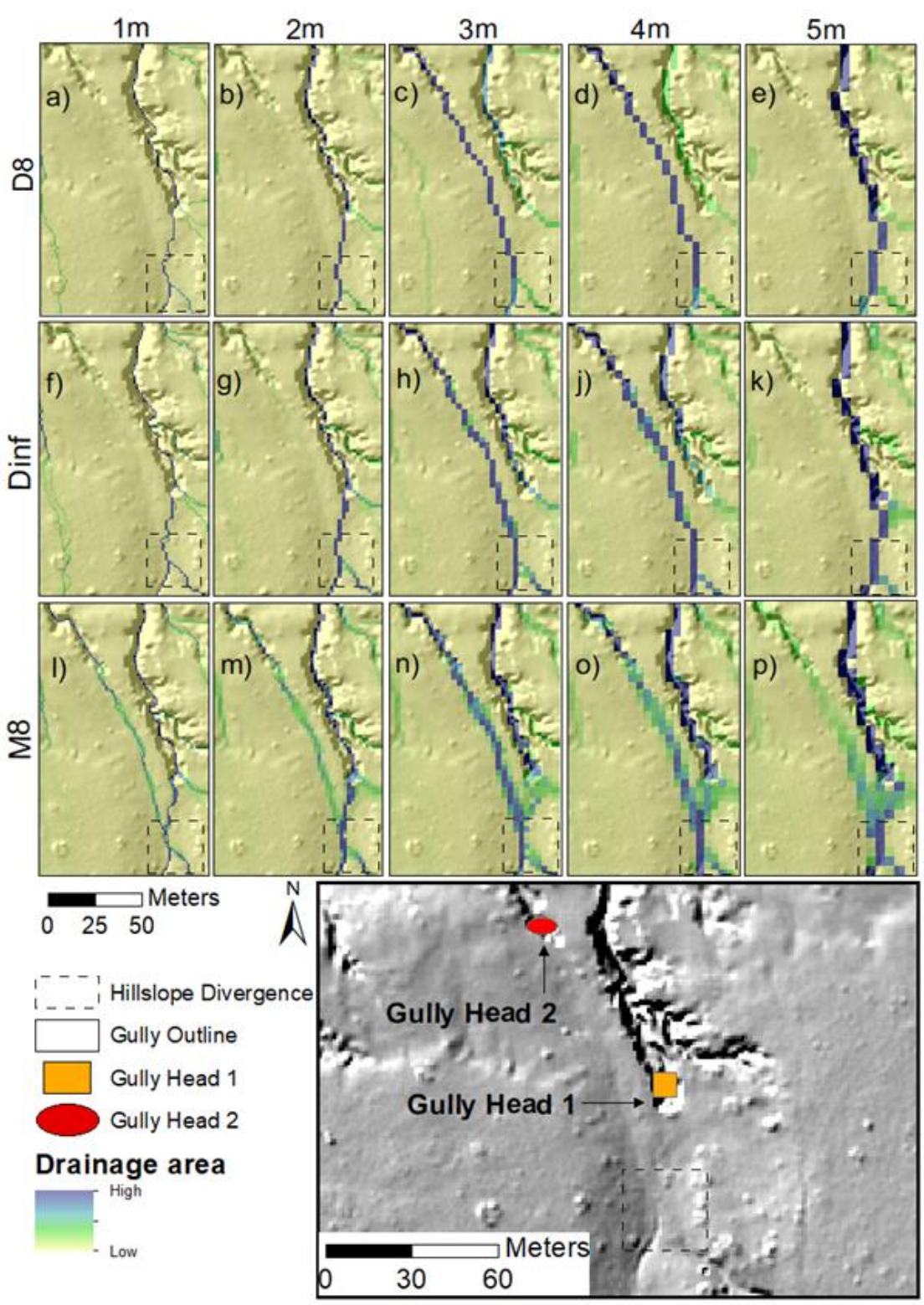

Figure 3.1: Visual comparison of drainage areas for (a) an eight-directional single-direction algorithm (D8), (b) the D-infinity algorithm that routes flow in a single-direction unrestricted to the eight grid-based directions, and (c) an eight-directional multiple-direction algorithm (M8). Each is run at 1, 2, 3, 4 and 5 m resolutions. The dashed square shows the zone where flow divergence occurs.

Gullies in Weany Creek are typically part of mature gully networks with multiple branches and have been well-established since at least 1945 when the earliest air photos are available (Wilkinson et al., 2018). Individual gully branches are typically confined to drainage lines with lengths ranging from 10–200 m and widths 5-15 m. Across the site gully density has been estimated at 4.5 km/km (Heine, 2002). Land use in the broader region is dominated by livestock grazing occurring over ~88% of the Upper Burdekin region (Jarihani et al., 2017). Our study site sits within the Virginia Park cattle grazing station which has been grazed for over 100 years (Bartley et al., 2010a).

Figure 3.2: Photos from the site taken in July 2019. Panel a) shows the form of a typical hillslope gully in Weany Creek (~15 m downstream of gully head) and panel b) a wall segment (~1 m high) from the same gully with live plant roots the full length down. Panel c) shows typical tree cover for the site and grass cover after the wettest January-June period in six years. Panel d) shows an active gully head during a runoff event.

The region has a tropical savannah climate (Beck et al., 2018) strongly modulated by the El-Niño Southern Oscillation (ENSO) over interannual timescales (Klingaman, 2012). Over the past 30 years the lowest recorded rainfall was 178 mm and the highest was 1286 mm, with an annual average (1981-2010) of ~650 mm y^{-1} and standard deviation of 285 mm (Australian Bureau of Meteorology, 2020). Rainfall intensities are high, and most rainfall occurs over the summer months (December-February) with ~70% of annual rainfall occurring over this period (Wilkinson et al., 2018). Extreme rainfall events in the region are also correlated with tropical cyclone activity (King et al., 2014). These climatic conditions also lead to high interannual variability of runoff, with flow in streams and rivers typically being event-driven (Petheram et al., 2008).

Due to the variable nature of climate, and resultant event-driven runoff, erosion and deposition also occur episodically (Koci et al., 2020b). Relief across the area is low with an average slope of ~2.3% (Koci et al., 2017). This low relief and periodic runoff create small-scale depositional fans that act to disperse flow on some hillslopes. These zones often occur at the terminal end of small gullies or rills upstream of larger gully heads (e.g. dashed square Figure 3.1).

Vegetation across the site is largely eucalypt open woodlands (Figure 3.2a and c) with a ground cover of Indian Couch (*Bothriochloa Pertusa*), an invasive exotic grass that grows quickly after rain and dies quickly during drought (Bartley et al., 2010a). Bare scald patches, measuring tens of metres, occur alongside gullies and streams across the catchment (Bartley et al., 2010a).

3.2.2 Data

We used a bare-earth DEM created from an airborne LiDAR capture with an average pulse density of 8 pulses m^{-2} (Tindall et al., 2014b). The bare-earth DEM was created by interpolating ground returns using the natural neighbor method described in (Sibson, 1981). The initial gridded resolution of the DEM was 0.5 m with a reported relative vertical accuracy of ±0.1 m (RMSE) and horizontal accuracy of ±0.5 m (RMSE) (see Tindall et al. (2014b) for further details).

3.2.3 Locating initial gully heads

Initially, we mapped all channel features across the study area following Walker et al. (2020). The method uses the topographic signature of gullies to map them across

large areas. We then intersected the mapped features with concentrated flow lines (>0.25 ha drainage area) to approximate the position of the gully heads (e.g., the pink square in Figure 3.3). The threshold of 0.25 ha was chosen pragmatically, by visually examining flow lines intersecting our mapped features: much lower thresholds produced too many intersecting points, while much higher thresholds excluded too many gullies. The resulting mapping contained 688 gully heads across the 40-km^2 study area.

3.2.4 Defining gully head drainage area

Calculating drainage area at a gully head is relatively simple when a gully head occupies only a single grid cell (as most gullies in this study site would at a resolution of ~10 m). However, with high-resolution data most gully heads occupy multiple cells. Hence, there are multiple candidate cells from which drainage area could be calculated. This issue was touched on by Strahler et al. (1986) who differentiated the two scenarios with the notation ‘H-resolution’ (objects occupying multiple cells or pixels) and ‘L-resolution’ (objects existing within a single cell). They suggest that appropriate analysis methods are governed by this relationship between object and data scale. For our study site (and many others) a resolution of 1 m places most gully heads in H-resolution, requiring a method to find the ‘best cell’ from which to calculate drainage area.

Finding the ‘best’ DEM cell has also been a consideration in other areas of hydrology (e.g., Hou et al., 2020) when the exact location of a channel is unknown with respect to any given cell in a remote sensing product. Walker and Willgoose (1999) compared drainage area estimates of streams across different DEMs and resolutions and found that the optimal cell from which to measure drainage area (i.e., the outlet) can change position due to small changes in DEM derivation. They used a type of ‘best cell’ approach to manage this but found errors occurred due to incorrect cells being compared when multiple possible stream outlet candidates existed close to one another. The authors noted that this can be managed by manually checking the results.

We found many cases where two gully heads were relatively close. With 688 gully heads, manually checking that the correct cell was used proved time-consuming, especially since multiple iterations of the analysis were performed. Hence, we

developed an analysis procedure to minimise comparison errors when moving between DEM resolutions and using different flow routing algorithms (Figure 3.3).

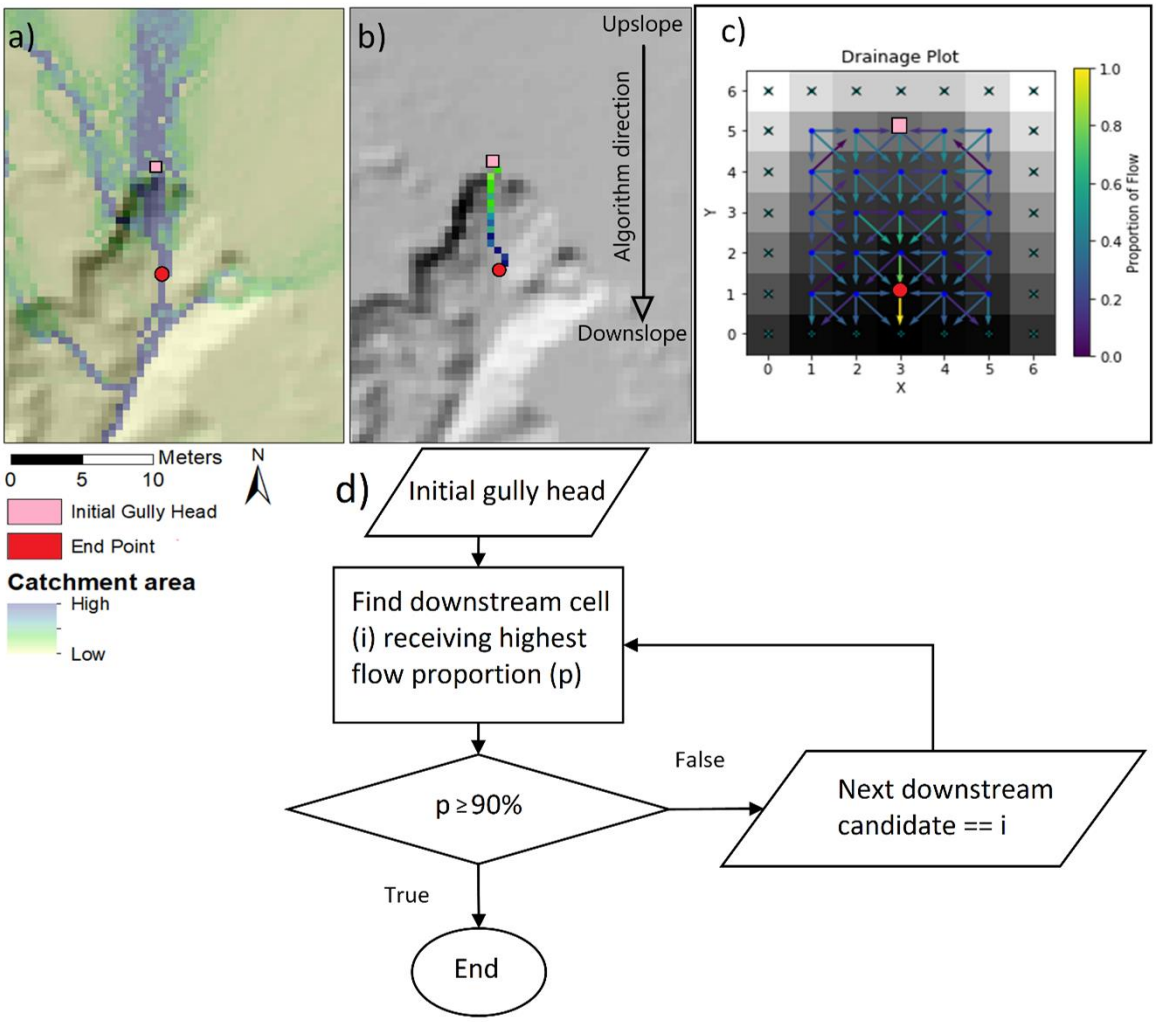

Figure 3.3: Schematic of subroutine to locate the 'best cell' from which to collect drainage area at the gully head. The pink square is the initial gully head found by intersecting the mapped gully with a flow line >0.25 ha. The red circle is the end point of the routine and is identified as the first point of convergence on the gully floor. Panel a) shows drainage area computed with a multiple-direction algorithm, b) is the most concentrated flow line, c) a representation of when the routine finds a point of concentrated flow (yellow arrow) and d) a schematic overview of the routine.

Qualitatively, we defined the gully head to be the first point of convergent flow on the gully floor. This is a similar conceptualisation used by Hancock and Evans (2006), who defined channel heads to be the first point on a hillslope where unconfined divergent flow converges to a concentrated flow line. Quantitatively, convergent flow on the gully floor was measured as the first point moving from upstream to downstream where a cell routes ≥ 90% of its drainage area to only one downslope cell (Figure 3.3c).

The subroutine provided an explicit and transparent way of defining drainage area at the gully head and enabled fully automated calculation of drainage areas. It also helped to bring the quantities of drainage area (*A*) and specific catchment area (*a*) closer by finding a concentrated point on the gully floor (where contour width approaches unity). After processing all 688 gully heads, a suitable cell was found at each of the five resolutions for 484 cases. The remaining 204 gully heads were discarded from further analyses. These discarded cases were gullies where flow convergence did not occur within a predefined distance (10 m) downstream of the initial gully head. No formal analysis was done on the excluded gullies but visual assessment of their size and shape using hillshade DEMs indicated they were typically either short in length (hence minimal opportunity to meet the criteria) or were discontinuous gullies where the most upslope segment faded into the hillslope again shortly downstream.

3.2.5 Routing algorithms

We first compared the widely used deterministic eight-node (D8) algorithm (O'Callaghan and Mark, 1984) to the eight-neighbor multiple-flow-direction algorithm (M8) proposed by (Quinn et al., 1991). These two algorithms can be considered two extremes among routing methods (Shelef and Hilley, 2013), with D8 constraining flow to only the steepest downslope cell while M8 sends some proportion of flow to all downslope cells.

The steepest downhill direction used by D8 is typically determined by:

$$S_i = \varphi(i)(z_9 - z_i)/\lambda \quad (2)$$

$$\varphi(i) = \begin{cases} 1, & cardinals \\ \frac{1}{\sqrt{2}}, & diagonals \end{cases} \quad (3)$$

Where z_9 is the elevation of the central grid cell of a 3 x 3 window, z_i is the elevation of the i^{th} neighbor and $\boldsymbol{\lambda}$ is the grid cell resolution (Wilson et al., 2007).

Partitioning of flow to the downslope receiving grid cells under the M8 routing scheme is given by:

$$\Delta A_i = A \frac{tan\beta_i L_i}{\sum_{j=1}^{n} tan\beta_j L_j} \quad (4)$$

Where ΔA_i is the proportion of flow directed to the i^{th} grid cell of the eight possible receivers, A is the total available upslope drainage area, β is the slope gradient in the

direction of the i^{th} or j^{th} grid cell, $\sum_{j=1}^{n}$ is a summation over all downslope grid cells and L is a factor dependent on grid-based contour length:

$$L = \begin{cases} 0.5, & cardinals \\ \frac{0.5}{\sqrt{2}}, & diagonals \end{cases} \quad (5)$$

D8 will always converge to a single cell under any scenario, while M8 will tend to disperse flow to multiple downslope cells, even on convergent hillslopes. We also used an M4 algorithm with the same rules as M8 but considering only the cardinal directions (90°, 180°, 270° and 360°). This was done because it is conceptually simpler and has a lower computational cost yet could conceivably produce equally reliable results.

We then tested the D-infinity (D_{inf}) routing algorithm proposed by Tarboton (1997) which sits conceptually between a single-direction and multiple-direction algorithm. The D_{inf} is not restricted to eight grid-based directions (at increments of 45°) and is able to route flow to a maximum of two downslope cells. However, these downslope cells must be adjacent (e.g., S and SW), unlike a true multiple-direction algorithm that can distribute flow to any number of downslope cells.

Finally, we tested an alternative version of an eight-node multiple-direction algorithm (FD8) proposed by (Freeman, 1991). This method uses similar rules to that of Quinn et al. (1991) but adds an exponent (p) to control the degree of flow convergence or divergence:

$$\Delta A_i = A \frac{Max(0, \beta_i^p)}{\sum_{j=1}^{n}(Max(0, \beta_i^p))} \quad (6)$$

Larger values of p emulate more convergent conditions and smaller values more dispersive. At p = 0, all surrounding cells receive equal flow and as p approaches infinity the behaviour approaches a single-direction algorithm. A value of p = 1 behaves in a similar way to the M8 proposed by Quinn et al. (1991). For this algorithm, we tested a range values for p to determine the effect on estimated threshold parameters.

Flow routing algorithms were implemented in Landlab (https://landlab.github.io/#/), a Python-based Earth surface process modelling package (Hobley et al., 2017b, Barnhart et al., 2020) and Whitebox (https://jblindsay.github.io/) a stand-alone geospatial analysis platform (Lindsay, 2016b)

3.2.6 DEM hydrologic-enforcement

Sinks and depressions in DEMs can represent real terrain forms, but most are caused by data errors and need to be corrected prior to routing flow (Rieger, 1998). We assessed several hydrologic-enforcement methods and their impact on estimated drainage areas and threshold analysis parameters. The first was a DEM filling procedure developed by Barnes et al. (2014). This Priority-Flood method progressively 'floods' a DEM inward from the edges until all cells are guaranteed to drain. The second was a DEM 'breaching' method proposed by Lindsay and Dhun (2015). Breaching, unlike filling, excavates channels in the DEM to ensure all cells drain correctly. Finally, we assessed a hybrid breaching-filling algorithm (Lindsay, 2016a) that first breaches channel,s and subsequently fills remaining pits and sinks. For each above method we also assessed the impact on the DEM in terms of areal extent of modified cells and total volume of change between the pre- and post-processed DEMs. These evaluations were conducted on a ~116 (ha) area of Weany Creek to provide an example at a scale closer to what many topographic threshold studies are conducted (e.g. Gutiérrez et al., 2009, Gudino-Elizondo et al., 2018, Yibeltal et al., 2019b). The area encompasses a large gully network previously studied by Wilkinson et al. (2018) and is known to have multiple active gully heads.

3.2.7 Flow conditions above gully heads

The influence of microtopography on hillslope flow paths can generally be resolved with high-resolution DEMs (Thomas et al., 2017). Visual examination of drainage area maps for our study site indicated that microtopography caused divergent flow to occur above some gully heads, affecting the estimate of drainage area (e.g. see Figure 3.1). We wanted to test how common this was across our study area. For this task, we developed a second subroutine to examine each gully head for indicators of upstream flow divergence (Figure 3.4). Using the M8 method, the subroutine starts at the gully head cell (found by the subroutine described in 2.4) and progresses upslope, following the most concentrated flow line until an arbitrary maximum distance is reached. We used a value of 100 m for this site because gully heads tend to exist between 50-300 m from the drainage divide and most points of flow divergence appeared to occur within 50 m of the gully head.

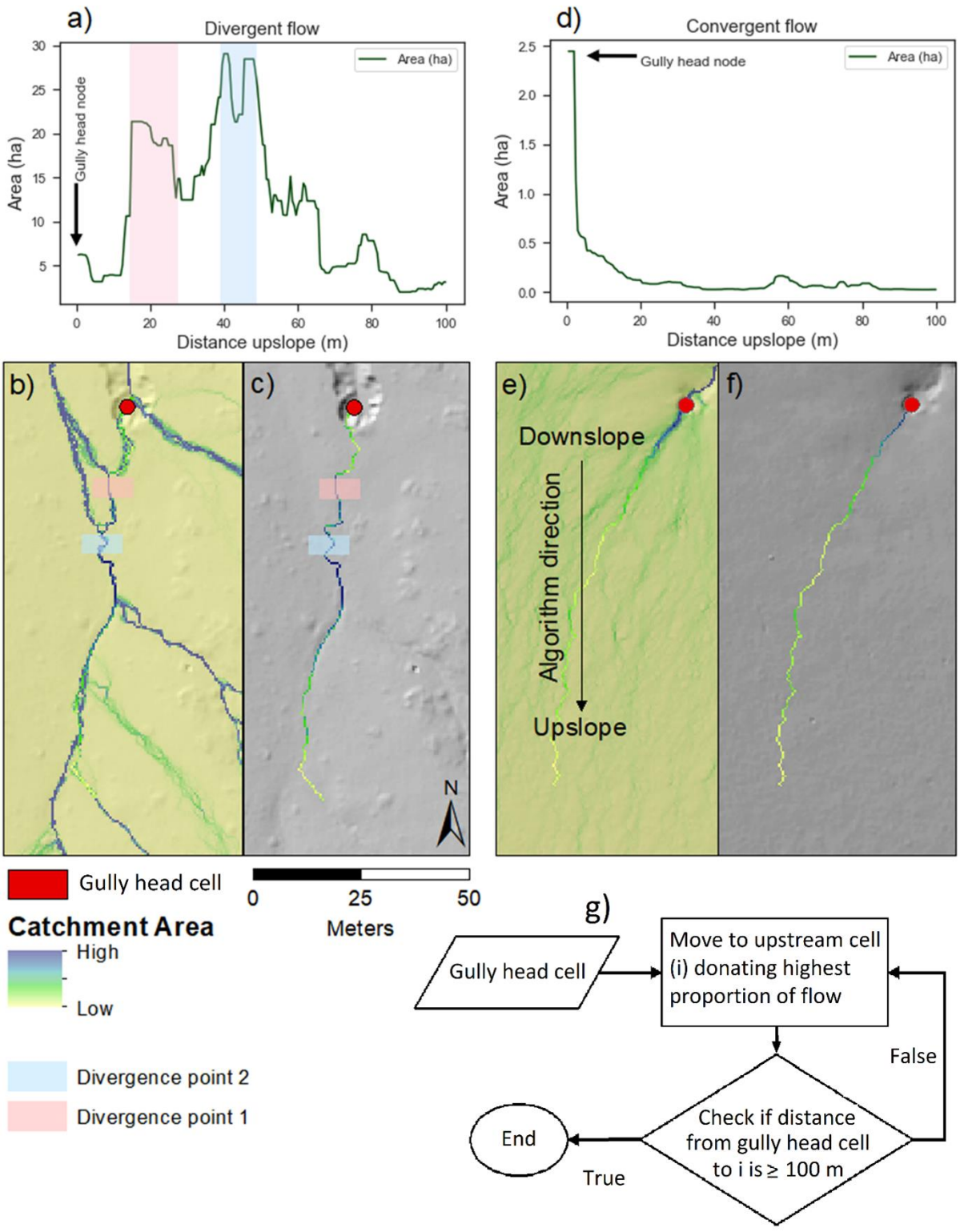

Figure 3.4: Schematic of a subroutine using a multiple-direction algorithm to test for hillslope flow divergence upstream of gully heads. Pink and blue bars in panel a) and d) correspond to pink and blue rectangles in panel b) and c) as the subroutine moves from downslope to upslope. Panel b) and e) show drainage area above a divergent and convergent gully, respectively. Panel c) and f) show the most concentrated flow line found by running the subroutine 100 m upslope of each gully head. Panel a) and d) plot the drainage area along the respective concentrated flow lines.

As the subroutine progresses upslope, it records the drainage area of each cell (Figure 3.4a and d). A one-dimensional kernel is passed over the distance-ordered drainage values, identifying points where drainage area increases upslope of the gully head (compare pink and blue shaded bars in Figure 3.4a). The kernel has a length of Δm divided into three segments of equal length. These include a segment of 'downstream' cells (D = {d_1, … d_n}), a segment of 'upstream' cells (U = {u_1, … u_n}) and a segment separating *D* from *U* by a distance $\left\lfloor \frac{\Delta m}{3} \right\rfloor$. The length of the kernel in cells depends on the resolution of the data (e.g., for Δm = 15 at 5 m resolution the kernel will be three cells). As the kernel is passed over the ordered drainage area values, the subroutine determines whether the drainage area of every cell in *U* is larger than the maximum cell value in *D* by at least factor of *y*:

$$C = u \in U | u \geq \max(D) \cdot y \quad (7)$$

Finally, comparing *C* to *U* the subroutine determines whether divergence (∇) is occurring above a gully head, assigning a value of 1 for divergence or 0 for no divergence:

$$\nabla = \begin{cases} 1, & C = U \\ 0, & C \neq U \end{cases} \quad (8)$$

A gully head was characterised as divergent if any point along the 100 m primary flow line was identified as divergent. This process does not assess divergence occurring on secondary flow paths into the gully head.

A segmented distance scheme was used because drainage values along the concentrated flow lines tended to be noisy from one cell to the next, making simpler schemes unreliable. We used values of Δm = 15 and *y* = 1.5, found by some trial and error. Larger values of Δm or *y* decreased the number of gully heads identified as having upstream divergence, while smaller values increased their number. Detecting divergence in DEMs with more noise would require larger values for Δm.

3.2.8 Comparing drainage area between routing algorithms and across resolutions

To analyse the difference in drainage area estimates at different resolutions we created five progressively coarser DEMs of 1, 2, 3, 4 and 5 m. The grids were resampled from the initial 0.5-m resolution DEM using bilinear interpolation implemented in the Python library 'Scipy' (https://www.scipy.org/). We computed

drainage area for each routing algorithm (Section 3.2.5), producing 484 individual drainage area estimates at each of the five resolutions.

We compared drainage area estimates by calculating Pearson's correlation coefficient (*r*) using the Python library 'Pandas' (https://pandas.pydata.org/) for each resolution pair and each routing algorithm. This was done to assess the consistency with which each routing method computes drainage areas across resolutions.

Next, we compared the correlation between pairs of flow routing algorithms at all five gridded resolutions. A priori, we expected the M8 algorithm to handle divergent flow scenarios better, hence our comparison between routing algorithms focused on how the D8, D_{inf} and M4 compared with the M8 method.

3.2.9 Estimating parameters for gully topographic thresholds

We measured the impact of flow routing method and resolution on estimated parameters *k* and *b* (Equation 1). These parameters describe the best-fitting straight line through the lower most points (the points with lowest slope for a given area) of a set of plotted gully heads; the 'topographic threshold'. There is no standardised approach for finding this line, with most studies either finding the line best fitting all data and then translating it to go through the lowest points or fitting a line directly through the lowest points (Torri and Poesen, 2014). Our automated method was intermediate to these two approaches.

We had many gully heads to work with (n = 484) due to the size (~40 km^2) and high gully density of the study area. This gave us the opportunity to assess the variability of parameter estimates and the statistical differences between divergent and convergent gully heads. To do this we performed a bootstrap simulation iteratively selecting random samples (*n* = 30) from the convergent and divergent gully head groups separately. For each sample, we estimated the two parameters *k* and *b* as follows:

1. find the best-fitting line through all data points in the sample using standard linear regression on log-transformed slope and area;
2. remove all sample data points above the best fit line;
3. exclude outliers in the remaining data exceeding a Cook's distance of $\frac{4}{n}$; and
4. find the best-fitting line for the remaining data points.

Outliers were removed because they occasionally had a large impact on parameter estimates. We needed an automatic approach to remove them that worked within our bootstrap simulation. For each routing algorithm and resolution, we took 10 000 bootstrap samples for each of the divergent and convergent gully head groups separately. Our analysis used drainage area (*A*) as a substitute for specific catchment area (*a*) in Equation 1. Results from the bootstrap simulation are presented alongside a slope-area plot for all gully heads together as one sample.

3.3 Results

3.3.1 Convergent and divergent flow above gully heads

Using our method to separate divergent and convergent gully approaches (section 2.7), we found that divergent flow above gully heads was common across our study site (Figure S3 in the supplementary material). At a resolution of 1 m, there were more gullies with divergent flow conditions above the head than convergent. As resolution was coarsened, the ratio of divergent to convergent cases decreased. We also found consistent differences between the statistical distribution of slope and drainage area for gullies with divergent and convergent flow patterns (Figure 3.5). Drainage areas were typically larger and with higher variability for divergent cases, while slopes were gentler.

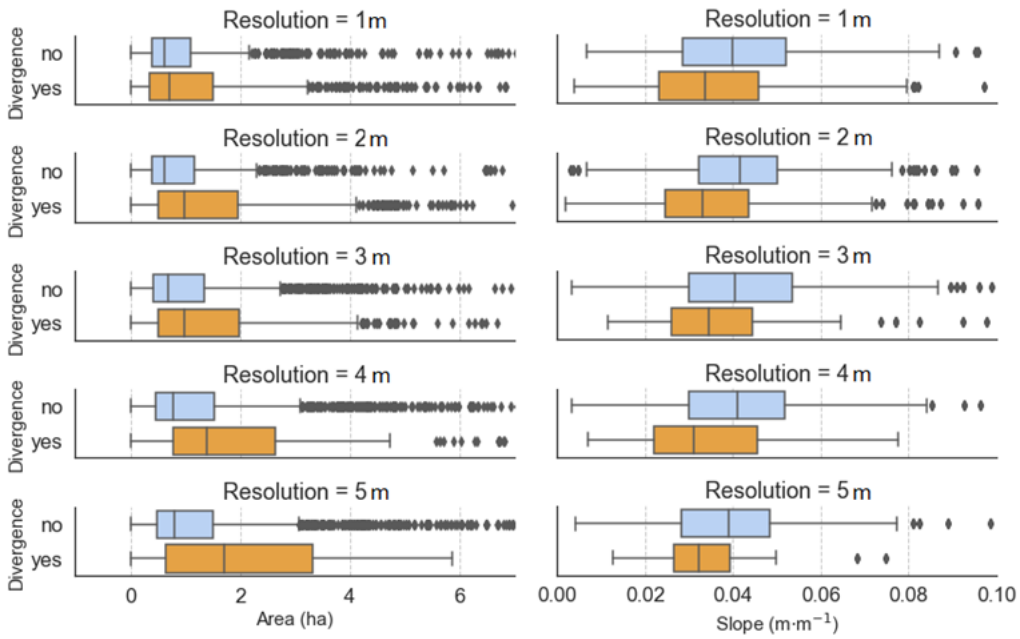

Figure 3.5: Average slope and drainage area for all gully heads (n = 484) grouped into divergent (orange) and convergent (blue) gully heads. Each row shows the distribution of slope and area values for a given spatial resolution.

A Mann-Whitney two-sample rank sum test showed that the difference between slope values for divergent and convergent cases was significant at every resolution. Drainage areas were also significantly different between the two types at all resolutions except 1 m (Table S1, supplementary material). The Mann-Whitney test was used because the gully head drainage area data tended to remain right-skewed under various attempted transformations.

3.3.2 Drainage area estimation across resolutions

In our correlation analysis comparing drainage area estimates of each flow routing algorithm we found all algorithms performed similarly for convergent cases (Figure 3.6).

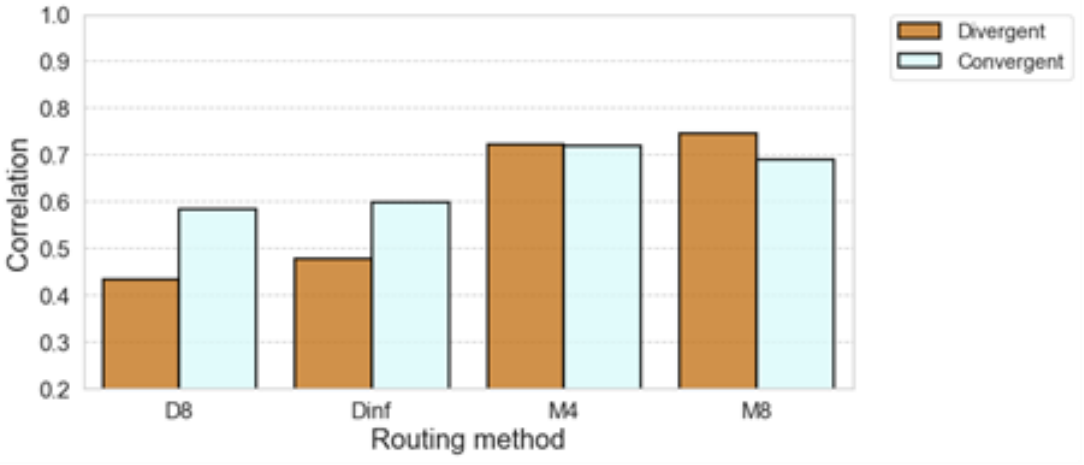

Figure 3.6: Average Pearson's r correlation for drainage area between all pairs of resolutions (1-2m, 1-3m, 1-4m 1-5m, 2-3m, 2-4m, 2-5m, 3-4m, 3-5m, 4-5m) for each flow routing method. Values represent the mean correlation between all possible pairs of resolutions. All 484 gully heads are separated according to divergent (orange) or convergent (blue) flow above the gully head.

There was greater variation for divergent cases. The D8 and D_{inf} algorithms had the lowest consistency with an average *r* of 0.43 and 0.48, respectively. The two multiple-direction algorithms were most consistent (r>0.7). Results for all resolution pairs are available in the supplementary material (Table S2).

3.3.3 Correlation between routing algorithms

For convergent cases, all routing algorithms showed good agreement (r> 0.9), except for the D8 at 3-m resolution (Table 3.1 and Figure S5).

Table 3.1: Pearson's r correlation between the M8 algorithm and each other routing algorithm conducted across five resolutions (1, 2, 3, 4 and 5 m). All 484 gully heads are separated according to divergent or convergent flow, respectively.

Resolution	Methods compared	Convergent (*r*)	Divergent (*r*)
1 m	D8-M8	0.98	0.73
	Dinf-M8	0.98	0.77
	M4-M8	0.92	0.85
2 m	D8-M8	0.95	0.76
	Dinf-M8	0.96	0.87
	M4-M8	0.98	0.62
3 m	D8-M8	0.86	0.89
	Dinf-M8	0.92	0.93
	M4-M8	0.94	0.94
4 m	D8-M8	0.92	0.88
	Dinf-M8	0.93	0.89
	M4-M8	0.97	0.91
5 m	D8-M8	0.92	0.99
	Dinf-M8	0.97	0.99
	M4-M8	0.96	0.99

For divergent cases, correlations were lower at resolutions ≤2 m with an average correlation of ~0.76 between algorithms. Conversely, the average correlation for convergent cases was ~0.96 for the same resolution range (1-2 m). For resolutions >2 m the average correlation was ~0.93 for both convergent and divergent cases.

3.3.4 Variation in gully head topographic thresholds

For a given drainage area divergent gullies typically have lower slopes above the head than convergent gullies (Figure 3.5). In threshold analysis, the lower position of divergent gullies in slope-area space gives them more influence over the threshold line (drawn through the lower data points). Figure 3.7, below, shows the location in slope-area space of the two divergent cases illustrated in Figure 3.1.

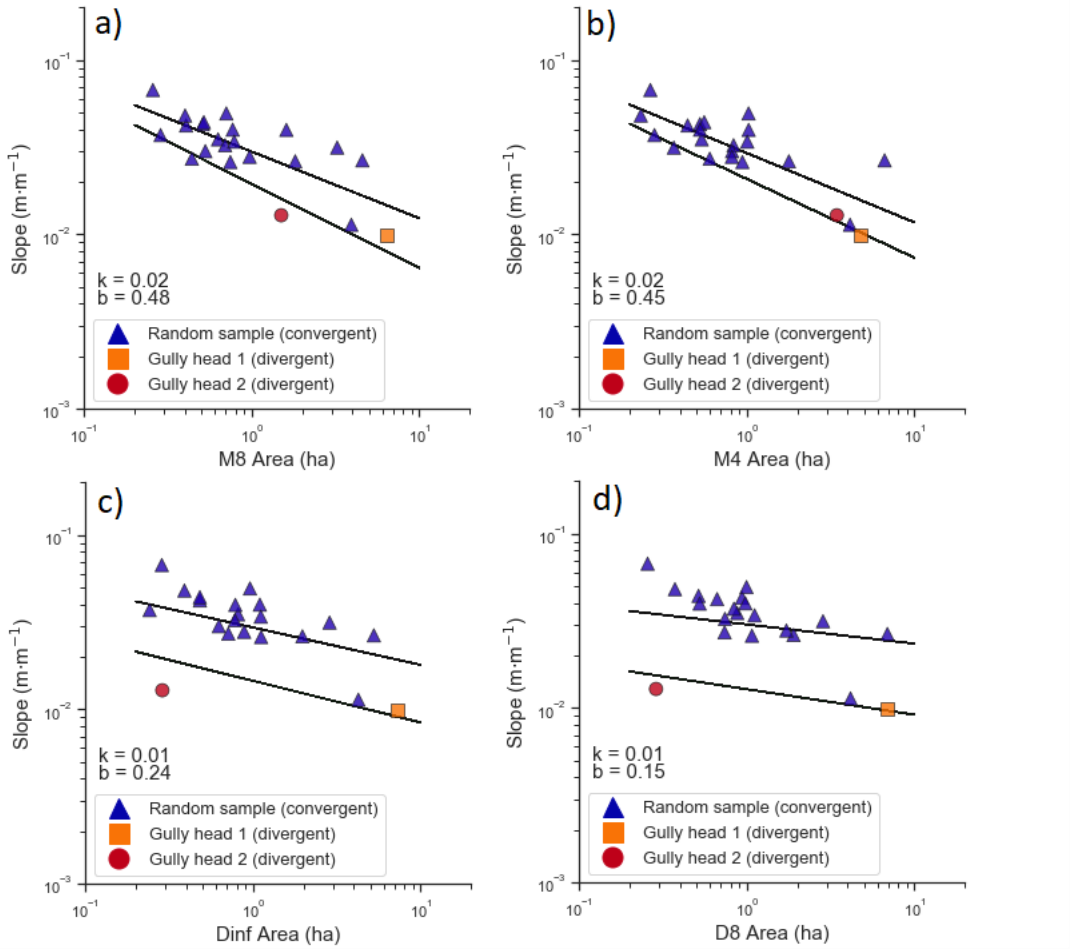

Figure 3.7: An illustration of how differences in computed drainage area can affect threshold parameter estimates. Blue triangles are a random sample of 20 convergent gully heads plotted with the two divergent gully heads from Figure 3.1 (orange square and red circle). In each panel the highest line is a simple OLS regression on log-transformed area and slope, and the lower line is the topographic threshold line found by following the steps in section 3.2.9.

In this example case, drainage areas estimated by the M8 and M4 algorithms place both divergent gully heads relatively close to each other in terms of area for a given slope (Figure 3.7a and b). However, the single-direction algorithms (D8 and D_{inf}) are unable to distribute flow to both gullies (e.g. Figure 3.1), leaving one gully head with a large area and the other with a small area (Figure 3.7c and d). In a slope-area plot both gully heads will sit on roughly the same line with respect to slope (y-axis) but will be separated in distance with respect to drainage area (x-axis). Calculating drainage area using a single-direction algorithm gives one gully an overestimate of drainage area for a given slope and the other an underestimate, hence they work in unison to flatten the slope of the threshold line (Figure 3.7c and d).

3.3.5 Estimating threshold parameters for Weany Creek

Results of threshold analysis using all 484 gully heads shows that the threshold for gully incision (k = 0.033) in this environment is low and the slope of the threshold line (b = 0.189) is relatively flat (Figure 3.8).

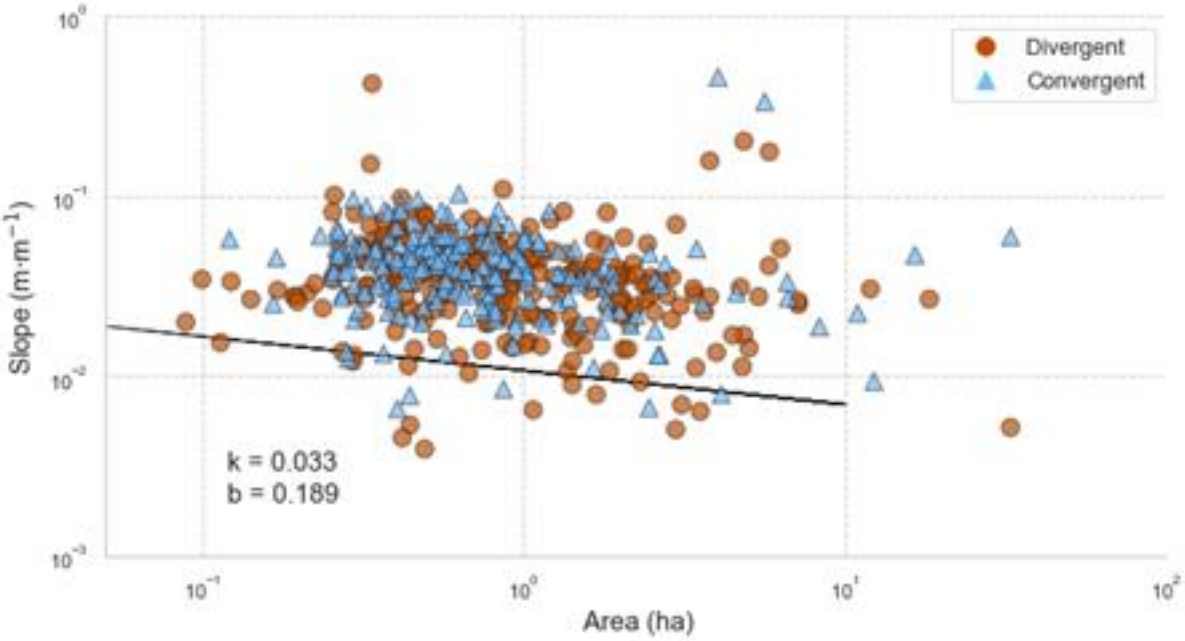

Figure 3.8: Gully topographic threshold for Weany Creek using an M8 multiple-direction routing algorithm on a 1 m DEM. Divergent and convergent gully heads are indicated with orange circles and blue triangles, respectively. The regression line is fitted through all data points and then translated through the lower-most 10th percentile of points.

Estimated parameter values in Figure 3.8 were found to vary when assessed within our bootstrap simulation procedure (Figure 3.9 and Table S3).

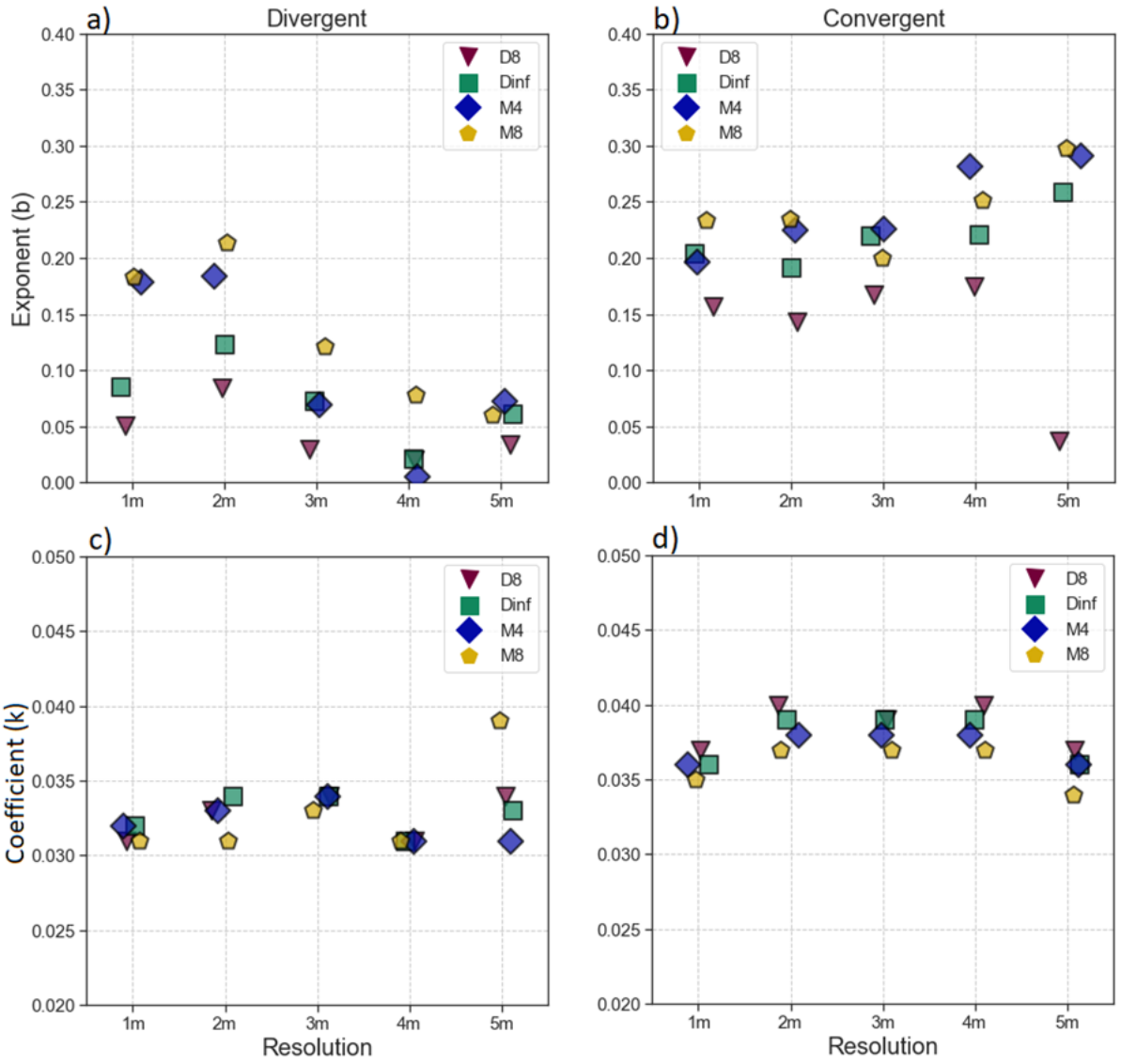

Figure 3.9: Estimates of the coefficient k and exponent b from topographic threshold analysis across five spatial resolutions (1, 2, 3, 4 and 5 m) and using four different flow routing algorithms (D8, Dinf, M4 and M8). The parameters are calculated for divergent (Panel a and c) and convergent (Panel b and d) groups of gullies separately.

After estimating *k* and *b* from a bootstrap simulation, three important observations emerge:

1. Estimates of the exponent *b* are typically higher for multiple-direction algorithms than single-direction and the difference is largest for divergent gullies at finer resolutions (Figure 3.9a and b).
2. At 1-2 m resolution the M4 and M8 show only small differences in estimated *b* values between divergent and convergent groups while the D8 and D_{inf} both show larger differences. All routing methods show large differences at ≥3 m resolutions (compare Panel a and b Figure 3.9).

3. The estimate of *k* is consistent for all routing algorithms, but convergent cases typically have a higher mean *k* than divergent cases (Figure 3.9c and d).

Point 2 is consistent with the example from Figure 3.7, showing that the slope of the line is flattened (*b* exponent is decreased) for the single-direction algorithms due to their inability to distribute flow to multiple gully heads downstream of divergent points on a hillslope.

Point 3 suggests that gullies with convergent flow characteristics above the head require a larger drainage area to incise (assuming the slope and area at the current gully head position provides an adequate approximation for the time of initial incision). This is somewhat of a contradictory finding because convergence implies more concentrated flow, and these gullies also occur on steeper hillslopes (Figure 3.5).

3.3.6 DEM hydrologic-enforcement and flow partitioning

Results of DEM hydrologic-enforcement show that most sinks occur in higher parts of the landscape near the catchment divide or in lower positions near the main stream channel (Figure 3.10). A sink filling algorithm must fill sinks to the brim to guarantee that all cells drain (Barnes et al., 2014). When filled, the largest sink in this part of the catchment covers an area of ~ 390 m^2 and is ~ 0.75 m deep at its deepest point (red box, Figure 3.10).

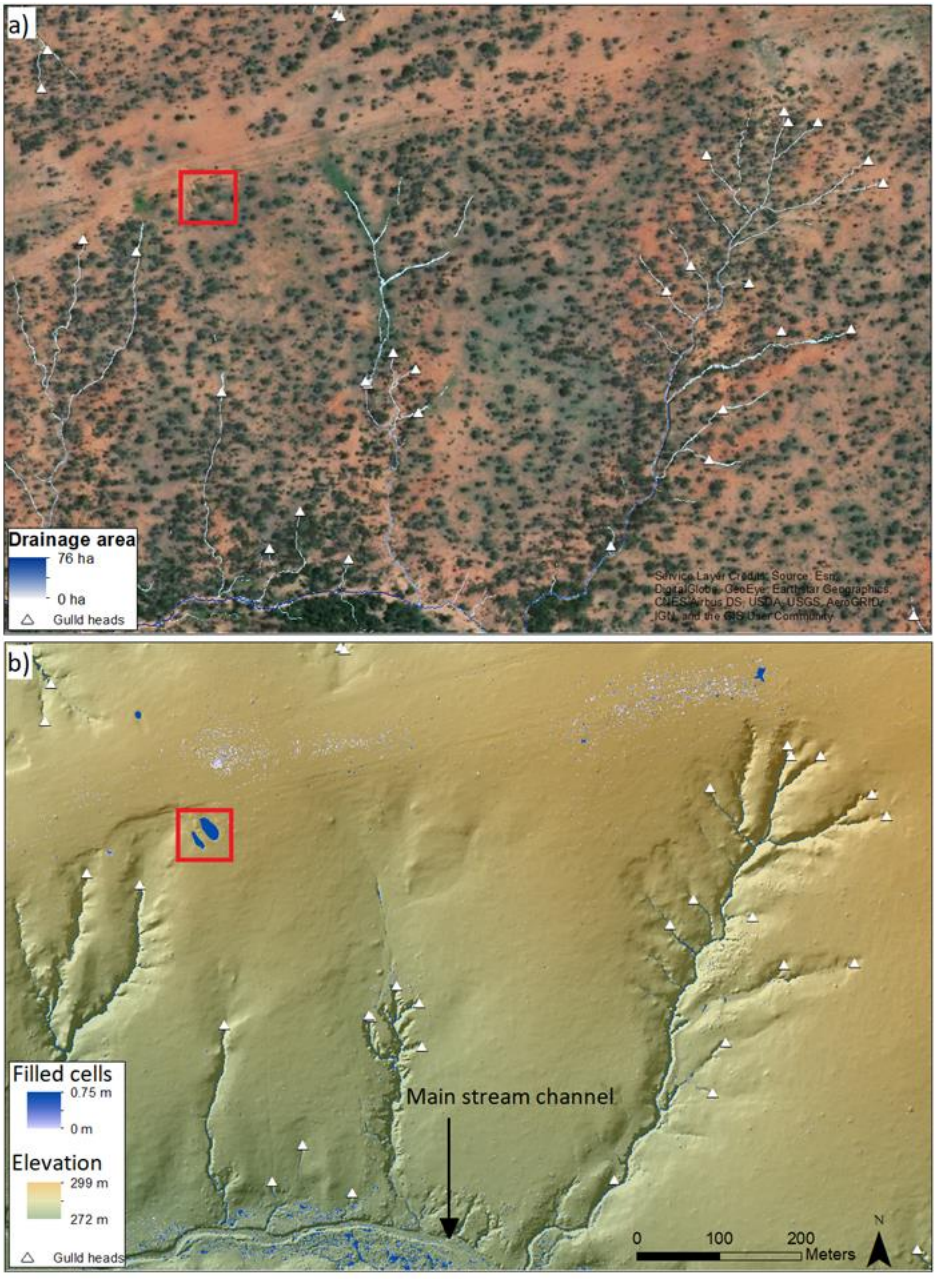

Figure 3.10: Location of pits and sinks, flow lines and gully heads in a section of Weany Creek with a high gully density. Panel a) shows the main drainage lines intersecting the mapped gully heads. Panel b) shows the hillshaded DEM with sinks filled using the Priority-Flood algorithm of Barnes et al. (2014) and the location of the main stream channel. Most sinks occur in either the higher positions along the ridgeline or lower positions adjacent to the main channel.

In total 1.67% of all cells were modified by sink filling, with an associated total volume change of ~609 m^3 over a test area of ~ 116 ha (Figure 3.10). Breaching changed approximately half the number of grid cells compared to filling (Table 3.2).

Table 3.2: Areal extent and total volume of change between the original DEM and the three hydrologic-enforcement methods tested (breaching, filling, and hybrid breaching-filling).

Hydrologic-enforcement	Areal extent of modified cells (%)	Total volume change (m^3)
Breach	0.88	135.17
Breaching-Filling	1.04	467.76
Fill	1.67	609.3

The choice of hydrologic-enforcement method also affected estimated parameters in threshold analysis. When sinks and pits were breached, estimates of *k* were ~10% higher compared to when they were filled (Table 3.3). The opposite was true for estimates of *b*, and the difference was much larger. The average estimate of *b* for a DEM that had been filled was ~188% larger than if breached. These differences were brought about by small variations in drainage areas computed on each of the hydrologically-enforced DEMs, and associated variability around the threshold line (Figure 3.11).

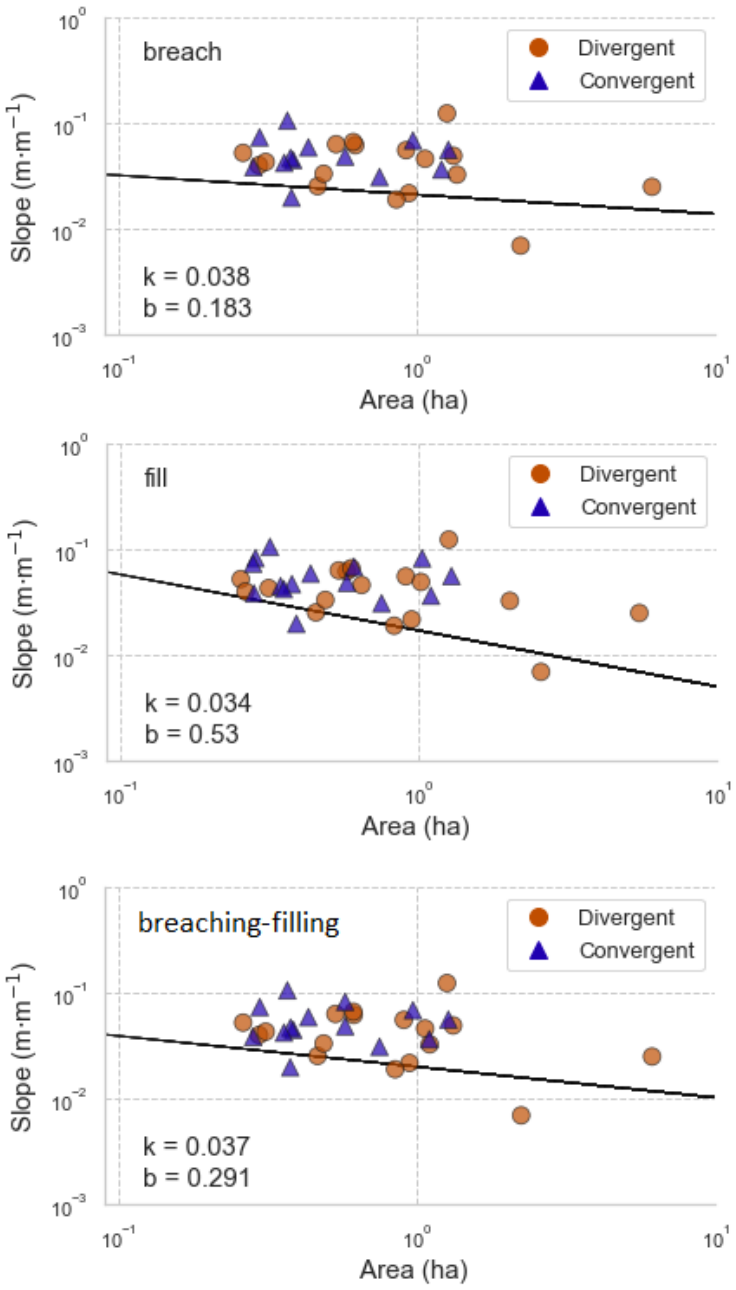

Figure 3.11: Slope-area threshold plots for a set of 32 gully heads in a subsection of Weany Creek (1 m resolution) using three different DEM hydrologic-enforcement methods (breaching, filling and hybrid breaching-filling). Drainage area was computed using the FD8 flow routing algorithm with p = 1.1. The threshold line is found by fitting a simple linear regression and translating the line to pass through the lowest 10th percentile of points.

When we varied the flow partitioning exponent *p* for the FD8 algorithm (Equation 6), we found that larger values of *p* increased the estimate of the coefficient *k* while decreasing the estimate of the exponent *b*. This general pattern remained consistent irrespective of the hydrologic-enforcement method used (Table 3.3).

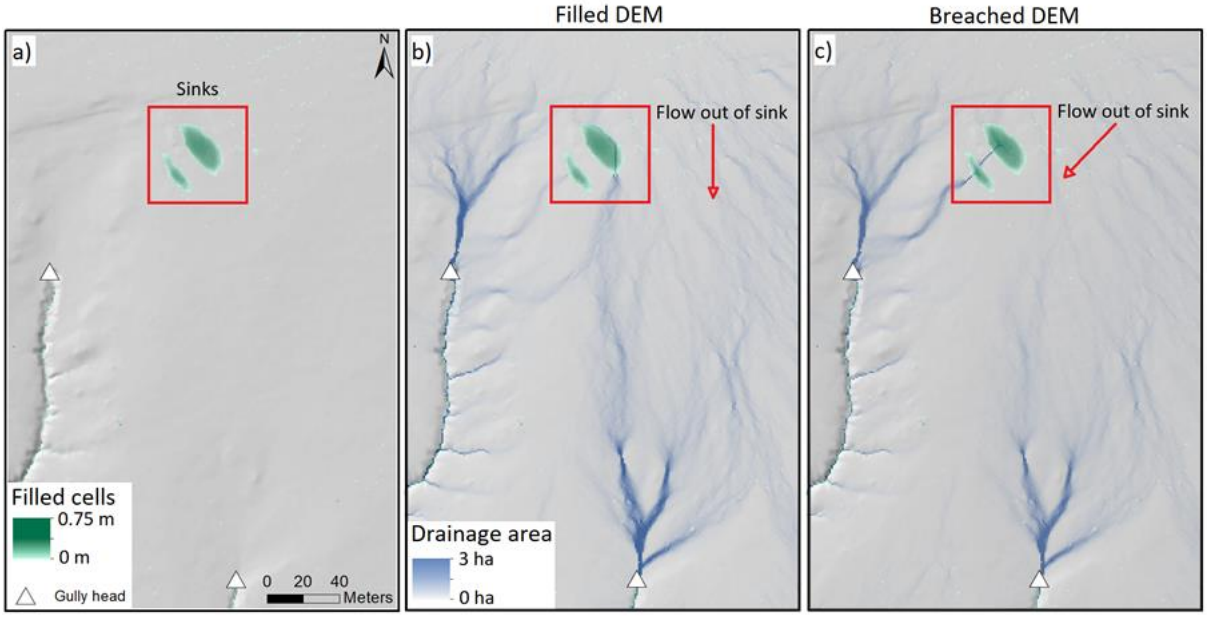

Figure 3.12: Example of how flow direction out of a sink can be affected by the hydrologic-enforcement method used. Panel a) shows the largest sink in the area and its location with respect to two nearby gully heads (white triangles). Panel b) and c) show flow accumulation values using the FD8 algorithm (p = 1) on a filled and breached DEM, respectively. Flow out of the sink takes a different path depending on the hydrologic-enforcement method employed.

The choice of hydrologic-enforcement also affected flow directions out of sinks. When the DEM is filled (Figure 3.12b) water exits the largest sink at the lowest point around the edge (pour point) but breaching carves a channel to the next lowest nearby cell (in this case another sink, Figure 3.12c). This behaviour impacts the drainage area estimated for the two gully heads (white triangles Figure 3.12).

Table 3.3: Estimated topographic threshold parameters under three different DEM hydrologic-enforcement methods; filling, breaching and hybrid breaching-filling. The routing exponent p from Equation 6 was also modified to test the effect on threshold parameter estimates. Low values of p (close to 1) emulate divergent flow conditions and high values convergent.

Threshold coefficient (*k*)			
Routing exponent *(p)*	**Breach**	**Breaching-Filling**	**Fill**
0.5	0.038	0.036	0.034
1	0.038	0.037	0.034
1.1	0.038	0.037	0.034
1.5	0.038	0.038	0.034
2	0.039	0.038	0.034
5	0.039	0.039	0.035
10	0.039	0.039	0.036
Threshold exponent (*b*)			
Routing exponent *(p)*	**Breach**	**Breaching-Filling**	**Fill**
0.5	0.202	0.347	0.509
1	0.186	0.300	0.528
1.1	0.183	0.291	0.530
1.5	0.174	0.264	0.534
2	0.167	0.244	0.533
5	0.154	0.203	0.472
10	0.141	0.169	0.370

3.4 Discussion

3.4.1 Convergent and divergent flow above gully heads

Gully head drainage areas computed from DEMs can only provide an estimate of the real drainage area (Rossi et al., 2015). Estimates are most uncertain where microtopography causes hillslope divergence upslope of gully heads (Nyssen et al., 2002, Gudino-Elizondo et al., 2018). An example of this would be small-scale depositional fans that are common between upslope and downslope sections of

discontinuous gullies (Selby, 1982). We observed this scenario where flow divergence happens due to pre-gully channelling upslope of gully heads, creating small-scale depositional zones (e.g., Figure 3.1). Across our site divergent conditions were common at finer resolutions (1-2 m) but the ratio of divergent to convergent cases decreased as cell size increased. A possible explanation is that land surface features are not represented when they exist at smaller scales than the resolution of the DEM (Sørensen and Seibert, 2007). In this case, microtopographic features such as small depositional fans are not resolved, and neither is the associated flow divergence. The same may be true for the influence vegetation has on elevation data at finer grid resolutions.

For divergent cases, drainage areas estimated by different flow routing algorithms varied more at finer resolutions than at coarser resolutions (Figure 3.9a). Hence, at finer resolutions (≤ 2 m) the larger number of divergent gullies indicates that the choice of flow routing algorithm is more important than it is at coarser resolutions. This supports Erskine et al. (2006), who found that the relative difference between single-direction and multiple-direction algorithms increases as resolution becomes finer. However, an important consideration is that DEM-based assessments of hillslope flow paths cannot consider variation in behaviour under different runoff scenarios, and this may play a role in determining where and how often flow divergence occurs.

3.4.2 Most suitable routing method

Early work by Desmet and Govers (1996) showed that single-direction algorithms produce unreliable results in their application as part of a simple model to predict the location of ephemeral gullies (Moore et al., 1988b). This was due to spurious concavities in the DEM causing local accumulation of upslope area and generating major drainage lines. The authors suggested that single-direction algorithms have been commonly used because of their conceptual and computational simplicity but proposed that multiple-direction algorithms are more suitable for predicting ephemeral gullies. Quinn et al. (1991) essentially recognised this issue and developed a multiple-direction algorithm in response. We find that the confinement of flow to concentrated pathways on hillslopes also leads to unrealistic gully head drainage area estimates in modern high-resolution DEMs.

For gullies with divergent flow upslope, both D8 and D_{inf} showed low consistency in calculated drainage areas across resolutions, while the M4 and M8 algorithms were much more consistent (Figure 3.6). In general, the D8 and D_{inf} algorithms behaved similarly (Figure S4). They have also been found to perform similarly for calculating topographic wetness index on a 1-m LiDAR DEM (Murphy et al., 2009). Studying soil moisture patterns in Alberta, Canada, those authors found a significant difference between the D8 and D_{inf} for a 10-m photogrammetric DEM that disappeared for a 1-m LiDAR DEM.

One limitation to multiple-direction algorithms is that they tend to over-disperse flow on hillslopes even in convergent scenarios (Tarboton, 1997, Shelef and Hilley, 2013). However, we found this same propensity to over-disperse also allows multiple-direction algorithms to better handle the many divergent cases across our study area, especially true at finer resolution (≤2 m). For a multiple-direction algorithm, small differences in elevation between downstream cells results in a proportionately small difference in drainage area routed to each of the cells, whereas for a single-direction algorithm it is the difference between all or nothing (Seibert and McGlynn, 2007).

Finally, we found that for the FD8 method of Freeman (1991) larger values of the routing exponent *p* gave slightly higher estimates of *k* and notably lower estimates of *b* compared to smaller values (Table 3.3). This is a similar result to using a single- rather than multiple-direction algorithm (Figure 3.9). This is because the routing exponent controls the degree of flow dispersion (Holmgren, 1994) with smaller values creating dispersive flow paths, similar to using the M8 of Quinn et al. (1991), and larger values creating convergent conditions similar to using the D8 method of O'Callaghan and Mark (1984).

3.4.3 Drainage area estimates and DEM resolution

The optimal DEM resolution for topographic analysis would be expected to depend on the combination of landscape morphology and the specific attribute investigated (Sørensen and Seibert, 2007). We found that in threshold analysis, estimates of the exponent *b* vary more between divergent and convergent cases at ≥3-m resolution (Figure 3.9), indicating that more reliable results are obtained at finer resolutions. We also found drainage area estimates from different routing algorithms varied more at finer (1-2 m) resolutions (Figure 3.9). Hence, in this landscape, finer

resolution is better suited to gully head drainage area estimation, but the choice of routing algorithm also becomes more important.

We did not investigate resolutions <1 m. However, recent work by Thomas et al. (2017) found that DEMs at 0.25-m resolution were unsuitable for predicting surface runoff, because microtopography influenced flow accumulation in a way that produced unrealistic confinement to irregular pathways (compared to field observations). Resampling their data to 1- or 2-m resolution represented flow pathways more realistically, while maintaining topographic detail. Similarly, Drover et al. (2015) found that higher-resolution DEMs are not necessarily better for hydrological assessments.

3.4.4 Gully topographic thresholds of Weany Creek

Threshold parameter estimates for Weany Creek (Figure 3.8 and 3.9) indicate a strong predisposition to gully erosion, when compared to many other study locations globally. Torri and Poesen (2014) found average parameter values for rangelands in Africa, Americas, Asia, Australasia and Europe of $k \approx 0.2$ and $b \approx 0.29$, compared to average values of $k \approx 0.033$ and $b \approx 0.2$ found here. However, direct comparisons between studies are difficult due to variation in exact methodologies. Our b estimates close to 0.2 found using multiple-direction algorithms appears reasonable but estimates closer to 0 found using single-direction algorithms would seem unrealistic.

The intercept of $k \approx 0.033$ is close to the estimated values found by other studies looking at gully thresholds in similar environments (e.g. Nazari Samani et al., 2009, Muñoz-Robles et al., 2010, Shellberg, 2020). A low k value may be expected because the study area is a semi-arid savannah landscape with poor ground cover and experiences intense rainstorms during the wet season. These conditions expose catchments to gully erosion (Sidle et al., 2019). It is also a strongly dissected landscape, and thresholds are expected to be inversely related to landscape dissection (Kirkby, 1988, Poesen et al., 2003).

Conversely, there are potential reasons why our threshold estimates might be incorrect, regardless of routing method or resolution. In threshold analysis, drainage area is used as a surrogate for runoff volume (Vandaele et al., 1996) under the assumption that the two increase proportionally (Leopold et al., 1964). If this proportionality is lost, estimated parameters may deviate from expected values. However, Hortonian overland flow has been found to be the dominant runoff

mechanism in our study region (Jarihani et al., 2017), which should make proportionality more likely. Similarly, the relationship between drainage area and runoff may change over time in response to changes in rainfall or soil infiltration (Hayas et al., 2017).

Estimated *k* values were higher for gullies with convergent than for those with divergent flow upslope, requiring larger drainage areas to initiate gullies. This seems contradictory given convergent cases typically had steeper slopes (Figure 3.5). A possible explanation for the higher *k* values for convergent cases is that a key soil property, clay content with depth, differs between depositional and non-depositional landscape positions in Weany Creek (Wilkinson et al., 2018). Hence, gullies in divergent and convergent cases may experience contrasting soil properties, accounting for differences in *k* values. It is also possible for contrasting gully erosion processes to act within a single landscape (Montgomery and Dietrich, 1988) and the gullies in the convergent scenarios may have been initiated and driven by different processes than those in divergent cases. These unresolved questions highlight the main shortcoming of DEM-based analysis without fieldwork: any peculiarities in the results must be left to speculation.

3.4.5 Application to other environments

We found larger variation in estimates of drainage area for gullies with divergent flow conditions. Those gullies generally had larger drainage areas and a flatter slope of the soil surface above the gully head (Figure 3.5). Multiple-direction algorithms were better able to handle these cases, producing more realistic flow paths (Figure 3.1) and threshold parameter estimates (Figure 3.9). This suggests that using a multiple-direction algorithm will be more important in landscapes with typically larger and flatter gully head catchments, such as in north-western Colorado where Patton and Schumm (1975) originally worked. In our test site the granitic lithology (producing duplex textured sandy clay loam soils across the area) and low average slope of the landscape create small-scale depositional fans that promote flow divergence. This likely plays a role in the large number of gully heads we observed with divergent flow conditions.

For convergent cases, the variation in drainage area estimates was smaller and the choice of flow routing algorithm became less important. This suggests that a

multiple-direction algorithm is less beneficial in steeper landscapes where hillslope flow divergence is less common. Sørensen et al. (2006) came to a similar conclusion with regards to topographic wetness index.

Landscape characteristics are also important when considering different methods of hydrologic-enforcement. For example, using breaching for a landscape with large depressions (e.g. lakes and wetlands) can lead to long deep breach channels (Lindsay, 2016a) which are undesirable. We found examples of similar behaviour but on a smaller scale when two sinks became connected by a ~25 m long breach channel between the two lowest cells (Figure 3.12c). Additionally, we observed that the direction of flow out of sinks was affected by whether the DEM was breached or filled. This has implications for topographic threshold studies because it can change estimated drainage areas by redirecting flow away from one gully head and toward another. We found that this had a substantial impact on estimated threshold parameters, particularly the exponent *b* (Table 3.3). However, our site has a low average slope (~2.3%) and landscapes with lower slopes typically have more pits and sinks (Lindsay, 2016a). This may exacerbate the impact of hydrologic-enforcement on threshold analysis compared to steeper landscapes with less sinks, such as the steep head water catchments studied by Parkner et al. (2006) and Parker et al. (2007) in New Zealand.

3.4.6 Implications for future gully topographic threshold studies

The conceptual model proposed by Montgomery and Dietrich (1994) implies that the coefficient *k* in Equation 1 depends on climate, soil type and land use, while the exponent *b* depends on the hydraulics of overland flow (i.e., turbulent or laminar) in the catchment above the gully head (Hayas et al., 2017). We found that estimates of *k* did not vary much between routing methods or resolutions, but the exponent *b* did. In their review, Torri and Poesen (2014) reported a large range of *b* estimates across studies but did not find any strong relationship with landscape types (i.e., cropland, rangelands/pastures, forests, and grasslands). We present evidence that different drainage area estimation methods, DEM hydrologic-enforcement methods and spatial resolutions can produce rather different *b* estimates, which may explain this lack of a relationship observed by Torri and Poesen (2014).

Estimates of $b \geq 0.2$ are generally taken to indicate erosion by Hortonian overland flow, while lower values indicate erosion by sub-surface flow processes (Morgan and Mngomezulu, 2003, Muñoz-Robles et al., 2010, Dong et al., 2013). Morgan and Mngomezulu (2003) studied topographic thresholds in Swaziland and found that

b<0.2, yet field investigation showed no sign of subsurface erosion. Similarly, Hortonian overland flow is the dominant runoff mechanism in our study area (Jarihani et al., 2017), supporting the likelihood of channel incision by overland flow, yet with single-direction algorithms our estimates of *b* were typically much lower than 0.2. This variation in parameter estimates due to different DEM-based methods possibly explains the apparent contradiction found by Morgan and Mngomezulu (2003) and in our own study. That estimates of *k* showed greater robustness may help to explain why Torri and Poesen (2014) were able to observe trends in *k* values with landscape type but not *b* values.

Threshold analysis has also been used as a method to predict spatial zones of gully susceptibility (e.g. Pederson et al., 2006, Gutiérrez et al., 2009, Shellberg, 2020). For this application, the variation in parameter estimates due to DEM-based methods will affect the spatial distribution of mapped gully susceptibility. This may in turn affect decisions about spatial priorities for gully remediation and prevention.

3.5 Conclusions

We examined alternative DEM-based techniques to determine gully head drainage areas for a semi-arid savannah landscape in north-eastern Australia using an airborne LiDAR DEM. Our goal was to support future efforts to apply gully topographic threshold analysis more readily across large areas. This included the development and application of two new subroutines: one to locate the 'best cell' from which to measure drainage area at gully heads, and another to separate gullies with respectively convergent or divergent flow conditions upslope.

Across the 40 km^2 study area small-scale topography caused hillslope flow paths to diverge upstream of many gully heads. This occurred for over half of the 484 studied gullies at a resolution of 1 m. Single-direction algorithms were not suitable in these cases, whereas multiple-direction algorithms performed better due to their ability to partition flow to multiple downslope cells when only small elevation differences existed. Assessing gully topographic thresholds across the site showed that the propensity for single-direction algorithms to incorrectly partition flow over dispersive parts of the landscape led to an associated underestimate of the exponent *b* (Equation 1). This has implications for the dominant erosional processes inferred, which is an important aspect of threshold analysis. The differences in *b* generated by choosing a single- or

multiple-direction algorithm were large enough to infer either subsurface or overland flow erosion, respectively. Threshold parameter estimates were also impacted by DEM hydrological-enforcement. If the DEM was filled, estimates of *k* were ~10% lower than if breached, and estimates of *b* were ~188% higher. This indicates that when comparing threshold analysis results between studies it is important to consider the method by which the DEM has been hydrologically-enforced.

In conclusion, we found finer resolution DEMs (≤2 m) and a multiple-flow direction algorithm produced most realistic threshold analysis results in a low-relief tropical savannah environment. Our threshold parameter estimates (k = 0.033 and b = 0.189) for Weany Creek indicate it is highly susceptible to gully erosion. This result was consistent with threshold studies from similar environments and reflects the influence that a highly variable climate, dispersive soils, and historic grazing have on exposing a landscape to gully erosion. We also found that threshold parameters, particularly the exponent *b*, are affected most by the choice of routing method and DEM hydrologic-enforcement. Future studies should consider these DEM-based sources of variability in threshold parameter estimates when comparing studies or using the parameters to predict locations susceptible to gullying.

Chapter 4: DEM-based geometric characterisation of gully heads to support topographic studies of gullies

Abstract

Advances in technology to acquire high-resolution digital elevation models (DEMs) have enabled many recent studies to develop increasingly accurate topographic models for gully erosion assessments. It has also enabled re-examination of well-established gully models. This increased ability to model gully erosion with greater ease and accuracy comes with an increased need for reliable and reproducible methods. We propose an automated programmatic approach for selecting points around gully heads from which to compute slope (gradient of the surrounding hillslope) as an input into gully topographic threshold analysis models using high-resolution DEMs. The method begins with pre-defined gully headcut locations and builds up a geometric model of the gully head. From this geometric model points are automatically located around the gully head and used to measure slope in an objective programmatic way. This new analysis removes arbitrary decisions regarding the computation of slope for input into gully topographic threshold models and in doing so removes bias otherwise introduced by inconsistent methods of slope estimation. It also enables consistent estimation of gully head dimensions such as width and depth. We tested the method across a ~1 200 km^2 area in the Fitzroy River Basin of north-eastern Australia where gully erosion is evident across a range of lithologies. Best practice field measurements of slope for input into gully topographic threshold analysis should measure slope 5 m upslope of the gully head and 5 m along each side. However, our results indicate that when using high-resolution DEMs, more robust estimates of slope are found by following the most concentrated flow line upslope of gullies and measuring slope along that line, avoiding slope estimates along the sides. We also compare automatically extracted measurements of gully head depth, width, and drainage area finding a statistically significant relationship between gully head depth and the gradient of the surrounding hillslope. This provides potentially valuable information for gully remediation projects looking to minimise the volume of sediment lost from erosive gullies in catchments of the Great Barrier Reef, Australia.

4.1 Introduction

Gully erosion has been the focus of many international studies due to the important role it can have in land and waterway degradation in a range of environments (Poesen et al., 2003). In recent years many gully erosion studies have been supported by advances in structure from motion photogrammetry (SfM) and light detection and ranging (LiDAR) technology enabling collection of high-resolution (metre-scale) topography data (e.g. Koci et al., 2017, Castillo et al., 2018, Gudino-Elizondo et al., 2018, Conoscenti and Rotigliano, 2020). High-resolution topography has allowed these studies and many others to develop increasingly accurate models of gully geometry (e.g., depth, width, length) and of the topographic settings of gullies (gradient of the surrounding hillslope and contributing drainage area). With this improved gully data more advanced and accurate models have been possible (e.g. Rengers and Tucker, 2015, Koci et al., 2020a, Castillo et al., 2021). It has also permitted the application of long-standing models, such as the widely used gully topographic threshold analysis model proposed by Patton and Schumm (1975), with improved accuracy and efficiency. However, with an increase in availability and accessibility of a new generation of topography data comes an increased need for consistency of application across studies and regions.

Past studies looking to compare gully erosion characteristics in different environments have encountered difficulties due to the range of data collection methods applied. For example, Torri and Poesen (2014) encountered difficulties with varying methodologies when they conducted a review of the topographic thresholds of gully incision across continents. Similarly, gully headcut retreat rate has been found to correlate with gully morphology (Poeson et al., 2003) and Vanmaercke et al. (2016) found that differences in methods for computing gully dimensions potentially masked relationships that may exist between the rate of gully headcut retreat and reported gully dimensions.

This problem has previously been recognised and various researchers have taken steps to address it. For example, Casalí et al. (2015) experimented with different methods for measuring gully cross-section widths and the resultant impact on estimated volume changes in gullies, they found that volume estimates could vary substantially. The same authors proposed a standardised method for measuring dimensions in the field so that results across studies could be more readily compared.

Objective methods are required in both geomorphology and geomorphometry to define landforms in a reproducible way (Sofia, 2020). Further progress in gully erosion research also requires clear definitions of methods to quantify gully morphology (Casalí et al., 2015). Among the most widely used methods for assessing gully erosion is gully topographic threshold analysis (Torri and Poesen, 2014). Originally proposed by Patton and Schumm (1975), later workers (Montgomery and Dietrich, 1994, Willgoose, 1994, Vandaele et al., 1996) looked to develop a theoretical basis for the observed slope-area relationship, which eventuated in the widely used model:

$$s \geq kA^{-b} \quad (1)$$

Where *s* is slope (gradient of the hillslope adjacent to a gully head), *A* is the contributing drainage area at the gully head, and *k* and *b* are empirical parameters. Recently Walker et al. (2021) looked at moving towards a standardised methodology for gully topographic threshold analysis by assessing the impact that the choice of routing method, DEM resolution and hydrological-enforcement have on estimated threshold parameters *k* and *b*. Computing drainage area using a consistent methodology on high-resolution DEMs provides half of the inputs for topographic models of gullies based on slope and area. The second required input to Equation 1 is slope of the soil surface at the gully head. The calculation of slope, however, can be easily subject to bias in terms of where exactly to calculate it. For example, 'standard' slope calculation methods implemented in many GIS programs (e.g. Burrough et al., 2015) use a moving 3 x 3 grid cell window to calculate the maximum rate of change of elevation between the central cell and its eight neighbours. Hence, the distance over which slope is calculated depends on the grid spatial resolution. Alternatively, previous studies measuring slope in the field often use an optical clinometer or similar device (e.g. Vandekerckhove et al., 1998, Nachtergaele et al., 2001), but this also requires a decision about the distance over which to calculate slope. To objectively measure slope for input into topographic threshold analysis, this potential bias needs to be removed.

4.1.1 Aims

The core goal of this work was to investigate the potential for an automated geometric characterisation of gully heads to objectively pinpoint locations around a gully from which to compute the gradient of the adjacent hillslope. Together with a reliable method for computing drainage area, Chapter 3, this method aims to move a

step closer to fully automated topographic threshold analysis of gullies using high-resolution DEMs. A secondary goal was to investigate the potential of this method to automatically extract dimensions of gully heads such as depth and width. Within these broader objectives we aimed to (1) assess the variation in estimates of slope brought about by different methods, (2) assess the influence of lithology on accuracy and precision of automatic methods, and (3) assess the impact of various slope estimations on topographic threshold parameter estimates.

4.2 Materials and methods

4.2.1 Study site

A range of sites were assessed over an area of ~1 200 km in the Fitzroy River Basin in Queensland, Australia (Figure 4.1). The region is typified by wet summers and relatively dry winters (Australian Bureau of Meteorology, 2020). The average annual rainfall across the site is 652.8 mm with a standard deviation of 36.6 mm. There is a gradual decrease in mean annual rainfall moving from the north-eastern part of the landscape (~710 $mm \cdot y^{-1}$) to the southwest (~600 $mm \cdot y^{-1}$). Elevation ranges from a low of 25.15 m along the banks of the Fitzroy River up to 458.4 m in the steeper forested parts of the landscape. Alluvial floodplains cover ~20% of the area with the remaining areas consisting primarily of a mix of igneous (~4%), volcanic (~37%), and sedimentary (~31%) lithologies.

Tree cover across the site is variable and has averaged ~49% over the past 30 years (Van Dijk and Rahman, 2019). Higher and steeper parts of the landscape tend to be where tree cover is concentrated, and lower flatter parts of the landscape have been cleared for grazing. The Fitzroy Basin more broadly is typified by agricultural landscapes with cattle grazing pastures constituting the primary agricultural land use (Gilbert and Brodie, 2001). This widespread grazing has reduced ground cover across

the Fitzroy Basin, exposing many areas to erosion (Rust and Star, 2018).

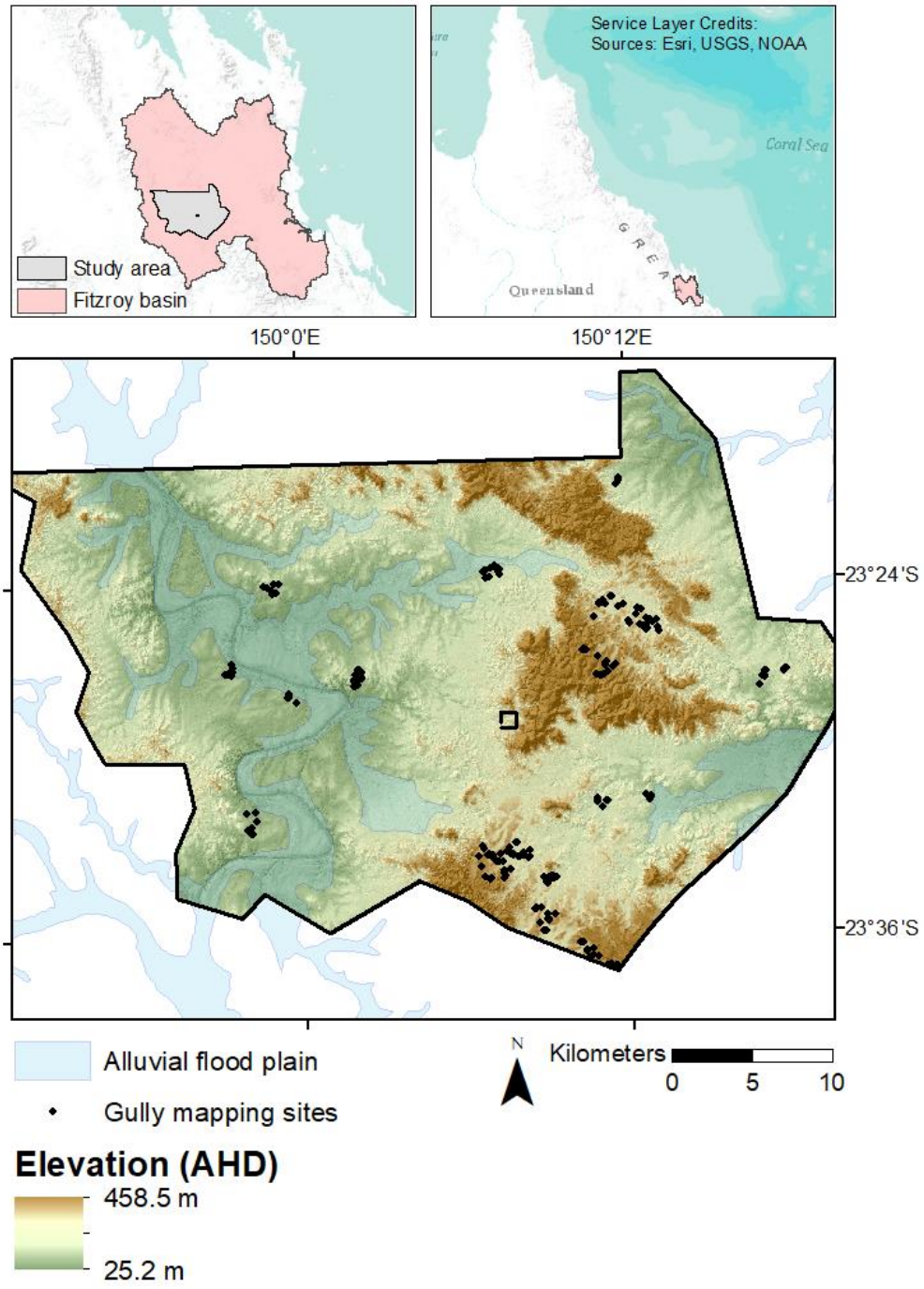

Figure 4.1: Study site in the Fitzroy River Basin. Black dots indicate locations where gullies were digitised.

4.2.2 Data

The primary dataset used was a bare-earth DEM derived from airborne-LiDAR. This dataset was collected by Atlass Aerometrex in June and July of 2018 for the Reef Trust (https://www.environment.gov.au/marine/gbr/reef-trust) with the project managed by the Commonwealth Scientific and Industrial Research Organisation

(CSIRO). The data acquisition was made with a target point density of 16 points per square meter. The reported positional accuracy of the data was ± 0.8 m at 95% confidence interval. The reported vertical accuracy was ± 0.2 m at 95% confidence interval with root mean square error of <0.05 m determined from ground control survey. The spatial resolution of the bare-earth DEM was provided at 0.5 m and for our study we resampled this using bilinear interpolation to a resolution of 1 m. An RGB image of the area was also captured with a spatial resolution of 0.15 m. This data was georeferenced to the elevation data.

We also used a map of surface geology developed by Geoscience Australia (Geoscience Australia, 2012b). This map is made available at a scale of 1:1M and contains information collected from a range of geological mapping sources.

4.2.3 Algorithm implementation

In a review of gully topographic threshold studies by Torri and Poesen (2014) they suggest the slope measurement procedure proposed by Rutherfurd et al. (1997) and later used by (Nyssen et al., 2002) who measured slope of the soil surface along a 10 m section parallel to the gully, 5 m above and 5 m below the gully head. We followed this guidance and developed a programming routine to fully automate the process of locating points above the head (S_H), on the left side (S_{L1}) and on the right side (S_{R1}) from which to calculate slope (Figure 4.2).

The algorithm requires an input set of initial estimated gully headcut locations. These can be mapped in the field and converted to points in a geographic information system, digitised by hand using optical imagery and digital topography (e.g. Morgan and Mngomezulu, 2003, Gutiérrez et al., 2009), or located automatically using an adapted form of algorithm for locating channel heads (e.g. Lashermes et al., 2007, Passalacqua et al., 2010, Pelletier, 2013, Clubb et al., 2014). For each initial gully headcut point, the algorithm begins by tracing a path along the most concentrated downstream flow line until a point of flow convergence (where a cell routes ≥ 90% of its drainage area to only one downslope cell) is identified on the gully floor denoted G_A (Figure 4.2). Specifics of this component are detailed in Chapter 3 (Walker et al., 2021).

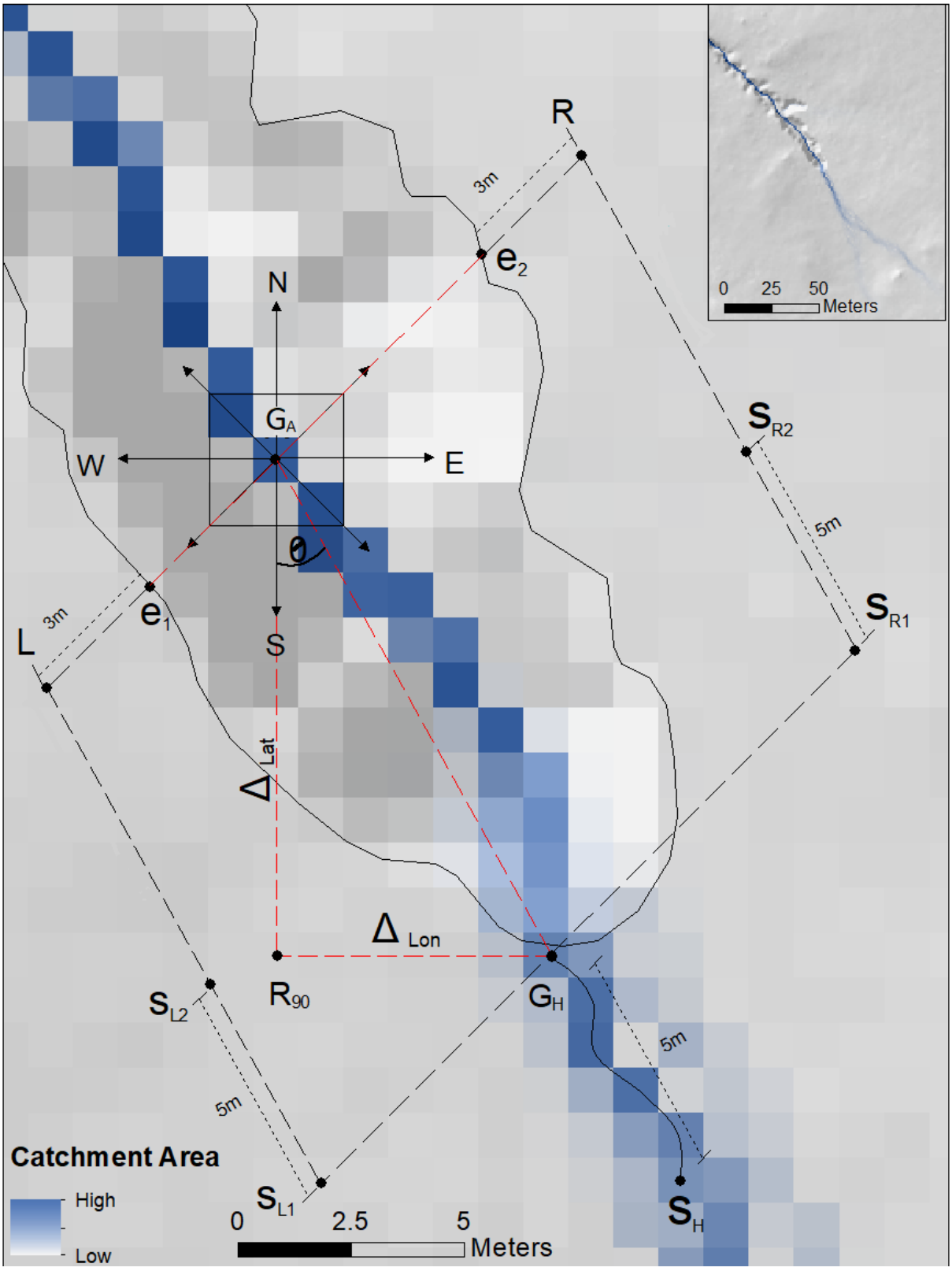

Figure 4.2: Geometric representation of the routine used to find points around a gully at which to calculate slope (S_R, S_L and S_H). The initial point collected is the point at which flow first converges to a single grid cell on the gully floor (G_A). All other points are then calculated automatically with reference to the position of G_A.

4.2.3.1 Change point detection

Starting from the point G_A the algorithm works back upslope searching for a breakpoint in elevation indicating the position of the gully headcut (Figure 4.3). The tool used for this is a statistical method named change-point analysis (Taylor, 2000). This method is primarily used for time series analysis and determining whether a change has taken place by taking the cumulative summary of a data series to search for points of change. We considered this method useful because the position of a gully headcut and the edges with respect to the gully floor will, in many cases, be clearly identified by a change in elevation values analogous to a change in some timeseries. In the initial step the algorithm searches for G_A within a maximum distance of 10 m downslope (Figure 4.3), and for detection of the gully head it searches back upslope along that same 10 m drainage line and then a further 10 m upslope from the initial approximated gully head (Figure 4.3). This gives the change-point analysis a total of 20 m (20 data points in a 1 m grid resolution DEM) to search for a change point indicating the position of the gully head (G_H). In cases where the exact location of the gully headcut is known *a priori* this step is not required; however, when only an approximation of the initial headcut location is known, this method seeks to define a more precise location and removes all subjectivity in deciding where the headcut is located.

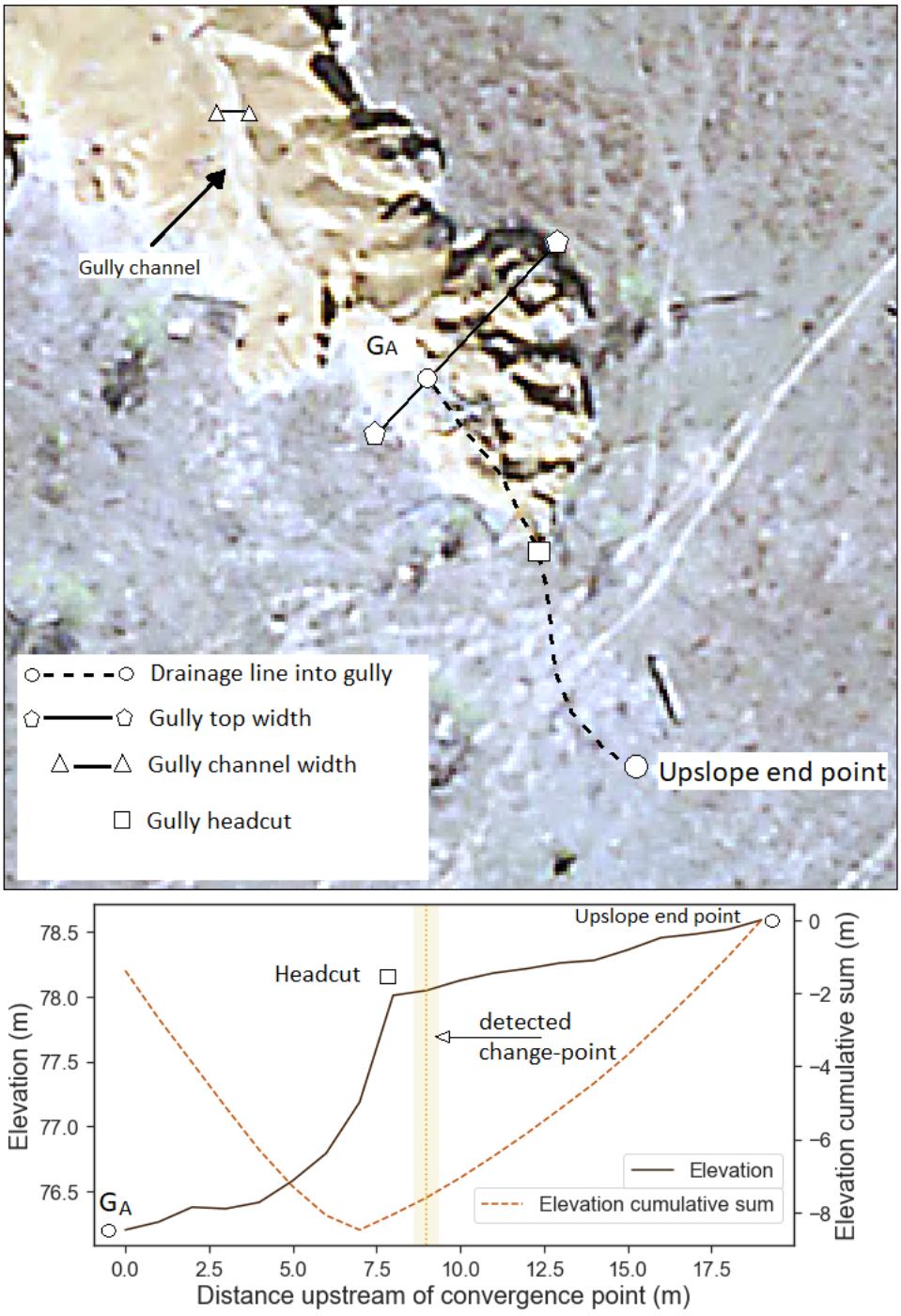

Figure 4.3: Example of the change-point analysis to find a gully headcut (white square). The algorithm for change-point analysis begins on the gully floor at the point G_A and progresses upslope following the most concentrated flow path until it reaches 10 m above the initial estimated gully headcut position. Elevation values are extracted along the line drawn from G_A to the most upslope point and used as input into change-point analysis.

4.2.3.2 Slope along on the left and right side of the gully

The routine for finding slope on the left and right side of the gully begins by finding where the gully head (G_H) exists with respect to the point G_A. This is done by finding the latitudinal and longitudinal distance between G_H and G_A:

$$\Delta_{Lat} = G_{H\ Lat} - G_{A\ Lat} \quad (2)$$

$$\Delta_{Lon} = G_{H\ Lon} - G_{A\ Lon} \quad (3)$$

This information is then used to plot a third point R90 (denoting the 90° angle of the right-angled triangle formed by G_A, G_H and R90). The point R90 is located Δ_{Lat} grid cells from G_A and Δ_{Lon} grid cells from G_H (Figure 4.2). From this triangle, the orientation of the line connecting G_H to G_A can then be found by calculating the unknown angle ΘG_A:

$$\theta G_A = arctan\left(\frac{\Delta_{Lon}}{\Delta_{Lat}}\right) \quad (4)$$

Initially, ΘG_A is used to approximate the orientation of the central flow line connecting G_A and G_H to a straight line ($\overleftrightarrow{G_A G_H}$). This line approximates the orientation of the gully. While a more advance scheme could facilitate any orientation of $\overleftrightarrow{G_A G_H}$, the method here restricts the range to increments of 45° starting from 0°. This is done primarily to keep the method simpler, but also because this scheme fits with the inherent restriction of directions outward from any cell on a regular grid (eight possible directions).

After finding $\overleftrightarrow{G_A G_H}$ the routine then strikes a line ($\overleftrightarrow{LR}$) normal to the orientation $\overleftrightarrow{G_A G_H}$ at the point G_A. The orientation of $\overleftrightarrow{LR}$ is necessarily restricted to increments of 45°. The line $\overleftrightarrow{LR}$ is then used as an input into the same routine used to locate the gully head (Section 4.2.3.1), except in this case it is used to find the gully edges (e_1 and e_2) proximal to G_A. The only difference in the two implementations (finding G_H or e_1 and e_2) is that instead of moving in a single direction from downstream to upstream along the central flow line to find G_H, the routine now moves in each direction outward from G_A along $\overleftrightarrow{LR}$ to find e_1 and e_2. Gullies are also typically longer than they are wide and so a second difference is that the search distance to find the edges is halved from 20 m to 10 m (designed for gullies between 1 – 15 m wide across our study site).

After locating the edges the routine then moves 3 m in each direction outward from the endpoints of the line segment $\overline{e_1 e_2}$ along $\overleftrightarrow{LR}$. The distance chosen (3 m) is

arbitrary but is considered far enough from the gully edges that the routine will not include some part of the edge in the calculation of slope, but not so far as to measure the slope of the soil surface at a distance that is no longer relevant. This process gives one side of a parallelogram with vertices L and R. From the properties of a parallelogram - opposite sides are congruent. The routine has already identified the distance from LR to its opposite side $S_{L1}S_{R1}$ as the length of the line segment $\overline{G_A G_H}$, hence the vertices S_{L1} and S_{R1} are also known and used as reference points to calculate slope on the left and right of the gully. Slope on the left is calculated by finding the elevation value at the point S_{L1} and at a second point, S_{L2}, 5 m downslope in the direction of L, and computing:

$$slope_L = \frac{(S_{L1})_z - (S_{L2})_z}{5} \quad (5)$$

Where $(S_{L1})_z$ and $(S_{L2})_z$ denote the elevation values at the points S_{L1} and S_{L2}, respectively. The same process is followed for the right side. Similarly, slope above the gully head was computed as:

$$slope_H = \frac{(S_H)_z - (G_H)_z}{5} \quad (6)$$

As a convention, S_R and S_L are used to denote slope measured on the left-hand and right-hand side of the gully head (looking downstream from the gully head). This system is used because it is always independent of the orientation of the gully (compass directions would not be).

This geometric construction has several advantages. It is simple to understand, can be applied to a gully of any size, and enables all computations to be vectorized allowing the routine to run very efficiently. Together, the processes described above remove all potential bias from the calculation of slope for input into topographic thresholds of gully heads on regular gridded DEMs.

4.2.4 Digitised set of gully heads

To compile a set of digitised polygons of gully heads to test the method against we first segmented the ~1 200 km^2 area according to mapped lithology (Geoscience Australia, 2012b). Digitising was carried out in ArcGIS 10.6 for desktop. Sites were grouped by lithology as a way of controlling for differences in geometry such as the relationship between stream bed particle size and slope found by Hack (1957). Previous gully morphology studies have also found that gully dimensions relate to

lithological setting (e.g. Parkner et al., 2006, Parkner et al., 2007, Frankl et al., 2013). Across the site there were seven predominant lithological classes (Table 4.1).

Table 4.1: Primary lithology types across our site and the associated topographic attributes for these areas.

		Topographic attributes				
	Lithology	Geologic age	Elevation mean	Elevation range	Slope mean	Slope range
Volcanic	Felsic	Cretaceous	154 .6 ± 15.0	71.5	3.8 ± 4.3	61.2
	Intermediate	Triassic	159.2 ± 64.3	199.35	6.0 ± 4.9	62.6
	Mafic	Cretaceous	118.1 ± 32.4	97.1	3.5 ± 3.1	51.3
Igneous	Felsic	Permian	180.9 ± 15.6	87.2	3.5 ± 4.0	59.6
	Mafic	Permian - Cretaceous	188.7 ± 21.1	138.3	5.4 ± 5.0	60.6
Sedimentary	Sandstone Mudstone Conglomerate	Permian	72.8 ± 11.7	49.5	4.0 ± 4.0	53.2
	Sandstone Mudstone Conglomerate	Cenozoic	61.1 ± 8.82	54.8	3.6 ± 3.3	52.4

To take a representative sample from each class, subsets of the DEM were created for each lithology and divided into equal areas of 1 km^2. For this set of 1 km^2 units, points were chosen at random and all gullies within the corresponding 1 km^2 area were digitized. This process was followed until a set of at least 30 gullies was digitized for each lithology class. Areas within the alluvial flood plain (Figure 4.1) were excluded from the analysis as the method is design primarily for studies of linear, or hillslope, gullies and processes driving gully erosion in alluvial flood plains are expected to differ (e.g. Shellberg et al., 2016).

Gully heads were digitized using RGB imagery following Morgan and Mngomezulu (2003) and Gutiérrez et al. (2009) together with maps of profile curvature (Figure 4.4). Profile curvature has been used to identify gully edges in several recent studies (e.g. Korzeniowska et al., 2018, Walker et al., 2020).

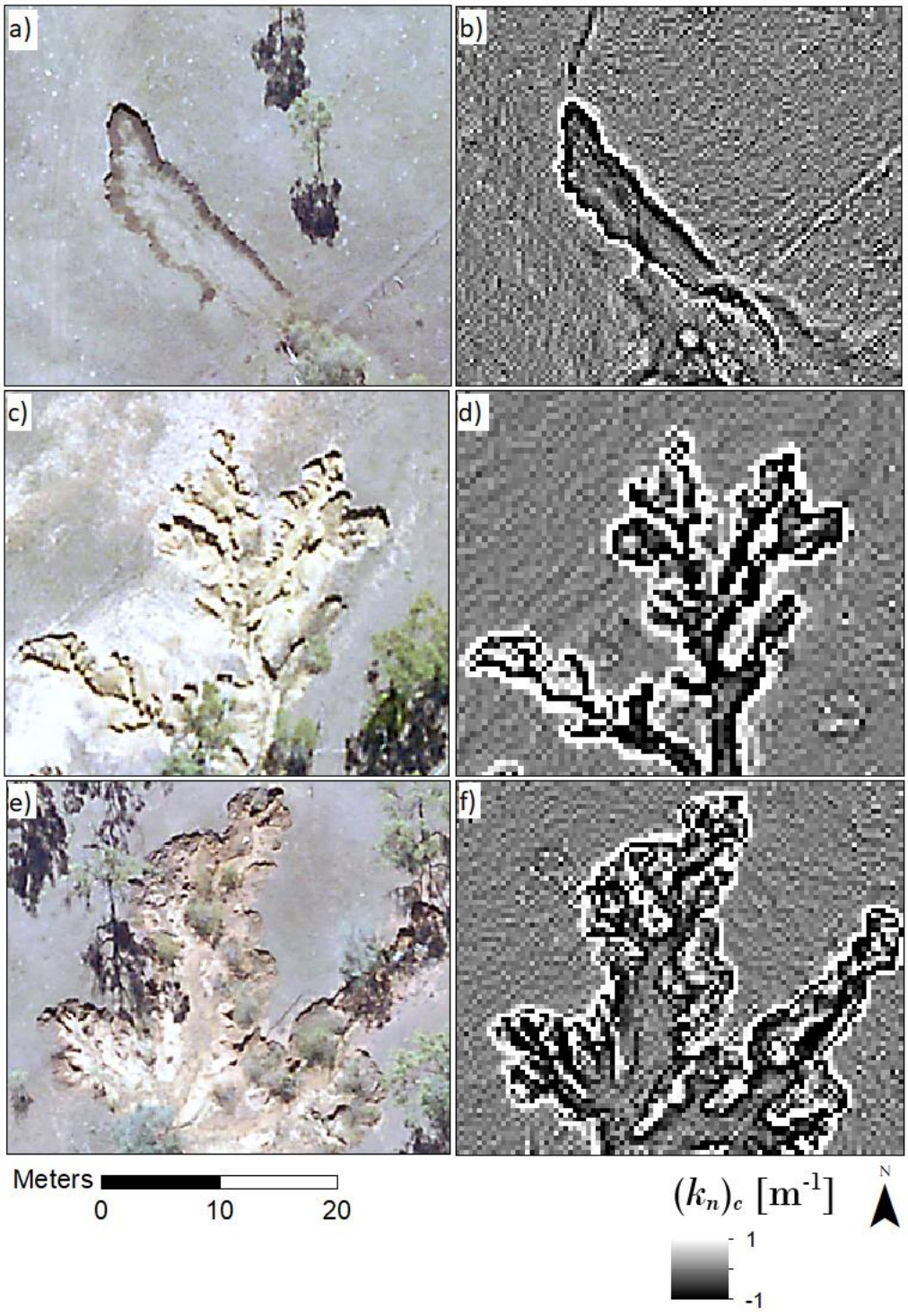

Figure 4.4: Visual identification of gully edges involved inspection of high-resolution RGB imagery and maps of profile curvature $(k_n)_c$. Panel a) and d) show a gully within an area of mafic volcanic lithology. Panel c) and d) show a gully in an area of mixed sedimentary lithology. Panel e) and f) show a gully in an area of felsic igneous lithology.

4.2.5 Testing accuracy of the algorithm

We used the F-score measure to compare the accuracy of our algorithmic results with the digitised gullies. This involved computing recall, precision, and F-score:

$$recall = \frac{TP}{TP+FN} \quad (7)$$

$$precision = \frac{TP}{TP+FP} \quad (8)$$

$$F - score = \frac{2}{recall^{-1}+precision^{-1}} \quad (9)$$

Where TP are true positives, FN are false negatives and FP are false positives. False negatives were assigned when the algorithm failed to detect any change (gully headcut or sides) and false positives were assigned when the algorithm estimated the headcut or sides to exist within the mapped feature. True positives were assigned when:

$$0 \leq M_e \leq T_d \quad (10)$$

Where M_e is the mapped edge of the gully (headcut or sides) and T_d is the target distance from the edge that is considered acceptable. This scheme allowed us to test the performance for three different levels of tolerance, 1 m from the mapped edge, 2 m, and 3 m.

4.2.6 Measuring gully geometry

As well as estimating gradient of the hillslope adjacent to the gully head, we also extracted gully width, floor slope, and depth. Width was given by the length of the line segment $\overline{e_1 e_2}$. Floor slope was measured by following the most concentrated flow path from G_A to a point 5 m downstream ($G_{A\text{-}5}$), finding elevation values at these two points $(G_A)_z$ and $(G_{A\text{-}5})_z$, and computing:

$$slope_F = \frac{(G_A)_z - (G_{A-5})_z}{5} \quad (11)$$

Depth was measured by subtracting the average elevation of cells along the line $\overleftrightarrow{G_A G_{A-5}}$ from the average elevation of cells along the line $\overleftrightarrow{G_H S_H}$.

We then used a simple linear regression with ordinary least squares to compare the relationship between each pair of geometric measurements.

4.2.7 Comparing slope estimates

As a final test we wanted to establish how robust slope estimates were along gully sides compared to slope estimates above gully headcuts. To do this we first measured the slope of a second line length taken upslope of the line $\overleftrightarrow{G_H S_H}$ found by following the most concentrated flow path 5 m upslope from the point S_H to a second point S_{H+5}, finding the elevation values of these two points $(S_H)_z$ and $(S_{H+5})_z$, and computing:

$$slope_{H2} = \frac{(S_{H+5})_z - (S_H)_z}{5} \quad (12)$$

We then compared the measurements $|slope_H - slope_{H2}|$ to $|slope_L - slope_R|$ for each gully head.

4.3 Results

4.3.1 Algorithm accuracy assessment

Lithologies were grouped into three general groups (a) sedimentary, (b) volcanic, or (c) igneous. For each group, algorithm performance was assessed for a distance tolerance of 1 m, 2 m and 3m, and the results for detection of gully sides and gully headcuts were assessed separately (Figure 4.5 and Table 4.2).

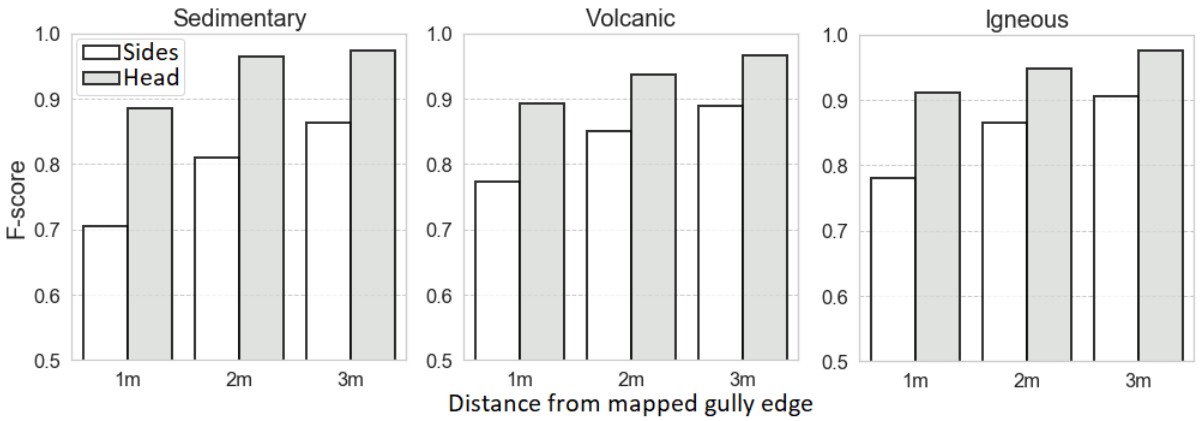

Figure 4.5: Accuracy results of the automated method for locating gully edges and headcuts. The accuracy results for detection of gully edges (sides) were assessed separately to detection of gully headcuts. Accuracy assessments were conducting for three different tolerance levels (within 1 m of the mapped gully, within 2 m and within 3 m).

For detection of gully sides, the algorithm had lowest accuracy in sedimentary areas with an average F-score of 0.7 at a tolerance of 1 m from the edge of the mapped feature, 0.8 at a tolerance of 2 m, and 0.86 at a tolerance of 3 m (Table 4.2). The best performance was in igneous landscapes with an average F-score of 0.78 at a

tolerance of 1 m from the edge of the mapped feature, 0.87 at a tolerance of 2 m, and 0.91 at a tolerance of 3 m (Table 4.2).

Table 4.2: Accuracy results for the automated method for each lithology. The column 'Dist.' indicates the tolerance level determined to be an acceptable distance for the edge of the mapped feature.

		Volcanic			Igneous		Sedimentary	
Dist.	Test	Felsic	Intermediate	Mafic	Felsic	Mafic	Sandstone Mudstone Conglomerate (Permian)	Sandstone Mudstone Conglomerate (Cenozoic)
Sides 1m	Recall	0.67	0.63	0.70	0.76	0.52	0.73	0.49
	Precision	0.98	0.85	0.93	1.0	1.0	0.83	0.83
	F-score	0.80	0.72	0.8	0.86	0.68	0.78	0.61
Sides 2m	Recall	0.77	0.73	0.84	0.89	0.63	0.87	0.66
	Precision	0.98	0.87	0.94	1.0	1.0	0.85	0.87
	F-score	0.86	0.80	0.89	0.94	0.78	0.86	0.75
Sides 3m	Recall	0.82	0.82	0.89	0.92	0.73	0.92	0.78
	Precision	0.98	0.89	0.94	1.0	1.0	0.86	0.88
	F-score	0.89	0.85	0.92	0.97	0.85	0.89	0.83
Head 1m	Recall	0.94	0.87	0.68	0.90	0.76	0.83	0.77
	Precision	1.0	0.96	0.90	1.0	1.0	1.0	0.95
	F-score	0.97	0.91	0.76	0.95	0.87	0.91	0.86
Head 2m	Recall	0.97	0.9	0.86	0.97	0.83	0.97	0.93
	Precision	1.0	0.96	0.92	1.0	1.0	1.0	0.96
	F-score	0.98	0.93	0.89	0.98	0.91	0.98	0.94
Head 3m	Recall	0.97	1.0	0.93	0.97	0.93	0.97	0.96
	Precision	1.0	0.97	0.93	1.0	1.0	1.0	0.96
	F-score	0.98	0.98	0.93	0.98	0.97	0.98	0.96

Accuracy of gully headcut detection was higher, compared to sides, for all lithologies with F-scores close to or above 0.9 at a tolerance of 1 m from the edge of the mapped gully feature.

Results from comparing geometric measurements reveal that width showed no relationship to slope of the gully floor or surround soil surface in any lithology (Table

4.3), and only a weak relationship with depth for gullies in igneous terrain. As expected, there was also a statistically significant relationship between drainage area and slope of the adjacent soil surface. The coefficient of determination for this relationship was highest for sedimentary landscapes ($R^2 = 0.49$, $p < 0.0005$).

Table 4.3: Values in the table represent the coefficient of determination from a simple linear regression using ordinary least squares (ns = not significant, * = significant at $p < 0.05$, ** = significant at $p < 0.005$ and * = significant at $p < 0.0005$.**

		Width	Depth	Floor slope	Hillslope
Volcanic	Width				
	Depth	0.03 ns			
	Floor slope	0.02 ns	0.10 ns		
	Hillslope	0.01 ns	0.31 ***	0.22 ***	
	Drainage area	0.00 ns	0.02 ns	0.29 ***	0.34 ***
Igneous	Width				
	Depth	0.05 *			
	Floor slope	0.04 ns	0.12 *		
	Hillslope	0.01 ns	0.28 ***	0.24 ***	
	Drainage area	0.01 ns	0.03 ns	0.17 ns	0.26 *
Sedimentary	Width				
	Depth	0.12 ns			
	Floor slope	0.07 ns	0.36 ***		
	Hillslope	0.03 ns	0.61 ***	0.43 ***	
	Drainage area	0.01 ns	0.09 ns	0.35 **	0.49 ***

We also found a significant relationship between gully depth and slope of the adjacent soil surface for all lithologies (Table 4.3 and Figure 4.6).

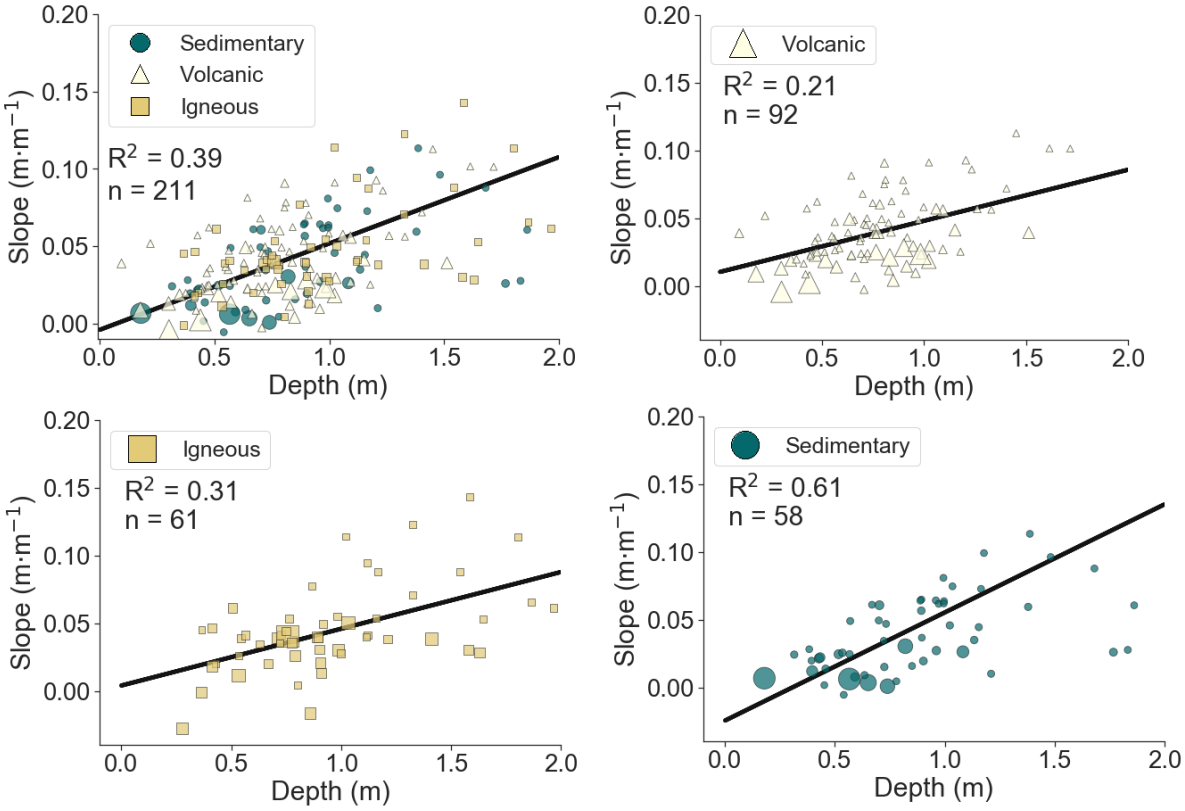

Figure 4.6: Relationship between depth of gully heads and slope of the surrounding soil surface for each lithology. Coefficient of determination values are found using simple linear regression with an ordinary least squares estimator. The relative size of individual points indicates relative differences in gully head drainage area (larger points have larger drainage areas).

The relationship between gully depth and slope of the adjacent soil surface was also strongest for sedimentary landscapes with an R^2 of 0.61 ($p < 0.0005$). The overall R^2 for this relationship across all gullies was 0.39 (Figure 4.6).

When we tested the robustness of slope estimates above gully heads and along gully sides, we found that slope estimates above gully heads were more consistent in all lithologies and a difference of means test confirmed the difference between the two groups was also statistically significant for each lithology (Figure 4.7).

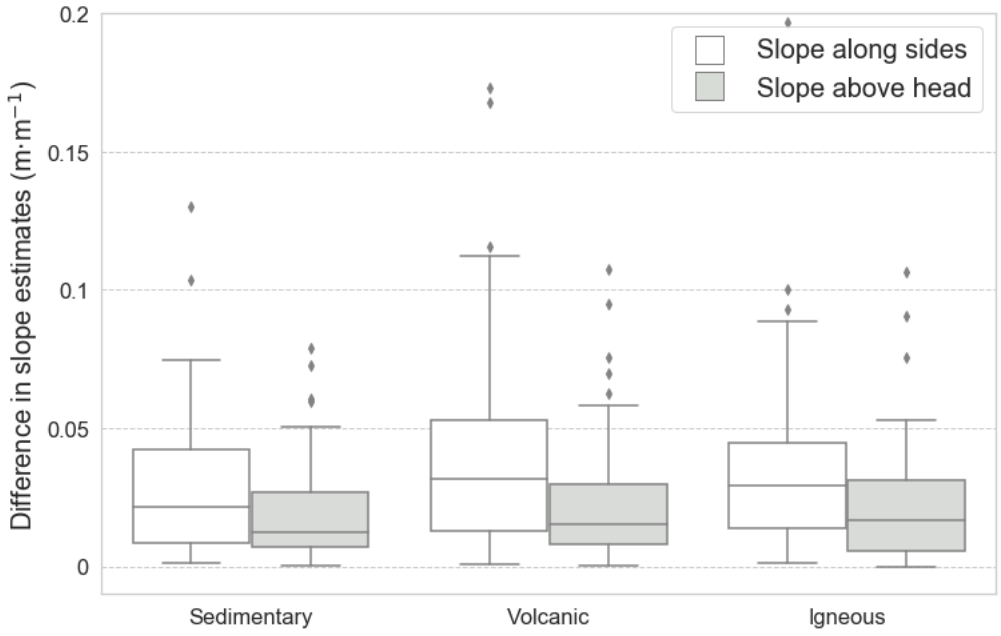

Figure 4.7: Comparison of variability in slope estimates above gully heads and along gully sides grouped by lithology.

The difference in slope estimates between gully sides and above gully heads was largest in volcanic and igneous landscapes and smallest in sedimentary landscapes. Gullies in sedimentary landscapes also tended to have a lower range of slope estimates than gullies in either volcanic or igneous landscapes. However, we also found that when we combined slope above the gully head with slope along the sides (taking the mean of all measurements) this reduced the scatter of data around the regression line (Figure 4.8).

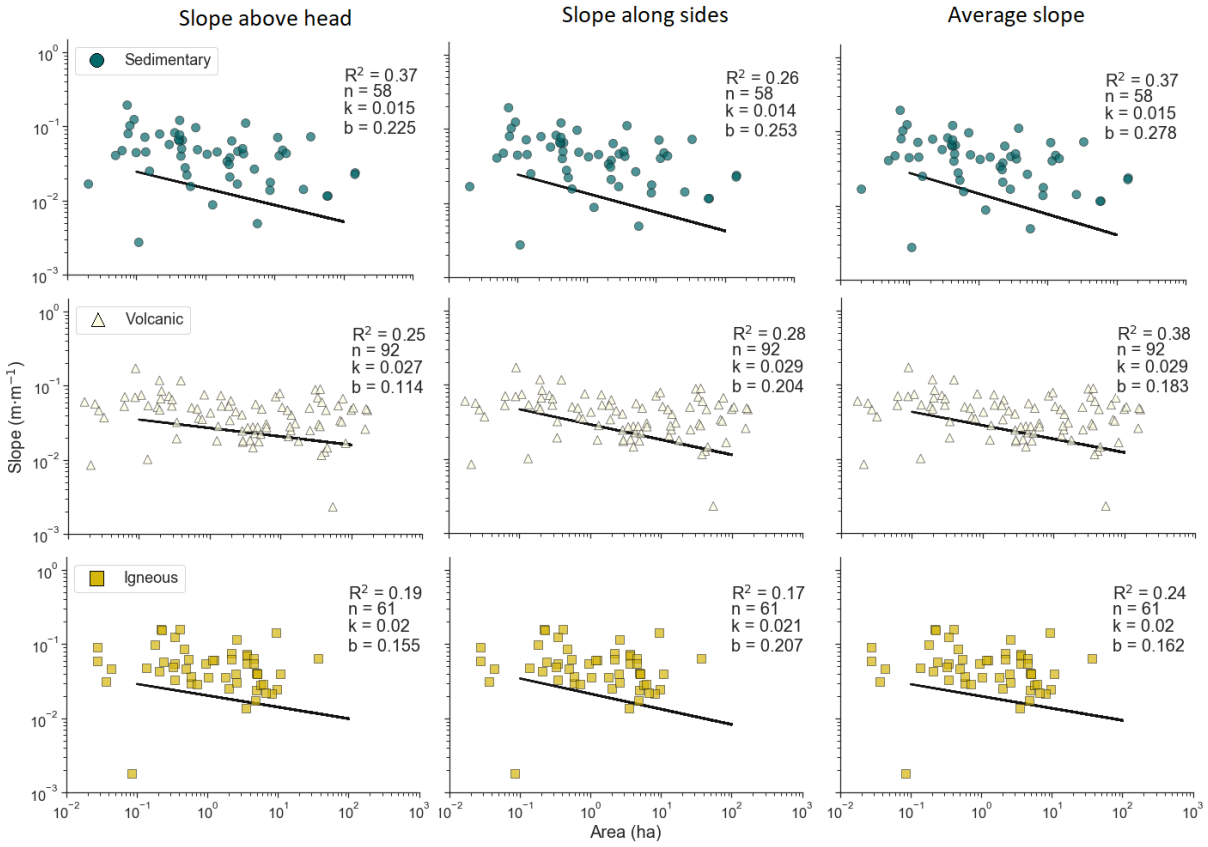

Figure 4.8: Comparison of topographic threshold analysis results for each lithology using three different measures of slope: (1) only along the sides, (2) only above the head, and (3) mean slope along sides and above the head.

4.4 Discussion

4.4.1 Usefulness of programmatic approaches

Quantifying gully geometry in a variety of landscapes has been found to have a range of uses, and comparisons of results between regions have revealed important relationships. For example, gully width and depth have been found to correlate with vegetation cover in parts of Southwestern China (Dong et al., 2013), while gully headcut height has been found to relate to stability, with increasing headcut height eventually leading to gully head collapse (Istanbulluoglu et al., 2005). Other studies have found that the retreat rate of gullies is related to headcut height (e.g. Vandekerckhove et al., 2001) and that the relationship between width and cross-sectional area provides a useful tool to estimate gully volumetric change when only a change in areal extent can be measured (Vanmaercke et al., 2016). Subjective decisions made by researchers and practitioners when collecting and analysing data on gully form and presence in the landscape introduce bias that can confound comparisons (Maugnard et al., 2014, Casalí et al., 2015). For example, while

Vanmaercke et al. (2016) found that the relationship between width and cross-sectional area was useful, they encountered difficulties comparing results across studies due to variation in measurement methods applied. The approach we outline in this paper has two useful contributions to mitigate these issues. Firstly, it enables better use of increasingly available high-resolution topography data, and secondly it brings more consistency to the study of gully dimensions across landscapes. The approach is fully automated and fits directly into a workflow for estimating gully topographic threshold parameters which no other current method does.

4.4.2 Factors influencing accuracy of automated gully edge detection

Our results indicate that automated methods of gully edge detection have more difficulty identifying gully side walls than gully headcuts (Figure 4.5). There are several possible reasons for this. Recent work by (Castillo et al., 2021) found that gully cross-section shape can vary with distance downstream from a gully head. Our method searches for gully edges adjacent to the first point of flow convergence on the gully floor. Differences in the cross-section morphology at different distances may be affecting the ability of our method to detect gully edges more in some gullies than others. Similarly, measured gully width can vary greatly even for a single gully depending on where the width measurement is taken (Höfle et al., 2013, Casalí et al., 2015). Gullies also do not necessarily always have a clear break in slope showing the location of edges, in some cases one side of a gully may be clearly definable and the other not, or it may also be the case that neither side is clearly defined (Casalí et al., 2015). The size and shape of gullies can also be affected by installation of remediation structures such as check dams (Frankl et al., 2013), which would affect the ability of an automated algorithm to detect edges using common rules. Many of our landscapes are used as cattle grazing stations and various structures can be seen constructed to stop the gullies.

Another source of error in our measurements could be that the location chosen to measure depth is not straightforward (Casalí et al., 2015) and discrepancies in the specific location used can affect results. However, we take care to mitigate against this type error by using a 5 m section along the gully thalweg to compute average elevation and compare this to the elevation above the gully head (where the algorithm performs better).

4.4.3 Gully morphometry

In many landscapes a decrease in slope with an increasing drainage area can have the effect of decreasing sediment transport capacity with a corresponding decrease in gully depth (Poesen et al., 2011). When comparing gully measurements across our dataset we found a statistically significant relationship between the slope of the soil surface adjacent to gully heads and the depth of the gully head (Figure 4.6). This finding supports Poesen et al. (2011) and provides important information about potential gully remediation options in this area. Shallower gullies on flatter slopes may provide better candidates for in-channel gully rehabilitation structures such as porous check dams used in other parts of the GBR catchments (e.g. Bartley et al., 2020, Koci et al., 2021).

Across our site lithology appears to play an important role in the relationship between gully geometric measurements. For example, the relationship between gully depth and slope of the soil surface adjacent to the gully head is clearer for sedimentary landscapes than for igneous or volcanic (Figure 4.6). Conversely, the automated edge detection algorithm employed here has more success detecting the sides and headcuts of gullies incised into volcanic or igneous terrain than it does on sedimentary terrain (Figure 4.5). Other studies have also found relationships between gully morphology and lithology. In a study of gully geometric relationships in northern Ethiopia, Frankl et al. (2013) found that lithology was one of the most important factors in explaining gully cross-section measurements. Likewise, Parkner et al. (2007) found that the morphology and location of gully features in the North Island of New Zealand was influenced by lithology.

In their global review of gully headcut retreat rates Vanmaercke et al. (2016) found no clear relationship between drainage area and the dimensions of gully headcuts (width and cross-sectional area). There are several reasons put forward for this lack of observed relationship including the wide range of data collection methods employed in the various studies reviewed. However, using a single objective method to assess the same relationships across our study area, we also find no clear relationship between drainage area and gully headcut dimensions (Table 4.3). Our dataset is smaller and does not have the geographic cover of the dataset used by Vanmaercke et al. (2016), but nevertheless supports the same finding while using a completely consistent measurement process. A second suggestion for this observation put

forward by Vanmaercke et al. (2016) is that the width of the 'gully channel' ought to correspond to drainage area (e.g. Nachtergaele et al., 2002) but that gully width is usually measured as the 'top width' of the gully which may not relate to drainage area. Our method used gully top width as the measure of 'gully width' and confirms that, at least across this site, there is no relationship between gully top width and drainage area. For many gullies across our site the difference between gully 'top width' and gully 'channel width' can be large (see Figure 4.3).

4.4.4 Implications for topographic thresholds

Our results indicate that measurements of slope above the gully head were more robust than estimates along the sides of gullies. For this reason, we recommend using slope above the gully head for topographic threshold analysis using high-resolution DEMs. However, we also found that taking the mean of slope along the sides and slope above the head reduced the scatter around the threshold line (Figure 4.8). For studies looking to reduce the scatter around the threshold line (e.g. Vandekerckhove et al., 1998), the mean slope is suggested. This also has relevance to the interpretation of topographic threshold results. For example, Makanzu Imwangana et al. (2014) found that large scatter around the threshold line can indicate influence of anthropogenic factors in an area; however, our results suggest that a larger scatter can also simply be due to the way slope is estimated. This point highlights again the need for consistency in measurement techniques.

4.5 Conclusion

This study presented an algorithm for DEM-based geometric characterisation of gully heads to extract dimensions and estimate slope of the surrounding soil surface. The primary goal was to support progress toward automated topographic threshold analysis by offering a method to objectively determine slope of the soil surface around a gully head. A secondary goal of the work was to design a computer program capable of automatically extracting gully head dimensions such as slope, width, and depth. The method was tested across a ~1 200 km^2 study site in the Fitzroy River Basin of north-eastern Australia.

When we compared extracted gully dimensions, we found no clear relationship between gully width and any other dimension measured. However, we found that for better insights into this relationship gully channel width and gully top width should both

be measured separately and tested for their relationship with other gully head geometric measurements. We did find a statistically significant relationship between the gradient of the adjacent hillslope and gully head depth. This finding supported previous findings and provided potentially useful information for ongoing gully erosion management efforts across catchments of the Great Barrier Reef.

Accuracy assessment of the algorithm suggested that automated methods are better able to locate gully headcuts (where the gully head transitions to un-gullied hillslope moving from the gully floor upslope along a concentrated drainage line) than locate gully sides (moving outward perpendicular to the gully thalweg). This finding suggests that for automated DEM-based topographic threshold analysis, using slope above the gully head will produce more reliable estimates than using slope along the sides of gullies. We found that estimating slope above the gully head provided more robust estimates than estimating slope from along the sides of gullies. However, we also found that taking the mean of slope along the sides and above the head reduced the scatter in slope-area plots, which may be preferred over more robust slope estimates. In conclusion, we found that the higher reliability of slope estimates above the head, together with the improved accuracy of gully headcut location, suggests that using only slope above gully heads is the best method for slope estimation in the context of automated DEM-based approaches to topographic threshold analysis.

Chapter 5: Fully automated estimation of gully topographic thresholds across catchments of the Great Barrier Reef using high-resolution DEMs

Abstract

Gully erosion is a widespread issue across all inhabited continents, with many costly environmental ramifications. Over recent decades analysis of gully head topographic position has become ubiquitous among methods to understand the phenomena. The widely accepted theoretical basis for this analysis relates the topographic position of gully heads to catchment area draining toward the gully head and gradient of the adjacent hillslope. Early published work, conducted prior to the availability of high-resolution digital elevation models (DEMs), relied on extensive fieldwork to gather required inputs for the analysis. This requirement restricted most previous studies to small scales, often with relatively few sample points. Availability of high-resolution terrain data is no longer a limitation in many areas, with DEMs derived from light detection and ranging (LiDAR) becoming increasingly available globally.

We propose the first attempt at fully automated gully topographic threshold analysis using LiDAR DEMs. The method uses a process to locate initial gully heads and then a geometric scheme to locate points around a gully head to measure slope and area. This new analysis removes arbitrary assumptions of previous methods to take full advantage of the finer resolution of LiDAR data.

The fully automated method is tested across a range of environments spanning ~1 200 km of catchments adjacent to the Great Barrier Reef, Australia. The sites were within four priority erosion management regions and the total area of high-resolution DEM coverage for these sites was 185 km^2. In total we estimated there were ~987 gully heads over this area with an estimated density of ~5.33 gully heads per square kilometre.

Results indicate that the method estimates threshold parameters close to those found using manual methods and confirm that among our sites the most susceptible to gully erosion were those in the Burdekin River Basin. We also found that sites in cleared areas were estimated to have a lower threshold for gully incision than sites in forested areas. This agrees with findings from previous global studies that a shift from

natural forests to cleared agricultural landscapes increases susceptibility to gully formation.

5.1 Introduction

Gully erosion affects many environments globally (Poesen et al., 2003) and can be an import source of fine sediment entering streams and rivers (Doriean et al., 2021). Many past studies have examined gully erosion at small scales to improve our understanding of relevant driving processes, particularly where accurate field data is available (e.g. Prosser and Soufi, 1998, Rengers and Tucker, 2014, Koci et al., 2020a). Large-scale assessments of landscape susceptibility to gullying aim to provide the necessary context for gully erosion management in cases where the scale of the problem cannot be addressed by plot-scale studies alone (Allen et al., 2018). However, there remain challenges to mapping and modelling gully erosion over large scales (De Vente et al., 2013, Poesen, 2018), and effective prioritisation of gully erosion management at these scales requires further research.

Large-scale assessment is particularly relevant to gully erosion management across the catchments of the Great Barrier Reef (GBR) in north-eastern Australia, where water quality is affected by fine sediment runoff from adjacent farmland (Brodie et al., 2005, Fabricius et al., 2005, Wooldridge, 2009, Pollock et al., 2014). The GBR catchment area is comprised of 40 drainage basins covering an area >400 000 km^2 and the reef itself extends ~2 000 km along the coastline (Gilbert and Brodie, 2001). There are estimated to be >87 000 km of gullies across this region, and spatial variation in gully density is high (Gilad et al., 2012). Gully erosion across this region has been found to contribute an amount of fine sediment to the GBR comparable to hillslope and streambank erosion (McCloskey et al., 2021). In recent years, the rapid development and deployment of technology to image the land surface has enabled studies to expand the scale of assessments, bringing more attention to gully erosion studies at large scales (regional to continental). For example, recently Karydas and Panagos (2020) used Google Earth to provide the first nation-wide gully inventory for Greece, and Vanmaercke et al. (2020) used Google Earth to develop a machine learning algorithm to estimate gully head densities across the Horn of Africa. Another source of new data that can help to address gully erosion across large areas is high-resolution topographic data typically collected by airborne light detection and ranging (LiDAR). Digital elevation models (DEMs) derived from airborne-LiDAR do not have

the level of accuracy possible with terrestrial-based systems (Goodwin et al., 2017), but have the advantage of areal coverage. Many areas of geomorphology stand to benefit from the proliferation of modern high-resolution topography (Mudd, 2020), and topographic studies of gullies is one such area. Gully topographic threshold analysis ('threshold analysis' herein) is one of the most widely used models of gully presence in the landscape (Majhi et al., 2021) and has been applied to many landscapes globally (Hayas et al., 2017). Originally proposed by Patton and Schumm (1975), threshold analysis uses the relationship between the contributing drainage area at gully heads and the gradient of the adjacent hillslope to establish the topographic limits of gully formation in a landscape. Despite its wide use, many past studies have varied in the way they conduct threshold analysis (Torri and Poesen, 2014), and there is a general need to improve the consistency with which gully measurements are made (Casalí et al., 2015). In recent work assessing gully erosion in northern parts of the GBR catchments, Shellberg (2020) concluded that improved threshold analysis of gullies using LiDAR DEMs should be a required component of decisions in land management projects in this region.

5.1.1 Aims

The objective of this method was to allow large-scale assessment of topographic thresholds where high-resolution data is available, and potentially identify areas that warrant further investigation with more detailed field campaigns. Specific aims of this research were to (1) assess the viability of fully automated gully topographic threshold analysis using high-resolution DEMs, (2) apply the new approach to a range of landscapes spanning ~1 200 km along the GBR catchments to investigate topographic thresholds of gully formation in these different locations, and (3) use the method to determine whether a clear difference in the threshold of gully formation is evident between forested and cleared landscapes. The overarching goal of this algorithm was to provide a means to conduct topographic modelling of gullies, using slope and area, with high-resolution DEMs within a programmatic framework, thereby improving the comparability of results between regions.

5.1.2 Regional setting

We assessed landscapes over an area spanning ~1 200 km from the Wet Topics adjacent to the northern end of the GBR down to the Burnett-Mary region adjacent to

the southern-most end of the GBR. The catchments of the GBR contain a wide range of diverse landscapes from steep wet rainforests and high energy streams to flat dry savannah plains with wide extensive floodplains (McKergow et al., 2005a). Among these landscapes we examined gully topographic thresholds for six locations (totalling 185 km^2) in four broad regions (1) the Wet Tropics, (2) the Burdekin River Basin, (3) the Fitzroy River Basin, and (4) the Burnett-Mary region (Figure 5.1). Four of our sites were located along major rivers in their respective region: a site near the Herbert River in the Wet Tropics, a second near the Bowen River in the Burdekin, a third near Fitzroy River and a fourth along the Mary River. The remaining two sites were both catchments of smaller creeks in the Burdekin Basin (Weany Creek and Main Creek). All four broader regions studied are characterised by agricultural land uses (Waterhouse et al., 2012). Cattle grazing is prevalent across all GBR catchments but covers a larger proportion of area in the Fitzroy and Burdekin basins (Gilbert and Brodie, 2001). The Wet Tropics has the proportionally smallest amount of grazing land at ~33% of the area, while 48% is assigned to conservation (Lewis et al., 2021), which is proportionally much higher than conservation in the Burdekin (5.2%), Fitzroy (8.8%) or Burnett-Mary (8.3%).

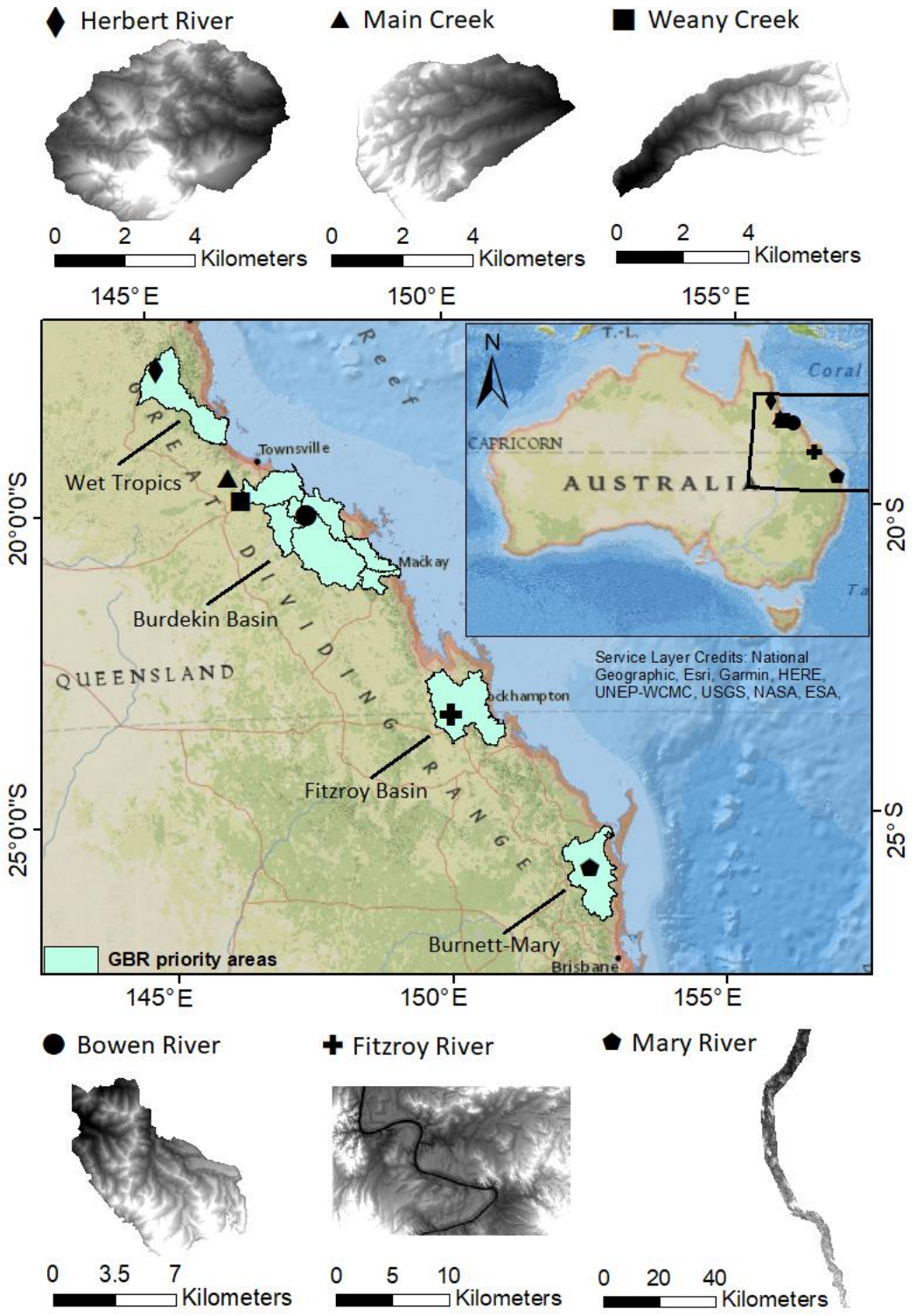

Figure 5.1: Study area map showing location of six study sites with respect to four priority erosion management regions (1) the Wet Tropics, (2) the Burdekin Basin, (3) the Fitzroy Basin, and (4) The Burnett-Mary Region.

Rainfall variability across the catchments of the GBR is typically high (Thorburn et al., 2013), and the climate across all our sites is typified by wet summers and dry winters, with this relationship being more marked for the Burdekin and Wet Tropics.

The Köppen-Geiger climate classification for our section of the Burnett-Mary is a temperate climate with hot summers and no dry season. Study sites in the Fitzroy, Burdekin and Wet Tropics all straddle the border between hot arid steppe and tropical savannah climates (Peel et al., 2007).

Weany Creek, Main Creek, and Bowen River are granodiorite landscapes with typically red chromosol soils known locally as ‘goldfields’ country (Bartley et al., 2010b). Weany Creek has been studied extensively and found to be a landscape highly susceptible to gully erosion (e.g. Bartley et al., 2010b, Wilkinson et al., 2018, Koci et al., 2020b, Walker et al., 2021). The Herbert River site is also entirely underlain by granodiorite. Along the Mary River two of the sites exist on coal measures and a third is a mixed sedimentary landscape. Soils across these three sites are typified by hard acidic yellow mottled soils (McKenzie et al., 2005). Near the Fitzroy River, all sites assessed are from areas of Permian age mixed sedimentary lithology consisting primarily of quartzose to lithic sandstone and siltstone (Geoscience Australia, 2012).

5.2 Materials and methods

Analysis of gully topographic thresholds requires two inputs, (1) an estimate of drainage area as a surrogate for discharge volume, and (2) an estimate of the gradient of the hillslope adjacent to the gully head as a proxy for flow velocity (Vandekerckhove et al., 1998). Together these two estimates enable an assessment of the topographic threshold of gully formation for a given landscape following the original proposition by Patton and Schumm (1975). Later workers (Montgomery and Dietrich, 1994, Willgoose, 1994, Vandaele et al., 1996) developed this observation further from a process-based approach eventuating in the widely used model $s \geq kA^b$, where *s* is the slope of the soil surface adjacent to the gully head, *A* is the contributing drainage area at the gully head and *k* and *b* are empirical parameters. Our fully automated method comprises three key components that operate as stand-alone programs working together to estimate slope and contributing drainage area. These components include a method for (1) automatically locating initial candidate gully heads to be used in the analysis, (2) estimating gully head drainage areas, and (3) estimating the gradient of the hillslope adjacent to gully heads.

5.2.1 Data

Soil types were identified using national soil data (McKenzie et al., 2005) provided by the Australian Collaborative Land Evaluation Program (ACLEP) from the Australian Soil Resource Information System (ASRIS) available at (http://www.asris.csiro.au). Cleared areas were identified using tree cover data derived from Landsat imagery (0.9 arcsecond resolution) downloaded from the Australia's Environment Explorer (http://ausenv.online).

Airborne LiDAR data used in the study was collected as part of a broader campaign to scan large gully-prone areas across catchments of the GBR. Specifications for the Weany Creek data are described in Chapter 3, and the Main Creek data was part of this same capture. Specifications for the Fitzroy River data was detailed in Chapter 4. The data for Bowen River, Herbert River and Mary River were captured by the same data provider and have the same specifications as the Fitzroy data. In all cases the data was resampled to a spatial resolution of 1 m using bilinear interpolation. This was done to match the resolution of the data used in Chapter 3 and 4, and because 1 m is the most common resolution among publicly available LiDAR DEMs (Walker et al., 2021).

Lithology was determined using a map of surface geology developed by Geoscience Australia (Geoscience Australia, 2012). This map is made available at a scale of 1:1M and contains information collected from a range of geological mapping sources.

Rainfall data was accessed through the Australian Bureau of Meteorology's online data resources (Australian Bureau of Meteorology, 2020). This data has a spatial resolution of 5 km interpolated from rainfall gauge data across Australia. Rainy day normal (RDN) was calculated by dividing the average annual rainfall ($mm \cdot y^{-1}$) by the number of rainy days (days with >1 mm of rainfall).

5.2.2 Locating initial gully head candidates

Chapter 3 and 4 provided the tools for estimating contributing drainage area and slope, but a fully automated algorithm also requires a method to automatically find initial gully head candidates to work with. Methods to identify stream networks in DEMs are fundamentally important to large-scale geomorphic investigations (Tarolli, 2014). Various studies (e.g. Lashermes et al., 2007, Passalacqua et al., 2010, Pelletier, 2013,

Clubb et al., 2014) have recognised this and developed methods to automatically map channel networks. These methods often rely on identification of points of flow convergence in the landscape (Tarolli, 2014) as an indicator of channel head locations (the beginning of the channel network). A common DEM-based method for identifying such points of convergence is to compute tangential curvature (Prasicek et al., 2014). We consider this a useful starting point for locating gully heads, being cautious that gully heads may or may not occur at the upstream limit of the channel network.

Our process borrows from concepts outlined in Pelletier (2013) but with some modifications. The first step is to smooth the DEM with a gaussian filter in preparation to compute curvature. Smoothing is done to help reduce noise in the DEM that otherwise affects curvature calculations (Pirotti and Tarolli, 2010). The gaussian filter is implemented using the Scipy library in Python with behaviour controlled by two parameters, 'sigma' (the standard deviation for the Gaussian kernel) and 'truncate', the radius of the kernel in terms of sigma. We use a sigma = 1 and a truncate = 3 which equates to a 7 x 7 rectangular smoothing window. Tangential curvature, also referred to as contour curvature (e.g. Mitášová and Hofierka, 1993), is then computed from the smoothed DEM using the definition given in Minár et al. (2020):

$$(k_n)_c = \frac{z_{xx}z_x^2+2z_{xy}z_xz_y+z_{yy}z_x^2}{(z_x^2+z_y^2)\sqrt{1+z_x^2+z_y^2}} \quad (1)$$

Then profile curvature is also computed using the definition from Minár et al. (2020):

$$(k_n)_s = \frac{z_{xx}z_x^2+2z_{xy}z_xz_y+z_{yy}z_y^2}{(z_x^2+z_y^2)\sqrt{(1+z_x^2+z_y^2)^3}} \quad (2)$$

Computing land surface curvatures requires a set of steps to first fit elevation values within a 3 x 3 moving window of grid cells to an idealised surface (differentiable polynomial) prior to estimating curvature (Pennock et al., 1987, Shary, 1995, Shary et al., 2002, Schmidt et al., 2003). For this task we primarily use methods outlined by Young and Evans (1978) and Hengl et al. (2003).

Profile curvature was incorporated because it has previously been found to be useful in mapping incised channel features (e.g. Korzeniowska et al., 2018, Walker et al., 2020). These land surface curvatures are used to approximate the position of gully heads. This requires a threshold curvature value, and we use the same value of -0.1 used by (Pelletier, 2013) for mapping channel heads (Figure 5.2b).

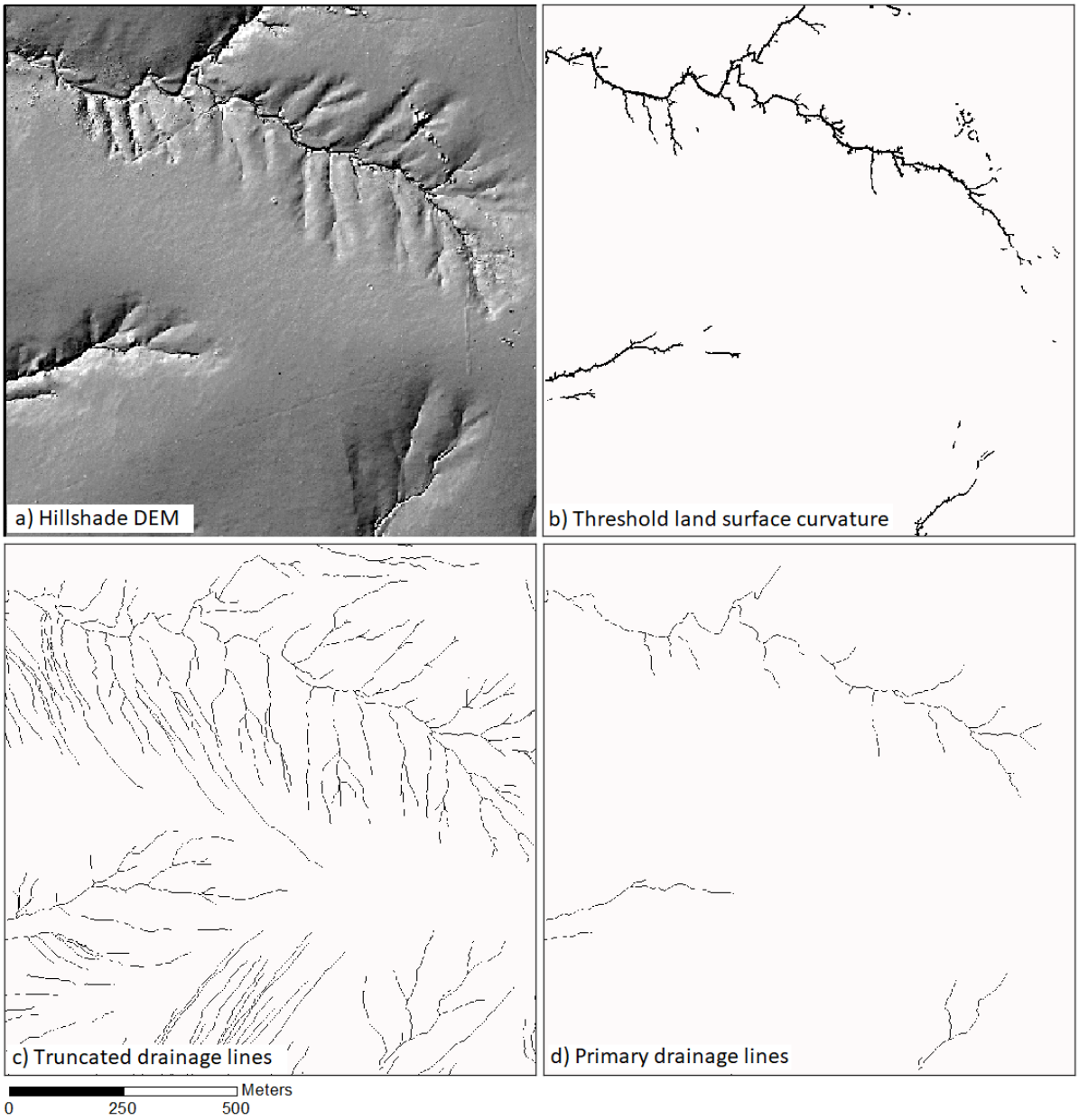

Figure 5.2: Example outputs from the process of finding initial estimates of gully head locations across a DEM. Panel a) shows the hillshade DEM. Panel b) shows the combined output of adding tangential curvature and profile curvature that have had a threshold of -0.1 applied. Panel c) shows a map of drainage lines truncated to an accumulated drainage area of 0.1 ha. Panel d) shows a map of drainage lines truncated to an accumulated drainage area of 1 ha.

Typically, channel head mapping methods will use drainage area computed with a flow routing algorithm (Callaghan and Wickert, 2019) and truncate values to some

threshold minimum value determined to be a good approximation of the beginning of the channel network (e.g. Passalacqua et al., 2010, Pelletier, 2013). For mapping gully heads, however, we found that simply using a single drainage area threshold created too many candidates (Figure 5.2c), and many, while reasonable candidates for channel network heads, did not contain gully heads. To manage this, we first used a larger threshold drainage area to reduce the size of the initial drainage network (Figure 5.2d), and subsequently extended those 'primary' drainage lines upslope to a distance defined by a smaller drainage area (Figure 5.2c). In this case we used a threshold drainage area for 'primary' drainage lines as 1 ha and extended those drainage lines upslope to minimum drainage area of 0.1 ha (Figure 3). Using the extended primary drainage lines, the algorithm tags the most upslope point of each drainage line as a point on the hillslope from which to begin searching back downslope for gully heads. It does this by following the most concentrated drainage line downslope until it intersects the estimated channel head position given by tangential curvature and profile curvature (Figure 5b).

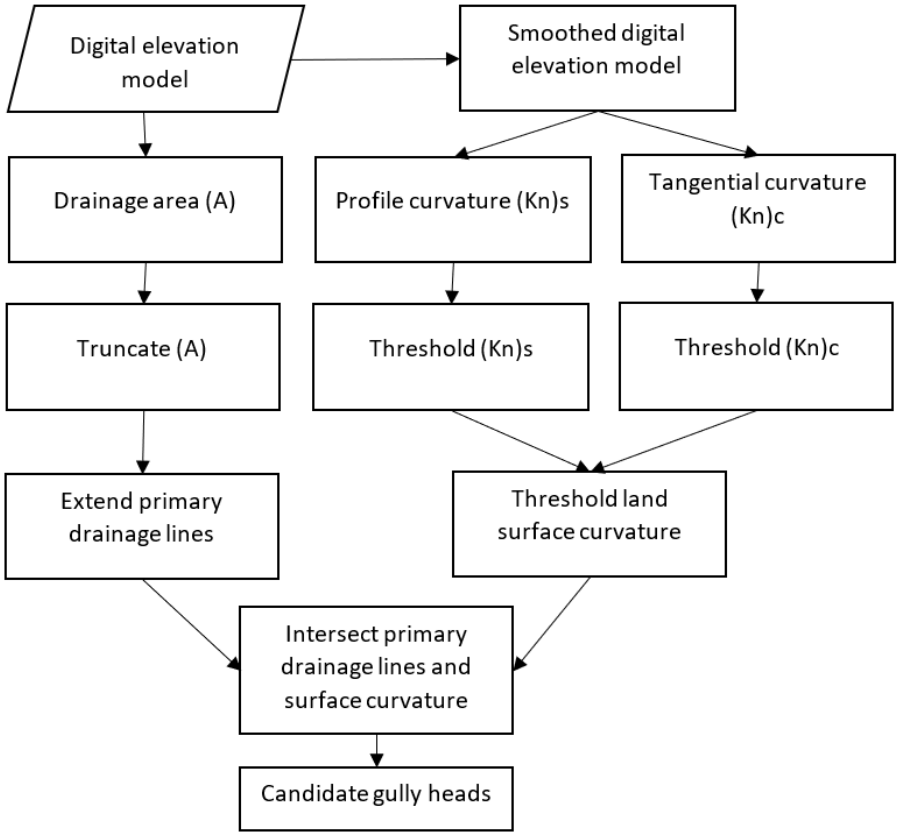

Figure 5.3: Process followed to find initial gully heads from an input digital elevation model.

5.2.3 Computing slope and drainage area

Once initial gully head candidates are found, the contributing drainage area at the gully head is estimated using the computer program described in Chapter 3 (Walker et al., 2021). This program automatically determines the optimal location from which to computer drainage area by searching for points of convergent flow on gully floors (where the drainage area *A* approaches the value for specific catchment area *a*).

Gradient of the hillslope adjacent to gully heads is computed using the algorithm outlined in Chapter 4. This algorithm begins at the point on the gully floor used to compute drainage area and works its way back upslope until it locates the gully head. It then moves 5 m upslope from this and computes slope along the 5 m line from the gully head to the point 5 m upstream of the gully head (and optionally 5 m along the gully sides).

5.2.4 Plotting the threshold line

Various methods have been used for plotting topographic threshold lines for sets of gully heads (Maugnard et al., 2014). Recent work examining topographic thresholds has suggested orthogonal regression, first used by Vandekerckhove et al. (1998) and Vanwalleghem et al. (2005a), is preferred as a method to find a line of best fit through the data (De Geeter et al., 2020, Majhi et al., 2021). The line is usually then translated through the lowest most data points (Torri and Poesen, 2014), with prior removal of outliers recommended (Majhi et al., 2021).

We use the above recommendations, excluding outliers that exceed a Cook's distance of $\frac{4}{n}$ (where *n* is the number of observations), then use orthogonal regression to fit a line through the data and translate that line through the lower-most points. In this case we define the lower-most points to be the lowest 10^{th} percentile of data. Orthogonal regression is implemented in Scipy library for Python which uses the steps outlined in (Boggs and Rogers, 1990).

5.2.5 Forested versus cleared areas

Previous gully studies have found that clearing of tree cover can lead to increased gullying (e.g. Prosser and Soufi, 1998, Parkner et al., 2006, Parkner et al., 2007), and values of the coefficient *k* from threshold analysis have been found to follow a general decreasing trend moving from natural forested to cleared agricultural landscapes (Torri and Poesen, 2014). We wanted to test whether we observe the same effect in our

sites and used several areas from the Fitzroy River dataset (Figure 5.7). These areas were used because estimated annual average tree cover for the past ~30 years varied considerably between the areas, and they were on the same lithology within a close distance (~7 km) to one another. This arrangement provided a reasonable control on relevant non-topographic variables such as rainfall variability. Threshold plots for forested and cleared sites were generated separately and results were compared using analysis of covariance (McDonald, 2009) to determine if there was a statistical difference between slope and intercept values.

5.2.6 DEM subsets

Estimating correct drainage areas for gullies requires that the DEM extends up to the drainage divide for a given gully. Ensuring this condition is met for all gullies in a DEM is an important pre-processing step for threshold analysis. Many parts of our DEMs required trimming to manage this. In the Burnett-Mary region we were only able to use three subsets of ~15 km^2 each that met this requirement.

We also only wanted to use areas that were sufficiently large to give a robust estimate of gully topographic thresholds. Maugnard et al. (2014) found that a sample of ≥40 gully heads provided a good estimate. For our sites this typically required using subsets no smaller than 8 km^2.

5.3 Results and discussion

5.3.1 Weany Creek comparison results

A comparison against a hand-digitised set of 484 gullies across Weany Creek (used in the analysis presented in Chapter 3) indicated that the automated approach produces statistically very similar results (Figure 5.4). We found no significant difference between the slope of the two regressions at $p < 0.05$ and no significant difference between the intercepts at $p < 0.1$.

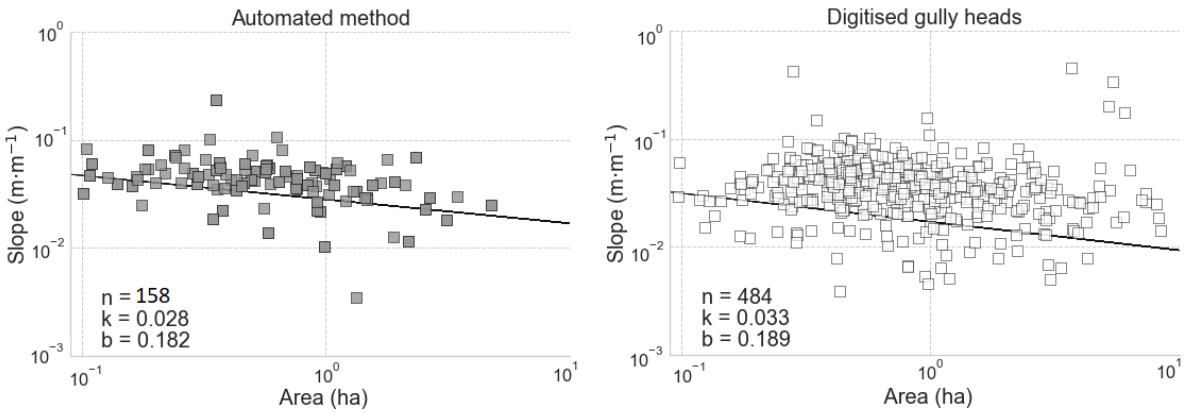

Figure 5.4: Comparison of topographic threshold analysis results between a semi-automated method using a set of digitised gully heads (Chapter 3) and the fully automated approach over the same area.

These two datasets however did not cover the exact same area. In Chapter 3 (Walker et al., 2021) digitised gullies in Weany Creek and the immediate surrounding area (~40km^2) whereas in the current study we assess only the Weany Creek catchment area (~14km^2). Second, to reduce manual processing Walker et al. (2021) only digitised gullies with drainage areas ≥ 0.25 ha whereas in the current study the minimum required drainage area is set to 0.1 ha. Despite these differences, estimated gully densities were similar, with the estimate from the automated method being 11.45 gullies km^{-2} while the density estimate from the digitised set was 12.1 gullies km^{-2}. However, this difference is also distorted by the difference in threshold drainage areas used which implies the fully automated method underestimates gully density compared to a semi-automated approach using hand-digitised gully heads.

5.3.2 Mary results

From upstream to downstream the three subsets of data used in the Mary Region show a progressive decrease of tree cover and associated decrease in *k* values (Figure 5.5). The highest value (*k* = 0.054) was found in the subset with average tree cover of ~73% from 1988 to 2017, an average elevation of ~90 m (ASL) and an average slope of ~20% (Figure 5.5c and Table 5.1). Downstream toward the river mouth tree cover decreases to 52% in subset b) and to 42% for subset a). This decrease is associated with a decrease in *k* values from *k* = 0.038 in subset *b*) to *k* = 0.031 in subset a). The average *k* value across all Mary subsets was *k* = 0.041 compared to the average across all sites of *k* = 0.033.

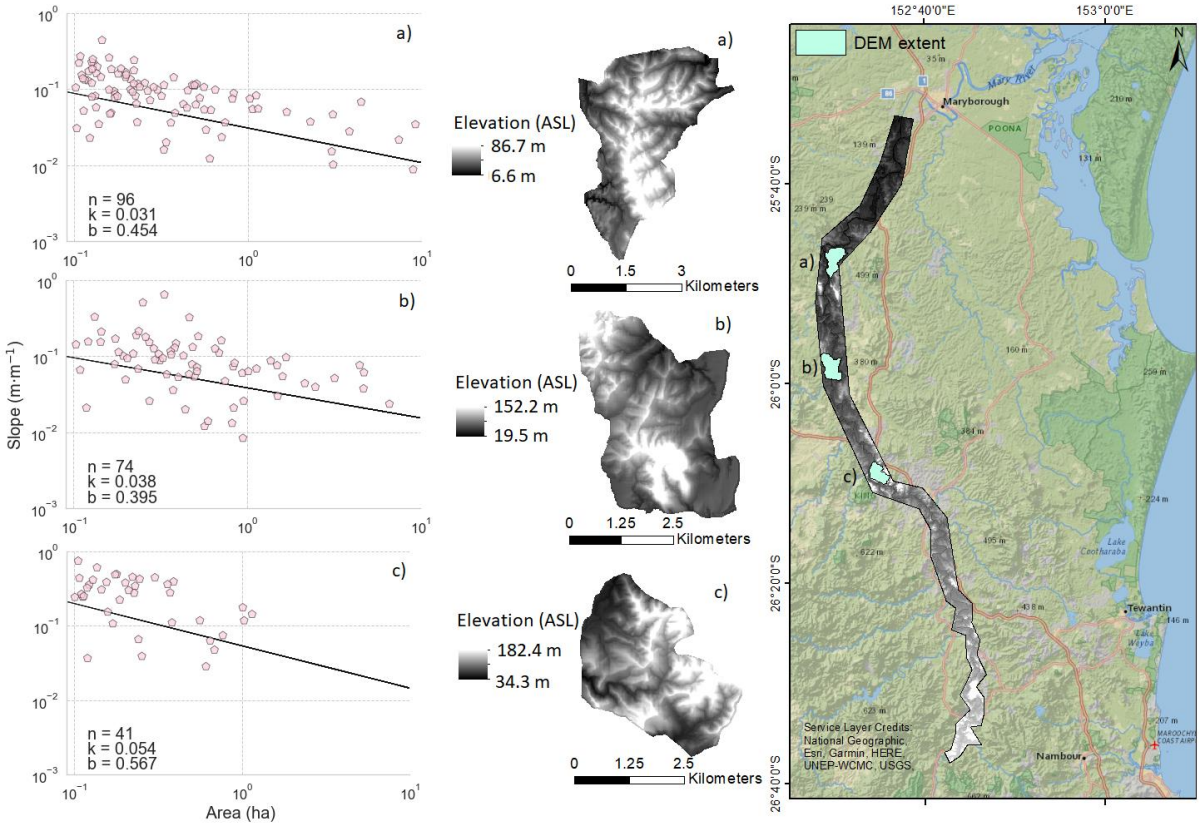

Figure 5.5: Results from topographic threshold analysis at the Mary River sites together with their geographic context. Only three subsets could be used based on requirements outlined in the methods.

The average rainy day normal across all Mary River sites was RDN = 11.93, which was lower than the average across all sites (RDN = 13.36). The slope of the threshold lines for all three DEM subsets in the Mary were relatively high, with an average of *b* = 0.47 compared to an average slope across all studied catchments of *b* = 0.36. Gully densities for all three sites followed the same trend as for *k* values, decreasing from upstream to downstream.

Table 5.1: Topographic threshold analysis results and study area characteristics for the Mary River sites.

	Mary River (a)	Mary River (b)	Mary River (c)
Elevation mean (m)	41.03 ± 14.34	55.93 ± 21.39	90.24 ± 29.41
Slope mean (%)	11.81 ± 9.85	11.70 ± 11.26	20.87 ± 15.29
Tree cover mean (%)	42.3 ± 37.5	51.9 ± 35.1	73.4 ± 35.3
Area (km^2)	12.67	13.25	9.04
Gully density ($n\ km^{-2}$)	7.58	5.58	4.53
Coefficient *k*	0.031	0.038	0.054
Exponent *b*	0.454	0.395	0.567
Rainy day normal	11.9	11.82	12.07
Rain seasonality	Wet summer and low winter rainfall	Wet summer and low winter rainfall	Wet summer and low winter rainfall
Rain ann. mean (mm)	929	909	1006
Lithology	Coal measures (Jurassic)	Coal measures (Jurassic)	Mixed sedimentary (Permian)
Köppen Geiger classification	Cfa	Cfa	Cfa

5.3.3 Burdekin results

In the Burdekin region the two catchments with very similar properties, Main Creek and Weany Creek, showed no statistical difference in either *k* or *b* (Figure 5.6a and b). Main Creek has, however, had a substantially higher tree cover over the past ~30 years and a history of lower grazing pressure (Wilkinson et al., 2018). Rainy day normal for all Burdekin Basin sites was higher than the average across all sites (RDN = 13.36). This was especially true for Weany Creek (RDN = 17.15).

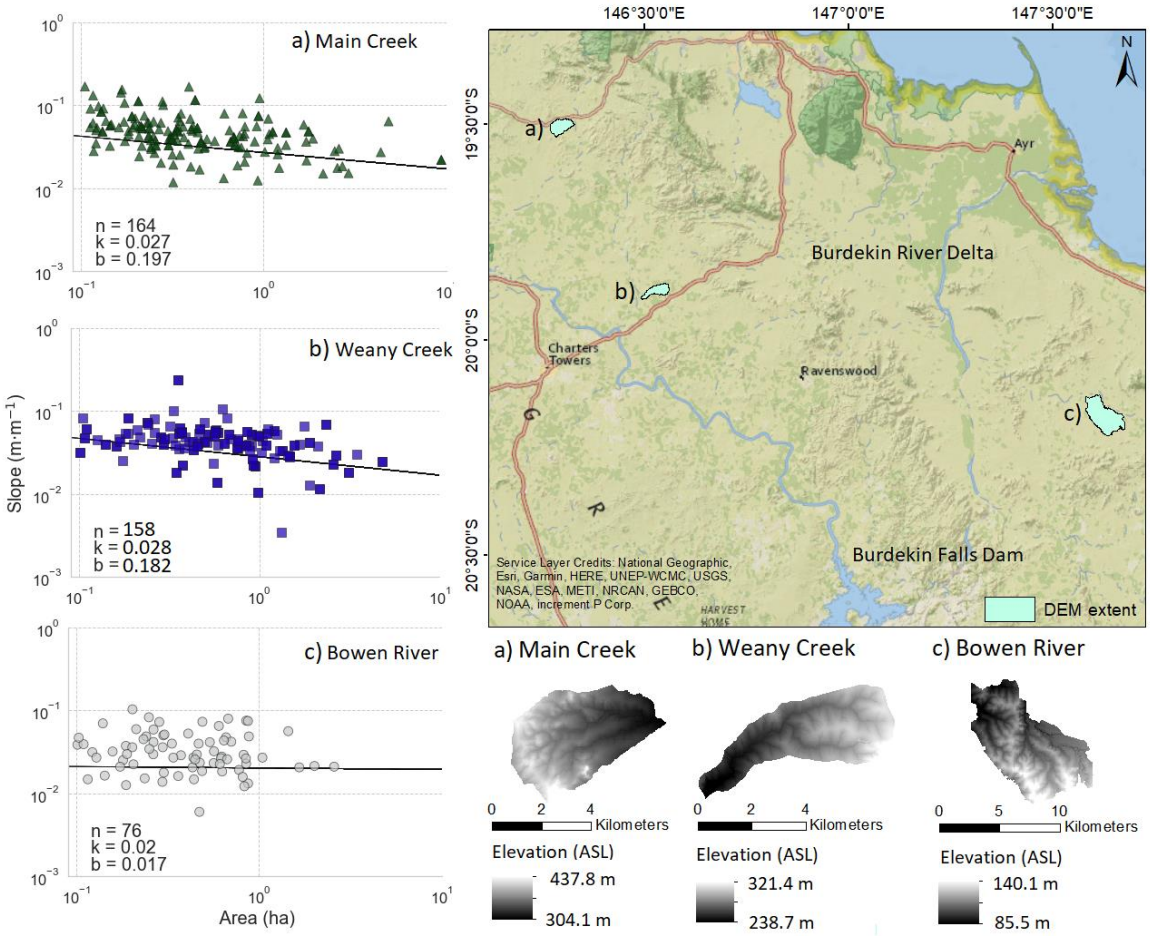

Figure 5.6: Result from topographic threshold analysis for sites located in the Burdekin Basin. Main Creek (a) and Weany Creek (b) are both located upstream of the Burdekin Falls Dam, while the Bowen River site is downstream closer to the river delta.

At the Bowen River site, the slope of the threshold line was very flat, indicating processes other than overland flow incision are likely driving gully erosion in that area. This low threshold slope was also associated with a low *k* value (*k* = 0.02), but the area had a relatively low gully density of only 1.32 gullies km^{-2} compared to its nearest neighbours Weany Creek and Main Creek. The primary difference between the Bowen River site and the other two Burdekin sites was that it has a much lower elevation, hence is much closer to the Burdekin River Delta in terms of altitude. This part of the basin is also downstream of the Burdekin Falls Dam (Figure 5.6) while Weany Creek and Main Creek are both upstream of the dam.

Table 5.2: Topographic threshold analysis results and study area characteristics for the Burdekin Basin sites.

	Main Creek	Weany Creek	Bowen River
Elevation mean (m)	346.09 ± 28.20	279.97 ± 23.24	111.48 ± 10.03
Slope mean (%)	6.62 ± 7.75	5.54 ± 7.10	4.25 ± 6.01
Tree cover mean (%)	92.2 ± 6.1	43.3 ± 17.8	38.0 ± 26.1
Area (km^2)	17.64	14.32	57.55
Gully density ($n\ km^{-2}$)	8.96	11.45	1.32
Coefficient *k*	0.027	0.028	0.02
Exponent *b*	0.197	0.182	0.017
Rainy day normal	14.71	17.15	14.61
Rain seasonality	Marked wet summer and dry winter	Marked wet summer and dry winter	Marked wet summer and dry winter
Rain ann. mean (mm)	745	650	656
Lithology	Felsic igneous (Ordovician)	Felsic igneous (Ordovician)	Felsic igneous (Carboniferous)
Köppen Geiger classification	Bsh	Bsh	Aw

5.3.4 Fitzroy results

The Fitzroy data was used to assess the topographic thresholds between forested and cleared areas. Forested areas were estimated to have $k = 0.042$ while cleared areas had an estimated $k = 0.024$ and the difference between these was found to be statistically significant at $p < 0.05$. Rainy day normal was lower than average for the Fitzroy sites with both forested and cleared areas having RDN ≈ 12.8.

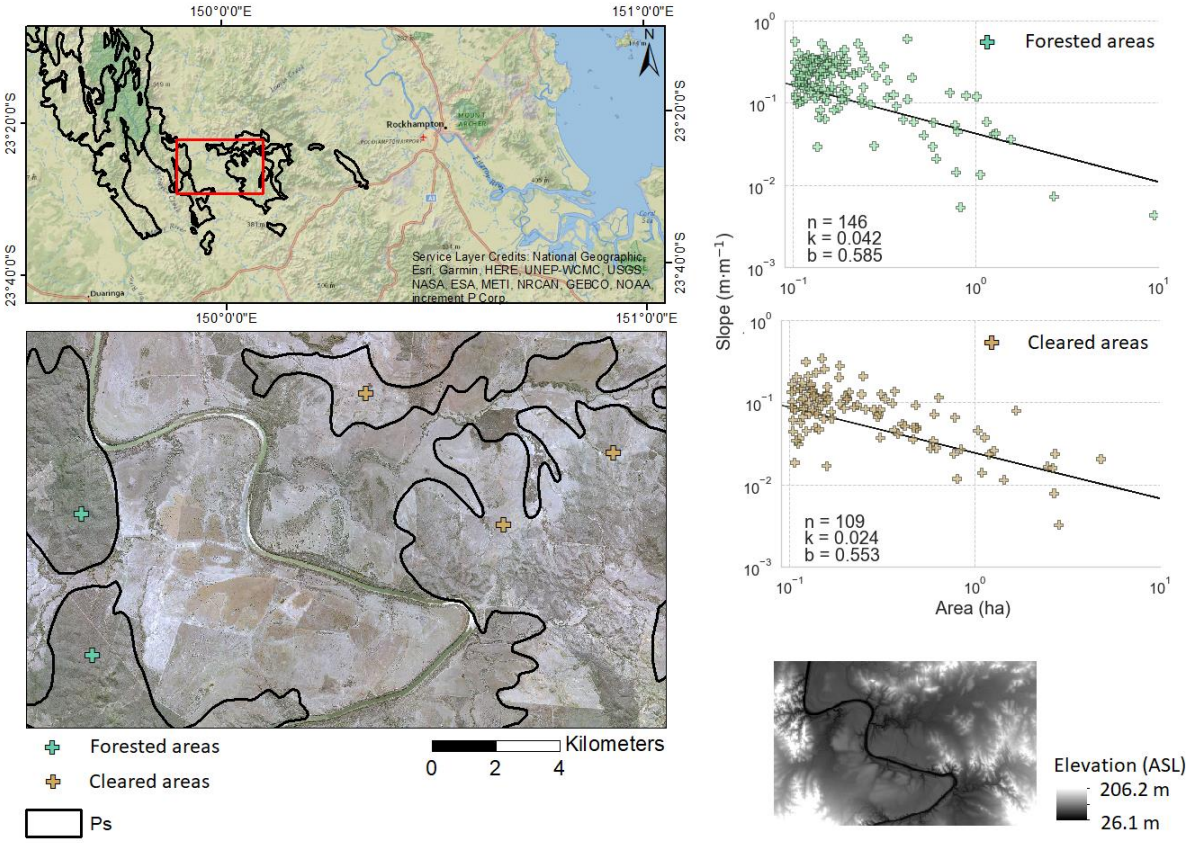

Figure 5.7: Results of comparing parameter estimates from topographic threshold analysis at Fitzroy River sites. All sites are located on Permian age mixed sedimentary lithology and are within close distance of one another. Cleared areas are marked by brown crosses and forested areas are green crosses.

Although *k* values were lower in the cleared areas, gully head densities were higher (7.67 km^{-2} for forested versus 6.0 km^{-2} for cleared). The exponent *b* showed no statistical difference between the two separate groups, but in both cases was higher than the average across all sites (*b* = 0.36).

Table 5.3: Topographic threshold analysis results and study area characteristics for the Fitzroy River sites.

	Forested	Cleared
Elevation mean (m)	90.48 ± 24.15	69.71 ± 12.23
Slope mean (%)	15.26 ± 11.87	6.71 ± 6.01
Tree cover mean (%)	90.8 ± 16.5	24.1 ± 14.7
Area (km^2)	19.02	18.17
Gully density (n km^{-2})	7.67	6.0
Coefficient *k*	0.042	0.024
Exponent *b*	0.585	0.553
Rainy day normal	12.76	12.86
Rain seasonality	Wet summer and low winter rainfall	Wet summer and low winter rainfall
Rain ann. mean (mm)	617	625
Lithology (geologic age)	Mixed sedimentary (Permian)	Mixed sedimentary (Permian)
Köppen Geiger classification	Bsh	Bsh

5.3.5 Herbert results

Despite having very similar settings to Weany Creek and Main Creek, the Herbert River site had a higher coefficient of k = 0.038. While the lithological setting was the same, the Herbert River site had higher average tree cover and lower RDN than Weany Creek and Main Creek.

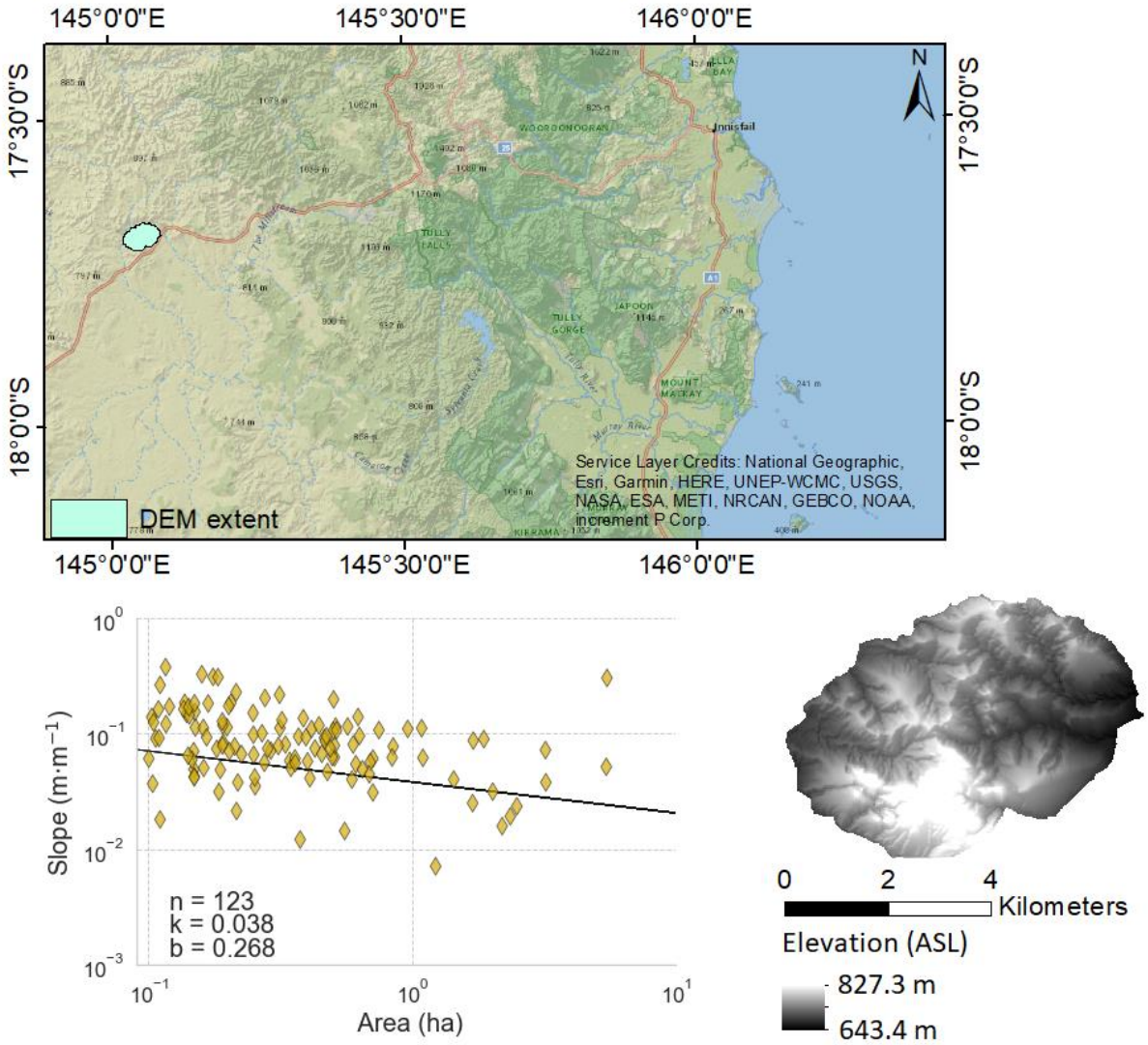

Figure 5.8: Results from topographic threshold analysis near the Herbert River in the Wet Tropics together with its geographic context.

Gully head density at the Herbert River site (5.16 km^{-2}) was approximately equal to the average across all sites (5.33 km^{-2}). The estimated value for the exponent b = 0.268 was similar here to the estimate for Main Creek (b = 0.197) and Weany Creek (b = 0.182).

Table 5.4: Topographic threshold analysis results and study area characteristics for the Herbert River site.

	Herbert River
Elevation mean (m)	691.09 ± 45.74
Slope mean (%)	12.45 ± 13.26
Tree cover mean (%)	96 ± 9.3
Area (km^2)	23.84
Gully density ($n\ km^{-2}$)	5.16
Coefficient *k*	0.038
Exponent *b*	0.268
Rainy day normal	12.43
Rain seasonality	Marked wet summer and dry winter
Rain ann. mean (mm)	785
Lithology	Felsic igneous (Carboniferous)
Köppen Geiger classification	Bsh

5.3.6 General and qualitative observations

Our analysis estimated a total of 987 gully heads spread over the combined study area of 185 km^2, an average gully head density of 5.33 km^{-2}. Weany Creek and Main Creek in the Burdekin Basin had the highest densities with 11.45 km^{-2} and 8.96 km^{-2}, respectively. This result agreed with past field studies of gully erosion across catchments of the GBR, finding that these cleared and heavily grazed landscapes of the Burdekin Basin are especially vulnerable to gully erosion (e.g. Bartley et al., 2010a, Wilkinson et al., 2018, Koci et al., 2021). These gully head density estimates across our sites are also similar to those found by Vanmaercke et al. (2020) across the Horn of Africa, a region with a climate described by Köppen-Geiger classifications as typically hot arid steppe (Peel et al., 2007), similar to our sites. Several previous studies have documented a relationship between rainfall variability and gully incision. For example, Eyles (1977) found that in parts of south-eastern Australia, most gullies were initiated during storms occurring after extended dry periods. Oostwoud Wijdenes and Bryan (2001) also found that in a flat semi-arid catchment in Kenya, a simple model accounting for the number of dry days in between storms of a given magnitude

was sufficient to explain 56% of variation in gully headcut retreat. In their review of global gully headcut retreat rates Vanmaercke et al. (2016) found a statistically significant relationship between rainy day normal (RDN), a measure of rainfall variability, and headcut retreat rate. We compared RDN to topographic thresholds across our sites and found that locations with lower *k* values (more susceptible to gullying) also had higher RDN (more variable rainfall), while sites with lower *k* values typically had lower RDN values. However, while the geographic extent of our study sites was relatively large, the total number of sites was only six which is not sufficient to draw any statistical conclusions from this observation.

When pre-processing the LiDAR data there were many sections of the DEMs that needed to be removed because full gully head drainage areas could not be computed (when the DEM did not extend to the drainage divide upslope of gully heads). Most models of gully erosion including threshold analysis (e.g. Patton and Schumm, 1975), statistical models of gully presence (e.g. Conoscenti and Rotigliano, 2020) and process based models (e.g. Rengers and Tucker, 2014) require estimates of the contributing area above gully heads. Without LiDAR coverage up to the drainage divide above gully heads it is not possible to get an accurate assessment. Pre-processing of the DEM to avoid this issue is essential for any future studies looking to use high-resolution DEMs to study gully erosion. Likewise, projects looking to capture airborne LiDAR for gully assessments should consider this requirement when planning flight paths.

5.3.7 Gully topographic thresholds and tree cover

When we compared cleared and forested areas in the Fitzroy Basin, we found a statistically significant difference between the *k* values (Figure 5.7). For the cleared areas we found $k = 0.24$ while in adjacent forested plots we found $k = 0.42$. There was no statistically significant difference between the slope of the two threshold lines. These comparison sites had the same underlying lithology and were sufficiently close (~7 km apart) that climate would not vary (confirmed by very similar rainy day normal values, Table 5.3). Our fully automated approach also removes bias otherwise introduced by subjective decisions regarding computation of slope and drainage area used in the model.

A difference in *k* values between forested and cleared sites was expected, as many previous studies have found a relationship between land clearing and gullying.

For example, Parkner et al. (2006) found that the topographic threshold for gullies under natural forest in New Zealand plotted far above that for nearby cleared pastures. Another New Zealand-based study by Gomez et al. (2003) documented severe gullying following a short period of forest clearing. In the Loess Plateau of China Chen and Cai (2006) found that in heavily gullied areas changes in forest cover were among the most important factors in controlling gully sediment yield. Deforestation has also been observed to directly lead to gully formation in other parts of Australia. For example, in south-eastern Australia Prosser and Soufi (1998) observed incision of gullies following a rainstorm shortly after their study catchment was cleared. Meanwhile Shellberg et al. (2013) found alluvial gullies along the banks of creeks and rivers in Queensland also expanded under agricultural clearing, and large-scale mapping by Gilad et al. (2012) found a strong relationship between gully presence and low tree cover.

The findings here are also consistent with the evidence from Chapter 2, finding that the potential area remaining for incised channels to extend into was larger for forested areas than for cleared areas in adjacent plots. These findings provide some useful insights into current challenges in global gully erosion management. For example, Vanmaercke et al. (2021) note that new tools are required to quantity the impacts of climate and land cover changes on gully erosion. Such tools would likely need to consider forest cover as an important factor.

Similarly, Poesen et al. (2003) found that, although few large-scale studies on gully processes had been conducted at that time, one important factor identified was the propensity for gullies to increase hydrological connectivity across the landscape. This property is an important driver of the cumulative degradation and negative impact on downstream water quality by gullies (Poesen et al., 2003). This also suggests that early intervention is the best way to mitigate against gully erosion as it may help stem the progression of hydrological connectivity, hence decrease the chances of gully networks establishing in the first place. Preservation of forest cover potentially offers an effective measure to achieve this and would reduce the need for costly post-gully formation interventions.

Over the past century there has been extensive clearing of forests across Queensland, and Australia generally (Bradshaw, 2012, Evans, 2016). Despite this, forest clearing is still ongoing in the absence of effective government policies to

mitigate against associated impacts on erosion and sediment deliver to streams and rivers (Shellberg, 2020).

5.3.8 Insights from topographic thresholds across the GBR catchments

In their global review of threshold analyses, Torri and Poesen (2014) found a clear trend in values for the coefficient *k* moving from cleared to forested landscapes; however, they found no clear trend in the exponent *b*. They propose that given no trend is evident a fixed value may be appropriate and adopt a value of $b = 0.38$ based on previous work (Nachtergaele et al., 2001, Knapen and Poesen, 2010). In our testing we also found a range of *b* values and when taking the average across all sites we found $b = 0.36$. This agrees rather well with the value proposed by (Torri and Poesen, 2014), and indicates that if future studies choose to fix the value for *b*, then the value of $b = 0.38$ proposed by Torri and Poesen (2014) seems appropriate. It was proposed by Torri and Poesen (2014) that fixing the value of *b* may help to simplify the threshold analysis model and in doing so allow further investigations into non-topographic factors controlling values for the coefficient *k*. The same authors suggest this is a way forward to a more comprehensive physically based model of the controls on gully head positions across landscapes.

In threshold analysis estimates of the exponent *b* are influenced by the hydraulics of overland flow (Montgomery and Dietrich, 1994, Hayas et al., 2017), and low values (≤0.2) are considered an indication of subsurface processes driving gully erosion (Morgan and Mngomezulu, 2003, Muñoz-Robles et al., 2010, Dong et al., 2013). In our study the only location with a *b* exponent substantially lower than $b = 0.2$ was the Bowen River site. This site was located downstream of the Burdekin Falls Dam and closer to the river delta than either of the other two Burdekin sites. There are not enough individual sites to draw any statistical conclusions, but it appears proximity to the river delta may be related to the flat slope of the threshold line (indicating dominance of subsurface processes) compared to Weany Creek or Main Creek with steeper (albeit still relatively flat) threshold slopes.

5.3.9 Strengths and limitations of fully automated threshold analysis

Allen et al. (2017) found that despite broad acceptance of gully erosion being a major issue, models to predict gullying at continental scales remain challenging. Our

automated method for threshold analysis offers a potential new tool to model gully occurrence in the landscape at large scales. Testing against a hand-digitised set of gullies in Weany Creek indicated that the automated method produced very similar results, with only a small variation in estimates of k and b (Figure 5.4). However, the hand-digitised set was not collected following the same procedural specifications used by automated approach and so comparison of individual points was not possible. We also found no statistical difference between *k* and *b* estimates from Weany Creek and Main Creek. These two locations have the same lithological and climatic setting, and Main Creek has lower stocking rates in recent history (Wilkinson et al., 2018) with substantially higher average tree cover (Table 5.2). This indicates that while the algorithm produced similar results to a digitised comparison set, it does not always clearly detect an effect from increased tree cover as observed in other locations. However, field assessments have determined gully density to be lower in Main Creek than Weany Creek and this is reflected in result showing gully head densities of 8.96 km^{-2} and 11.45 km^{-2} in Main Creek and Weany Creek, respectively.

The fully automated approach relies on accurate detection of gully heads using the process outlined in Section 5.2.2 together with the algorithm described in Chapter 4 (to find slope above the gully head). Results were tested in Weany Creek, where we also had a large set of digitised gully heads. In this landscape the automated algorithm produced similar results, but this is also a relatively homogenous granitic landscape, and the results of the gully head detection method are better in igneous landscapes than in sedimentary landscapes (Chapter 4). This may be impacting the results from the Fitzroy River and Mary River sites, both on sedimentary lithologies. Weany Creek is also relatively cleared, with average tree cover ~43%, and LiDAR-derived DEMs can have varying accuracy depending on whether they are under a tree canopy or not (James et al., 2007).

While results for our automated method are promising, there a several potential sources of error to consider. Factors determining vulnerability to gully erosion can include geologic setting, soil erodibility, rainfall erosivity and conditions otherwise preventing the establishment of vegetation (Castillo and Gómez, 2016). Topographic threshold analysis does not consider the role of non-topographic variables and in cases where these play a larger role on gully channel incision, results are expected to be less reliable. Secondly, we rely on an automated method to estimate the position

of initial gully heads. While we use an approach adapted from a rigorously tested channel mapping method (Pelletier, 2013), it remains the case that accurately mapping channel heads can generally only be achieved with extensive field investigation. For example, a common definition of a channel head is the most upslope location of concentrated flow within defined banks (e.g. Montgomery and Dietrich, 1989). However, Clubb et al. (2014) found that when applying this definition in the field, even when using evidence such as alignment of pine needles, sediment sorting and bedrock polishing it was still not always clear where channels began. This uncertainty in channel mapping extends to gully heads and is exacerbated by using automated DEM-based methods.

Another important consideration is the role of artificial agricultural structures such as dams, roads, and flow diversion banks. Poesen et al. (2003) found that infrastructure development can act to increase runoff concentration and hence exacerbate gully development. Nyssen et al. (2002) found that the impact of roads on gully formation and development can often be easily identified in the field. The mechanisms by which roads can alter hydrological regimes to favour gully formation include the concentration of surface flow as well as increased catchment size (Nyssen et al., 2002). It was also found by Yibeltal et al. (2019a) that the density of gully heads may be expected to be higher in cultivated areas. We took no measures to identify and account for such agricultural structures in our analyses. Results may be affected in locations where these are prevalent.

Finally, in locations where channels are actively extending there may be a coincident active change in drainage density, and this will impact scatter of the data in a slope-area plot (Montgomery and Dietrich, 1989). The original work by Patton and Schumm (1975) also states that the analysis reported was limited to the experimental domain of Piceance Creek and Yellow Creek in north-western Colorado and that results from less homogeneous environments may not follow the same patterns.

5.4 Conclusion

In this chapter a method for fully automated gully topographic threshold analysis was presented. The method combines previous algorithms from Chapter 3 and Chapter 4 together with a method for automatically estimating the position of gully heads across a landscape. The primary goal of this work was to offer a method capable of estimating topographic thresholds of gullies across large areas where there

is a suitable high-resolution DEM available. We tested this algorithm across a range of environments spanning ~1 200 km of catchments adjacent to the Great Barrier Reef, Australia. The sites were in four priority erosion management regions and the total area of high-resolution DEM coverage for these sites was 185 km^2.

Results of a comparison with a digitised set of gully heads (Chapter 3) found that the automated method can produce results comparable to those found using a manual method, indicating that the automated approach can provide reliable threshold estimates, at least under the scenario tested. When we used the algorithm to compare cleared and forested areas, we found that our estimates for the coefficient *k* were larger in forested than for cleared areas and that this difference was statistically significant. This finding was in line with expectations based on findings from previous global studies showing that a shift from natural forest to cleared landscapes increases the susceptibility of a landscape to gully erosion.

After estimating the slope of the threshold line for each location, we found that the average of these values (*b* = 0.36) was close to previous recommendations of a 'fixed' value of the exponent *b* = 0.38. Fixing the exponent *b* may help to simplify the model and shed light on controls of the coefficient *k*, and our findings support a fixed value of *b* = 0.38.

Despite these promising results, there are limitations to automating the process. Topographic threshold analysis does not involve assessment of non-topographic drivers of gully erosion, and in cases where these are more important it is expected that the results will be less reliable. We tested the automated method against previously obtained results for a low-gradient semi-arid environment but in cases where the environmental conditions deviate from this, and are further from the experimental domain, results may be less reliable.

When undertaking pre-processing of the LiDAR data there were many sections of the DEMs that needed to be removed because full gully head drainage areas could not be computed (when the DEM did not extend to the drainage divide upslope of gully heads). Future studies looking to collect airborne LiDAR for gully modelling studies should consider this need to accurately compute drainage areas for gully erosion assessments.

In conclusion, we find that a fully automated approach to estimating gully topographic thresholds from high-resolution DEMs has shown promising results and

may be suitable as a first assessment of gully topographic thresholds across large areas. However, it is still recommended that for best results the method should be combined with more detailed information of specific sites, such as information collected during a field campaign.

Chapter 6: Discussion and conclusions

6.1 Overview

Since European settlement ~200 years ago coral and seagrass ecosystems of the Great Barrier Reef (GBR) have experienced decreasing water quality due primarily to large-scale agricultural modification of the landscape (Belperio, 1983, Haynes and Michalek-Wagner, 2000, McCulloch et al., 2003). Gully erosion in catchments of the GBR is believed to be an important source of terrigenous fine sediment impacting water quality in adjacent marine ecosystems (e.g. Wilkinson et al., 2013, Bartley et al., 2014a, Wilkinson et al., 2015a, Wilkinson et al., 2018). Prioritising gully erosion across the >400 000 km^2 area making up the catchments of the GBR requires a range of approaches and tools to pinpoint potential gully erosion management sites. High-resolution topographic data offers one such tool and the recent proliferation of this data, including recently available datasets across the GBR, offers a new opportunity to use this data for mapping gullies and prioritising erosion mitigation sites. Many recent studies have looked at gully mapping and modelling using high-resolution data but there has been a lack of consistency in applied methods, partly due to the generally sparce availability of suitable data. Accordingly, the primary goal of this thesis was to examine the potential for high-resolution topography to contribute to gully erosion spatial prioritisation across catchments of the GBR. A secondary goal was to develop a set of publicly available computer programs to bring a higher level of reliability and reproducibility to DEM-based topographic studies of gullies using high-resolution topography. Below I discuss the key findings of the thesis with respect to the four initial objectives outlined in the introduction, and how the various outputs from the work contributed to these findings.

Objective 1: *Investigate the potential to map and identify gullies in high-resolution topographic data and use this information to assess relative erosion risk across landscapes.*

Mapping the presence and extent of gullies across a landscape is a necessary first step toward developing effective erosion management strategies. Previous studies have recognised the potential for high-resolution digital elevation models

(DEMs) to enable automated mapping of gullies (e.g. Eustace et al., 2009, Evans and Lindsay, 2010, Höfle et al., 2013, Castillo et al., 2014, Korzeniowska et al., 2018), and have proposed methods that typically involve geometric characterisation of the target landform element (gullies). Similarly, the potential for DEMs to map locations susceptible to gully erosion has also been recognised as a useful tool for assisting erosion management decisions (e.g. Daba et al., 2003, Kheir et al., 2007, Conforti et al., 2011, Daggupati et al., 2013, Conoscenti et al., 2014, Shit et al., 2015, Conoscenti and Rotigliano, 2020). The research in Chapter 2 was the first time a study had attempted to combine mapping of gullies and estimating areas at risk of gullying into a single algorithm capable of operating across arbitrarily large areas.

The algorithm was used to develop an index of potential for future channel incision, called the Potential Channel Development Index. Results from testing the method across various environments indicated that index values are plausible, and that the algorithm has potential to identify candidate areas for erosion mitigation. However, the algorithm did not incorporate non-topographic factors like soil, geology, and rainfall, which are important to gully erosion (Valentin et al., 2005). Sensitivity analysis also indicated that, while the algorithm was designed to work across large areas, results are more reliable for landscapes with lower topographic variation. For these reasons, results are best suited for analysis of relative gully erosion risk within catchments and not between catchments.

Objective 2: *Establish reliable and reproducible methods to estimate important properties of gullies, including contributing drainage area and gradient of the surrounding hillslope, using high-resolution topographic data.*

One of the most widely used models for examining gully presence in the landscape is gully topographic threshold analysis originally proposed by Patton and Schumm (1975). This method plots contributing drainage area of gully heads against the slope of the surrounding soil surface to estimate the topographic threshold of gully formation for a given environment (Majhi et al., 2021). A study by Torri and Poesen (2014) sought to move towards more reliable and physically based predictive models of gully topographic thresholds by reviewing reported threshold results from studies across a range of global locations. However, differences in methodologies employed

by the various studies made it difficult for clear comparisons of results. The objective of Chapter 3 was to evaluate alternative approaches to using high-resolution DEMs so that gully topographic models can be more readily applied to any area with suitably high-resolution data. This involved the development of two stand-alone computer programs. The first was developed to determine whether there were indications of divergent flow upstream of gully heads by examining changes in upslope drainage area. The purpose of this program was to help determine why drainage area estimates vary more for some gullies than others and was found to provide a useful indicator. The second program was designed to locate points on gully floors where flow convergence occurred. This point was considered the optimal location from which to compute gully head drainage area. Results from this work found that parameter estimates for topographic thresholds of gully formation were affected most by the choice of flow routing method and DEM hydrologic-enforcement. Our goal was to support future efforts to apply gully topographic threshold analysis more readily across large areas. We found that finer resolution DEMs (≤2 m) together with multiple-direction flow routing algorithms provided the most realistic threshold analysis results.

Chapter 4 also focused on development of reliable and reproducible methods for improving gully topographic threshold analysis and other topographic models of gullies. This chapter presented an algorithm for DEM-based geometric characterisation of gully heads, automating the procedure for extracting the gradient of the hillslope adjacent to gully heads for input into threshold analysis models.

Results revealed more robust estimates of slope adjacent to gully heads are found by following the most concentrated drainage line upslope of the gully head and estimating gradient along that line. Slope estimates taken from along either side of gullies were more variable. However, taking the mean of slope along the sides and above the head of a gully reduced the scatter topographic threshold analysis plots. Results also show a statistically significant relationship between hillslope gradient and gully headcut depth, providing potentially important information for gully remediation priorities.

Objective 3: *Assess the potential to fully automate established gully topographic threshold models that have historically required fieldwork to collect the required inputs.*

Given the widespread use of gully topographic threshold analysis (Majhi et al., 2021) and the difficulties encountered when attempting to compare results between regions due to variation in applied methodologies, Chapter 5 outlined the development of an algorithm to fully automate gully topographic threshold analysis using high-resolution DEMs. This algorithm combined the computer programs presented in Chapter 3 and 4 with a method to automatically estimate the location of a representative set of gully heads. The broader goal of this was to offer an open-source method to conduct fully automated gully topographic threshold analysis and remove bias associated with subjective decisions around computation of gully head drainage area and slope of the soil surface adjacent to gullies. The method was applied to a total area of 185 km^2 of gullied landscapes located in priority erosion management regions of the GBR catchments. Tested against topographic threshold estimates derived from a large (484) gully head sample used in Chapter 3, the automated method estimated very similar parameter values. However, some notable limitations were that it was not capable of identifying all gullies that can be made out easily by eye and was potentially affected by agricultural structures such as dams, roads, and flow diversion banks. Nevertheless, it offers a useful option to provide large-scale topographic threshold assessments that may help set priorities for more detailed plot-scale assessments. It would be used as a rapid initial assessment of the topographic threshold of gully formation for a given catchment and would indicate whether more detailed investigation of gully erosion mitigation is required.

Objective 4: *Develop a set of computer programs that work in unison to provide potential prioritisation of gully erosion remediation from regional scales down to the sub-catchment scale.*

Through Chapters 2, 3, 4 and 5 a series of open-source computer programs are developed and structured in a way to work together to prioritise gully erosion across catchments of the GBR and other global locations. The fully automated method for gully topographic threshold analysis is suited to assessment of gully erosion across large scales and showed potential, when comparing multiple catchments to one another, to identify those with high susceptibility to gully erosion. The algorithm from

Chapter 2, on the other hand, is suited to assessing relative risk of erosion between gullies in the same landscape. Together, these two open-source computer programs offer an integrated workflow to first assess catchments for their susceptibility to gully erosion at large scales and subsequently to assess locations within those catchments at small scales.

Each of the two above mentioned algorithms were used to assess the apparent impact of tree clearing on gully formation. In both cases, results from controlled conditions indicated that a transition from natural forests to cleared agricultural landscapes leads to increased susceptibility to gully erosion. This finding is consistent with many studies globally. For example, several studies of gully erosion in New Zealand have documented correlations between decreased tree cover and gully erosion (Gomez et al., 2003, Parkner et al., 2006, Parkner et al., 2007). Similarly, in Australia, tree clearing has been linked to gully formation (Prosser and Soufi, 1998), and locations with lower tree cover have generally higher levels of gullying (Gilad et al., 2012, Shellberg, 2020). Spatially predicting potential for future incision is important because early control can avoid further land degradation (Castillo and Gómez, 2016), and once a gully has started, they are generally difficult to stop (Selby, 1982). The evidence presented above points to the importance of maintaining tree cover in preventing gullies from forming, thereby offering a useful indication of areas to prioritise for prevention of gully formation, a cost-effective gully erosion management strategy. This also allows for pinpointing of relatively well-preserved areas that require protection. Such locations offer potential to make sediment savings at relatively lower cost by preserving the intact places that have so far avoided significant degradation.

6.2 Concluding remarks

This study examined the potential for high-resolution topography to improve our understanding of the topographic controls on gully formation across catchments of the Great Barrier Reef, Australia. This has involved the development of a set of open-source computer programs designed to enable researchers to rapidly assess susceptibility of landscapes to gully erosion where a suitable high-resolution DEM is available. A secondary benefit to the approaches detailed here are that they bring an enhanced degree of reliability and reproducibility to DEM-based methods of gully

topographic modelling, which should help with comparison of results between studies and regions.

Results from applying the methods developed indicate that an important component of gully erosion mitigation is to reduce land clearing and preserve natural tree cover. Under controlled assessments results indicate that a shift from natural forests to cleared agricultural landscapes exposes a landscape to gully erosion. This result was found when comparing broader areas to one another, and when comparing the future potential expansion of individual gullies between sites. Once formed gullies are generally difficult and expensive to remediate. Efforts to preserve current intact areas across the GBR catchments will likely help to reduce otherwise costly gully remediation works required following post-clearing gully incision events. Methods proposed in this thesis have aimed to identify such locations and are suitable for areas where high-resolution topographic data is available.

References

AKSOY, H. & KAVVAS, M. L. 2005. A review of hillslope and watershed scale erosion and sediment transport models. *Catena,* 64**,** 247-271.

ALEXANDER, I., WILSON, P. A. & COOPER, M. J. 2001. New constraints on the origin of the Australian Great Barrier Reef: results from an international project of deep coring. *Geology,* 29**,** 483-486.

ALLEN, P. M., ARNOLD, J. G., AUGUSTE, L., WHITE, J. & DUNBAR, J. 2018. Application of a simple headcut advance model for gullies. *Earth Surface Processes and Landforms,* 43**,** 202-217.

AMATULLI, G., MCINERNEY, D., SETHI, T., STROBL, P. & DOMISCH, S. 2020. Geomorpho90m, empirical evaluation and accuracy assessment of global high-resolution geomorphometric layers. *Scientific Data,* 7**,** 162.

AUSTRALIAN BUREAU OF METEOROLOGY, B. O. M. 2016. *Climate classification Maps* [Online]. Commonwealth of Australia. Available: http://www.bom.gov.au/jsp/ncc/climate_averages/climate-classifications [Accessed 20/04/2109].

AUSTRALIAN BUREAU OF METEOROLOGY, B. O. M. 2020. *Climate Data Online* [Online]. Australian Bureau of Meteorology. Available: http://www.bom.gov.au/climate/ [Accessed 10/10/2020].

BARNES, R., LEHMAN, C. & MULLA, D. 2014. Priority-flood: An optimal depression-filling and watershed-labeling algorithm for digital elevation models. *Computers & Geosciences,* 62**,** 117-127.

BARNHART, K. R., HUTTON, E. W. H., TUCKER, G. E., GASPARINI, N. M., ISTANBULLUOGLU, E., HOBLEY, D. E. J., LYONS, N. J., MOUCHENE, M., NUDURUPATI, S. S., ADAMS, J. M. & BANDARAGODA, C. 2020. Short communication: Landlab v2.0: a software package for Earth surface dynamics. *Earth Surf. Dynam.,* 8**,** 379-397.

BARTLEY, R., BAINBRIDGE, Z. T., LEWIS, S. E., KROON, F. J., WILKINSON, S. N., BRODIE, J. E. & SILBURN, D. M. 2014a. Relating sediment impacts on coral reefs to watershed sources, processes and management: A review. *Science of The Total Environment,* 468**,** 1138-1153.

BARTLEY, R., CORFIELD, J. P., ABBOTT, B. N., HAWDON, A. A., WILKINSON, S. N. & NELSON, B. 2010a. Impacts of improved grazing land management on sediment yields, Part 1: Hillslope processes. *Journal of Hydrology,* 389**,** 237-248.

BARTLEY, R., CORFIELD, J. P., HAWDON, A. A., KINSEY-HENDERSON, A. E., ABBOTT, B. N., WILKINSON, S. N. & KEEN, R. J. 2014b. Can changes to pasture management reduce runoff and sediment loss to the Great Barrier Reef? The results of a 10-year study in the Burdekin catchment, Australia. *The Rangeland Journal,* 36**,** 67-84.

BARTLEY, R., CROKE, J., BAINBRIDGE, Z. T., AUSTIN, J. M. & KUHNERT, P. M. 2015. Combining contemporary and long-term erosion rates to target erosion hot-spots in the Great Barrier Reef, Australia. *Anthropocene,* 10**,** 1-12.

BARTLEY, R., POESEN, J., WILKINSON, S. & VANMAERCKE, M. 2020. A review of the magnitude and response times for sediment yield reductions following the rehabilitation of gullied landscapes. *Earth Surface Processes and Landforms,* 45**,** 3250-3279.

BARTLEY, R., THOMPSON, C., CROKE, J., PIETSCH, T., BAKER, B., HUGHES, K. & KINSEY-HENDERSON, A. 2018. Insights into the history and timing of post-European land use disturbance on sedimentation rates in catchments draining to the Great Barrier Reef. *Marine pollution bulletin,* 131**,** 530-546.

BARTLEY, R., WILKINSON, S. N., HAWDON, A. A., ABBOTT, B. N. & POST, D. A. 2010b. Impacts of improved grazing land management on sediment yields. Part 2: Catchment response. *Journal of Hydrology,* 389**,** 249-259.

BECK, H. E., ZIMMERMANN, N. E., MCVICAR, T. R., VERGOPOLAN, N., BERG, A. & WOOD, E. F. 2018. Present and future Köppen-Geiger climate classification maps at 1-km resolution. *Scientific Data,* 5**,** 180214.

BELPERIO, A. 1983. Terrigenous sedimentation in the central Great Barrier Reef lagoon: a model from the Burdekin region. *BMR Journal of Australian Geology and Geophysics,* 8**,** 179-190.
BENNETT, S. J. & WELLS, R. R. 2019. Gully erosion processes, disciplinary fragmentation, and technological innovation. *Earth Surface Processes and Landforms,* 44**,** 46-53.
BEVEN, K. J. & KIRKBY, M. J. 1979. A physically based, variable contributing area model of basin hydrology / Un modèle à base physique de zone d'appel variable de l'hydrologie du bassin versant. *Hydrological Sciences Bulletin,* 24**,** 43-69.
BOGGS, P. T. & ROGERS, J. E. 1990. Orthogonal distance regression. *Contemporary Mathematics,* 112**,** 183-194.
BRADSHAW, C. J. 2012. Little left to lose: deforestation and forest degradation in Australia since European colonization. *Journal of Plant Ecology,* 5**,** 109-120.
BRODIE, J., FABRICIUS, K., DE'ATH, G. & OKAJI, K. 2005. Are increased nutrient inputs responsible for more outbreaks of crown-of-thorns starfish? An appraisal of the evidence. *Marine pollution bulletin,* 51**,** 266-278.
BRODIE, J. & WATERHOUSE, J. 2012. A critical review of environmental management of the 'not so Great'Barrier Reef. *Estuarine, Coastal and Shelf Science,* 104**,** 1-22.
BROOKS, A. P., SHELLBERG, J. G., KNIGHT, J. & SPENCER, J. 2009. Alluvial gully erosion: an example from the Mitchell fluvial megafan, Queensland, Australia. *Earth Surface Processes and Landforms,* 34**,** 1951-1969.
BUCHANAN, B. P., FLEMING, M., SCHNEIDER, R. L., RICHARDS, B. K., ARCHIBALD, J., QIU, Z. & WALTER, M. T. 2014. Evaluating topographic wetness indices across central New York agricultural landscapes. *Hydrol. Earth Syst. Sci.,* 18**,** 3279-3299.
BURROUGH, P. A., MACMILLAN, R. A. & DEURSEN, W. 1992. Fuzzy classification methods for determining land suitability from soil profile observations and topography. *Journal of Soil Science,* 43**,** 193-210.
BURROUGH, P. A., MCDONNELL, R., MCDONNELL, R. A. & LLOYD, C. D. 2015. *Principles of geographical information systems*, Oxford university press.
CALLAGHAN, K. L. & WICKERT, A. D. 2019. Computing water flow through complex landscapes – Part 1: Incorporating depressions in flow routing using FlowFill. *Earth Surf. Dynam.,* 7**,** 737-753.
CASALÍ, J., GASTESI, R., ÁLVAREZ-MOZOS, J., DE SANTISTEBAN, L. M., LERSUNDI, J. D. V. D., GIMÉNEZ, R., LARRAÑAGA, A., GOÑI, M., AGIRRE, U., CAMPO, M. A., LÓPEZ, J. J. & DONÉZAR, M. 2008. Runoff, erosion, and water quality of agricultural watersheds in central Navarre (Spain). *Agricultural Water Management,* 95**,** 1111-1128.
CASALÍ, J., GIMÉNEZ, R. & CAMPO-BESCÓS, M. A. 2015. Gully geometry: what are we measuring? *SOIL,* 1**,** 509-513.
CASALí, J., LÓPEZ, J. J. & GIRÁLDEZ, J. V. 1999. Ephemeral gully erosion in southern Navarra (Spain). *CATENA,* 36**,** 65-84.
CASTILLO, C. & GÓMEZ, J. A. 2016. A century of gully erosion research: Urgency, complexity and study approaches. *Earth-Science Reviews,* 160**,** 300-319.
CASTILLO, C., MARÍN-MORENO, V. J., PÉREZ, R., MUÑOZ-SALINAS, R. & TAGUAS, E. V. 2018. Accurate automated assessment of gully cross-section geometry using the photogrammetric interface FreeXSapp. *Earth Surface Processes and Landforms,* 43**,** 1726-1736.
CASTILLO, C., MOMM, H. G., WELLS, R. R., BINGNER, R. L. & PÉREZ, R. 2021. A GIS focal approach for characterizing gully geometry. *Earth Surface Processes and Landforms,* 46**,** 1809-1827.
CASTILLO, C., TAGUAS, E. V., ZARCO-TEJADA, P., JAMES, M. R. & GÓMEZ, J. A. 2014. The normalized topographic method: an automated procedure for gully mapping using GIS. *Earth Surface Processes and Landforms,* 39**,** 2002-2015.
CHEN, H. & CAI, Q. 2006. Impact of hillslope vegetation restoration on gully erosion induced sediment yield. *Science in China Series D,* 49**,** 176-192.
CLUBB, F. J., MUDD, S. M., MILODOWSKI, D. T., HURST, M. D. & SLATER, L. J. 2014. Objective extraction of channel heads from high-resolution topographic data. *Water Resources Research,* 50**,** 4283-4304.

COATES-MARNANE, J., OLLEY, J., BURTON, J. & SHARMA, A. 2016. Catchment clearing accelerates the infilling of a shallow subtropical bay in east coast Australia. *Estuarine, Coastal and Shelf Science,* 174**,** 27-40.

CONFORTI, M., AUCELLI, P. P., ROBUSTELLI, G. & SCARCIGLIA, F. 2011. Geomorphology and GIS analysis for mapping gully erosion susceptibility in the Turbolo stream catchment (Northern Calabria, Italy). *Natural hazards,* 56**,** 881-898.

CONOSCENTI, C., ANGILERI, S., CAPPADONIA, C., ROTIGLIANO, E., AGNESI, V. & MÄRKER, M. 2014. Gully erosion susceptibility assessment by means of GIS-based logistic regression: A case of Sicily (Italy). *Geomorphology,* 204**,** 399-411.

CONOSCENTI, C. & ROTIGLIANO, E. 2020. Predicting gully occurrence at watershed scale: Comparing topographic indices and multivariate statistical models. *Geomorphology,* 359**,** 107123.

CROKE, J., BARTLEY, R., CHAPPELL, J., AUSTIN, J. M., FIFIELD, K., TIMS, S. G., THOMPSON, C. J. & FURUICHI, T. 2015. 10Be-derived denudation rates from the Burdekin catchment: The largest contributor of sediment to the Great Barrier Reef. *Geomorphology,* 241**,** 122-134.

CROSBY, C. J., ARROWSMITH, J. R. & NANDIGAM, V. 2020. Chapter 11 - Zero to a trillion: Advancing Earth surface process studies with open access to high-resolution topography. *In:* TAROLLI, P. & MUDD, S. M. (eds.) *Developments in Earth Surface Processes,* 23, 317-338.

DABA, S., RIEGER, W. & STRAUSS, P. 2003. Assessment of gully erosion in eastern Ethiopia using photogrammetric techniques. *Catena,* 50**,** 273-291.

DAGGUPATI, P., DOUGLAS-MANKIN, K. R. & SHESHUKOV, A. Y. 2013. Predicting ephemeral gully location and length using topographic index models. *Transactions of the ASABE,* 56**,** 1427-1440.

DARNELL, R., HENDERSON, B., KROON, F. J. & KUHNERT, P. 2012. Statistical power of detecting trends in total suspended sediment loads to the Great Barrier Reef. *Marine pollution bulletin,* 65**,** 203-209.

DE GEETER, S., POESEN, J. & VANMAERCKE, M. 2020. Does the topographic threshold concept explain the initiation points of sunken lanes in the European loess belt? *CATENA,* 192**,** 104586.

DE VENTE, J., POESEN, J., VERSTRAETEN, G., GOVERS, G., VANMAERCKE, M., VAN ROMPAEY, A., ARABKHEDRI, M. & BOIX-FAYOS, C. 2013. Predicting soil erosion and sediment yield at regional scales: where do we stand? *Earth-Science Reviews,* 127**,** 16-29.

DELONG, S. B., PRENTICE, C. S., HILLEY, G. E. & EBERT, Y. 2012. Multitemporal ALSM change detection, sediment delivery, and process mapping at an active earthflow. *Earth Surface Processes and Landforms,* 37**,** 262-272.

DESMET, P. J. J. & GOVERS, G. 1996. Comparison of routing algorithms for digital elevation models and their implications for predicting ephemeral gullies. *International Journal of Geographical Information Systems,* 10**,** 311-331.

DEVLIN, M. & BRODIE, J. 2005. Terrestrial discharge into the Great Barrier Reef Lagoon: nutrient behavior in coastal waters. *Marine pollution bulletin,* 51**,** 9-22.

DEVLIN, M. & SCHAFFELKE, B. 2009. Spatial extent of riverine flood plumes and exposure of marine ecosystems in the Tully coastal region, Great Barrier Reef. *Marine and Freshwater Research,* 60**,** 1109-1122.

DEVLIN, M., WATERHOUSE, J., TAYLOR, J. & BRODIE, J. 2001. Flood plumes in the Great Barrier Reef: spatial and temporal patterns in composition and distribution. *GBRMPA research publication,* 68.

DONG, Y., XIONG, D., SU, Z. A., LI, J., YANG, D., ZHAI, J., LU, X., LIU, G. & SHI, L. 2013. Critical topographic threshold of gully erosion in Yuanmou Dry-hot Valley in Southwestern China. *Physical Geography,* 34**,** 50-59.

DORIEAN, N. J. C., BENNETT, W. W., SPENCER, J. R., GARZON-GARCIA, A., BURTON, J. M., TEASDALE, P. R., WELSH, D. T. & BROOKS, A. P. 2021. Intensive landscape-scale remediation improves water quality of an alluvial gully located in a Great Barrier Reef catchment. *Hydrol. Earth Syst. Sci.,* 25**,** 867-883.

DROVER, D. R., JACKSON, C. R., BITEW, M. & DU, E. 2015. Effects of DEM scale on the spatial distribution of the TOPMODEL topographic wetness index and its correlations to watershed characteristics. *Hydrol. Earth Syst. Sci. Discuss.,* 2015**,** 11817-11846.

ERSKINE, R. H., GREEN, T. R., RAMIREZ, J. A. & MACDONALD, L. H. 2006. Comparison of grid-based algorithms for computing upslope contributing area. *Water Resources Research,* 42.

EUSTACE, A., PRINGLE, M. & WITTE, C. 2009. Give me the dirt: detection of gully extent and volume using high-resolution lidar. In: Jones S., Reinke K. (eds) Innovations in Remote Sensing and Photogrammetry. Lecture Notes in Geoinformation and Cartography. Springer, Berlin, Heidelberg.

EVANS, I. S. 2012. Geomorphometry and landform mapping: What is a landform? *Geomorphology,* 137**,** 94-106.

EVANS, M. & LINDSAY, J. 2010. High resolution quantification of gully erosion in upland peatlands at the landscape scale. *Earth Surface Processes and Landforms,* 35**,** 876-886.

EVANS, M. C. 2016. Deforestation in Australia: drivers, trends and policy responses. *Pacific Conservation Biology,* 22**,** 130-150.

EYLES, R. 1977. Changes in drainage networks since 1820, Southern Tablelands, NSW. *Australian Geographer,* 13**,** 377-386.

FABRICIUS, K., DE'ATH, G., MCCOOK, L., TURAK, E. & WILLIAMS, D. M. 2005. Changes in algal, coral and fish assemblages along water quality gradients on the inshore Great Barrier Reef. *Marine pollution bulletin,* 51**,** 384-398.

FABRICIUS, K., LOGAN, M., WEEKS, S. & BRODIE, J. 2014. The effects of river run-off on water clarity across the central Great Barrier Reef. *Marine pollution bulletin,* 84**,** 191-200.

FRANKL, A., POESEN, J., SCHOLIERS, N., JACOB, M., HAILE, M., DECKERS, J. & NYSSEN, J. 2013. Factors controlling the morphology and volume (V)–length (L) relations of permanent gullies in the northern Ethiopian Highlands. *Earth Surface Processes and Landforms,* 38**,** 1672-1684.

FREEMAN, T. G. 1991. Calculating catchment area with divergent flow based on a regular grid. *Computers & Geosciences,* 17**,** 413-422.

FURNAS, M. M. & MITCHELL, A. A. Biological oceanography of the Great Barrier Reef. The Great Barrier Reef: Science, Use and Management: A National Conference. Proceedings. 25-29 November 1996 James Cook University of North Queensland, Townsville, Queensland, Australia-pages: 1: 75-87, 1997. Great Barrier Reef Marine Park Authority & CRC Reef Research.

GALLANT, J. C. & DOWLING, T. I. 2003. A multiresolution index of valley bottom flatness for mapping depositional areas. *Water resources research,* 39.

GALLANT, J. C. & HUTCHINSON, M. F. 2011. A differential equation for specific catchment area. *Water Resources Research,* 47.

Great Barrier Reef Marine Park Authority. 2017. *Facts about the Great Barrier Reef* [Online]. Townsville, Australia: Great Barrier Reef Marine Partk Authority. [Accessed 2017].

GEOSCIENCE AUSTRALIA, G. A. 2012. *Australian and Region Surface Geology* [Online]. Commonwealth of Australia. Available: http://maps.ga.gov.au/interactive-maps/#/theme/minerals/map/geology [Accessed 15/03/2019].

GILAD, U., DENHAM, R. & TINDALL, D. Gullies, Google Earth and the Great Barrier Reef: A remote sensing methodology for mapping gullies over extensive areas. Proceedings of the International Archives of the Photogrammetry, Remote Sensing and Spatial Information Science, XXII ISPRS Congress, Melbourne, Australia, 2012. B8.

GILBERT, M. & BRODIE, J. 2001. Population and major land use in the Great Barrier Reef catchment area spatial and temporal trends. Research Publication Series, Great Barrier Reef Marine Park Authority, Townsville (2001)

GOMEZ, B., BANBURY, K., MARDEN, M., TRUSTRUM, N. A., PEACOCK, D. H. & HOSKIN, P. J. 2003. Gully erosion and sediment production: Te Weraroa Stream, New Zealand. *Water Resources Research,* 39.

GOODWIN, N. R., ARMSTON, J. D., MUIR, J. & STILLER, I. 2017. Monitoring gully change: A comparison of airborne and terrestrial laser scanning using a case study from Aratula, Queensland. *Geomorphology,* 282**,** 195-208.

GRUBER, S. & PECKHAM, S. 2009. Land-surface parameters and objects in hydrology. *Developments in Soil Science,* 33**,** 171-194.

GUDINO-ELIZONDO, N., BIGGS, T. W., CASTILLO, C., BINGNER, R. L., LANGENDOEN, E. J., TANIGUCHI, K. T., KRETZSCHMAR, T., YUAN, Y. & LIDEN, D. 2018. Measuring ephemeral gully erosion rates and topographical thresholds in an urban watershed using unmanned aerial systems and structure from motion photogrammetric techniques. *Land Degradation & Development,* 29**,** 1896-1905.

GUERSCHMAN, J. P., HILL, M. J., RENZULLO, L. J., BARRETT, D. J., MARKS, A. S. & BOTHA, E. J. 2009. Estimating fractional cover of photosynthetic vegetation, non-photosynthetic vegetation and bare soil in the Australian tropical savanna region upscaling the EO-1 Hyperion and MODIS sensors. *Remote Sensing of Environment,* 113**,** 928-945.

GUTIÉRREZ, Á. G., SCHNABEL, S. & CONTADOR, F. L. 2009. Gully erosion, land use and topographical thresholds during the last 60 years in a small rangeland catchment in SW Spain. *Land Degradation & Development,* 20**,** 535-550.

HACK, J. T. 1957. *St*udies of longitudinal stream profiles in Virginia and Maryland, U.S. Geol. Surv. Prof. Pap., 294-B, 97

HAIRSINE, P. B. 2017. Sediment-related controls on the health of the Great Barrier Reef. *Vadose Zone Journal,* 16.

HANCOCK, G. & EVANS, K. 2006. Channel head location and characteristics using digital elevation models. *Earth Surface Processes and Landforms,* 31**,** 809-824.

HANCOCK, G. J., WILKINSON, S. N., HAWDON, A. A. & KEEN, R. J. 2014. Use of fallout tracers 7Be, 210Pb and 137Cs to distinguish the form of sub-surface soil erosion delivering sediment to rivers in large catchments. *Hydrological Processes,* 28**,** 3855-3874.

HAYAS, A., POESEN, J. & VANWALLEGHEM, T. 2017. Rainfall and vegetation effects on temporal variation of topographic thresholds for gully initiation in Mediterranean cropland and olive groves. *Land degradation & development,* 28**,** 2540-2552.

HAYNES, D. & MICHALEK-WAGNER, K. 2000. Water quality in the Great Barrier Reef World Heritage Area: past perspectives, current issues and new research directions. *Marine Pollution Bulletin,* 41**,** 428-434.

HEINE, A. 2002. Characterisation of gully erosion by airphoto interpretation and GIS techniques of rangelands in semiarid northeastern Australia. *Graduate Diploma. University of Ruhr, Bochum, Germany*.

HENGL, T., GRUBER, S. & SHRESTHA, D. 2003. Digital terrain analysis in ILWIS. *International Institute for Geo-Information Science and Earth Observation Enschede, The Netherlands,* 62.

HOBLEY, D. E., ADAMS, J. M., NUDURUPATI, S. S., HUTTON, E. W., GASPARINI, N. M., ISTANBULLUOGLU, E. & TUCKER, G. E. 2017a. Creative computing with Landlab: an open-source toolkit for building, coupling, and exploring two-dimensional numerical models of Earth-surface dynamics. *Earth Surface Dynamics,* 5**,** 21.

HOBLEY, D. E. J., ADAMS, J. M., NUDURUPATI, S. S., HUTTON, E. W. H., GASPARINI, N. M., ISTANBULLUOGLU, E. & TUCKER, G. E. 2017b. Creative computing with Landlab: an open-source toolkit for building, coupling, and exploring two-dimensional numerical models of Earth-surface dynamics. *Earth Surf. Dynam.,* 5**,** 21-46.

HÖFLE, B., GRIESBAUM, L. & FORBRIGER, M. 2013. GIS-Based Detection of Gullies in Terrestrial LiDAR Data of the Cerro Llamoca Peatland (Peru). *Remote Sensing,* 5**,** 5851-5870.

HOLMGREN, P. 1994. Multiple flow direction algorithms for runoff modelling in grid based elevation models: an empirical evaluation. *Hydrological processes,* 8**,** 327-334.

HOU, J., VAN DIJK, A. I. J. M. & BECK, H. E. 2020. Global satellite-based river gauging and the influence of river morphology on its application. *Remote Sensing of Environment,* 239**,** 111629.

HUGHES, A. O., OLLEY, J. M., CROKE, J. C. & MCKERGOW, L. A. 2009. Sediment source changes over the last 250 years in a dry-tropical catchment, central Queensland, Australia. *Geomorphology,* 104**,** 262-275.

HUTCHINGS, P., KINGSFORD, M. & HOEGH-GULDBERG, O. 2019. *The Great Barrier Reef: biology, environment and management,* Csiro publishing.

IRVIN, B. J., VENTURA, S. J. & SLATER, B. K. 1997. Fuzzy and isodata classification of landform elements from digital terrain data in Pleasant Valley, Wisconsin. *Geoderma,* 77**,** 137-154.

ISTANBULLUOGLU, E., BRAS, R. L., FLORES-CERVANTES, H. & TUCKER, G. E. 2005. Implications of bank failures and fluvial erosion for gully development: Field observations and modeling. *Journal of Geophysical Research: Earth Surface,* 110.

JAMES, L. A., WATSON, D. G. & HANSEN, W. F. 2007. Using LiDAR data to map gullies and headwater streams under forest canopy: South Carolina, USA. *CATENA,* 71**,** 132-144.

JARIHANI, B., SIDLE, R. C., BARTLEY, R., ROTH, C. H. & WILKINSON, S. N. 2017. Characterisation of hydrological response to rainfall at multi spatio-temporal scales in savannas of semi-arid Australia. *Water,* 9**,** 540.

KAKEMBO, V., XANGA, W. W. & ROWNTREE, K. 2009. Topographic thresholds in gully development on the hillslopes of communal areas in Ngqushwa Local Municipality, Eastern Cape, South Africa. *Geomorphology,* 110**,** 188-194.

KARYDAS, C. & PANAGOS, P. 2020. Towards an assessment of the ephemeral gully erosion potential in Greece using Google Earth. *Water,* 12**,** 603.

KHEIR, R. B., WILSON, J. & DENG, Y. 2007. Use of terrain variables for mapping gully erosion susceptibility in Lebanon. *Earth Surface Processes and Landforms: The Journal of the British Geomorphological Research Group,* 32**,** 1770-1782.

KING, A. D., KLINGAMAN, N. P., ALEXANDER, L. V., DONAT, M. G., JOURDAIN, N. C. & MAHER, P. 2014. Extreme Rainfall Variability in Australia: Patterns, Drivers, and Predictability. *Journal of Climate,* 27**,** 6035-6050.

KINSEY-HENDERSON, A., SHERMAN, B. & BARTLEY, R. 2007. Improved SedNet modelling of grazing lands in the Burdekin catchment. CSIRO, Townsville

KIRKBY, M. 1988. Hill slopes and hollows. *Nature,* 336**,** 201-201.

KLINGAMAN, N. P. 2012. *Rainfall in Queensland: Part 1: a literature survey of key rainfall drivers in Queensland Australia: rainfall variability and change*, Queensland Government.

KNAPEN, A. & POESEN, J. 2010. Soil erosion resistance effects on rill and gully initiation points and dimensions. *Earth Surface Processes and Landforms,* 35**,** 217-228.

KNIGHT, J., SPENCER, J., BROOKS, A. & PHINN, S. Large-area, high-resolution remote sensing based mapping of alluvial gully erosion in Australia's tropical rivers. Proceedings of the 5th Australian Stream Management Conference, 2007. Charles Sturt University, 199-204.

KOCI, J., JARIHANI, B., LEON, J. X., SIDLE, R. C., WILKINSON, S. N. & BARTLEY, R. 2017. Assessment of UAV and Ground-Based Structure from Motion with Multi-View Stereo Photogrammetry in a Gullied Savanna Catchment. *ISPRS International Journal of Geo-Information,* 6**,** 328.

KOCI, J., SIDLE, R. C., JARIHANI, B. & CASHMAN, M. J. 2020a. Linking hydrological connectivity to gully erosion in savanna rangelands tributary to the Great Barrier Reef using structure-from-motion photogrammetry. *Land Degradation & Development,* 31**,** 20-36.

KOCI, J., SIDLE, R. C., KINSEY-HENDERSON, A. E., BARTLEY, R., WILKINSON, S. N., HAWDON, A. A., JARIHANI, B., ROTH, C. H. & HOGARTH, L. 2020b. Effect of reduced grazing pressure on sediment and nutrient yields in savanna rangeland streams draining to the Great Barrier Reef. *Journal of Hydrology,* 582**,** 124520.

KOCI, J., WILKINSON, S. N., HAWDON, A. A., KINSEY-HENDERSON, A. E., BARTLEY, R. & GOODWIN, N. R. 2021. Rehabilitation effects on gully sediment yields and vegetation in a savanna rangeland. *Earth Surface Processes and Landforms,* 46**,** 1007-1025.

KORZENIOWSKA, K., PFEIFER, N. & LANDTWING, S. 2018. Mapping gullies, dunes, lava fields, and landslides via surface roughness. *Geomorphology,* 301**,** 53-67.

KROON, F. J., KUHNERT, P. M., HENDERSON, B. L., WILKINSON, S. N., KINSEY-HENDERSON, A., ABBOTT, B., BRODIE, J. E. & TURNER, R. D. 2012. River loads of suspended solids, nitrogen, phosphorus and herbicides delivered to the Great Barrier Reef lagoon. *Marine pollution bulletin,* 65**,** 167-181.

KROON, F. J., THORBURN, P., SCHAFFELKE, B. & WHITTEN, S. 2016. Towards protecting the Great Barrier Reef from land-based pollution. *Global change biology,* 22**,** 1985-2002.

LARCOMBE, P. & CARTER, R. 2004. Cyclone pumping, sediment partitioning and the development of the Great Barrier Reef shelf system: a review. *Quaternary Science Reviews,* 23**,** 107-135.

LASHERMES, B., FOUFOULA-GEORGIOU, E. & DIETRICH, W. E. 2007. Channel network extraction from high resolution topography using wavelets. *Geophysical Research Letters,* 34.

LE ROUX, J. J. & SUMNER, P. D. 2012. Factors controlling gully development: Comparing continuous and discontinuous gullies. *Land Degradation & Development,* 23**,** 440-449.
LEOPOLD, L. B., WOLMAN, M. G. & MILLER, J. P. 1964. Fluvial processes in geomorphology, 2nd edn. New York: Dover Publishers. 522.
LEWIS, S. E., BARTLEY, R., WILKINSON, S. N., BAINBRIDGE, Z. T., HENDERSON, A. E., JAMES, C. S., IRVINE, S. A. & BRODIE, J. E. 2021. Land use change in the river basins of the Great Barrier Reef, 1860 to 2019: A foundation for understanding environmental history across the catchment to reef continuum. *Marine Pollution Bulletin,* 166**,** 112193.
LEWIS, S. E., OLLEY, J., FURUICHI, T., SHARMA, A. & BURTON, J. 2014. Complex sediment deposition history on a wide continental shelf: Implications for the calculation of accumulation rates on the Great Barrier Reef. *Earth and Planetary Science Letters,* 393**,** 146-158.
LEWIS, S. E., SHIELDS, G. A., KAMBER, B. S. & LOUGH, J. M. 2007. A multi-trace element coral record of land-use changes in the Burdekin River catchment, NE Australia. *Palaeogeography, Palaeoclimatology, Palaeoecology,* 246**,** 471-487.
LINDSAY, J. B. 2016a. Efficient hybrid breaching-filling sink removal methods for flow path enforcement in digital elevation models. *Hydrological Processes,* 30**,** 846-857.
LINDSAY, J. B. 2016b. Whitebox GAT: A case study in geomorphometric analysis. *Computers & Geosciences,* 95**,** 75-84.
LINDSAY, J. B. & DHUN, K. 2015. Modelling surface drainage patterns in altered landscapes using LiDAR. *International Journal of Geographical Information Science,* 29**,** 397-411.
LIU, H., KIESEL, J., HÖRMANN, G. & FOHRER, N. 2011. Effects of DEM horizontal resolution and methods on calculating the slope length factor in gently rolling landscapes. *CATENA,* 87**,** 368-375.
MACMILLAN, R. A., PETTAPIECE, W. W., NOLAN, S. C. & GODDARD, T. W. 2000. A generic procedure for automatically segmenting landforms into landform elements using DEMs, heuristic rules and fuzzy logic. *Fuzzy Sets and Systems,* 113**,** 81-109.
MACMILLAN, R. A. & SHARY, P. A. 2009. Chapter 9 Landforms and Landform Elements in Geomorphometry. *In:* HENGL, T. & REUTER, H. I. (eds.) *Developments in Soil Science,* 33, 227-254
MAERKER, M., SOMMER, C., ZAKERINEJAD, R. & CAMA, E. An integrated assessment of soil erosion dynamics with special emphasis on gully erosion: Case studies from South Africa and Iran. EGU General Assembly Conference Abstracts, 2017. 18568.
MAGUYA, A. S., JUNTTILA, V. & KAURANNE, T. 2013. Adaptive algorithm for large scale dtm interpolation from lidar data for forestry applications in steep forested terrain. *ISPRS Journal of Photogrammetry and Remote Sensing,* 85**,** 74-83.
MAJHI, A., NYSSEN, J. & VERDOODT, A. 2021. What is the best technique to estimate topographic thresholds of gully erosion? Insights from a case study on the permanent gullies of Rarh plain, India. *Geomorphology,* 375**,** 107547.
MAKANZU IMWANGANA, F., DEWITTE, O., NTOMBI, M. & MOEYERSONS, J. 2014. Topographic and road control of mega-gullies in Kinshasa (DR Congo). *Geomorphology,* 217**,** 131-139.
MAUGNARD, A., VAN DYCK, S. & BIELDERS, C. L. 2014. Assessing the regional and temporal variability of the topographic threshold for ephemeral gully initiation using quantile regression in Wallonia (Belgium). *Geomorphology,* 206**,** 165-177.
MCCLOSKEY, G. L., BAHEERATHAN, R., DOUGALL, C., ELLIS, R., BENNETT, F. R., WATERS, D., DARR, S., FENTIE, B., HATELEY, L. R. & ASKILDSEN, M. 2021. Modelled estimates of fine sediment and particulate nutrients delivered from the Great Barrier Reef catchments. *Marine Pollution Bulletin,* 165**,** 112163.
MCCULLOCH, M., FALLON, S., WYNDHAM, T., HENDY, E., LOUGH, J. & BARNES, D. 2003. Coral record of increased sediment flux to the inner Great Barrier Reef since European settlement. *Nature,* 421**,** 727-730.
MCDONALD, J. H. 2009. *Handbook of biological statistics*, sparky house publishing Baltimore, MD.
MCKENZIE, N. J., JACQUIER, D. W. & GREGORY, L. J. 2005. The Australian Soil Resource Information System. *Technical specifications. Version,* 1**,** 93.

MCKERGOW, L. A., PROSSER, I. P., HUGHES, A. O. & BRODIE, J. 2005a. Regional scale nutrient modelling: exports to the Great Barrier Reef world heritage area. *Marine pollution bulletin,* 51**,** 186-199.
MCKERGOW, L. A., PROSSER, I. P., HUGHES, A. O. & BRODIE, J. 2005b. Sources of sediment to the Great Barrier Reef World Heritage Area. *Marine Pollution Bulletin,* 51**,** 200-211.
MCNAMARA, J. P., ZIEGLER, A. D., WOOD, S. H. & VOGLER, J. B. 2006. Channel head locations with respect to geomorphologic thresholds derived from a digital elevation model: A case study in northern Thailand. *Forest Ecology and Management,* 224**,** 147-156.
MENÉNDEZ-DUARTE, R., MARQUÍNEZ, J., FERNÁNDEZ-MENÉNDEZ, S. & SANTOS, R. 2007. Incised channels and gully erosion in Northern Iberian Peninsula: Controls and geomorphic setting. *CATENA,* 71**,** 267-278.
MINÁR, J. & EVANS, I. S. 2008. Elementary forms for land surface segmentation: The theoretical basis of terrain analysis and geomorphological mapping. *Geomorphology,* 95**,** 236-259.
MINÁR, J., EVANS, I. S. & JENČO, M. 2020. A comprehensive system of definitions of land surface (topographic) curvatures, with implications for their application in geoscience modelling and prediction. *Earth Science Reviews,* 211**,** 103414.
MITÁŠOVÁ, H. & HOFIERKA, J. 1993. Interpolation by regularized spline with tension: II. Application to terrain modeling and surface geometry analysis. *Mathematical Geology,* 25**,** 657-669.
MOMM, H., BINGNER, R., WELLS, R. & WILCOX, D. 2012. *AGNPS GIS-Based Tool for Watershed-Scale Identification and Mapping of Cropland Potential Ephemeral Gullies*.
MONTGOMERY, D. R. & DIETRICH, W. E. 1988. Where do channels begin? *Nature,* 336**,** 232.
MONTGOMERY, D. R. & DIETRICH, W. E. 1989. Source areas, drainage density, and channel initiation. *Water Resources Research,* 25**,** 1907-1918.
MONTGOMERY, D. R. & DIETRICH, W. E. 1994. Landscape dissection and drainage area-slope thresholds. *Process models and theoretical geomorphology: theoretical geomorphology and its applications.* New York: Wiley & Sons.
MOORE, I., BURCH, G. & MACKENZIE, D. 1988. Topographic effects on the distribution of surface soil water and the location of ephemeral gullies. *Transactions of the ASAE,* 31**,** 1098-1107.
MOORE, I. D., GESSLER, P., NIELSEN, G. & PETERSON, G. 1993. Soil attribute prediction using terrain analysis. *Soil Science Society of America Journal,* 57**,** 443-452.
MORGAN, R. P. C. & MNGOMEZULU, D. 2003. Threshold conditions for initiation of valley-side gullies in the Middle Veld of Swaziland. *CATENA,* 50**,** 401-414.
MUDD, S. M. 2020. Chapter 4 - Topographic data from satellites. *In:* TAROLLI, P. & MUDD, S. M. (eds.) *Developments in Earth Surface Processes,* 23, 91-128.
MUÑOZ-ROBLES, C., REID, N., FRAZIER, P., TIGHE, M., BRIGGS, S. V. & WILSON, B. 2010. Factors related to gully erosion in woody encroachment in south-eastern Australia. *CATENA,* 83**,** 148-157.
MURPHY, P. N. C., OGILVIE, J. & ARP, P. 2009. Topographic modelling of soil moisture conditions: a comparison and verification of two models. *European Journal of Soil Science,* 60**,** 94-109.
NACHTERGAELE, J., POESEN, J., SIDORCHUK, A. & TORRI, D. 2002. Prediction of concentrated flow width in ephemeral gully channels. *Hydrological Processes,* 16**,** 1935-1953.
NACHTERGAELE, J., POESEN, J., VANDEKERCKHOVE, L., OOSTWOUD WIJDENES, D. & ROXO, M. 2001. Testing the Ephemeral Gully Erosion Model (EGEM) for two Mediterranean environments. *Earth Surface Processes and Landforms,* 26**,** 17-30.
NAZARI SAMANI, A., AHMADI, H., JAFARI, M., BOGGS, G., GHODDOUSI, J. & MALEKIAN, A. 2009. Geomorphic threshold conditions for gully erosion in Southwestern Iran (Boushehr-Samal watershed). *Journal of Asian Earth Sciences,* 35**,** 180-189.
NEIL, D. T., ORPIN, A. R., RIDD, P. V. & YU, B. 2002. Sediment yield and impacts from river catchments to the Great Barrier Reef lagoon: a review. *Marine and Freshwater Research,* 53**,** 733-752.
NYSSEN, J., POESEN, J., MOEYERSONS, J., LUYTEN, E., VEYRET-PICOT, M., DECKERS, J., HAILE, M. & GOVERS, G. 2002. Impact of road building on gully erosion risk: a case study from the Northern Ethiopian Highlands. *Earth Surface Processes and Landforms,* 27**,** 1267-1283.

O'CALLAGHAN, J. F. & MARK, D. M. 1984. The extraction of drainage networks from digital elevation data. *Computer Vision, Graphics, and Image Processing,* 28**,** 323-344.
OLLEY, J., BROOKS, A., SPENCER, J., PIETSCH, T. & BOROMBOVITS, D. 2013. Subsoil erosion dominates the supply of fine sediment to rivers draining into Princess Charlotte Bay, Australia. *Journal of environmental radioactivity,* 124**,** 121-129.
OOSTWOUD WIJDENES, D. & BRYAN, R. 2001. Gully-head erosion processes on a semi-arid valley floor in Kenya: a case study into temporal variation and sediment budgeting. *Earth Surface Processes and Landforms,* 26**,** 911-933.
PARKER, C., THORNE, C., BINGNER, R., WELLS, R. & WILCOX, D. 2007. Automated mapping of the potential for ephemeral gully formation in agricultural watersheds. *US Department of Agriculture, Agricultural Research Service, National Sedimentation Laboratory Research Report, Oxford, MS*.
PARKNER, T., PAGE, M., MARDEN, M. & MARUTANI, T. 2007. Gully systems under undisturbed indigenous forest, East Coast region, New Zealand. *Geomorphology,* 84**,** 241-253.
PARKNER, T., PAGE, M. J., MARUTANI, T. & TRUSTRUM, N. A. 2006. Development and controlling factors of gullies and gully complexes, East Coast, New Zealand. *Earth Surface Processes and Landforms,* 31**,** 187-199.
PASSALACQUA, P., DO TRUNG, T., FOUFOULA-GEORGIOU, E., SAPIRO, G. & DIETRICH, W. E. 2010. A geometric framework for channel network extraction from lidar: Nonlinear diffusion and geodesic paths. *Journal of Geophysical Research: Earth Surface,* 115.
PATTON, P. C. & SCHUMM, S. A. 1975. Gully erosion, Northwestern Colorado: a threshold phenomenon. *Geology,* 3**,** 88-90.
PEDERSON, J. L., PETERSEN, P. A. & DIERKER, J. L. 2006. Gullying and erosion control at archaeological sites in Grand Canyon, Arizona. *Earth Surface Processes and Landforms: The Journal of the British Geomorphological Research Group,* 31**,** 507-525.
PEEL, M. C., FINLAYSON, B. L. & MCMAHON, T. A. 2007. Updated world map of the Köppen-Geiger climate classification. *Hydrol. Earth Syst. Sci.,* 11**,** 1633-1644.
PELLETIER, J. D. 2004. Persistent drainage migration in a numerical landscape evolution model. *Geophysical Research Letters,* 31.
PELLETIER, J. D. 2013. A robust, two-parameter method for the extraction of drainage networks from high-resolution digital elevation models (DEMs): Evaluation using synthetic and real-world DEMs. *Water Resources Research,* 49**,** 75-89.
PENNOCK, D. J., ZEBARTH, B. J. & DE JONG, E. 1987. Landform classification and soil distribution in hummocky terrain, Saskatchewan, Canada. *Geoderma,* 40**,** 297-315.
PERROY, R. L., BOOKHAGEN, B., ASNER, G. P. & CHADWICK, O. A. 2010. Comparison of gully erosion estimates using airborne and ground-based LiDAR on Santa Cruz Island, California. *Geomorphology,* 118**,** 288-300.
PERRY, C. T. & SMITHERS, S. G. 2011. Cycles of coral reef 'turn-on', rapid growth and 'turn-off'over the past 8500 years: A context for understanding modern ecological states and trajectories. *Global Change Biology,* 17**,** 76-86.
PETHERAM, C., MCMAHON, T. A. & PEEL, M. C. 2008. Flow characteristics of rivers in northern Australia: Implications for development. *Journal of Hydrology,* 357**,** 93-111.
PIROTTI, F. & TAROLLI, P. 2010. Suitability of LiDAR point density and derived landform curvature maps for channel network extraction. *Hydrological Processes,* 24**,** 1187-1197.
POESEN, J. 2018. Soil erosion in the Anthropocene: Research needs. *Earth Surface Processes and Landforms,* 43**,** 64-84.
POESEN, J., NACHTERGAELE, J., VERSTRAETEN, G. & VALENTIN, C. 2003. Gully erosion and environmental change: importance and research needs. *CATENA,* 50**,** 91-133.
POESEN, J. W. A., TORRI, D. B. & VANWALLEGHEM, T. 2011. Gully Erosion: Procedures to Adopt When Modelling Soil Erosion in Landscapes Affected by Gullying. *Handbook of Erosion Modelling.*
POLLOCK, F. J., LAMB, J. B., FIELD, S. N., HERON, S. F., SCHAFFELKE, B., SHEDRAWI, G., BOURNE, D. G. & WILLIS, B. L. 2014. Sediment and turbidity associated with offshore dredging increase coral disease prevalence on nearby reefs. *PLOS one,* 9**,** e102498.

POST, D., HAWDON, A., HENDERSON, A., BARTLEY, R., HODGEN, M., KEEN, R., KEMEI, J., BERTHELSEN, S., BAKER, G. & TINK, M. 2005. Sustainable grazing for a healthy Burdekin catchment. CSIRO Land and Water.

PRASICEK, G., OTTO, J.-C., MONTGOMERY, D. R. & SCHROTT, L. 2014. Multi-scale curvature for automated identification of glaciated mountain landscapes. *Geomorphology,* 209**,** 53-65.

PROSSER, I., RUSTOMJI, P., YOUNG, B., MORAN, C. & HUGHES, A. 2001. Constructing river basin sediment budgets for the National Land and Water Resources Audit. *CSIRO Land and Water Technical Report,* 15**,** 2001.

PROSSER, I. P. & SOUFI, M. 1998. Controls on gully formation following forest clearing in a humid temperate environment. *Water Resources Research,* 34**,** 3661-3671.

QUINN, P., BEVEN, K., CHEVALLIER, P. & PLANCHON, O. 1991. The prediction of hillslope flow paths for distributed hydrological modelling using digital terrain models. *Hydrological processes,* 5**,** 59-79.

RENGERS, F. K. & TUCKER, G. E. 2014. Analysis and modeling of gully headcut dynamics, North American high plains. *Journal of Geophysical Research: Earth Surface,* 119**,** 983-1003.

RENGERS, F. K. & TUCKER, G. E. 2015. The evolution of gully headcut morphology: a case study using terrestrial laser scanning and hydrological monitoring. *Earth Surface Processes and Landforms,* 40**,** 1304-1317.

RIEGER, W. 1998. A phenomenon-based approach to upslope contributing area and depressions in DEMs. *Hydrological Processes,* 12**,** 857-872.

RITCHIE, J. C., GRISSINGER, E. H., MURPHEY, J. B. & GARBRECHT, J. D. 1994. Measuring channel and gully cross-sections with an airborne laser altimeter. *Hydrological Processes,* 8**,** 237-243.

ROA-GARCÍA, M., BROWN, S., SCHREIER, H. & LAVKULICH, L. 2011. The role of land use and soils in regulating water flow in small headwater catchments of the Andes. *Water Resources Research,* 47.

ROSSI, M., TORRI, D. & SANTI, E. 2015. Bias in topographic thresholds for gully heads. *Natural Hazards,* 79**,** 51-69.

RUST, S. & STAR, M. 2018. The cost effectiveness of remediating erosion gullies: a case study in the Fitzroy. *Australasian Journal of Environmental Management,* 25**,** 233-247.

RUTHERFURD, I. D., PROSSER, I. & DAVIS, J. 1997. Simple approaches to predicting rates and extent of gully development. In *Proceedings of the Conference on Management of landscapes distrubed by channel incision* (pp. 1125 - 1130). Center for Computational Hydroscience and Eng.

SAXTON, N. E., OLLEY, J. M., SMITH, S., WARD, D. P. & ROSE, C. W. 2012. Gully erosion in sub-tropical south-east Queensland, Australia. *Geomorphology,* 173**,** 80-87.

SCHMIDT, J. & ANDREW, R. 2005. Multi-scale landform characterization. *Area,* 37**,** 341-350.

SCHMIDT, J., EVANS, I. S. & BRINKMANN, J. 2003. Comparison of polynomial models for land surface curvature calculation. *International Journal of Geographical Information Science,* 17**,** 797-814.

SCHMIDT, J. & HEWITT, A. 2004. Fuzzy land element classification from DTMs based on geometry and terrain position. *Geoderma,* 121**,** 243-256.

SCHUMANN, G. J.-P. & BATES, P. D. 2018. The Need for a High-Accuracy, Open-Access Global DEM. *Frontiers in Earth Science,* 6.

SEIBERT, J. & MCGLYNN, B. L. 2007. A new triangular multiple flow direction algorithm for computing upslope areas from gridded digital elevation models. *Water Resources Research,* 43.

SELBY, M. J. 1982. Hillslope materials and processes. *Hillslope materials and processes*. Oxford Univ. Press, New York.

SHARY, P. A. 1995. Land surface in gravity points classification by a complete system of curvatures. *Mathematical Geology,* 27**,** 373-390.

SHARY, P. A., SHARAYA, L. S. & MITUSOV, A. V. 2002. Fundamental quantitative methods of land surface analysis. *Geoderma,* 107**,** 1-32.

SHELEF, E. & HILLEY, G. E. 2013. Impact of flow routing on catchment area calculations, slope estimates, and numerical simulations of landscape development. *Journal of Geophysical Research: Earth Surface,* 118**,** 2105-2123.

SHELLBERG, J., BROOKS, A., SPENCER, J. & WARD, D. 2013. The hydrogeomorphic influences on alluvial gully erosion along the Mitchell River fluvial megafan. *Hydrological Processes,* 27**,** 1086-1104.

SHELLBERG, J. G. 2021. Agricultural Development Risks Increasing Gully Erosion and Cumulative Sediment Yields from Headwater Streams in Great Barrier Reef Catchments. *Land Degradation & Development,* 32, 1555-1569.

SHELLBERG, J. G., SPENCER, J., BROOKS, A. P. & PIETSCH, T. J. 2016. Degradation of the Mitchell River fluvial megafan by alluvial gully erosion increased by post-European land use change, Queensland, Australia. *Geomorphology,* 266**,** 105-120.

SHIT, P. K., PAIRA, R., BHUNIA, G. & MAITI, R. 2015. Modeling of potential gully erosion hazard using geo-spatial technology at Garbheta block, West Bengal in India. *Modeling Earth Systems and Environment,* 1**,** 2.

SIBSON, R. 1981. A brief description of natural neighbor interpolation. In: Barnett, V., Ed., Interpreting Multivariate Data, John Wiley & Sons, New York, 21-36.

SIDLE, R. C., JARIHANI, B., KAKA, S. I., KOCI, J. & AL-SHAIBANI, A. 2019. Hydrogeomorphic processes affecting dryland gully erosion: Implications for modelling. *Progress in Physical Geography: Earth and Environment,* 43**,** 46-64.

SOFIA, G. 2020. Combining geomorphometry, feature extraction techniques and Earth-surface processes research: The way forward. *Geomorphology,* 355**,** 107055.

SØRENSEN, R. & SEIBERT, J. 2007. Effects of DEM resolution on the calculation of topographical indices: TWI and its components. *Journal of Hydrology,* 347**,** 79-89.

SØRENSEN, R., ZINKO, U. & SEIBERT, J. 2006. On the calculation of the topographic wetness index: evaluation of different methods based on field observations. *Hydrol. Earth Syst. Sci.,* 10**,** 101-112.

SPEIGHT, J. G. 1990. Landform. *In:* MCDONALD, R. C., ISBELL, R. F., SPEIGHT, J. G., WALKER, J. & HOPKINS, M. S. (eds.) *Australian Soil and Land Survey Field Handbook.* 2nd ed. Melbourne: Inkata Press, pp. 9-57.

STRAHLER, A. H., WOODCOCK, C. E. & SMITH, J. A. 1986. On the nature of models in remote sensing. *Remote Sensing of Environment,* 20**,** 121-139.

STRAHLER, A. N. 1957. Quantitative analysis of watershed geomorphology. *Eos, Transactions American Geophysical Union,* 38**,** 913-920.

TARBOTON, D. G. 1997. A new method for the determination of flow directions and upslope areas in grid digital elevation models. *Water Resources Research,* 33**,** 309-319.

TAROLLI, P. 2014. High-resolution topography for understanding Earth surface processes: Opportunities and challenges. *Geomorphology,* 216**,** 295-312.

TAYLOR, W. A. 2000. Change-point analysis: a powerful new tool for detecting changes. Available at: http://www.variation.com/cpa/tech/changepoint.html (accessed 6 March 2020).

TEBEBU, T. Y., ABIY, A. Z., ZEGEYE, A. D., DAHLKE, H. E., EASTON, Z. M., TILAHUN, S. A., COLLICK, A. S., KIDNAU, S., MOGES, S., DADGARI, F. & STEENHUIS, T. S. 2010. Surface and subsurface flow effect on permanent gully formation and upland erosion near Lake Tana in the northern highlands of Ethiopia. *Hydrol. Earth Syst. Sci.,* 14**,** 2207-2217.

THOMAS, I. A., JORDAN, P., SHINE, O., FENTON, O., MELLANDER, P. E., DUNLOP, P. & MURPHY, P. N. C. 2017. Defining optimal DEM resolutions and point densities for modelling hydrologically sensitive areas in agricultural catchments dominated by microtopography. *International Journal of Applied Earth Observation and Geoinformation,* 54**,** 38-52.

THORBURN, P. J., WILKINSON, S. & SILBURN, D. 2013. Water quality in agricultural lands draining to the Great Barrier Reef: a review of causes, management and priorities. *Agriculture, ecosystems & environment,* 180**,** 4-20.

TINDALL, D., MARCHAND, B., GILAD, U., GOODWIN, N., BYER, S. & DENHAM, R. 2014a. Reef Water Quality Science Project RP66G: Gully mapping and drivers in the grazing lands of the Burdekin catchment. *In:* DEPARTMENT OF SCIENCE, I. T., INNOVATION AND THE ARTS (ed.). Brisbane, Queensland: The Queensland Government, Australia.

TINDALL, D., MARCHAND, B., GILAD, U., GOODWIN, N., DENHAM, R. & BYER, S. 2014b. Gully mapping and drivers in the grazing lands of the Burdekin catchment. RP66G Synthesis Report. *In:* QUEENSLAND DEPARTMENT OF SCIENCE, I. T., INNOVATION AND THE ARTS (ed.). Brisbane.

TORRI, D. & POESEN, J. 2014. A review of topographic threshold conditions for gully head development in different environments. *Earth-Science Reviews,* 130**,** 73-85.

TUCKER, G. E., CATANI, F., RINALDO, A. & BRAS, R. L. 2001. Statistical analysis of drainage density from digital terrain data. *Geomorphology,* 36**,** 187-202.

VALENTIN, C., POESEN, J. & LI, Y. 2005. Gully erosion: Impacts, factors and control. *CATENA,* 63**,** 132-153.

VAN DIJK, A. I. J. M. & RAHMAN, J. 2019. Synthesising multiple observations into annual environmental condition reports: the OzWALD system and Australia's Environment Explorer. *In:* ELSAWAH, S. (ed.) *MODSIM2019, 23rd International Congress on Modelling and Simulation. Modelling and Simulation Society of Australia and New Zealand.*

VANDAELE, K., POESEN, J., GOVERS, G. & WESEMAEL, B. V. 1996. Geomorphic threshold conditions for ephemeral gully incision. *Geomorphology,* 16**,** 161-173.

VANDEKERCKHOVE, L., POESEN, J., OOSTWOUD WIJDENES, D., NACHTERGAELE, J., KOSMAS, C., ROXO, M. J. & DE FIGUEIREDO, T. 2000. Thresholds for gully initiation and sedimentation in Mediterranean Europe. *Earth Surface Processes and Landforms,* 25**,** 1201-1220.

VANDEKERCKHOVE, L., POESEN, J., OOSTWOUD WIJDENES, D. & DE FIGUEIREDO, T. 1998. Topographical thresholds for ephemeral gully initiation in intensively cultivated areas of the Mediterranean. *CATENA,* 33**,** 271-292.

VANDEKERCKHOVE, L., POESEN, J., OOSTWOUD WIJDENES, D. & GYSSELS, G. 2001. Short-term bank gully retreat rates in Mediterranean environments. *CATENA,* 44**,** 133-161.

VANMAERCKE, M., CHEN, Y., HAREGEWEYN, N., DE GEETER, S., CAMPFORTS, B., HEYNDRICKX, W., TSUNEKAWA, A. & POESEN, J. 2020. Predicting gully densities at sub-continental scales: a case study for the Horn of Africa. *Earth Surface Processes and Landforms,* 45**,** 3763-3779.

VANMAERCKE, M., PANAGOS, P., VANWALLEGHEM, T., HAYAS, A., FOERSTER, S., BORRELLI, P., ROSSI, M., TORRI, D., CASALI, J., BORSELLI, L., VIGIAK, O., MAERKER, M., HAREGEWEYN, N., DE GEETER, S., ZGŁOBICKI, W., BIELDERS, C., CERDÀ, A., CONOSCENTI, C., DE FIGUEIREDO, T., EVANS, B., GOLOSOV, V., IONITA, I., KARYDAS, C., KERTÉSZ, A., KRÁSA, J., LE BOUTEILLER, C., RADOANE, M., RISTIĆ, R., ROUSSEVA, S., STANKOVIANSKY, M., STOLTE, J., STOLZ, C., BARTLEY, R., WILKINSON, S., JARIHANI, B. & POESEN, J. 2021. Measuring, modelling and managing gully erosion at large scales: A state of the art. *Earth-Science Reviews,* 218**,** 103637.

VANMAERCKE, M., POESEN, J., VAN MELE, B., DEMUZERE, M., BRUYNSEELS, A., GOLOSOV, V., BEZERRA, J. F. R., BOLYSOV, S., DVINSKIH, A. & FRANKL, A. 2016. How fast do gully headcuts retreat? *Earth-Science Reviews,* 154**,** 336-355.

VANWALLEGHEM, T., POESEN, J., NACHTERGAELE, J. & VERSTRAETEN, G. 2005a. Characteristics, controlling factors and importance of deep gullies under cropland on loess-derived soils. *Geomorphology,* 69**,** 76-91.

VANWALLEGHEM, T., POESEN, J., VAN DEN EECKHAUT, M., NACHTERGAELEL, J. & DECKERS, J. 2005b. Reconstructing rainfall and land-use conditions leading to the development of old gullies. *The Holocene,* 15**,** 378-386.

WALKER, J. P. & WILLGOOSE, G. R. 1999. On the effect of digital elevation model accuracy on hydrology and geomorphology. *Water Resources Research,* 35**,** 2259-2268.

WALKER, S. J., VAN DIJK, A. I. J. M., WILKINSON, S. N. & HAIRSINE, P. B. 2021. A comparison of hillslope drainage area estimation methods using high-resolution DEMs with implications for topographic studies of gullies. *Earth Surface Processes and Landforms,* 46**,** 2229-2247.

WALKER, S. J., WILKINSON, S. N., VAN DIJK, A. I. J. M. & HAIRSINE, P. B. 2020. A multi-resolution method to map and identify locations of future gully and channel incision. *Geomorphology,* 358**,** 107115.

WASSON, R., CAITCHEON, G., MURRAY, A. S., MCCULLOCH, M. & QUADE, J. 2002. Sourcing sediment using multiple tracers in the catchment of Lake Argyle, Northwestern Australia. *Environmental Management,* 29**,** 634-646.

WATERHOUSE, J., BRODIE, J., LEWIS, S. & MITCHELL, A. 2012. Quantifying the sources of pollutants in the Great Barrier Reef catchments and the relative risk to reef ecosystems. *Marine pollution bulletin,* 65**,** 394-406.

WATERS, D. K., CARROLL, C., ELLIS, R., HATELEY, L. R., MCCLOSKEY, G. L., PACKETT, R. & DOUGALL, C. 2014. Modelling reductions of pollutant loads due to improved management practices in the Great Barrier Reef catchments. *In:* QUEENSLAND DEPARTMENT OF NATURAL RESOURCES AND MINES, D. (ed.). Toowoomba, Queensland.

WHITFORD, J., NEWHAM, L., VIGIAK, O., MELLAND, A. & ROBERTS, A. 2010. Rapid assessment of gully sidewall erosion rates in data-poor catchments: a case study in Australia. *Geomorphology,* 118**,** 330-338.

WILKINSON, S., BARTLEY, R., HAIRSINE, P., BUI, E., GREGORY, L. & HENDERSON, A. 2015a. Managing gully erosion as an efficient approach to improving water quality in the Great Barrier Reef lagoon. Report to the Department of the Environment. CSIRO Land and Water: Canberra, Australia.

WILKINSON, S. N., BARTLEY, R., HAIRSINE, P., BUI, E., GREGORY, L. & HENDERSON, A. 2015b. Managing gully erosion as an efficient approach to improving water quality in the Great Brrier Reef lagoon. CSIRO Land and Water: Canberra, Australia.

WILKINSON, S. N., HANCOCK, G. J., BARTLEY, R., HAWDON, A. A. & KEEN, R. J. 2013. Using sediment tracing to assess processes and spatial patterns of erosion in grazed rangelands, Burdekin River basin, Australia. *Agriculture, Ecosystems & Environment,* 180**,** 90-102.

WILKINSON, S. N., KINSEY-HENDERSON, A. E., HAWDON, A. A., HAIRSINE, P. B., BARTLEY, R. & BAKER, B. 2018. Grazing impacts on gully dynamics indicate approaches for gully erosion control in northeast Australia. *Earth Surface Processes and Landforms,* 43**,** 1711-1725.

WILKINSON, S. N., PROSSER, I. P. & HUGHES, A. O. 2006. Predicting the distribution of bed material accumulation using river network sediment budgets. *Water Resources Research,* 42.

WILKINSON, S. N., PROSSER, I. P., RUSTOMJI, P. & READ, A. M. 2009. Modelling and testing spatially distributed sediment budgets to relate erosion processes to sediment yields. *Environmental Modelling & Software,* 24**,** 489-501.

WILLGOOSE, G. 1994. A physical explanation for an observed area-slope-elevation relationship for catchments with declining relief. *Water Resources Research,* 30**,** 151-159.

WILSON, J. P. 2012. Digital terrain modeling. *Geomorphology,* 137**,** 107-121.

WILSON, J. P., LAM, C. S. & DENG, Y. 2007. Comparison of the performance of flow-routing algorithms used in GIS-based hydrologic analysis. *Hydrological Processes: An International Journal,* 21**,** 1026-1044.

WONG, V. N., GREENE, R., DALAL, R. & MURPHY, B. W. 2010a. Soil carbon dynamics in saline and sodic soils: a review. *Soil Use and Management,* 26**,** 2-11.

WONG, V. N., GREENE, R., DALAL, R. C. & MURPHY, B. W. 2010b. Soil carbon dynamics in saline and sodic soils: a review. *Soil use and management,* 26**,** 2-11.

WOODS, K. T. & RIENKS, I. 1992. New Insights into the Structure and Subdivision of the Ravenswood Batholith — A Geophysical Perspective. *Exploration Geophysics,* 23**,** 353-359.

WOOLDRIDGE, S. A. 2009. Water quality and coral bleaching thresholds: Formalising the linkage for the inshore reefs of the Great Barrier Reef, Australia. *Marine Pollution Bulletin,* 58**,** 745-751.

YIBELTAL, M., TSUNEKAWA, A., HAREGEWEYN, N., ADGO, E., MESHESHA, D. T., AKLOG, D., MASUNAGA, T., TSUBO, M., BILLI, P., VANMAERCKE, M., EBABU, K., DESSIE, M., SULTAN, D. & LIYEW, M. 2019a. Analysis of long-term gully dynamics in different agro-ecology settings. *CATENA,* 179**,** 160-174.

YIBELTAL, M., TSUNEKAWA, A., HAREGEWEYN, N., ADGO, E., MESHESHA, D. T., MASUNAGA, T., TSUBO, M., BILLI, P., EBABU, K. & FENTA, A. A. 2019b. Morphological characteristics and topographic thresholds of gullies in different agro-ecological environments. *Geomorphology,* 341**,** 15-27.

YOUNG, M. & EVANS, I. 1978. Statistical Characterization of Altitude Matrices by Computer. Report 5. Terrain Analysis: Program Documentation.

ZADEH, L. A. 1965. Fuzzy sets. *Information and Control,* 8**,** 338-353.

ZUCCA, C., CANU, A. & DELLA PERUTA, R. 2006. Effects of land use and landscape on spatial distribution and morphological features of gullies in an agropastoral area in Sardinia (Italy). *CATENA,* 68**,** 87-95.

Appendix A

Supplementary material for Chapter 2: A multi-resolution method to map and identify locations of future gully and channel incision

1.1 Zones of concentrated flow

Requiring that ILE floors only exist in zones of concentrated flow serves two purposes. First, it meets the description of gullies given by (Speight, 1990) as areas that experience concentrated flow. Second, it helps to reduce misidentification of ILE floors for grid cells existing in low-lying areas that may be part of, for example, a road running along a ridgeline in higher parts of a landscape. At each scale of analysis, these zones are identified by using equation 1 from the main paper to transform stream power index:

$$flow\_zone_{L,L} = 1 - N\left(SPI_{L+1,L}, 18, 4\right) \quad \text{(A.1)}$$

Where the stream power grid used is always extracted at one level of generalization higher ($SPI_{L+1,\ L}$) to ensure that these zones always encompass the low-lying flat grid cells provisionally identified as ILE floors.

1.2 Calculating primary topographic attributes

Slope (S) is calculated using the same slope algorithm implemented in the ArcGIS Desktop 10.5 software and outlined in (Burrough et al., 2015). Profile curvature (C_p) is calculated using the approach developed by (Zevenbergen and Thorne, 1987) following the methodology outlined in (Chang, 2006,Pp 284). It is defined as the first derivative of slope taken in the direction of highest change (Schmidt et al., 2003). Positive C_p values represent areas of flow acceleration, or increasing potential energy where a slope is increasing in steepness, and negative values are areas of decreasing potential energy where a slope is flattening out (Wilson, 2012). In terms of geometry, C_p values are zero for flat areas, positive where the surface is

upwardly convex and negative where it is upwardly concave (Chang et al., 2007). Larger absolute values of C_p indicate areas of faster rate of change in slope.

Elevation percentile (P_i) is calculated following Gallant and Dowling (2003). A circular moving window of radius r is used to assess a grid cell's elevation with respect to its local neighborhood.

$$\boldsymbol{P_i} = \frac{\sum_{i=1}^{n} \boldsymbol{z_i < z}}{\boldsymbol{n}} \quad \text{(A.2)}$$

Where $\boldsymbol{n}$ is proportional to r, and $\boldsymbol{z_i}$ is the elevation of the $\boldsymbol{i}$th grid cell of a moving window centered on z.

The function returns percentiles determined by the rank of the central grid cell's elevation with respect to its neighboring grid cells. Fewer grid cells with a lower elevation relative to the elevation of the central grid cell will return smaller function values.

A fixed radius of 6 cells is used for extracting each of the four components of ILEs (Section 2.1 of the paper).

1.3 Testing for presence of ILEs at each scale

The algorithm only considers ILEs to exist at a given scale if all four components are reasonably represented in the final output for the given scale. At the finest scale of analysis ($DEM_{1,1}$), threshold and shape parameter values were selected to give the best balance between separation of classes while maintaining roughly equal representation of each individual component in the final delineated ILE (eq. 2 in the main body of the paper). After identifying each ILE component and combining them together into a single grid, the algorithm assesses the relative representation of each as a percentage of the total number of grid cells classified as belonging to the ILE class. In a model scenario each component would represent 25% of the total area classified as ILEs.

If, at the finest scale, any component is represented by <10% of grid cells then the algorithm does not consider ILEs to exist. Beyond the finest scale, the algorithm reassesses the representation of each component. If at any scale greater than the base resolution the representation of a component decreases by >50% of its initial representation, the algorithm considers this component to no longer be sufficiently identifiable at that scale and will stop.

1.4 Combining areas at risk across scales

Combining outputs of ILE identification at different scales begins by combining the broadest scale of analysis ($AR_{Lmax,\ Lmax}$) with the second broadest scale of analysis ($AR_{Lmax\ -\ 1,\ Lmax\ -\ 1}$):

$$ARC_1 = w_1\left(1 + AR_{Lmax-1,Lmax-1}\right) + (1 - w_1)AR_{Lmax,Lmax} \quad \text{(A.3)}$$

Where w_1 is a weighting derived using equation (1) as follows:

$$w_1 = 1 - N\left(AR_{Lmax-1,Lmax-1}, 0.4, 6.68\right) \quad \text{(A.4)}$$

Setting $t = 0.4$ and $p = 6.68$ ensures that ARC_1 values = 1.5 when $AR_{Lmax\ -\ 1,\ Lmax\ -\ 1} = 0.6$ and $AR_{Lmax,\ Lmax} = 0$. For each subsequent step (L) the combined grid is calculated as follows:

$$ARC_L = w_L\left(1 + AR_{Lmax-\ L,Lmax-L}\right) + (1 - w_L)ARC_{L-1} \quad \text{(A.5)}$$

Where w_L is calculated such that ARC_L is always $\geq L - 0.5$ when $AR_{Lmax\ -\ L,Lmax\ -\ L} \geq 0.6$:

$$w_L = 1 - N\left(ARC_{L-1,L-1}, 0.4, p_L\right) \quad \text{(A.6)}$$

With the shape parameter (p_L) given by:

$$p_L = \frac{ln\left(\frac{L-0.5}{0.1}\right)}{ln(1.5)} \quad \text{(A.7)}$$

1.5 Assessing lowness for estimating areas at risk of incision

For assessing areas at risk of incision, the window size used to calculate elevation percentiles increases as the algorithm progresses such that the area being assessed is always roughly the same size. To achieve this the window is increased by a factor of three at each step (matching the resolution changing by a factor of three). The window size that was found to best identify low-lying areas while minimizing noise in the output and maintaining manageable memory limits was a circle window of radius = 100 at the finest resolution (1m) decreasing through 32, 12, 4 and final 2 at the broadest scale (81m). A circular window of this radius assesses an area of ~6ha.

Appendix B

Supplementary material for chapter 3: A comparison of hillslope drainage area estimation methods using high-resolution DEMs with implications for topographic studies of gullies

Figure S4: Divergent flow above a gully head in Aranda Snowgums Reserve, Australian Capital Territory.

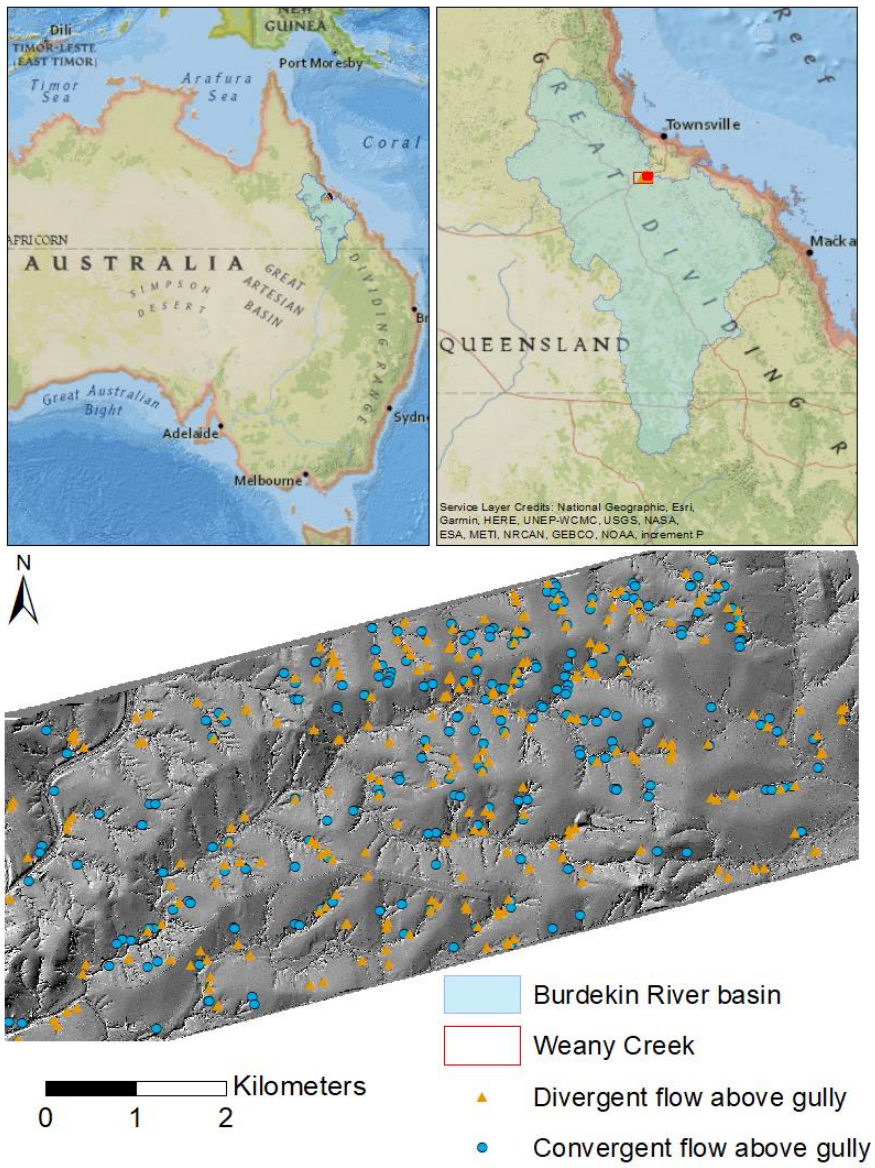

Figure S2: Weany Creek study site in the Burdekin River basin of north-eastern Australia. Orange triangles and blue dots are locations of gully heads (n = 484) with divergent or convergent flow, respectively (section 2.6).

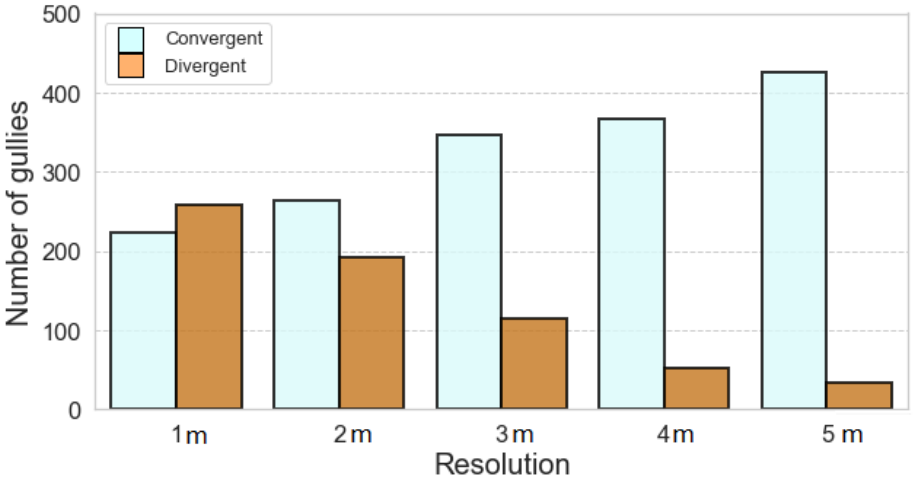

Figure S3: Number of gullies with divergent flow above the head (orange bars) compared to number of gullies with convergent flow (blue) at each of five spatial resolutions (1m, 2m, 3m, 4m and 5m).

*Table S1: Average slope and drainage area measurements for all 484 gully heads. Errors are expressed as standard deviation. In brackets are the significance levels of the difference between the two groups (ns = not significant, * = significant at p < 0.05, ** = significant at p < 0.005 and *** = significant at p < 0.0005. The subscripts div and conv denote divergent gullies and convergent gullies, respectively.*

		Routing method			
Resolution		**D8**	**Dinf**	**M4**	**M8**
1m	Area (ha)	$\bar{x}_{div} = 1.32 \pm 1.99$	$\bar{x}_{div} = 1.37 \pm 1.99$	$\bar{x}_{div} = 1.5 \pm 2.64$	$\bar{x}_{div} = 1.27 \pm 1.93$
		$\bar{x}_{conv} = 1.48 \pm 3.38$	$\bar{x}_{conv} = 1.47 \pm 3.33$	$\bar{x}_{conv} = 1.28 \pm 2.78$	$\bar{x}_{conv} = 1.14 \pm 2.22$
	$H_0 : \bar{x}_{div} = \bar{x}_{conv}$	H_0 : (ns)	H_0 : (ns)	H_0 : (*)	H_0 : (ns)
	Slope ($m.m^{-1}$)	$\bar{x}_{div} = 0.039 \pm 0.035$			
		$\bar{x}_{conv} = 0.044 \pm 0.038$			
	$H_0 : \bar{x}_{div} = \bar{x}_{conv}$	H_0 : (**)			
2m	Area (ha)	$\bar{x}_{div} = 1.7 \pm 2.17$	$\bar{x}_{div} = 1.73 \pm 2.22$	$\bar{x}_{div} = 1.9 \pm 3.15$	$\bar{x}_{div} = 1.49 \pm 1.84$
		$\bar{x}_{conv} = 1.28 \pm 2.59$	$\bar{x}_{conv} = 1.28 \pm 2.57$	$\bar{x}_{conv} = 1.24 \pm 2.39$	$\bar{x}_{conv} = 1.04 \pm 2.25$
	$H_0 : \bar{x}_{div} = \bar{x}_{conv}$	H_0 : (***)	H_0 : (***)	H_0 : (***)	H_0 : (***)
	Slope ($m.m^{-1}$)	$\bar{x}_{div} = 0.036 \pm 0.021$			
		$\bar{x}_{conv} = 0.045 \pm 0.026$			
	$H_0 : \bar{x}_{div} = \bar{x}_{conv}$	H_0 : (***)			
3m	Area (ha)	$\bar{x}_{div} = 1.74 \pm 2.51$	$\bar{x}_{div} = 1.76 \pm 2.47$	$\bar{x}_{div} = 1.81 \pm 2.6$	$\bar{x}_{div} = 1.37 \pm 1.63$
		$\bar{x}_{conv} = 1.43 \pm 2.78$	$\bar{x}_{conv} = 1.47 \pm 2.78$	$\bar{x}_{conv} = 1.5 \pm 3.15$	$\bar{x}_{conv} = 1.22 \pm 2.16$
	$H_0 : \bar{x}_{div} = \bar{x}_{conv}$	H_0 : (*)	H_0 : (*)	H_0 : (**)	H_0 : (**)
	Slope ($m.m^{-1}$)	$\bar{x}_{div} = 0.038 \pm 0.02$			
		$\bar{x}_{conv} = 0.044 \pm 0.025$			
	$H_0 : \bar{x}_{div} = \bar{x}_{conv}$	H_0 : (**)			
4m	Area (ha)	$\bar{x}_{div} = 2.68 \pm 4.85$	$\bar{x}_{div} = 2.7 \pm 4.88$	$\bar{x}_{div} = 2.86 \pm 4.82$	$\bar{x}_{div} = 2.71 \pm 4.51$
		$\bar{x}_{conv} = 1.9 \pm 5.07$	$\bar{x}_{conv} = 1.85 \pm 4.89$	$\bar{x}_{conv} = 2.0 \pm 5.85$	$\bar{x}_{conv} = 1.55 \pm 3.91$
	$H_0 : \bar{x}_{div} = \bar{x}_{conv}$	H_0 : (**)	H_0 : (**)	H_0 : (***)	H_0 : (***)
	Slope ($m.m^{-1}$)	$\bar{x}_{div} = 0.034 \pm 0.016$			
		$\bar{x}_{conv} = 0.044 \pm 0.022$			
	$H_0 : \bar{x}_{div} = \bar{x}_{conv}$	H_0 : (**)			
5m	Area (ha)	$\bar{x}_{div} = 4.71 \pm 10.07$	$\bar{x}_{div} = 4.57 \pm 10.14$	$\bar{x}_{div} = 4.04 \pm 10.17$	$\bar{x}_{div} = 4.06 \pm 10.03$
		$\bar{x}_{conv} = 1.69 \pm 4.1$	$\bar{x}_{conv} = 1.77 \pm 4.16$	$\bar{x}_{conv} = 1.86 \pm 4.1$	$\bar{x}_{conv} = 1.57 \pm 3.57$
	$H_0 : \bar{x}_{div} = \bar{x}_{conv}$	H_0 : (***)	H_0 : (***)	H_0 : (*)	H_0 : (***)
	Slope ($m.m^{-1}$)	$\bar{x}_{div} = 0.034 \pm 0.013$			
		$\bar{x}_{conv} = 0.039 \pm 0.017$			
	$H_0 : \bar{x}_{div} = \bar{x}_{conv}$	H_0 : (*)			

Table S2: Pearson's r correlation values for all pairs of resolutions under each routing method. Correlations for gullies with divergent flow above the head are in bold and convergent not bold. Low correlations (< 0.5) are shaded blue.

	Resolution	1m	2m	3m	4m	5m
D8	1m	-	**0.52**	**0.68**	**0.33**	**0.48**
	2m	0.70	-	**0.48**	**0.18**	**0.40**
	3m	0.49	0.65	-	**0.48**	**0.41**
	4m	0.30	0.41	0.88	-	**0.36**
	5m	0.57	0.75	0.64	0.45	-
D_{inf}	1m	-	**0.68**	**0.71**	**0.35**	**0.48**
	2m	0.71	-	**0.60**	**0.22**	**0.47**
	3m	0.51	0.67	-	**0.44**	**0.47**
	4m	0.31	0.41	0.89	-	**0.35**
	5m	0.59	0.76	0.66	0.46	-
M4	1m	-	**0.94**	**0.90**	**0.46**	**0.77**
	2m	0.88	-	**0.89**	**0.54**	**0.80**
	3m	0.65	0.75	-	**0.58**	**0.79**
	4m	0.42	0.49	0.90	-	**0.56**
	5m	0.59	0.69	0.94	0.88	-
M8	1m	-	**0.80**	**0.85**	**0.73**	**0.76**
	2m	0.68	-	**0.72**	**0.83**	**0.64**
	3m	0.56	0.86	-	**0.73**	**0.73**
	4m	0.39	0.55	0.83	-	**0.67**
	5m	0.47	0.72	0.91	0.92	-

Table S3: Coefficient k and exponent b estimates for divergent ('div') and convergent ('con') gullies at each resolution (1, 2, 3 ,4 and 5 m). Columns show results for each routing algorithm. Errors are expressed as standard error. H_0 is the null hypothesis $\bar{x}_{div} = \bar{x}_{conv}$ *and in brackets are the significance levels of the difference between the two groups (ns = not significant, * = significant at p < 0.05, ** = significant at p < 0.005 and *** = significant at p < 0.0005.*

	Flow routing method			
Cell size	D8	Dinf	M4	M8
		Exponent (*b*)		
1 m	$\bar{x}_{div}$ = 0.051 ± 0.002 $\bar{x}_{con}$ = 0.157 ± 0.01 H_0 : (***)	$\bar{x}_{div}$ = 0.085 ± 0.002 $\bar{x}_{con}$ = 0.204 ± 0.001 H_0 : (***)	$\bar{x}_{div}$ = 0.179 ± 0.001 $\bar{x}_{con}$ = 0.197 ± 0.001 H_0 : (*)	$\bar{x}_{div}$ = 0.183 ± 0.003 $\bar{x}_{con}$ = 0.234 ± 0.002 H_0 : (*)
2 m	$\bar{x}_{div}$ = 0.084 ± 0.004 $\bar{x}_{con}$ = 0.143 ± 0.004 H_0 : (***)	$\bar{x}_{div}$ = 0.123 ± 0.004 $\bar{x}_{con}$ = 0.192 ± 0.005 H_0 : (***)	$\bar{x}_{div}$ = 0.184 ± 0.005 $\bar{x}_{con}$ = 0.225 ± 0.006 H_0 : (*)	$\bar{x}_{div}$ = 0.214 ± 0.006 $\bar{x}_{con}$ = 0.235 ± 0.006 H_0 : (ns)
3 m	$\bar{x}_{div}$ = 0.03 ± 0.003 $\bar{x}_{con}$ = 0.167 ± 0.005 H_0 : (***)	$\bar{x}_{div}$ = 0.073 ± 0.004 $\bar{x}_{con}$ = 0.22 ± 0.006 H_0 : (***)	$\bar{x}_{div}$ = 0.07 ± 0.004 $\bar{x}_{con}$ = 0.226 ± 0.006 H_0 : (***)	$\bar{x}_{div}$ = 0.121 ± 0.004 $\bar{x}_{con}$ = 0.2 ± 0.007 H_0 : (*)
4 m	$\bar{x}_{div}$ = 0.02 ± 0.003 $\bar{x}_{con}$ = 0.175 ± 0.006 H_0 : (***)	$\bar{x}_{div}$ = 0.021 ± 0.003 $\bar{x}_{con}$ = 0.221 ± 0.006 H_0 : (***)	$\bar{x}_{div}$ = 0.006 ± 0.003 $\bar{x}_{con}$ = 0.282 ± 0.01 H_0 : (***)	$\bar{x}_{div}$ = 0.078 ± 0.003 $\bar{x}_{con}$ = 0.252 ± 0.007 H_0 : (*)
5 m	$\bar{x}_{div}$ = 0.034 ± 0.002 $\bar{x}_{conv}$ = 0.037 ± 0.0 H_0 : (***)	$\bar{x}_{div}$ = 0.061 ± 0.003 $\bar{x}_{conv}$ = 0.259 ± 0.008 H_0 : (***)	$\bar{x}_{div}$ = 0.073 ± 0.003 $\bar{x}_{conv}$ = 0.292 ± 0.01 H_0 : (***)	$\bar{x}_{div}$ = 0.06 ± 0.011 $\bar{x}_{conv}$ = 0.298 ± 0.011 H_0 : (*)
		Coefficient (*k*)		
1 m	$\bar{x}_{div}$ = 0.036 ± 0.0 $\bar{x}_{con}$ = 0.032 ± 0.0 H_0 : (***)	$\bar{x}_{div}$ = 0.036 ± 0.0 $\bar{x}_{con}$ = 0.032 ± 0.0 H_0 : (***)	$\bar{x}_{div}$ = 0.037 ± 0.0 $\bar{x}_{con}$ = 0.031 ± 0.0 H_0 : (***)	$\bar{x}_{div}$ = 0.038 ± 0.0 $\bar{x}_{con}$ = 0.031 ± 0.0 H_0 : (***)
2 m	$\bar{x}_{div}$ = 0.033 ± 0.0 $\bar{x}_{con}$ = 0.04 ± 0.0 H_0 : (***)	$\bar{x}_{div}$ = 0.034 ± 0.0 $\bar{x}_{con}$ = 0.039 ± 0.0 H_0 : (***)	$\bar{x}_{div}$ = 0.033 ± 0.0 $\bar{x}_{con}$ = 0.038 ± 0.0 H_0 : (***)	$\bar{x}_{div}$ = 0.031 ± 0.0 $\bar{x}_{con}$ = 0.037 ± 0.0 H_0 : (***)
3 m	$\bar{x}_{div}$ = 0.034 ± 0.0 $\bar{x}_{con}$ = 0.039 ± 0.0 H_0 : (***)	$\bar{x}_{div}$ = 0.034 ± 0.0 $\bar{x}_{con}$ = 0.039 ± 0.0 H_0 : (***)	$\bar{x}_{div}$ = 0.034 ± 0.0 $\bar{x}_{con}$ = 0.038 ± 0.0 H_0 : (***)	$\bar{x}_{div}$ = 0.033 ± 0.0 $\bar{x}_{con}$ = 0.037 ± 0.0 H_0 : (***)
4 m	$\bar{x}_{div}$ = 0.031 ± 0.0 $\bar{x}_{con}$ = 0.04 ± 0.0 H_0 : (***)	$\bar{x}_{div}$ = 0.031 ± 0.0 $\bar{x}_{con}$ = 0.039 ± 0.0 H_0 : (***)	$\bar{x}_{div}$ = 0.031 ± 0.0 $\bar{x}_{con}$ = 0.038 ± 0.0 H_0 : (***)	$\bar{x}_{div}$ = 0.031 ± 0.0 $\bar{x}_{con}$ = 0.037 ± 0.0 H_0 : (***)
5 m	$\bar{x}_{div}$ = 0.034 ± 0.0 $\bar{x}_{con}$ = 0.037 ± 0.0 H_0 : (***)	$\bar{x}_{div}$ = 0.033 ± 0.0 $\bar{x}_{con}$ = 0.036 ± 0.0 H_0 : (***)	$\bar{x}_{div}$ = 0.031 ± 0.0 $\bar{x}_{con}$ = 0.036 ± 0.0 H_0 : (***)	$\bar{x}_{div}$ = 0.039 ± 0.0 $\bar{x}_{con}$ = 0.034 ± 0.0 H_0 : (**)

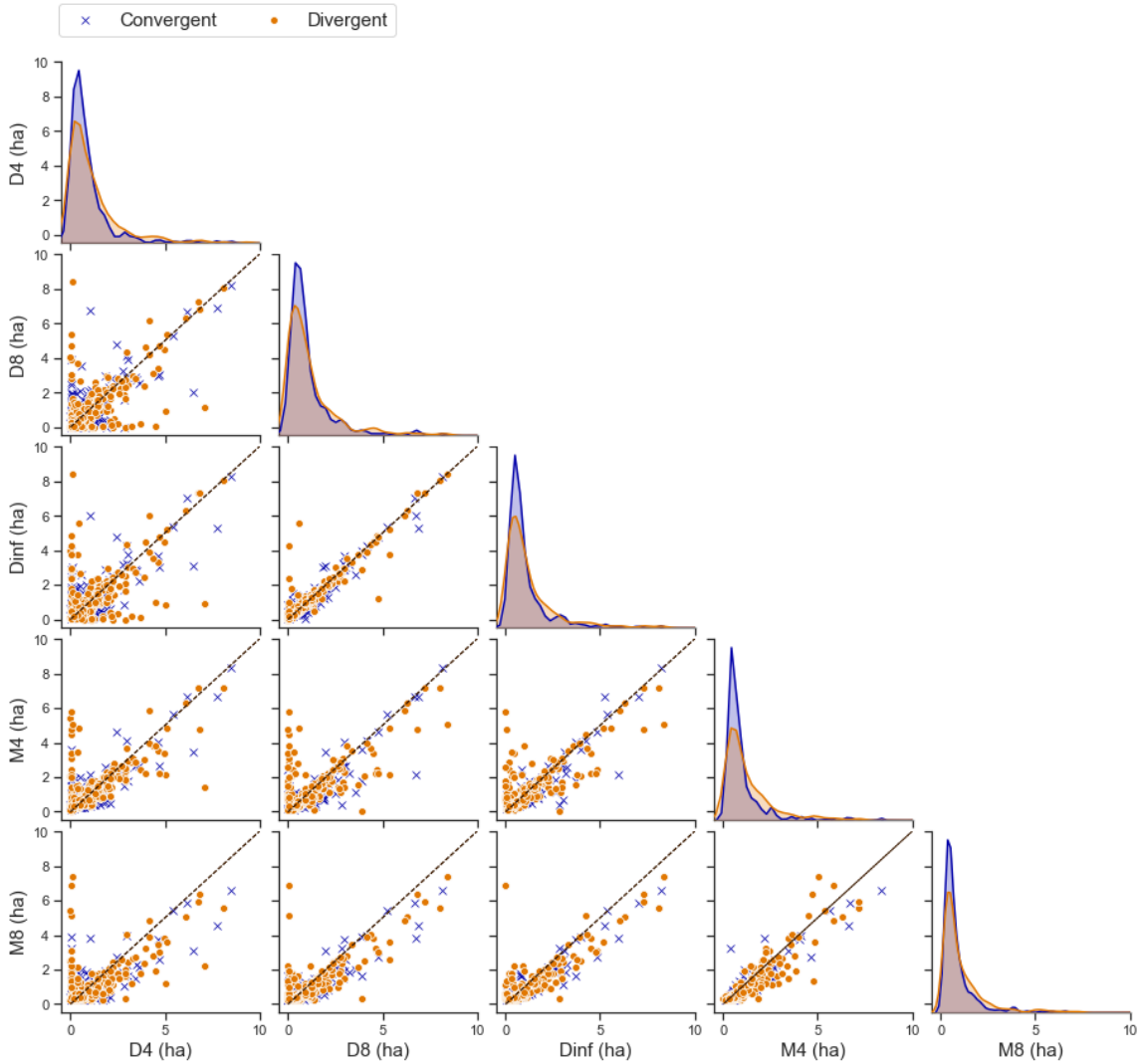

Figure S4: Correlations between all pairs of routing algorithms at 1m spatial resolution. All 484 gully heads are separated according to divergent (orange) or convergent (blue) flow above the gully head. The top row of each column shows the distribution of the estimated drainage areas.

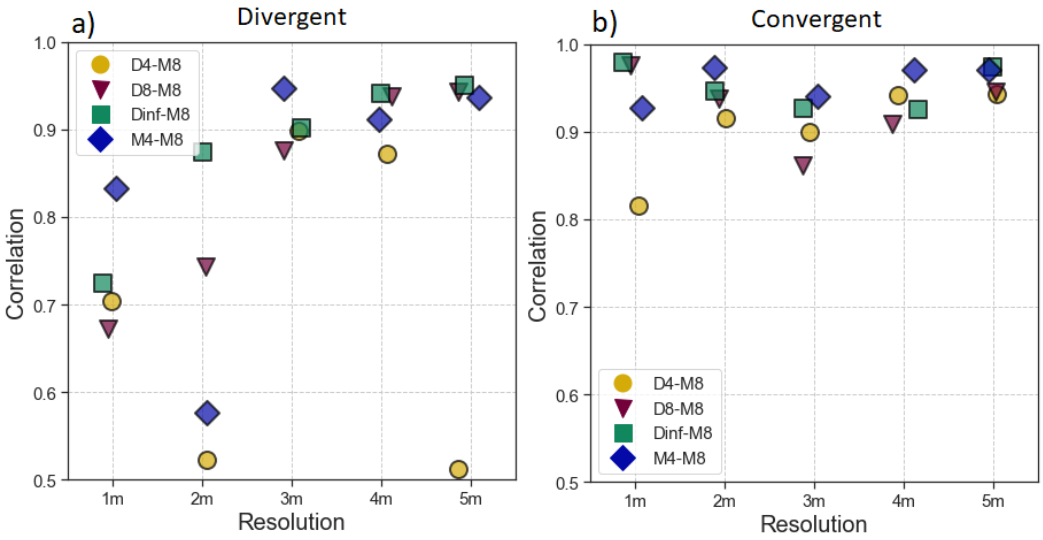

Figure S5: Pearson's r correlation between the M8 algorithm and each other routing algorithm. Each point represents one correlation pair, with resolution increasing along the x-axis. All 484 gully heads are separated according to divergent (Panel a) or convergent (Panel b) flow above the gully head.